



**HAL**  
open science

# Exploring the Low-Mass Initial Mass Function in Young Clusters and Star-Forming Regions

Andrew S. M. Burgess

► **To cite this version:**

Andrew S. M. Burgess. Exploring the Low-Mass Initial Mass Function in Young Clusters and Star-Forming Regions. Astrophysics [astro-ph]. Université de Grenoble, 2010. English. NNT: . tel-00576460

**HAL Id: tel-00576460**

**<https://theses.hal.science/tel-00576460>**

Submitted on 14 Mar 2011

**HAL** is a multi-disciplinary open access archive for the deposit and dissemination of scientific research documents, whether they are published or not. The documents may come from teaching and research institutions in France or abroad, or from public or private research centers.

L'archive ouverte pluridisciplinaire **HAL**, est destinée au dépôt et à la diffusion de documents scientifiques de niveau recherche, publiés ou non, émanant des établissements d'enseignement et de recherche français ou étrangers, des laboratoires publics ou privés.



UNIVERSITÉ DE GRENOBLE

---

THÈSE  
pour obtenir le grade de  
DOCTEUR DE L'UNIVERSITÉ DE GRENOBLE  
Spécialité : ASTROPHYSIQUE ET MILIEUX DILUÉS  
Arrêtés ministériels du 7 août 2006

présentée et soutenue publiquement par

**A. S. M. BURGESS**

le 15<sup>ième</sup> décembre 2010

---

**Exploring the Low-Mass Initial Mass Function in  
Young Clusters and Star-Forming Regions<sup>1</sup>**

-

**Exploration de la fonction de faible masse initiale  
dans les amas jeunes et les régions de formation  
stellaire**

---

Thèse dirigée par Jerome Bouvier et corrigée par Estelle Moraux

**JURY**

M.	Jean-Louis MONIN	Président
Mme.	France ALLARD	Rapporteur
M.	Eduardo MARTÍN	Rapporteur
M.	Jérôme BOUVIER	Examinateur
M.	Nicolas LODIEU	Examinateur
Mme.	Estelle MORAUX	Examinateur

Thèse préparée au sein du  
*Laboratoire d'Astrophysique et Observatoire de Grenoble dans l'École Doctorale de  
Physique*

UMR-5571 (OSUG/UJF/CNRS), BP 53, F-38041 Grenoble Cedex 9

---

<sup>1</sup>Based on observations obtained with WIRCam, a joint project of CFHT, Taiwan, Korea, Canada, France, at the Canada-France-Hawaii Telescope (CFHT) which is operated by the National Research Council (NRC) of Canada, the Institute National des Sciences de l'Univers of the Centre National de la Recherche Scientifique of France, and the University of Hawaii. Research supported by the Marie Curie Research Training Network "CONSTELLATION" under grant no. MRTN-CT-2006-035890



# **Exploring the Low-Mass Initial Mass Function in Young Clusters and Star-Forming Regions**

Andrew S. M. Burgess

A thesis submitted to the University of Joseph Fourier  
in accordance with the requirements of the degree of  
Doctor of Philosophy  
in the Ecole Doctorale

*Laboratoire d'Astrophysique et  
Observatoire de Grenoble  
414 Rue de la Piscine  
Domaine Universitaire  
38400 Saint-Martin d'Hères  
FRANCE*

15<sup>th</sup> October 2010

~ 50,000 words



# Abstract

The determination of the lower-end of the initial mass function (IMF) provides strong constraints on star formation theories. We report here on a search for isolated planetary-mass objects in the 3 Myr-old star-forming region IC 348 and on a wider survey of the 30 Myr-old open cluster IC 4665. IC 4665 is a fairly young ( $\sim 30$  Myr) star cluster and is 356 pc distant towards the constellation Ophiuchus. Proper motion is low at  $-4$  to  $-7.5$  mas/yr and extinction is also low and present at  $A_V \sim 0.59 \pm 0.15$  mag. WIRCam  $Y$ ,  $J$ ,  $H$  and  $K_s$  observations were made using the CFHT and spanned 10 cluster fields (of total footprint  $\sim 1.1$  sq.deg) and two control fields of  $20' \times 20'$  each. Colour/magnitude diagrams were used to compare the catalogue objects to the 30 and 50 Myr BT-SETTL models for photometric selection. Further colour/colour diagrams were then iteratively used to further filter these objects into a final cluster candidate member list, with 590 unique objects. Contamination by field stars can be assessed using the control fields and M- and L- dwarf space densities. This part requires further analysis.

Probing into the lowest-mass end of the IMF in IC 348 required deep, narrowband  $CH_4$ off and  $CH_4$ on images. These were obtained with CFHT/WIRCam over 0.11 sq.deg. over the central part of IC 348, along with  $z'$ ,  $J$ ,  $H$  and  $K_s$  band images. Young T-dwarfs were identified from their  $1.69 \mu\text{m}$  methane absorption bands. Three faint T-dwarf candidates were detected with  $CH_4\text{on} - CH_4\text{off}$  colours  $> 0.4$  mag. Extinction was estimated for each candidate and lies in the range  $A_V \sim 5 - 12$  mag. Comparisons with T-dwarf spectral models, and colour/colour and colour/magnitude diagrams, reject two of the three candidates because of their extreme  $z' - J$  blueness. The one remaining object is not thought to be a foreground field dwarf because of a number density argument and also its strong extinction  $A_V \sim 12$  mag, or thought to be a background field T-dwarf which would be expected to be much fainter. Models and diagrams give this object a preliminary T6 spectral type. With a few Jupiter masses, the young T-dwarf candidate reported here is potentially amongst the youngest, lowest mass objects detected in a star-forming region so far. Its frequency is consistent with the extrapolation of current lognormal IMF estimates down to the planetary mass domain.



### *Le Résumé en Français*

La détermination de l'extrémité inférieure de la fonction de masse initiale (FMI) prévoit de fortes contraintes sur les théories de la formation des étoiles. IC4665 est un amas d'étoile jeune (30Myr) et il se situe à 356pc de la Terre. L'extinction est  $A_V \sim 0.59 \pm 0.15$  mag. WIRCam Y, J, H et K observations ont été faites par le CFHT et a comprise 10 champs (de 1.1sq.deg totale) et deux zones de contrôle de 20'x20' chacun. Diagrammes couleur/magnitude et couleur/couleur ont été utilisés pour comparer les candidats sélectionnés par les modèles BT-SETTL 30 et 50Myr.

Les images  $CH_4$ off et  $CH_4$ on ont été obtenus avec CFHT/WIRCam plus 0.11 sq.deg. dans IC348. Naines-T ont ensuite été identifiés à partir de leur couleur de  $1.69\mu\text{m}$  d'absorption du méthane et trois candidats nain-T ont été trouvés avec  $CH_4\text{on}-CH_4 > 0.4$  mag. Extinction a été estimée à  $A_V \sim 5 - 12$  mag. Les comparaisons avec les naines-T modèles, et des diagrammes couleur/couleur et magnitude, rejeter 2 entre 3 candidats en raison de leur extrême  $z' - J$  couleur. L'objet reste n'est pas considéré comme un nain avant l'amas en raison d'un argument de densité en nombre ou l'extinction forte  $A_V \sim 12$  mag, ni d'être un champ de fond nain-T qui serait devrait être beaucoup plus faible. Les modèles et les schémas de donner cet objet un type T6 préliminaires spectrale. Avec un peu de la masse de Jupiter, ce jeune candidat nain-T est potentiellement parmi les plus jeunes, des objets de masse plus faible détectée dans une région de formation d'étoiles à ce jour. Sa fréquence est conforme à l'extrapolation du courant lognormal FMI estimée à au domaine de masse planétaire





# Contents

Abstract . . . . .	iii
Table of Contents . . . . .	vii
List of Figures . . . . .	xi
List of Tables . . . . .	xv
Acknowledgments . . . . .	xvii
<b>1 Introduction and Review</b>	<b>1</b>
1.1 Overview . . . . .	1
1.2 Introduction . . . . .	3
1.2.1 Temperature & Luminosity . . . . .	4
1.2.2 Absorption & Emission . . . . .	7
1.2.3 Extinction & Reddening . . . . .	8
1.3 Stellar and Sub-Stellar Mass Objects . . . . .	12
1.3.1 Stellar Objects . . . . .	12
1.3.2 Sub-Stellar Objects . . . . .	12
1.3.3 Models . . . . .	14
1.3.4 Youth & Gravity Considerations . . . . .	18
1.4 Initial Mass Function (IMF) . . . . .	18
1.4.1 Observations . . . . .	20
1.4.2 Formation Mechanisms & Simulations . . . . .	22
1.5 Motivation . . . . .	25
1.5.1 Observational Strategy . . . . .	26
1.6 Summary . . . . .	28
1.7 Résumé . . . . .	31
<b>2 Data Acquisition and Pipeline Development</b>	<b>33</b>
2.1 Instrumentation & Observations . . . . .	34
2.1.1 Principal Observatory - Canada France Hawaii Telescope (CFHT) . . . . .	34
2.1.2 Observed Data . . . . .	38

2.2	Infrared Surveys & Astronomical Databases . . . . .	45
2.2.1	2Micron All Sky Survey (2MASS) . . . . .	45
2.2.2	UKIRT Infrared Deep Sky Survey (UKIDSS) . . . . .	45
2.2.3	Spitzer Space Telescope . . . . .	46
2.2.4	Online Respositories . . . . .	47
2.3	Pipeline Development . . . . .	48
2.3.1	SExtractor First-Pass . . . . .	49
2.3.2	SExtractor Optimisation . . . . .	50
2.3.3	Point Source Function Extractor (PSFEx) . . . . .	53
2.3.4	PSFEx Optimisation . . . . .	55
2.3.5	SExtractor Second-Pass . . . . .	55
2.3.6	Catalogue Amalgamation . . . . .	56
2.3.7	Calibration . . . . .	56
2.4	Summary . . . . .	62
2.5	Résumé . . . . .	63
<b>3</b>	<b>Sub-Stellar Census of the Open Cluster IC 4665</b>	<b>65</b>
3.1	Introduction . . . . .	66
3.1.1	The Open Cluster IC 4665 . . . . .	67
3.2	Object Catalogue Extraction . . . . .	71
3.2.1	Data Testing . . . . .	71
3.2.2	Specifics of Object Detection . . . . .	72
3.2.3	Flags . . . . .	74
3.3	Calibration . . . . .	75
3.3.1	Short & Long Amalgamation . . . . .	81
3.3.2	Completeness . . . . .	82
3.4	Candidate Selection . . . . .	87
3.4.1	Colour/Magnitude Diagram Selection . . . . .	87
3.4.2	Colour/Colour Diagram Selection . . . . .	88
3.4.3	Candidate Cleaning . . . . .	88
3.5	Discussion . . . . .	92
3.5.1	Recovered Known Members . . . . .	92
3.5.2	Selection Considerations . . . . .	92
3.5.3	Contamination . . . . .	94
3.6	Summary . . . . .	96
3.7	Résumé . . . . .	97

<b>4</b>	<b>Young T-dwarf Candidates in IC 348</b>	<b>99</b>
4.1	Introduction & Context . . . . .	99
4.1.1	Searching for T-dwarfs . . . . .	100
4.1.2	The Young Star-Forming Region IC 348 . . . . .	101
4.2	Specific Data Treatment . . . . .	103
4.2.1	Photometric Catalogue . . . . .	104
4.2.2	Photometric Comparison . . . . .	104
4.2.3	Methane Photometry . . . . .	106
4.3	Results . . . . .	109
4.3.1	T-dwarf Candidate Selection . . . . .	109
4.3.2	Reddening & Spectral Type Estimates . . . . .	111
4.4	Discussion . . . . .	112
4.4.1	Membership . . . . .	112
4.4.2	Contaminants . . . . .	114
4.4.3	Comparison of IC348_CH4_2 with S Ori 70 . . . . .	115
4.4.4	The Lower End of the IMF . . . . .	119
4.5	Conclusions . . . . .	120
4.6	Résumé . . . . .	121
<b>5</b>	<b>Discussion and Conclusions</b>	<b>123</b>
5.1	IC 4665 & IC 348 Revisited . . . . .	123
5.2	Future Work . . . . .	124
5.3	Context . . . . .	125
5.4	Conclusion . . . . .	127
5.5	Résumé . . . . .	129
	<b>Appendix</b>	<b>141</b>



# List of Figures

1.1	Wien's Law for various temperatures as an example of the peak temperature of a black body. . . . .	4
1.2	A Hertzsprung-Russell diagram . . . . .	6
1.4	The absorption spectrum of water by the Earth's atmosphere over the 2MASS $J$ , $H$ , and $K_s$ passbands. . . . .	7
1.3	Observed spectra for the Sun and example object Wolf 359, for a comparison between black-body temperatures. . . . .	10
1.5	The normalised curves of various O and B stars' interstellar extinction are plotted as a function $\frac{1}{\lambda}$ against $E(\lambda - V)$ . . . . .	11
1.6	Relation between the increase in dust and the reduction in temperature of an object. . . . .	17
1.7	The IMFs of three young ( $\sim 100$ Myr) clusters compared to the older Hyades (625 Myr) and the field system IMF. . . . .	21
1.8	Dynamical simulation isochrones for different starting parameters, which are then plotted over an empirical IMF of the young star-forming region IC 348. . . . .	22
1.9	Formation of a brown dwarf with its own disk of gas and dust. . . . .	23
1.10	IMFs of three dynamical simulations at different accretion radii and/or Jeans masses. . . . .	24
1.11	An HII region/dust mapped schematic view (from Drimmel and Spergel (2001)) of the Milky Way as seen from above. . . . .	28
2.1	WIRCam CCD layout and detector imprint with gaps of order $\sim 45''$ ; and MegaCam detector mosaic layouts and detector imprint showing the location of gaps, ranging from $\sim 13$ to $\sim 80''$ . . . . .	36
2.2	Raw filter responses from the WIRCam detector where the $Y$ , $J$ , $H$ and $K_s$ are shown, along with the $CH_4$ off/ $CH_4$ on narrowband filters and the quantum efficiency of the detector. . . . .	37
2.3	MegaCam $u'$ , $g'$ , $r'$ , $i'$ and $z'$ filters and associated CFHT quantum efficiency of the detector. . . . .	38

2.4	IC 348 data showing the $J$ -band image extended using blank pixel to the FOV of the MegaCam images, additionally the $J$ -band weight map is superimposed onto the $J$ -band image. . . . .	40
2.5	The FOV of fields A through to J observations of IC 4665. The two control fields are located out of the frame of this image. . . . .	41
2.6	Field of view of IC 348, showing the WIRCam and MegaCam fields of view superimposed onto the $20' \times 20'$ $CH_4$ off image. . . . .	44
2.7	Data taken from the DR2 UKIDSS release showing the offset of the $Y$ -band compared to the field stars. . . . .	47
2.8	Schematic of the the pipeline used in this work from the CFHT observations to the use of Source Extractor and PSFEx and the calibration of the IC 4665 data onto UKIDSS. . . . .	58
2.9	Cut-outs of the $Y$ -band long image of IC 4665, depicting the problem with the detection of objects within the PSF of a saturated star. . . . .	59
2.10	Gaussian and mexhat filters and their respective detections overplotted onto observed IC 4665 images. . . . .	59
2.11	CMD of mag-auto vs mag-aperture–mag-auto for IC 4665 field A for aperture size determination. . . . .	60
2.12	IC4665 field A, $J$ -band: Comparison background estimates using different background sizes that SExtractor uses as a zero point for the photometry and detection objects. . . . .	60
2.13	$J$ -band diagnostic maps outputted by PSFEx for IC 4665 field A. . . . .	61
3.1	A composite image of IC 4665 using $J$ , $H$ , and $K_s$ band data. . . . .	66
3.2	137 Manzi et al. (2008) candidate objects taken from the literature are plotted on an $I-I-Z$ CMD. . . . .	69
3.3	Manzi et al. (2008) radial velocity data. . . . .	70
3.4	Image cut-outs for the long $Y$ , $J$ , $H$ and $K_s$ bands to expose the difference between these images and to see which one to use for detection. . . . .	73
3.5	Long exposure $J$ saturation plots showing the offsets between the CFHT IC 4665 data and UKIDSS data over the same FOV. . . . .	75
3.6	$Y$ vs. $Y - K_s$ CMDs showing objects detected from our fields, matched with data that was taken from the DR5 UKIDSS catalogue . . . . .	78
3.7	The plots of the offsets between those models convolved with the CFHT and those with UKIDSS. . . . .	84
3.8	Real offset for the data in field J for the amalgamated $Y$ -band. . . . .	85

3.9	Diagnostic sample showing the saturation limit, completeness limit, rms error, and the flux radius, as a function of magnitude for the amalgamated short and long exposures. . . . .	86
3.10	IDL selection criteria including the x and y axis error bars for each object in the input catalogue. . . . .	87
3.11	CMD candidate selection using the 30 and 50 Myr BT-Settl isochrones. . . . .	90
3.12	$Y - J$ vs $J - H$ and $J - H$ vs $H - K_s$ COLD candidate selection using the 30 and 50 Myr BT-Settl isochrones. . . . .	91
3.13	$Y - J/J - H$ COLD showing the location of the final selected candidates compared to the 30 and 50 Myr BT-Settl isochrones. . . . .	93
3.14	Distribution of selected candidates over the FOV of the IC 4665 observations. . .	95
4.1	A composite image of IC 348 using $J$ , $H$ , and $K_s$ band data. . . . .	102
4.2	$\log(N_{Obj})$ vs. magnitude completeness plots, and photometric error vs. magnitude plots. . . . .	105
4.3	$CH_{4on} - CH_{4off}$ vs. spectral type, showing how the increasing methane colour is related to the spectral type. . . . .	107
4.4	$T_{eff}$ vs $CH_{4on} - CH_{4off}$ plots describing the relation between colour and effective temperature. . . . .	108
4.5	$CH_{4on} - CH_{4off}$ vs $CH_{4off}$ CMD of IC 348. . . . .	110
4.6	Thumbsized $CH_{4off}$ images of the three T-dwarf candidates. . . . .	111
4.7	$J - H$ , $J - K_s$ and $H - K_s$ vs $CH_{4on} - CH_{4off}$ CMDs showing the method for dereddening the candidates towards the 3 Myr COND model. . . . .	112
4.8	$J$ vs $J - K_s$ CMD showing the location of IC 348 M6–M9dwarfs, reddened and dereddened candidates and S Ori 70 for comparison. . . . .	113
4.9	$z' - J$ vs $J - H$ CMD with S Ori 70 and COND and DUSTY models. . . . .	115
4.10	$J - H$ vs $H - K_s$ CMD, as Figure 4.8. . . . .	116
4.11	$K_s - 3.6$ vs $3.6 - 4.5$ CFHT/ <i>Spitzer</i> COLD, comparing IC 348 objects with disks, the candidates with <i>Spitzer</i> data, and S Ori 70 for comparison. . . . .	118
5.1	Detected objects in $\sigma$ Orionis and IC 348 overplotted onto IMF predictions based upon different initial condition. . . . .	127
2	Saturation plots showing the offsets between the CFHT IC 4665 data and UKIDSS data over the same FOV. . . . .	152





# List of Tables

1.1	A list of stellar and sub-stellar spectral types from O as the hottest down the newly allocated Y dwarfs. . . . .	5
1.2	Summaries of various cluster surveys using infrared data to prove the IMF. . . . .	20
2.1	Field of view (FOV), filters, FWHM's and extinction co-efficients of the associated CFHT MegaCam ( $z'$ ) and WIRCam (Y, J, H, K <sub>s</sub> , methane-off and methane-on) filters. . . . .	35
2.2	The FOV, fields and associated central coordiantes of the WIRCam <i>Y</i> , <i>J</i> , <i>H</i> and <i>K<sub>s</sub></i> fields of IC 4665 including the location of the two control fields. . . . .	42
2.3	List of the observing programs and respective exposure and integration times for the <i>Y</i> , <i>J</i> , <i>H</i> and <i>K<sub>s</sub></i> long and short exposure observations of IC 4665. . . . .	43
2.4	Field of view and pointings towards IC 348; filters and integration are also summerised. . . . .	43
2.5	SExtractor configuration options for both the first- and second-pass extraction routines for IC 4665 and IC 348 . . . . .	51
2.6	Configuraton options that were changed for the analysis with PSFEx. . . . .	54
3.1	Aperture selection offsets for aperture optimisation converging to 0.03 for an aperture footprint of 31. . . . .	72
3.2	Calibration values for the 2MASS calibration attempt. Median values, dispersion values and the average number of stars used are shown. Note the lack of <i>Y</i> -band data in order to calibrate the short exposures onto 2MASS. . . . .	77
3.3	Median differences and dispersion values between the short exposures and UKIDSS, and the long exposures and UKIDSS, which were then used for calibration. . . . .	79
3.4	Comparison between the 2MASS and UKIDSS calibration methods. . . . .	80
3.5	Median <i>Y</i> -band calibration values of C1 and C2 compared to median of other 10 fields . . . . .	81
3.6	Average completeness magnitudes are shown over all cluster fields, as well as associated masses for both 30 and 40 Myr BTCOND models . . . . .	82

3.7	Sample final candidate list whose objects have made it through the CMD, COLD and visual inspection analysis. . . . .	89
4.1	PSF photometry and photometric errors of the three T-dwarf candidates, in magnitudes . . . . .	111
4.2	Summary of values for the three IC 348 candidates. . . . .	112
4.3	Spitzer PSF photometry and photometric errors of the three T-dwarf candidates. .	117
1	. . . . .	146

# Acknowledgments

I hope this will be a description of how the completion of this work has been made possible, from how the all the people I have been in contact with over the journey have helped along the way, to how it has been possible for me to arrive at point A, and come to point B.

It was the advice from my friends and family in the UK that made it possible for me to complete a PhD which, up until a few years ago, I would have dismissed a dream. The very nature of being human is to be able to change and improve yourself until you are happy with the result; indeed if you are unhappy then you should isolate the negative aspects and focus on changing them for the better. In order for me to have achieved this I must take into account and thank those who have made it possible so, I shall just reel off a few words of great thank you to various parties:

Avon Huxor who initially suggested that I apply to the Constellation Network, all the node leaders and the network mastermind for the network creation and, of course, the People of Europe who through their taxes and hard work (mine included!) made such a great network possible and are *all* deserving of my thanks for this opportunity of betterment. Special consideration goes to Jerome & Estelle who have guided me through the maze known as research. Thanks to the all of the great people I have met through this network and my best wishes for the future goes out to them all. Thanks to the various post-docs who have attended LAOG throughout the years; Gareth Murphy, Catarina Alves de Oliveria and Philippe Delorme for their expertise, and especially Adam Hill who offered reams of advice and made available a wealth of experience about "How to Write a Thesis in 42 Days and Nights". And thanks to Steph Renard and Mickael Bonnefoy for their unfaltering camaraderie in Bureau 13.

Gnu Chess I found to be extremely annoying throughout the difficult period of writing the manuscript, because of the continual beating I was mercilessly given for pretty much the whole thesis write up. Mr. Oban 14yrs Old also deserves a mention for giving the added motivation at the end of the long day to do. Just. One. More. Page... I thank also the Druids Pub and the Hasard, both in Grenoble for their comfortable and relaxing environments in order to reset after the (many) annoying days of analysis and bug-finding. But of course, these places would be all for naught without the good friends I have met and gotten to know whilst in Grenoble, to all of my friends

both native and international it has been a pleasure to get to know you and I hope that we shall keep in touch for all the time to come.

Andrew Stuart Manvell Burgess

Disclaimer: This work is not part of any ecclesiastical or other religious body.

The work presented here has made use of NASA's Astrophysics Data System (ADS), the Vizier Database, and the SIMBAD database, operated at CDS, Strasbourg, France. Based on observations obtained with MegaPrime/MegaCam and WIRCam, a joint project of CFHT, Taiwan, Korea, Canada, France, at the Canada-France-Hawaii Telescope (CFHT) which is operated by the National Research Council (NRC) of Canada, the Institut National des Sciences de l'Univers of the Centre National de la Recherche Scientifique of France, and the University of Hawaii. We thank the QSO team at CFHT for their efficient work at the telescope and the data pre-reduction as well as the Terapix group at IAP for the image reduction. This work is based in part on data products produced and image reduction processes conducted at TERAPIX. This research has made use of the NASA/ IPAC Infrared Science Archive, which is operated by the Jet Propulsion Laboratory, California Institute of Technology, under contract with the National Aeronautics and Space Administration. Spitzer. This publication makes use of data products from the Two Micron All Sky Survey, which is a joint project of the University of Massachusetts and the Infrared Processing and Analysis Center/California Institute of Technology, funded by the National Aeronautics and Space Administration and the National Science Foundation. This research has benefitted from the M, L, and T dwarf compendium housed at DwarfArchives.org and maintained by Chris Gelino, Davy Kirkpatrick, and Adam Burgasser.





# Chapter 1

## Introduction and Review

### Contents

---

<b>1.1 Overview</b> . . . . .	<b>1</b>
<b>1.2 Introduction</b> . . . . .	<b>3</b>
1.2.1 Temperature & Luminosity . . . . .	4
1.2.2 Absorption & Emission . . . . .	7
1.2.3 Extinction & Reddening . . . . .	8
<b>1.3 Stellar and Sub-Stellar Mass Objects</b> . . . . .	<b>12</b>
1.3.1 Stellar Objects . . . . .	12
1.3.2 Sub-Stellar Objects . . . . .	12
1.3.3 Models . . . . .	14
1.3.4 Youth & Gravity Considerations . . . . .	18
<b>1.4 Initial Mass Function (IMF)</b> . . . . .	<b>18</b>
1.4.1 Observations . . . . .	20
1.4.2 Formation Mechanisms & Simulations . . . . .	22
<b>1.5 Motivation</b> . . . . .	<b>25</b>
1.5.1 Observational Strategy . . . . .	26
<b>1.6 Summary</b> . . . . .	<b>28</b>
<b>1.7 Résumé</b> . . . . .	<b>31</b>

---

### 1.1 Overview

The present knowledge of star formation is incomplete, resulting in the European Commission FP6 Marie Curie Research Training Network, CONSTELLATION<sup>1</sup>. Within this CONSTELLATION

---

<sup>1</sup><http://www.constellation-rtn.eu/>



framework there are three packages<sup>2</sup> envisaged to further our understanding of the universe in this stellar domain; how the collapse of molecular clouds affect the stellar initial mass function (IMF) from brown dwarfs to massive  $>5 M_{\odot}$  stars; modeling the formation of massive stars and their effect on the surrounding environment; and how the lower-mass end of this stellar formation compares with planetary objects. The work presented in this thesis is predominantly focussed towards Work Package 3<sup>3</sup> where the modus operandi is to search for the origin of brown dwarfs, be it from turbulent cloud collapse or formation within the disk of higher-mass objects; the description of physical parameters that these objects have to help further brown dwarf models; and finally, at the lowest masses, how these objects compare and/or overlap with the planetary domain. This Chapter deals with the current understanding of brown dwarf formation and the associated observable details and mechanisms with which to interpret the observable data. Stellar and brown dwarf formation is discussed in the context of having a statistically significant sample of stars and sub-stellar objects to calculate and to compare the mass function of young stellar clusters. Advanced theoretical models of the atmospheres and photospheres of these sub-stellar objects are also discussed with respect to the formation of molecules and dust grains at varying temperatures, and the convection and cloud formations in the lowest-mass objects. The formation of these materials in the atmospheres have a direct impact on the spectra of these objects. Finally, this work builds upon previous work on the IMF of two young clusters with tighter constraints in particular for the lower mass end of the IMF.

The second Chapter is a complete overview of the data acquisition by two wide-field optical and near infrared (NIR) detectors (MegaCam and WIRCam) at the Canada France Hawaii Telescope (CFHT), a summary of its treatment within those pipelines, and then a full review of the development of a custom made pipeline to treat and test this data to achieve a high data quality that is ready for analysis. The particulars of this analysis, and cluster-specific data treatment, are discussed in Chapter 3 for the young open cluster IC 4665, and in Chapter 4 for the young star-forming region IC 348. A full discussion of these two clusters with respect to the literature, and the impact that this research has for astronomy and astrophysics can be found in Chapter 5; finishing with the conclusions and a description of further work and prospects necessary for the advancement of the current understanding of brown dwarfs and the IMF.

The Appendix holds standard information about this work, for example the configuration details for the extraction programs, example programs to help deal with large amounts of data and also the routine used to extract candidate members from clusters for census and IMF purposes.

---

<sup>2</sup>[http://www.constellation-rtn.eu/wiki/index.php/Science\\_overview](http://www.constellation-rtn.eu/wiki/index.php/Science_overview)

<sup>3</sup>[http://www.constellation-rtn.eu/wiki/index.php/Work\\_Package\\_3](http://www.constellation-rtn.eu/wiki/index.php/Work_Package_3)

## 1.2 Introduction

The first light-sensitive cyanobacteria were formed on Earth more than 4 billion years ago. More complex, multi-cellular, organisms found it advantageous to evolve to move towards regions of less light and away from regions with stronger light as strong light denatured their food source (Weiss-Schaber, priv. comm). Organelles adapted to use light to change its everyday behaviour and through larger and more sophisticated evolutionary changes, was then used more as a means to find more advantageous living spots and food, evolving from light-sensitive cells, to insect eyes and to focusing animal eyes most recently at 540 million years, (Halder et al., 1995). Eyes have changed little since then, so all the early humans needed after looking upwards to see seen points of light on the celestial sphere was just increased brain power and interpretation or perception. The eye detects radiation logarithmically and ours is tuned to the peak wavelength gained from the Sun through the atmosphere of Earth, which at about  $0.51 \mu\text{m}$  known as the concept 'green'. This energy originates via hydrogen nucleosynthesis in stars more massive than  $\sim 0.075 M_{\odot}$ , depending on their impurities of elements heavier than hydrogen and helium, so-called metallicities, otherwise for lower mass objects there can exist deuterium burning as the lowest temperature and pressure mass-energy changing mechanism. The typical energy conversion out-put from one proton-proton chain equates to 26.7 MeV, where all of this outwards radiating energy supports the Sun from the impending gravitational collapse. This radiation is produced in the vast central regions of a star, where one  $\gamma$ -ray photon can take a random-walk path of more than 1 million years to escape from the centre, changing from  $\gamma$ -ray energies to the optical at  $\sim 0.48 \mu\text{m}$  from countless energy-sapping subatomic interactions. The majority of this emitted energy is in the form of thermal radiation, and accounts for most of the emission from stars. The form of radiation that sub-stellar objects and brown dwarfs emit, however, originates primarily from the thermal energy left over from their formation, excepting some small deuterium fusion in the large sub-stellar mass objects. For the lowest mass objects there is no major form of thermal radiation creation, except what is left from their formation, when the material collapsed and was heated using the excess rotational and gravitational potential energy as it fell into its gravitational well. For interest, non-fusion originated thermal radiation is found in more massive and exotic cosmic entities which usually have very high energy signatures, for example quasars and neutron-black hole binaries, where mass can be transformed directly into energy at various efficiencies (depending on the spin and the size of the gravitational well), independent of the stellar fusion process.

### 1.2.1 Temperature & Luminosity

Stellar and sub-stellar objects emit radiation which is highly dependent on and proportional to the temperature of the body, described as the effective temperature, set out as the Stefan-Boltzmann law, in Equation 1.1:

$$P = \sigma T_{Eff}^4 \quad (1.1)$$

where P is the power radiated per unit area,  $T_{Eff}$  is the effective temperature of the object in kelvins, and  $\sigma = 5.67 \times 10^{-8} \text{ W M}^{-2} \text{ K}^{-4}$  is the Stefan-Boltzmann constant. The luminosity of an object described in Equation 1.2, however, is the total amount of power that an object radiates, and assuming that the output per unit area on the surface of a sphere is equal then the total power output of a spherical object would be:

$$P = \sigma T_{Eff}^4 4 \pi R^2 \quad (1.2)$$

where R is the radius of the object.

Wien's law allows the peak wavelength of the radiation to be calculated from the temperature of the black body, shown graphically in Figure 1.1, and described shown in Equation 1.3:

$$\lambda_{peak} = \frac{b}{T_{Eff}} \quad (1.3)$$

where  $\lambda_{peak}$  is the wavelength for an homogeneous object at a given temperature in kelvin, T, and  $b = 2.8977686 \times 10^{-3} \text{ m K}$  is Wien's constant. For example, when the Universe became transparent to radiation its initial temperature was  $\sim 3000 \text{ K}$ , but is now detected at  $\sim 1.06 \text{ mm}$  and known as the cosmic microwave background (CMB) whose temperature has dropped to just  $2.725 \text{ K}$  at the present day, after being redshifted by the expansion of the universe.

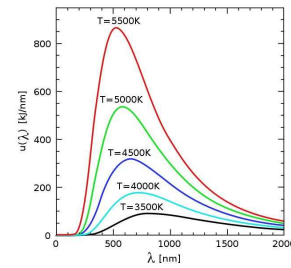


Figure 1.1: Wien's Law for various temperatures as an example of the peak temperature of a black body.

The Hertzsprung-Russell (HR) diagram can show the relationship between different luminosities, effective temperatures and also spectral types. Varying types of stellar objects can be plotted in order to form a scatter diagram as shown in Figure 1.2, taken from Wuchterl and Tscharnuter (2003). The spectral type of a stellar object is based on its effective temperature, which are summarised for 5 Gyr field objects from M to Y in Table 1.1. This data is usually gleaned from photometry or spectroscopy, though data for the M, L, T and Y-dwarf spectral types listed here were taken from the AMES theoretical models (see Section 1.3.3). Objects with these fainter spectral types have large differences in their masses because of the spread of detected ages which

Table 1.1: A list of stellar and sub-stellar spectral types from O as the hottest, (Habets and Heintze, 1981) down through to M, L and T-dwarfs to the newly allocated Y dwarfs. The M, L, T and Y-dwarf data were taken from the AMES models for 5 Gyr objects.

Class	Temperature K	Mass $M_{\odot}$	Radius $R_{\odot}$
O	$>3.3 \times 10^4$	$>16.0$	$>6.60$
B	$1.0\text{--}3.0 \times 10^4$	2.10–16.0	1.80–6.60
A	$7.5\text{--}10 \times 10^3$	1.40–2.10	1.40–1.80
F	$6.0\text{--}7.5 \times 10^3$	1.04–1.40	1.15–1.40
G	$5.2\text{--}6.0 \times 10^3$	0.80–1.04	0.96–1.15
K	$3.7\text{--}5.2 \times 10^3$	0.45–0.80	0.70–0.96
M	$2.0\text{--}3.7 \times 10^3$	$\sim 0.03\text{--}0.45$	0.25–0.70
L	$1.3\text{--}2.0 \times 10^3$	$\sim 0.015\text{--}0.03$	0.10–0.25
T	$0.7\text{--}1.3 \times 10^3$	$\sim 0.005\text{--}0.015$	0.01–0.10
Y	$<0.7 \times 10^3$	$<0.005$	$<1 \times 10^{-2}$

in turn have an effect on the effective temperature. The hottest and brightest objects are O stars, whilst the sun is a G2-type star. The lowest temperature objects in this scale are Y-dwarfs which can overlap with the planetary mass domain. A ‘dwarf’ is defined as being an object that has a luminosity class ‘V’ in the Morgan-Keenan system and is part of the main sequence on the HR diagram. For example, an object classified as a ‘M5V’, is an M-dwarf that is half as bright when compared to an M0 dwarf.

Visually, the luminosity of an object can only be compared to other luminous objects and, as the first observations were taken by eye, so takes the form of a logarithmic scale. This is the magnitude system, where each object is catalogued and assigned a value in comparison to some standard star, which has historically been (and still is) Vega or a Vega-type star. Vega is defined as being an A0 star where the definition of this system holds that the gradient across its spectrum, or colour, of a star of spectral type A0 is equal to zero. Through improved observations Vega takes a modern value of 0.03 mag. The apparent magnitude,  $m$ , is related to the amount of flux that is obtained via Equation 1.4:

$$m = -2.5 \log_{10} \left( \frac{F}{F_0} \right) \quad (1.4)$$

where  $F$  is the flux from the object and  $F_0$  is the zero-point flux, dependent on the photometric system. The total luminosity is obtained from the amount of flux over the whole spectrum, where the intensity of the radiation is given by the integral of the flux density per wavelength. In this work both the Vega and AB magnitude systems are used, where the AB system is independent of Vega.

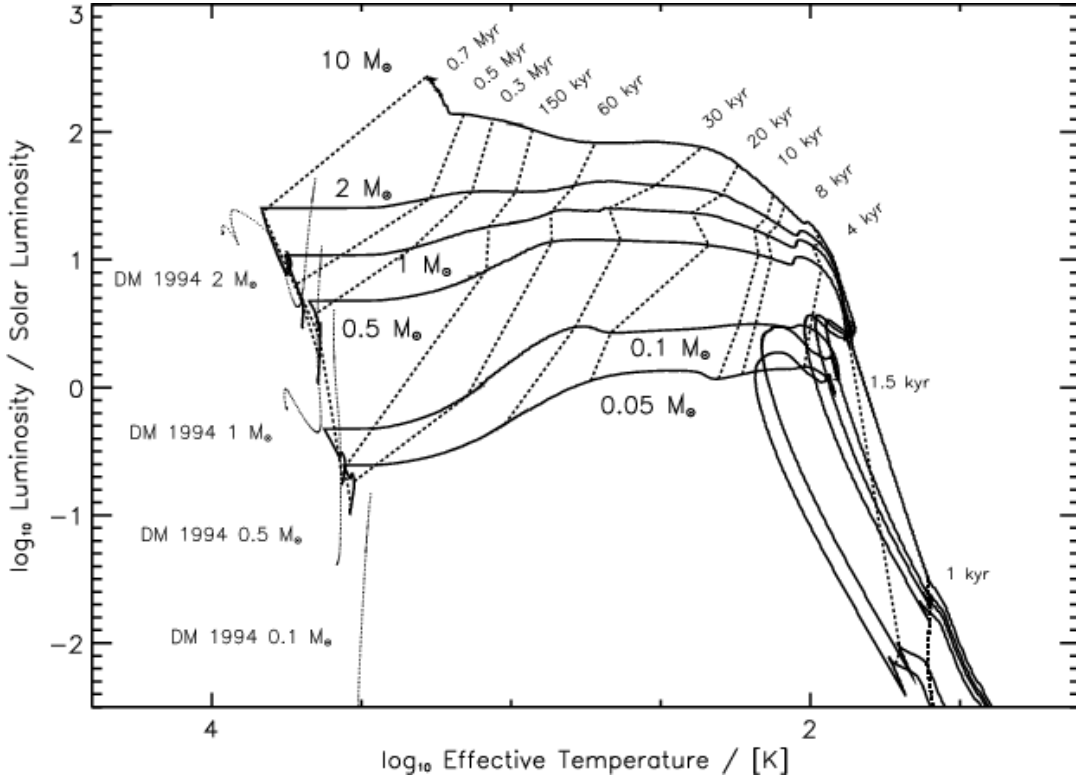


Figure 1.2: Example Hertzsprung-Russell diagram here showing the evolution of collapsing clouds of masses between 0.05 and 10  $M_{\odot}$  against the effective temperature. Isochrones are the evolutionary tracks at various ages. Figure taken from Wuchterl and Tscharnuter (2003), their figure 3.

A magnitude in the Vega photometric system is related to the flux at a particular wavelength or in a particular band from the object arriving at the observer, divided by the flux at that wavelength of Vega, shown in Equation 1.5:

$$m_{Vega} = -2.5 \log\left(\frac{\int (F\lambda_{star} S\lambda d\lambda)}{\int (F\lambda_{Vega} S\lambda d\lambda)}\right) \quad (1.5)$$

where  $F\lambda$  is the flux at a particular wavelength in  $W M^{-2}$  and  $S\lambda$  is the instrument response which depends on the telescope, filter and detector used. Usually the unit  $W M^{-2}$  is too large so the Jansky unit is used instead where  $1 Jy = 10^{-26} W m^{-2} Hz^{-1}$ .

In addition, the AB system is also used although this is independent of any variations in the magnitude of Vega at a given wavelength, and is given by Equation 1.6<sup>4</sup>:

$$m_{AB} = -2.5 \left(\log\left(\frac{\int (F\lambda_{star} S\lambda d\lambda)}{\int (S\lambda d\lambda)}\right) - 48.6\right) \quad (1.6)$$

where again the flux is in  $W M^{-2}$ . Note that if the flux is in Janskys then there is an additional

<sup>4</sup><http://dls.physics.ucdavis.edu/calib/vegaab.html>

multiplying factor to the logarithm of 26 (from the definition of the Jansky). Agreement is shown with the Vega system, as if the flux is constant then the same magnitude is achieved and all colours again equal zero. Conversion between the Vega and AB systems usually involve a correction factor, tabulated and discussed further in Chapter 2.

The apparent magnitude is the luminosity *as is* with no form of corrections with respect to distance or extinction, whilst the absolute magnitude,  $M$ , is the magnitude of that objects at source. If the distance to this object is known then and extinction is negligible then it is possible to change between apparent and absolute magnitudes using Equation 1.7:

$$m - M = 5 \log_{10}(D) - 5 \quad (1.7)$$

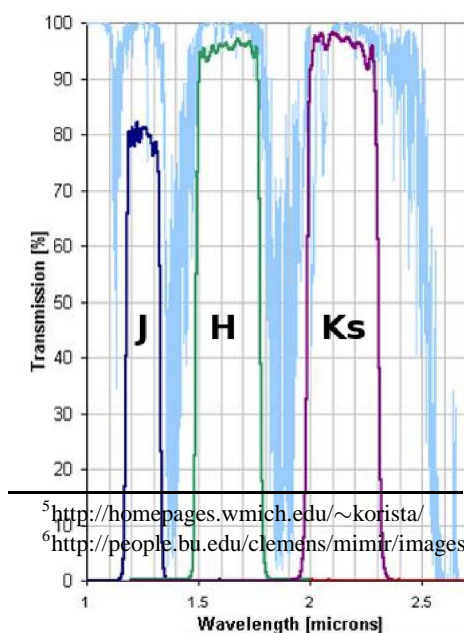
where  $D$  is the distance between the observer and the object.

## 1.2.2 Absorption & Emission

The luminosity of an object can be imaged spectroscopically as shown in Figure 1.3 (*top*) for the Sun and fit<sup>5</sup>, and (*bottom*) for an M6 dwarf, Wolf 359 (McLean et al., 2003) and depends on the resolution of the spectrometer to observe thinner and weaker line features. Note the difference in energies and also the appearance of emission and absorption lines caused by the presence of various elements and molecules in the objects' atmospheres.

Molecules in the line of sight absorb and re-emit radiation depending on the incident energy of the photon, appearing as peaks and troughs in the spectrum. Extending this means that any material in between the source of the radiation and the observer is liable to absorb and re-emit the incident radiation. Space is permeated with small amounts of dust and gas which is the interstellar medium and reduces the amount of light by  $\sim 1-2 \text{ mag kpc}^{-1}$ .

This is in addition to any non-space based observation platforms which also have to deal with the molecules existent in Earth's atmosphere, where the most troublesome of these for optical or IR astronomy is  $\text{H}_2\text{O}$  (Bessell, 2005). An absorption spectrum of water is shown in Figure 1.4<sup>6</sup>, traversing the optical to infrared regions of the electromagnetic spectrum. For this reason, modern telescopes tend to be located in regions of low atmospheric water vapour, usually in geographical and meteorological dry spots and/or at great heights, for example



<sup>5</sup><http://homepages.wmich.edu/~korista/>

<sup>6</sup>[http://people.bu.edu/clemens/mimir/images/images\\_in\\_web\\_pages/](http://people.bu.edu/clemens/mimir/images/images_in_web_pages/)

Figure 1.4: The absorption spectrum of water by the Earth's atmosphere. 2MASS

Hawaii on Mauna Kea, Chile or even the middle of Antarctica on the Trans-antarctic mountain range. A discussion on the telescopes and surveys used in this work can be found in Chapter 2.

### 1.2.3 Extinction & Reddening

Extinction is the term given to the amount of flux lost between the originating object, be it a star or brown dwarf, and the observer due to preferential scattering and absorption of shorter, bluer wavelengths and/or re-emission to longer, redder wavelengths. The amount of reddening is affected by the transmitting medium which can be the interstellar medium (ISM) or more local and compact conditions such as molecular clouds, dust clouds or circumstellar disks. This amount of material in the line of sight has a particle density per unit volume, referred to as a column density, where the average ISM column density is  $\sim 1 \text{ atom cm}^{-3}$ .

The best way to estimate the extinction is from a group of Spectral Energy Distributions (SEDs) taken from objects across the region of interest where the different absorption features can be distinguished from features that are not so readily absorbed by the intervening medium. These extinction curves can be collectively plotted for various stars, as shown in Figure 1.5 (taken from Savage and Mathis (1979), their Figure 1), to gain the average normalised interstellar extinction. Generally, the longer the wavelength of the incident emission compared to the size of the molecule or dust grain in the line of sight, the less the extinction. Another method is to observe large-scale images using surveys and then modeling varying extinctions and comparing with  $\chi^2$  deviation maps to ascertain the confidence of a particular extinction value (Chapman et al., 2008). Applying the average extinction for a given region will then not work in the cases of individual objects. Here, it is possible to retract the individual objects to theoretical isochrones, adjusted to be at the same distance as the object, where the difference is the amount of flux lost, giving the level of extinction.

To this end there is the empirical interstellar extinction law which relates the magnitude of an object in a particular band with a value for the amount flux lost, (Savage and Mathis, 1979). This law is shown in Equation 1.8 where at least one bands absolute magnitude is known, usually the optical  $V$ -band:

$$\frac{A_\lambda}{E(B - V)} = \frac{E(\lambda - V)}{E(B - V)} + R \quad (1.8)$$

where  $A_\lambda$  is the extinction at a particular wavelength,  $E(B-V)$  is the colour excess in magnitudes, where a value of  $E(B-V) = 1$  equates to a hydrogen column density of  $5.8 \times 10^{21}$  atoms  $\text{cm}^{-2}$  (Savage and Mathis, 1979). Extinction is usually given as the total-to-selective extinction ratio,  $R$ , as a function of the V-band flux,  $A_V$  shown in Equation 1.9, although this can be convolved with the wavelength to get a value  $A_\lambda$ .

$$R = \frac{A_V}{E(B-V)} \quad (1.9)$$

where  $R$  takes the value 3.09 for the ISM. Rieke and Lebofsky (1985) confirm this interstellar extinction law and improve the estimates between 1 and 13  $\mu\text{m}$ . Extinction is split into two components which are the diffuse ISM component and thermal emission from this component from dust grains, and a variable and generally thicker component originating from the local dust and gas formations in the line of sight. Various methods are used in order to calculate the extinction in the line of sight, (Wegner, 2003), and whilst it is not sufficient to use an average of the interstellar extinction because the values will take errors which are sample specific (Fitzpatrick and Massa, 2007), this method should hold for obtaining good estimates of the extinction towards particular areas. The colour-excess is shown in Equation 1.10:

$$E(B-V) = A_B - A_V = (B-V) - (B-V)_0 \quad (1.10)$$

where  $(B-V)$  is the observed optical colour,  $(B-V)_0$  is the star's intrinsic colour, and  $A_x$  is the extinction for that particular photometric band,  $x$ . It is possible to extrapolate the extinction curve to find values for the detectors and bands used in this work,  $z'$ ,  $Y$ ,  $J$ ,  $H$ ,  $K_s$  and  $\text{CH}_4$ off/on narrowbands. For the purposes of this work the extinction values have been taken from the Spanish Virtual Observatory (SVO) who convolved the bands with the detector responses of the various telescopes and instruments, and are tabulated in Chapter 2 for the specific telescopes and instruments used in this work (Table 2.1).



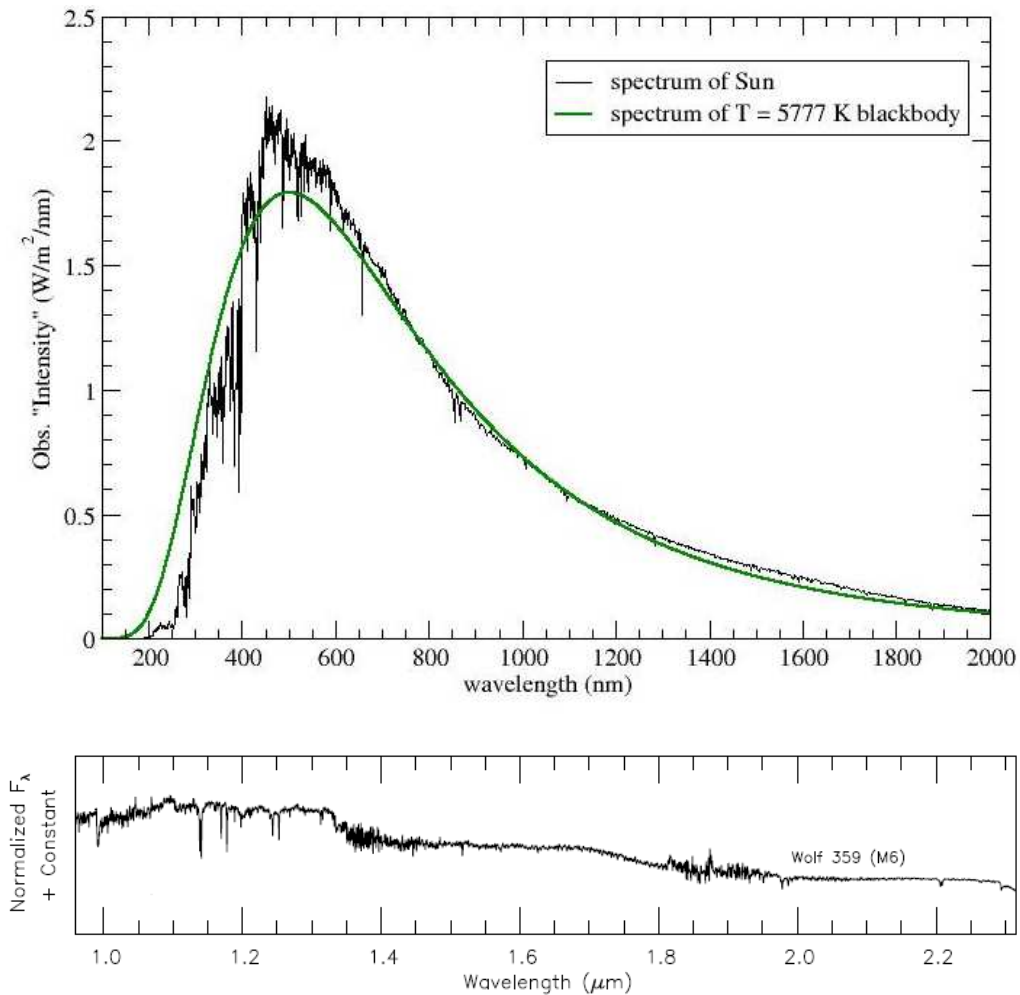


Figure 1.3: Observed spectra for the Sun and Wolf 359 for a comparison between and examples of black-body temperatures. (*top*): Spectrum of the Sun with the fitted black-body effective temperature of 5777 K. (*bottom*): infrared spectrum of a low-mass object, Wolf 356 which is an M6 dwarf of mass  $0.09M_{\odot}$ , where the effective temperature of this object is  $\sim 2800$  K. The peak flux emits at  $1.03 \mu\text{m}$ . These two plots overlap from  $1.0$  to  $2.0 \mu\text{m}$ . Note the increased absorption in the infrared domain occurring at lower temperatures due to the presence of more abundant molecules in the atmosphere. (See text for references).

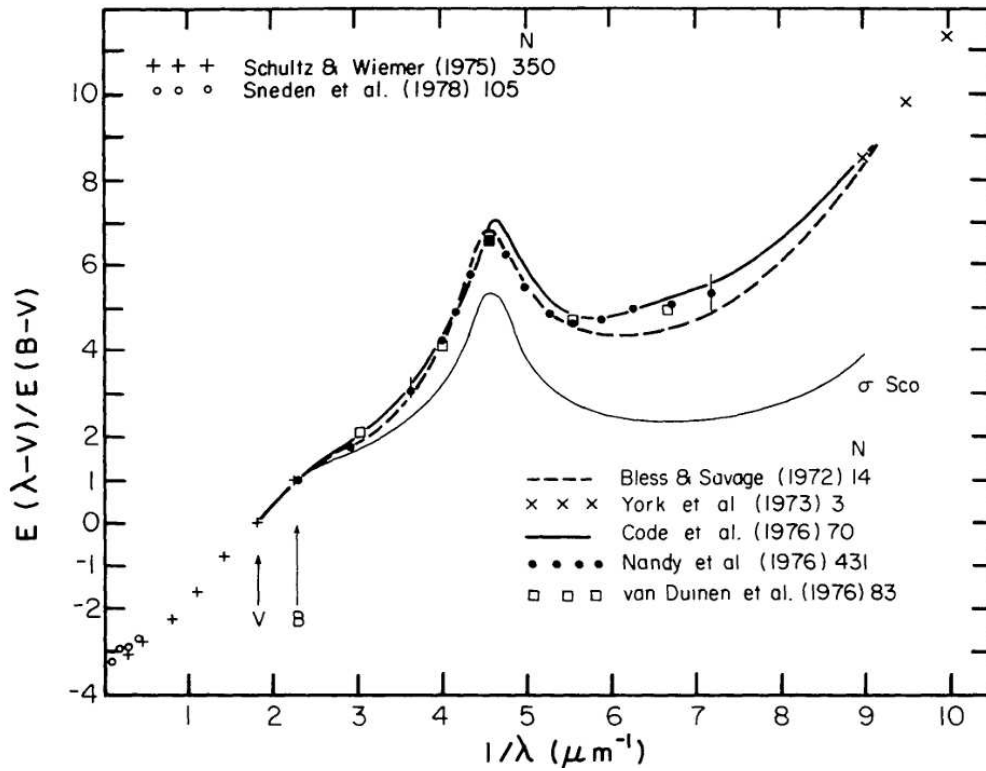


Figure 1.5: The normalised curves of various O and B stars' interstellar extinction are plotted as a function  $\frac{1}{\lambda}$  against  $E(\lambda - V)$ . Each curve is derived from a sample of stars, where the total extinction can be found by including the total-to-selective extinction ratio,  $R \sim 3.09$ . (See text for plot origin).

## 1.3 Stellar and Sub-Stellar Mass Objects

### 1.3.1 Stellar Objects

Field ( $\sim 5$  Gyr) M-stars are better understood as they are brighter from being more massive and have had a longer history of detection. These objects are perfectly capable of hydrogen burning and usually have low levels of dust in their atmospheres because of their higher local temperatures which prevent grain formation. The first oxide molecules and high-temperature condensate grains begin to form in the cooler parts of the atmospheres of mid- to late-type M-dwarfs. The M to L spectral type transition occurs with the formation of silicate dust that is dense enough to become a major factor at temperatures less than 2500 K which redden of the spectrum of the star, characterised by the disappearance of the TiO and VO lines between 500 and 900  $\mu\text{m}$  (Jones and Tsuji, 1997). Hydrogen burning is thought to occur down to masses of  $0.075 M_{\odot}$  for the solar abundance, (Burrows et al., 2001), though Burrows (2009) reaffirms that this is not known for sure. This equates to the early L spectral type with temperatures down to  $T_{\text{Eff}} \sim 2200$  K for the most massive of the field (5 Gyr) brown dwarfs. Objects that are not massive enough to fuse hydrogen are termed ‘brown dwarfs’.

### 1.3.2 Sub-Stellar Objects

The first bona fide detections of brown dwarfs occurred within months of each other; firstly Teide Pleiades 1 discovered by Rebolo et al. (1995) with a constrained mass of between 20 and 50  $M_J$  and revised spectral type of M8 (Martin et al., 1996) using WHT spectra and  $H\alpha$  and Li detection; and then secondly, though not much later, the companion dwarf to the nearby star G1299B by Nakajima et al. (1995). Further work on clarifying the properties of G1299B such as its temperature at  $T_{\text{Eff}} \sim 900$  K, and the existence of IR  $\text{CH}_4$  and  $\text{H}_2\text{O}$  absorption lines (Oppenheimer et al., 1996), and its spectrum (Oppenheimer et al., 1998) has been done. Since this discovery and proof of the existence of brown dwarfs according to theory, there have been many surveys with the express aim of expanding our knowledge of the formation and population of these objects down to the planetary mass regime.

The Sloan Digital Sky Survey (SDSS)<sup>7</sup> and the 2Micron All Sky Survey (2MASS)<sup>8</sup> surveys have been instrumental through their sheer coverage but also from their complimentary nature from the optical  $u'$  at  $\sim 0.3 \mu\text{m}$  to the centre of the  $K_s$  band at  $2.17 \mu\text{m}$ . More recent brown dwarf surveys exploited the UKIRT Infra-red Deep Sky Survey (UKIDSS) where the  $Z$ ,  $Y$ ,  $J$ ,  $H$  and  $K_s$  bands are available between  $0.83$ - $2.37 \mu\text{m}$ , (Lodieu et al., 2007, 2009a,b). A comprehensive database of all  $\sim 1300$  currently known brown dwarfs, not candidates, is kept at the

---

<sup>7</sup><http://www.sdss.org/>

<sup>8</sup><http://www.ipac.caltech.edu/2mass/>

Dwarf Archives<sup>9</sup>. There are 536 M-dwarfs, 601 L-dwarfs and 205 T-dwarfs currently catalogued in this database at time of writing.

A brown dwarf is held to be an object that is less than  $0.08 M_{\odot}$  and is too lightweight to sustain hydrogen burning whose limit occurs at approximately  $0.075$  to  $0.08 M_{\odot}$ , depending on the metallicity of the object. The effect of age on this limit is unclear, but the younger the object the lower the mass for a given effective temperature. Brown dwarfs can overlap with the M and L spectral types, where the newer T and Y-dwarf classes describe the coolest objects. Deuterium burning can exist, however, down to masses of  $\sim 0.012 M_{\odot}$  (Saumon et al., 1996; Chabrier et al., 2000) or lower, again depending on the age and temperature of the object. The effective temperature of the object defines its spectral type, whilst its age defines its mass. Younger brown dwarfs, therefore, should be less massive than field brown dwarf for a given spectral type. It then follows that the thermal entropy of these young objects must have originated from the gravitational potential energy and rotational potential energy imparted from the formation mechanism, where the associated temperature with an object would then be greatest just after formation. Sequentially, these objects are similar to gaseous planets and should differ in few areas, where Fortney et al. (2008) discuss an interesting proposition that brown dwarfs and planets can be differentiated by their metallicities. Their metallicities should be directly related to the composition of the birthing cloud, the mass of the clump and also the disk formation process. Indeed, the lower the mass of the object the higher the likelihood of having proportionally greater amounts of impurities arising from the settling of heavier elements within the disk, from the parent cloud, over time compared to the major compositional stellar elements H, He, C N and O.

More complex molecules and dusts form in the atmosphere as the L-dwarfs get later and this burning reduces to deuterium burning. There is also the formation of cloud layers and internal convection and mixing, where the cloud bases occur at thermoclines and are dependent on the lower temperatures needed for upper atmosphere dust formation. When these clouds are cool enough to allow the heavier materials to drop out from a higher to a lower cloud base, this clears the upper atmosphere which now dominates the spectrum of this object, discussed in detail as the L – T transition by Burrows et al. (2006). Of note here is the emergence of  $\text{CH}_4$  as one of the dominant absorbers in this spectral range and is a definite marker of the T-dwarf spectral type. Y-dwarfs are cooler than T-dwarfs and are defined by the emergence of stronger  $\text{CH}_4$  and  $\text{NH}_3$  absorption, whilst the  $\text{H}_2\text{O}$  lines is thought to reduce because of sedimentation in the atmosphere. For a more detailed description of the elements, materials and physics involved in the models of the brown dwarfs over their spectral types, look towards Section 1.3.3.

Observationally, without spectroscopic data it is possible to use broadband magnitudes and colours to broadly classify objects into spectral types. The appearance of dust in the outer

---

<sup>9</sup><http://spider.ipac.caltech.edu/staff/davy/ARCHIVE/index.shtml>

atmosphere of these late-M, L and early-T dwarfs faintens the spectrum through absorption and emission, but affects the redder part of the spectrum lesser compared to dust-free field stars or early M-dwarfs. The  $K_s$  magnitude is then fainter, but then  $J$ -band gets even fainter giving the comparatively redder  $J - K_s$  observed colours. The  $J$ -band and the  $Y$ - and  $z$ -bands brighten for early T-dwarfs because of the cloud ‘clearing’ of dust, whilst youth is also suspected to causes these bands to brighten. The  $J$ -band brightening in particular is thought to be a consequence of the rapid clearing of the cloud levels at around  $\sim T3$ . The region of interest in the  $H$ -band is, specifically, the  $\text{CH}_4$  molecule that dominates absorption at temperatures lower below  $T_{\text{Eff}} \sim 1300$  K (Burrows et al., 1997). The colours of the younger objects are usually redder than the field colours, excepting the  $z - J$  colour as discussed above.

Currently, brown dwarf spectral types can be approximated using theoretical models, where it is possible to use a  $\chi^2$  test in order to best fit a spectral type to a spectrum (Alves de Oliveira et al., 2010). These associations are not always accurate as the spectra can be noisy due to the extreme faintness of these objects, due to obfuscation of the emitted radiation by dust or disks (Scholz and Jayawardhana, 2008), but also by the incompleteness of the theoretical models. Additional difficulties in assigning spectral type to these young objects via low-resolution spectroscopy is that age, and so gravity, are significant factors which greatly affect the absorptivity and emissivity of the molecular lines, making it hard to assign a correct effective temperature. For high-resolution spectroscopy it is mainly due to gravity that the spectral types are hard to derive because of the overlapping of the spectral lines. Usually these methods give the spectral type to an error of within a few sub-types. The treatment of dust within theoretical models is currently the major source of errors for derived observational properties as its behaviour is still far from being well-understood across the brown dwarf regime (Burrows, 2009). The most recent BT-model spectra take into account updated solar abundances which are based on radiative hydrodynamic simulations by Asplund et al. (2009).

### 1.3.3 Models

Theoretical models are of immense value to not only help identify candidate objects, but to also estimate the level of extinction suffered due to the inherent nature of local, stellar, dust and from interstellar extinction. The problem is relating observations to theory as the age, mass and temperature are interdependent. Theoretical models are necessary in order to ally observational discoveries and puzzles with the usually established but hard-to-apply theory. This research makes use of model atmospheres proposed for M, L and T dwarfs over the past two decades. These models attempt to predict masses, ages and temperatures to bridge the gap between stars and planets, and have an associated magnitude for various, user-defined observational bands.

The ‘NextGen’ model (Baraffe and Chabrier, 1996; Baraffe et al., 1998; Hauschildt et al.,

1999) was the initial model to describe solar-type stars, very low mass objects (VLMs) and early-type brown dwarfs, for solar metallicities. Magnitudes are given for various masses, and their associated temperatures, radii and luminosities, and are in good agreement with empirically-derived relations. These models are more uncertain for lower spectral types and can have large errors for objects temperatures  $< 3700$  K. This uncertainty was expected to be directly related to incomplete optical opacities and grain formation in the atmosphere and incomplete solar abundances.

Initial problems with modeling atmospheres reduce to the problem of having incomplete molecular line lists, and the poor understanding of the mixing of materials between cloud layers. This translates to underestimating the level of dust grain formation in the atmosphere, the treatment within the upper and lower atmospheres, and then the *settling* over time of these grains whilst reducing the formation rate as they condense out, so removing the molecular species necessary for particular grain formation. A typical zirconium dioxide,  $ZrO_2$ , grain forms at a temperature of  $\sim 2800$  K, whilst other grains form at lower temperatures; for example at 1800 K for corundum,  $Al_2O_3$ , and at 1600 K for VO and enstatite,  $MgSiO_3$ . A detailed discussion of the astro- and atmospheric physics involved is discussed in the review by Allard et al. (1997), and the mixing is discussed in detail by Freytag et al. (2010). There are two sets of models used in this paper, the Lyon-AMES models that are based upon the Langhoff and Bauschlicher (1994); Partridge and Schwenke (1997) molecular line lists and Noels & Grevisse, 1993 solar abundances, and the BT-models which have updated opacities for grain and molecular species in the atmospheres (Allard et al. (2003, 2007) and Allard et al. (in. prep.)), and use the Asplund et al. (2009) abundances. Both of these sets of models are available as theoretical isochrones or as spectra and can be queried from the Phoenix simulator<sup>10</sup>.

The ‘Dusty-AMES’ model (Allard et al., 2001; Chabrier et al., 2000) was created to place limits on the range of colours that brown dwarfs could have. They also give a good account of what spectra could be observed of hotter brown dwarfs with respect to dust grain formation, because the dust was found to be in equilibrium with the gas in the photospheric layers in the atmospheres. This model applies to L and T dwarfs which are not reproduced by dust-free models, though below  $\sim 2800$  K dust grains and opacities are needed which were then incomplete, discussed Chabrier et al. (2000) and references therein. These L and T-dwarfs have bluer NIR and IR colours due to the presence of  $H_2O$  and methane absorbers (Burgasser et al., 1999). Grain formation was discussed in relation to low-mass brown dwarfs and planetary mass objects by Allard et al. (2001). Gravitational grain settling allowed ‘backwarming’ which is the increase in brightness due to reduced infrared absorption by the  $H_2O$  present. Missing sources of opacities to give the observed colours, to be included in future models, are discussed by Baraffe et al. (1998). In all, the Dusty

---

<sup>10</sup><http://phoenix.ens-lyon.fr/simulator/>

models underestimate the opacity, and do not account for sedimentation or settling within the atmospheres. Further discrepancies with observed colours could be due to the presence of the strong K I and Na I lines in the optical and near-infrared (Allard et al., 2007).

The ‘Cond-AMES’ model was developed by Allard et al. (2001); Baraffe et al. (2003) and favours cooler,  $<1300$  K brown dwarfs where the gas is treated condensing into molecules rather than forming silicate features, so affecting the spectrum with many absorption and emission lines. As these properties change with time, a hotter object may cool and so transit from the Dusty model domain through to the Cond model domain. This model is similar to the NextGen model in that there are no dust features, although it should bridge the brown dwarf-planet regime. The size and composition of the core is physically a good representation of the difference between a *bona fide* brown dwarf and a planet; a planet should have more of a rock and ice core which can relate to a 5% difference in the radius. The cooling theory of a brown dwarf and extrasolar giant planet is similar, where the differences are more the metallicities and composition (Fortney et al., 2008), expected because of the different mechanisms of formation.

Atmospheres of these very low mass stars, substellar objects, cooler brown dwarfs and planetary-mass objects allow the formation of molecules within their atmospheres from the reduced temperatures. Indeed, low-mass objects have large quantities of molecular hydrogen,  $H_2$ , and carbon found as carbon monoxide, CO, (Chabrier et al., 2000). Objects with masses lower than  $0.075$  and  $0.08 M_{\odot}$  have reached hydrogen burning limit depending on the metallicity of the object, for example the aforementioned seminal discovery of the first brown dwarf, Gl299B, weighs in at  $\sim 50 M_J$  and is thought not to be able to sustain hydrogen burning. There exist titanium oxide, TiO, vanadium oxide, VO, and water,  $H_2O$ , among others in varying amounts, and are found to be the main mechanisms with which to lock up free oxygen - burning indeed! These molecules greatly affect the optical and infrared spectrum and so influences the overall observed brightness of the object, where  $H_2O$  absorption are dominant in the near and mid-infrared down to  $\sim 1300$  K. Below this temperature the  $CH_4$  is the dominating absorber (Burrows et al., 1997).

The new ‘BT-Settl’ model is finished and available for querying from the Phoenix database. Allard et al. (2003, 2007) are the main contributors to the theory. The updated solar abundances laid out in Asplund et al. (2009) are used for all of the new BT models, (F. Allard, priv. comm) as opposed to the Noels & Grevisse (1993) abundances as discussed for the previous AMES models. The major change in these abundances is the reduction in the oxygen abundance which affected the previous models by predicting too-high water absorption in the M-dwarfs. The treatment of the atmospheric water within these models are based on data from Barber & Tennyson, (2009).

The input physics to this new model has been described in Allard et al. (2003) and Helling et al. (2008a), where the cloud is treated as a diffusing medium where material can be convected from

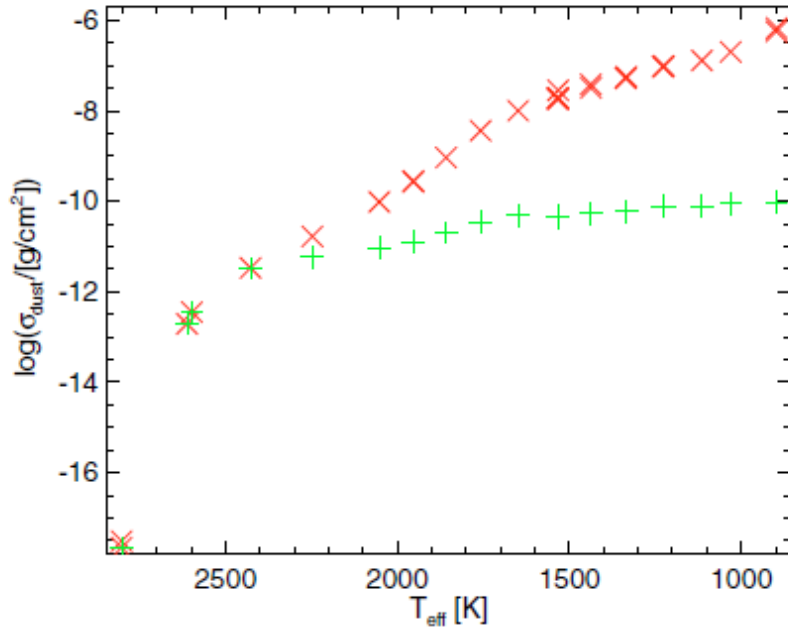


Figure 1.6: The total dust level is clearly related to the reduction in temperature from the hydrodynamical models by Freytag et al. (2010), where the crosses depict the total dust level in the atmosphere, and the plus signs follow the dust present only in the layers of the atmosphere with an optical depth of  $10^{-2}$ , showing the settling of the dust as the temperature decreases. (See text for figure reference).

the depths to the upper cloud layers. These are based upon the cloud segmentation and dust grain settling models described by Freytag et al. (2010) in their hydrodynamical simulations of the influence of the underlying convection zone on this settling. The total dust present in the atmosphere can be clearly seen to increase with lowering temperature, shown in Figure 1.6, (their Figure 10 *bottom left*), compared to the atmosphere layers that have a lower optical depth. As the spectral type latens, the clouds can form thicker and more lasting clouds that begin to have their own mini-convective mechanisms, creating layers of mixed species and grains, which are dependent on the local conditions (Helling et al., 2008b). This cloud segmentation and dust grain settling is dealt with in the BT-Settl model, over the full range of  $T_{\text{eff}}$ , but is not yet dealt with within the ‘BT-NextGen’, ‘BT-Dusty’ and ‘BT-Cond’ models.

The ‘BT-Dusty’ and ‘BT-Cond’ models (Allard et al. (in. prep.)) are not quite finished at time of writing (August 2010) as they take a lot of computer processing power to calculate the new grids down to the brown dwarf regime. The models outputted from the Phoenix simulator can be adjusted for different metallicities and can span from 1 Myr to 10 Gyr. Optical and IR bands are included and are also convolved with a large number of different telescopes and detectors in order to match the models to the photometric systems of the user.



### 1.3.4 Youth & Gravity Considerations

The effects that youth has on the spectrum of an object are addressed in these models which are related to the gravity of the object. As discussed, the younger an object the less massive it is for a given temperature. Strong alkali K I doublet ( $0.77 \mu\text{m}$ ) and Na I resonance lines are also major absorbers in the deeper atmospheres of brown dwarfs. These are greatly affected by reduced gravity for younger objects and in turn have a discernible effect on the colours of these objects and spectral types (Martín et al., 1999a). As gravity decreases so the convection within the atmosphere, and the cloud layers, becomes more efficient as the gravitational drag is reduced, consequently the dust formation is also more efficient to later spectral types. Additionally, the resonance lines can change the shape of spectrum differently in lower gravity objects, as the greater the mixing the more that these K I and Na I lines will broaden and overlap in the optical, reducing the expected flux for a given  $T_{\text{Eff}}$ .  $\text{H}_2\text{O}$  vapour will form in lower density mediums for a lower gravity and increases the strength of these bands, increasing the water absorption in the spectra. The molecular hydrogen bands in  $\text{K}_s$  are weaker in lower gravities which will increase the brightness in this band. Additionally, the presence of lithium in the atmosphere, specifically the Li I (at 670.8 nm) absorption is a sign of youth (Martín et al., 1999a) and can help classification (Martín et al., 1999b). For T-dwarfs, this lower gravity can increase the radius of the atmosphere and can increase the observed ‘coolness’ of the  $J$ -band part of the spectrum for a given temperature due to the presence of  $\text{H}_2\text{O}$  and  $\text{CH}_4$  being created in the extended and cooler atmosphere. Gravity and youth have been addressed for their effect in the mid-infrared by Leggett et al. (2007).

## 1.4 Initial Mass Function (IMF)

Data for particular regions can be plotted using colour/magnitude (CMD) and colour/colour diagrams (COLDs) in order to extract candidate cluster members for analysis. Membership of an object can be fickle to assign and usually require confirmation using a variety of technological and data processing techniques. The data must be selected using theoretical isochrones. Further membership tests involve using spectroscopic observations, and so compare the relative compositions of the objects, for example  $\text{H}\alpha$  emission, Li absorption and any red excess, or using proper motion surveys for more dynamically evolved clusters. Further, the local reddening is a problem as it can distort and make it very difficult to achieve accurate absolute magnitudes, which are necessary in order to accurately assign magnitudes and so masses or spectral types from theoretical models and/or from the spectra. The cluster mass function, or the distribution of masses within a particular cluster, can then be derived, where the masses are based on observed magnitudes and luminosities.

The mass function (MF) was first put forward by Salpeter (1955) and captured the relative

numbers of the observed luminosity function as a function of stellar mass across the Galaxy, or in particular globular clusters or regions. The luminosity of an object is a function of mass where hot stars are the most luminous, described for main-sequence stars in Equation 1.11:

$$\frac{L}{L_{\odot}} = \left(\frac{M}{M_{\odot}}\right)^{3.5} \quad (1.11)$$

where  $L$  is the luminosity and  $M$  the mass, as functions of the solar luminosity and mass,  $L_{\odot}$  and  $M_{\odot}$ . The power co-efficient takes lower values for sub-stellar objects. It is also worth noting that the more massive the object the shorter its life span as it burns its fuel as a function of mass. It can be shown that star formation occurs at a uniform rate, at least within the solar neighbourhood by comparing the number of stars as a function of the luminosity at a point in time,  $\phi_t(M_{\nu})$ , shown in Equation 1.12:

$$dN = \phi_t(M_{\nu}) dM \quad (1.12)$$

and where  $dN$  is the total number of stars per cubic parsec of absolute visual magnitude between  $M_{\nu}$  and  $M_{\nu} + dM$ . Through the use of deeper surveys from improved technology, the range of masses now exceed more than five orders of magnitude meaning that it is now more useful to use a logarithmic definition of the mass. A recent review by Chabrier (2003) thoroughly discusses the modern interpretation of the MF. Here the mass function is reiterated and shown in Equation 1.13 in log form:

$$\xi(\log m) = \frac{dn}{d \log m} \quad (1.13)$$

or

$$\xi(m) = \frac{1}{m(\ln 10)} \xi(\log m) = \frac{dn}{dm} \quad (1.14)$$

where  $n$  is the number of observed stars per cubic parsec of space at one point in time, as a function of the mass interval,  $d \log m$ . The MF can also be expressed as a power-law:

$$\xi(\log m) \propto m^{-x} \quad (1.15)$$

and

$$\xi(m) \propto m^{-\alpha} \quad (1.16)$$

where  $x = \alpha - 1$  and the Salpeter value of  $\alpha = 2.35$ . It can also be expressed as a log-normal law :

$$\xi(m) \propto e^{\left[ -\frac{(\log m - \log m_0)^2}{2\sigma^2} \right]} \quad (1.17)$$

where  $\log m_0$  is the peak mass (mode) of the distribution, and  $\sigma$  the width of the dispersion, confirmed by Moraux et al. (2007) for the young open cluster Blanco 1. The power-law seems to more accurately describe the higher-mass portion of the IMF, above  $0.3 M_{\odot}$ , whilst the log-normal law, Equation 1.17, describes more accurately the lower-mass end of the IMF.

### 1.4.1 Observations

There have been many surveys into the IMF for various clusters of age and size including  $\alpha$  Persei (Barrado y Navascués et al., 2002); Hyades (Bouvier et al., 2008); Blanco 1 (Moraux et al., 2007); NGC 2264 (Kendall et al., 2005); Pleiades (Moraux et al., 2004, 2003); Upper Sco (Lodieu et al., 2007);  $\sigma$  Orionis (Caballero et al., 2007; Barrado y Navascués et al., 2004) and NGC 2516 (Moraux et al., 2005). Table 1.2 lists a few surveys with some basic parameters such as age,  $\alpha$ , or  $\log m_0$  and  $\sigma$  depending on the use of the power or log-normal relations for these IMF cluster surveys. Figure 1.7 is taken from Moraux et al. (2005), and plots the IMFs for three young open

Table 1.2: Summaries of various cluster surveys using infrared data to probe the IMF. The mass range is given for those clusters where the IMF  $\alpha$  value is given, rather than the peak mass,  $M_0$ . *Data origin:* 1) Barrado y Navascués et al. (2002) 2) Moraux et al. (2007) 3) Moraux et al. (2004) 4) Moraux et al. (2003) 5) Caballero et al. (2007) 6) Barrado y Navascués et al. (2004) 7) Lodieu et al. (2007).

Age / Myr	Distance / pc	$\alpha$	mass range or $M_0 / M_{\odot}$	$\sigma$	Cluster Name
90	176	$0.59 \pm 0.05$	–	–	$\alpha$ Persei <sup>1</sup>
100–150	260	$0.67 \pm 0.15$	$(M_0) 0.36 \pm 0.07$	$0.58 \pm 0.06$	Blanco 1 <sup>2</sup>
120	125	$0.60 \pm 0.11$	0.03–10	$\sim 0.52$	Pleiades <sup>3,4</sup>
$3 \pm 2$	360	$0.60 \pm 0.20$	0.006–0.11	–	$\sigma$ Orionis <sup>5,6</sup>
5	120	$0.60 \pm 0.10$	0.01–0.3	–	Upper Sco <sup>7</sup>

clusters; Blanco 1 (100-150 Myr), the Pleiades (120 Myr), NGC 2516 (150 Myr) and the older Hyades (625 Myr) which is used to compare the young clusters. Also plotted is the field MF from Chabrier (2003) for systems with both solitary and multiple objects. The peak mass varies as expected because of the differing ages of the clusters, but could also be from the different totals of member populations and so mass distribution from formation. The Hyades appears to have fewer lower mass objects and so the peak mass is significantly higher than for the younger cluster, suggested to be the evaporation of low-mass members over the dynamical time-scale of

the cluster. Cooling of low mass members is not sufficient to reduce the observed deficit in the low-mass brown dwarf populations.

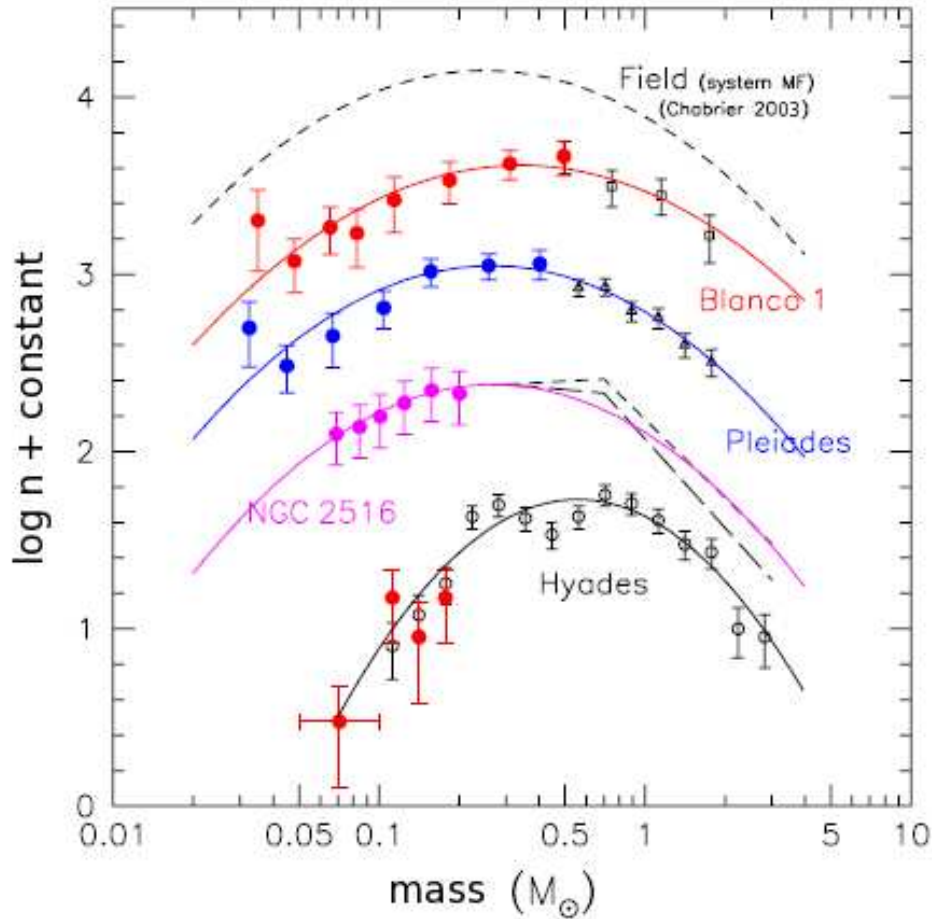


Figure 1.7: The IMFs of three young ( $\sim 100$  Myr) clusters compared to the older Hyades (625 Myr) and the field system IMF, separated by a constant. It can be seen that the three young clusters show broad agreement with the log-normal law, Equation 1.17, similarly with the field system IMF and the Hyades. The peak masses,  $\log m_0$ , are different as expected for clusters of such differing sizes and total masses.

So far only the ‘present day’ mass function has been discussed. The initial mass function (IMF) is the number of stellar objects that had originally been created in a particular region, be it a galaxy or stellar cluster, and can only be extrapolated from the present day MF. This has been discussed but only in relation to clusters losing lower-mass members through dynamical interactions, and in relation to lower-mass objects cooling over time and therefore being much harder to detect. This has implications, for example, for the percentage of baryonic matter compared to dark matter in our Galaxy. Further implications are the size and formation of the molecular cloud that condensed to form the cluster, as the total mass of the cluster is some fraction of the total mass of the parent

cloud. Luhman et al. (2000) discuss that what actually is being observed in a star forming region is the star creation function as similar molecular clouds can still create a different distribution of objects depending on the initial conditions, and discuss quiescent or turbulent clouds that can create differing populations in a given mass range.

### 1.4.2 Formation Mechanisms & Simulations

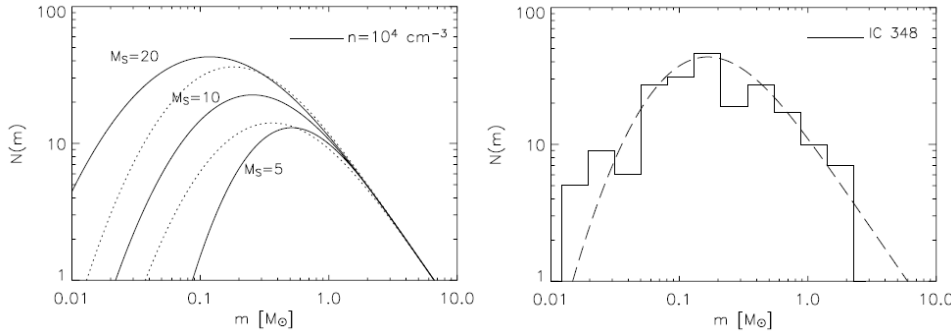


Figure 1.8: *left*: Dynamical simulation isochrones from Padoan and Nordlund (2004) for different starting parameters, which are then plotted over an empirical IMF of the young star-forming region IC 348 from Luhman et al. (2003) *right*.  $M_S$  is the Mach number (rms of the cloud’s initial turbulence). (See text for reference).

After the discovery and confirmation of the theoretical existence of brown dwarfs, the origin of the population of brown dwarfs was still unclear. Models describing the activity in molecular clouds were needed in order to describe the formation of dense cores (Padoan and Nordlund, 1997) that then go on to form stars and sub-stellar mass objects. Padoan and Nordlund (2002) introduced turbulent fragmentation into theoretical 2D simulations that then reduced the allowed Jeans mass required for classically stable, free-falling gravitational collapsing clouds going on to form a pre-stellar core. They conclude that turbulence is a necessary mechanism for the formation of stellar and sub-stellar objects. Turbulence can be modeled via hierarchical fragmentation where the minimum mass required for star formation has been shown to vary between 0.007 and 0.010  $M_{\odot}$  in newer 3D simulations (Boyd and Whitworth, 2005), which is still heavier than some isolated planetary mass objects observed, for example  $\sigma$  Orionis 70 for example (Zapatero Osorio et al., 2002, 2008). More advanced methods are required to model this formation when presented by evidence of isolated planetary mass objects of masses lower than this. Fragmentation simulations are required in order to attempt to explain the frequency of brown dwarfs which are two orders of magnitude lighter (Padoan and Nordlund, 2004). An example their simulation is shown in Figure 1.8 *left* showing the IMF lognormal curve for different initial conditions whilst the *right* describes the IC 348 IMF from Luhman et al. (2003) with the lognormal

IMF curve from the best-fitting initial simulation parameters.

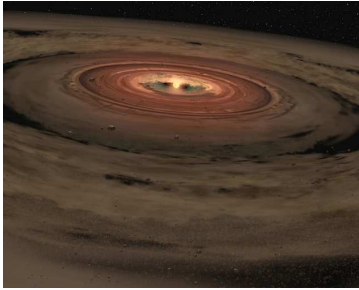


Figure 1.9: Formation of a brown dwarf with its own disk of gas and dust.

A large proportion of brown dwarfs also show no evidence of either being ejected from angular momentum interactions with a parent star and disk, as proposed by Reipurth and Clarke (2001), or being formed from further interactions within the disk, or from possible photo-erosion of pre-stellar cores by external massive stars (Whitworth and Zinnecker, 2004). Still, these have all been shown, however, to produce brown dwarf-mass and planetary-mass objects. The ejection mechanism can still be one method of brown dwarf formation, though they occur less in the more advanced models which include radiative feedback (Bate, 2009c). Bate et al. (2002b) also discuss from simulations that star/brown dwarf multiple systems can also occur at a higher frequency around more massive stars, indicating that fragmentation is not the only mechanism for brown-dwarf production. Guieu et al. (2007) discuss the star/disk-brown dwarf interaction which whilst thought to be the *dominant* formation mechanism, requires the numbers produced by the ejection mechanism to be increased by  $\sim 25\text{-}30\%$  to agree with observations. To this end, it is necessary to model one-pass turbulence within a molecular cloud, originating with soliton shocks from either a relatively nearby supernova or a nearby and recently turned-on O or B-type star, present in many star forming regions. The minimum masses for this can be less than as discussed and proposed by Boyd and Whitworth (2005) when using 2D fragmentation simulations to be as low as  $0.003 M_{\odot}$  (or  $3 M_J$ ) for specific shock parameters, and conclude that isolated brown dwarfs with these masses can form from shock-compression in turbulent clouds. In addition, further work by Whitworth and Stamatellos (2006) reduces the masses formed from *in-disk* formation scenarios to just  $1 M_J$ . In this case, there is also a constraint on the minimum distance, 30 AU, from the star at which these objects can form due to the temperature and ease of fragmentation within the disk. There is evidence of more disks present around brown dwarfs, with further disks observed by Luhman et al. (2007a); Scholz and Jayawardhana (2008). There is also recent evidence for small brown dwarfs which have formed within a disk where Luhman (2004) made the first discovery of a wide ( $\sim\text{pc}$ ) brown dwarf binary, modeled with success by Whitworth and Stamatellos (2006) with a parent star. There is also further evidence for brown dwarf-brown dwarf binaries that can form in isolation (Luhman et al., 2009). A possible brown dwarf forming in isolation is rendered in Figure 1.9 1.9. A further problem with the current understanding is the proposed brown dwarf deficit detected (or not, as it were) in many clustered regions, although perhaps the origin of this deficit can be partially explained by the generally small FOV of cluster observations (Guieu et al., 2006), leading to the lower-mass

brown dwarfs being missed from the census, due to wide cluster orbits or having been ejected completely. Further, turbulent fragmentation simulations also manage to produce the predicted number of brown dwarfs from mass function estimates which again are not observed in these numbers, an improvement on previous simulations by Bate et al. (2002a) which overproduced the numbers of brown dwarfs (Bate, 2009a). More recent tweaking of the models by Bate (2009b) indicated a certain robustness of the initial formation conditions where the level of turbulence, referred to as a ‘power velocity field’, seems not to greatly influence the stellar properties or distribution. Bate (2009c) summarise their previous hydrodynamical simulations (Bate et al., 2003; Bate and Bonnell, 2005) between the initial conditions and the formation of cores via radiative feedback from the more massive stars. The radii used and the initial masses, and so Jeans masses, resulted in differing distributions of stars and brown dwarfs. The inclusion of radiative feedback was shown to reduce the number of pre-stellar (or sub-stellar) cores by a factor of  $\sim 4$  by reducing the fragmentation rate of the larger stellar disks and so the occurrence of lower mass embryos. These are summarised in the standard logN IMF plot in Figure 1.10 (their Figure 7), along with the IMFs from Chabrier (2003); Kroupa (2001) and Salpeter (1955). The accretion radii is the limit at which a simulation (SPH) particle falls in and onto the sink particle which is created when the central density of a particular region in the simulation exceeds  $10^{-11} \text{ g cm}^{-3}$ ; particles greater than this distance join the sink particle in a circular orbit. Bate (2009c) proposed that the similarities between the observed IMFs in nearby clusters are fundamentally based upon radiative feedback between the cloud-star-disk interactions, which more accurately explain the observed numbers of brown dwarfs.

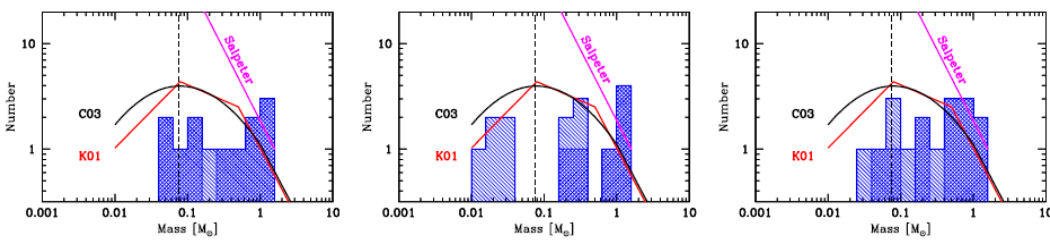


Figure 1.10: From *left to right*: results from the Bate et al. (2003) at an accretion radius of 0.5 AU, Bate et al. (2003) with a different accretion radius of 5 AU, and the denser initial cloud results from Bate and Bonnell (2005) with accretion radius 5 AU. The curved, broken, and straight line are the empirical IMFs from Chabrier (2003); Kroupa (2001) and Salpeter (1955) respectively. The singularly hashed area defines the accretion and the doubly hashed regions define the non-accretion set of the sample.

## 1.5 Motivation

Two clusters have been observed that should give us the greatest chances of success in detection low mass objects and to constrain the low-mass end of the initial mass function (IMF), are the star-forming region IC 348 and the open cluster IC 4665. It is hoped that with narrowband photometry the lowest mass members of IC 348 can be catalogued, whilst a cluster census of IC 4665 of M to L-dwarfs can be divined using a large survey with  $Y$  and NIR broadband photometry.

Finally, the open questions attempted to be addressed in this work are:

- How do the lowest mass objects form?
- How do the lowest-mass objects affect the IMF?
- How do the lowest-mass objects overlap with the largest planets?
- How does this work add to the current scientific understanding?

To answer these questions, the two young cluster regions should be observed with respect to frequency and distribution of the lowest-mass brown dwarfs to attempt to find how many brown dwarfs form. It is expected that the lowest mass objects form in all scenarios and clusters but many of these remain undetected; from ejection due to dynamically shifting interactions from within the cluster itself; from cooling to below present detection limits; and from regions of high local extinction which, when in the foreground of these faint objects, also prevents detection. It can be simple to assume that whilst the lowest mass objects should be the most numerous; the formation methods could prove that the lowest mass objects are too light to form via unaided gravitational collapse (*i.e.* as a lone brown dwarf and disk), or that they experience too much interaction leaving their formation stunted due to the close proximity of its neighbours located nearby in the cluster region. This then reduces the number of low-mass objects being formed whose material could remain as dust and some gas orbiting around a more massive brown dwarf or star, indicated by large disk fractions in star forming regions yet low numbers of low-mass objects. This affects the low-mass part of the IMF which can be skewed to either a powerlaw or lognormal dependence.

The lowest-mass objects should overlap with planets with respect to the materials making up these objects and their coalescence into planet-like objects from parent disks. The types and amounts of dusts and gases are purely dependent on the materials present in the originating cloud, and specifically the material present in the original collapsing cloud.

The work presented in this thesis hopes to expand the number of the lowest-mass objects ever detected in a star-forming region with the discovery of a candidate  $T5.5_{-0.5}^{+1}$  dwarf in the 3 Myr old star-forming region IC 348, and the work done towards a full census and candidate list ready for spectroscopic followup of the  $\sim 40$  Myr open cluster IC 4665 down to a completeness of  $0.015 M_{\odot}$  or  $\sim L3$  dwarf regime. Both of these regions have not been observed at such a depth to date and this work should greatly expand the information on and confirmation of the lower mass



end of the initial mass function.

### 1.5.1 Observational Strategy

- Why observe clusters and not field objects?
- Why observe different clusters?
- Why choose star forming regions and young open clusters?

These are the main questions to think about when deciding what sort of observations to take. The possible telescope integration time and the size of the telescope are main limitations on current searches for low-mass objects in the field and in star-forming regions. Dedicated surveys are available but the trade off is depth against survey coverage, which are all dependent on the observation time allocation. The survey depth should be optimised to the expense of the coverage to find the lowest mass objects. It is important, then, to carefully balance the telescope and detector with respect to the regions of interest. To this end we must ask ourselves what the best solution is when using the available time and technology.

These questions can be answered forthwith. Old, 5 Gyr, sub-stellar mass objects are typically field objects which have long since evaporated from their birth clusters and are now roaming free betwixt the stars. They are usually more massive for a given effective temperature as they have lost thermal energy since their formation and are not producing energy from hydrogen synthesis, though depending on mass and original temperature or spectral type these objects could have had some small amount of deuterium burning. There will certainly be some decay from radioactive isotopes within the confines of the object, similar to that in the core and mantle of the Earth, though the energy that this would produce would likely be negligible over such a time frame. Young,  $< 50$  Myr sub-stellar mass objects are very similar except that if a young and old object have similar temperatures or spectral types then it follows that the young object should be less massive as they have not had 4.5 billion years to expel heat, and a very little mass, to reduce their effective temperatures. An additional factor is that sub-stellar objects contract when they cool, reducing their luminosity further whilst increasing and conserving their gravitational potential energy, however, a young object will still be more luminous than an old field object. Given that field objects are likely to be single, or at most small bound systems, it seems more ideal to observe a cluster which should have a large population of sub-stellar mass objects in one place, without the need for a large scale survey.

A cluster, therefore, would seem the best place to observe sub-stellar mass objects as the relatively low coverage area should yield useful numbers of bona fide objects. Additionally, the youth of a cluster is especially important as it partially determines the magnitude of the lowest mass objects that can be detected. The distance to the cluster is also as important as the youth as it determines how much extinction is present, excepting the local cluster extinction, and so the

magnitude and depth of the observations. Additionally, in the case of a young star-forming region, all of the objects should be approximately the same age, with a dispersion of the age of the cluster. Young clusters are also still evolving through dynamical interactions and so fewer objects should have been ejected from the cluster, or found in large ( $>$  cluster radius) orbits meaning there should be less contamination in a given region. Extinction also helps this contamination issue as in star-forming regions there is usually still a lot of dust and gas which occlude background stars, and also give most objects within the cluster a red excess which is non-existent in the objects found in the foreground. So, the younger the brighter the object, the closer the brighter the object and, finally, the lower the extinction the brighter the object. To this end the young ( $\sim 3$  Myr) star-forming region IC 348 is observed for the lowest mass objects  $< 10 M_J$ , and the young ( $\sim 40$  Myr) open cluster IC 4665 is observed to find the initial mass function across this cluster.

### 1.5.1.1 Coordinate System & Galactic Locations

A coordinate system is used to ascertain the location of the object with respect to the location of Earth. The most recent coordinate system is the J2000 system, where the tiny variations in the movement of the Earth around the sun over the course of its orbit requires the coordinate system to be re-calculated every 50 years. Older data can be found in the J1950 system. All data in this work is given in the J2000 coordinate system for clarity.

A map of the Galaxy can be found in Figure 1.11, taken from Momany et al. (2006) and shows decimal J2000 coordinates and the location of the Sun and also the major features. The Galactic centre and anticentre, the bar (Freudenreich, 1998) of length  $\sim 3$  kpc (Vallée, 2005), along with some of the spiral arms are labeled. The two clusters IC 4665 and IC 348 are located towards Ophiuchus and Perseus respectively, where the distances are approximately the same distance, 300-350 pc, from the Sun as shown in the spherical inset. IC 4665 has a distance taken to be  $356 \pm 15$  pc for this work, whilst the distance to IC 348 has been taken to be  $300 \pm 15$  pc. IC 4665 is a young ( $\sim 40$  Myr) open cluster that contains low-mass objects currently observable to a spectral type  $\sim L3$ ; and IC 348 is a very young ( $\sim 3$  Myr) star forming region T-dwarfs of spectral type later than  $\sim T3$  should be observable. The difference in observable spectral types are due to the cooling and ejection of low-mass members, and the allotted telescope time for this work. The properties of and the work done on these clusters are discussed further in their respective chapters, 3 and 4.

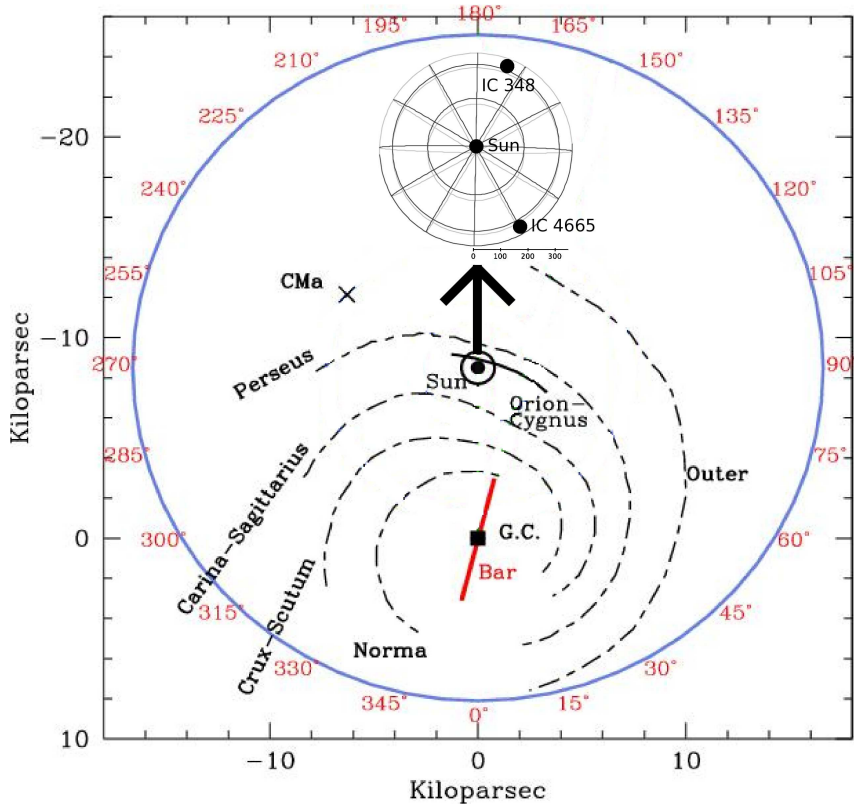


Figure 1.11: An HII region/dust mapped schematic view (from Drimmel and Spergel (2001)) of the Milky Way as seen from above. The Galactic center, the Sun and the names of the spiral arms (dashed) are plotted. The Galactic bar was added with an orientation angle of  $14^\circ$  and is of length 3 kpc. The large blue circle is a fixed heliocentric distance at 17 kpc for scale, with the coordinates in decimal degrees. The two clusters IC 4665 and IC 348 discussed in this work are within the black circle around the Sun, expanded in the spherical inset of radius 350 pc (arrowed).

## 1.6 Summary

The basics of the physics behind the luminosity and temperatures of stars and other celestial bodies has been discussed with respect to the apparent and absolute magnitude systems that are in use today. Further, the loss of energy leading to the differences between this systems occurs from reddening of the radiation along the line of sight which is referred to as extinction. Galactic star formation originating from dense molecular clouds forming dark cores is also discussed and can be greatly affected by the local conditions which can be the turbulence from supernova shocks or from quiescent gravitational collapse. Angular momentum is conserved as this mass of gas and dust flattens and collapses into a spinning disk. Low-mass star formation is mainly affected by the mass of the parent cloud. Turbulent ejection scenarios and ad hoc low-mass brown dwarf formation is thought not to be the dominant mechanism for the formation of low-mass brown dwarfs as predicted by hydrodynamical models, rather the majority of these objects form within the influence of a parent star or disk.

The Lyon theoretical models are discussed in depth, to explain why these models are used as the principal isochrones used for this thesis. The updated BT models are the most recent and are superior in that they take into account the work done over this past decade on the opacities and distribution of known species and grains in the atmospheres and photospheres of brown dwarfs.

The mass function (MF) and initial mass function (IMF) usually originates with colour/magnitude (CMD) and colour/colour diagram (COLD) analysis, involving fit-by-eye cluster regions or using comparisons to theoretical isochrones. Following the feasibility of further study and proposal acceptance of spectroscopic follow-up, candidates members can be accepted or rejected. The mass distribution of accepted members can then be plotted against the mass, usually on logarithmic axes, and the MF or IMF can be found to follow either a power-law distribution for solar and higher-mass stars and more of a log-normal curve for sub-stellar objects. Additionally, the current understanding of the IMF is summarised for a sample of young star forming and open cluster regions from the literature.

Finally, the open questions that are posed encourage further research into the low-mass initial mass function of star forming regions and open clusters with a view to looking at the overlap between brown dwarf and planetary mass objects. This is based upon the feasibility of new ground and space based telescopes and improved detectors that are capable of delving ever deeper into space, and with it a deepening of our understanding of the cosmos.



## 1.7 Résumé

Les bases de la physique derrière la luminosité et des températures des étoiles et autres corps célestes a été discutée en ce qui concerne les systèmes de magnitude apparente et absolue qui sont en usage aujourd'hui. En outre, la perte d'énergie conduit à des différences entre les systèmes de ce produit à partir de rougissement du rayonnement le long de la ligne de visée qui est appelée extinction. La formation des étoiles galactique provenant de nuages moléculaires denses formant des noyaux sombres est également discutée et peut être grandement affectée par les conditions locales, par exemple les turbulences des chocs supernova ou de l'effondrement gravitationnel de repos. La conservation du moment angulaire que cette masse de gaz et de poussière aplatit et s'effondre dans un disque en rotation. La formation des étoiles de faible masse est principalement affectée par la masse du nuage parente. Scénarios d'éjection turbulent et formation ad hoc de faible masse naine brune est la pensée de ne pas être le mécanisme dominant pour la formation de faible masse des naines brunes que prévu par les modèles hydrodynamiques, plutôt la majorité de ces objets forme sous l'influence d'une étoile parent ou disque.

Les modèles théoriques de Lyon sont discutées en profondeur, d'expliquer pourquoi ces modèles sont utilisés comme isochrones principal utilisé pour cette thèse. Les modèles-BT mis à jour sont les plus récentes et sont supérieurs à ce qu'ils prennent en compte le travail accompli au cours de cette dernière décennie sur les opacités et de la distribution des espèces connues et les grains dans les atmosphères et photosphères des naines brunes.

La fonction de masse (FM) et la fonction de masse initiale (FMI) provient généralement de couleur / magnitude (CMD) et la couleur / couleur (COLD) analyse, impliquant des régions cluster ajustement par les yeux ou en utilisant des comparaisons à isochrones théoriques. Suite à la faisabilité d'une étude plus approfondie et l'acceptation de la proposition de spectroscopie de suivi, les membres de candidats peuvent être acceptés ou rejetés. La distribution massive de membres acceptés peut ensuite être tracée en fonction de la masse, le plus souvent sur des axes logarithmiques, et le FM ou le FMI se trouve à suivre soit une distribution en loi de puissance pour les étoiles de type solaire et plus de masse et plus d'une courbe log-normale pour les objets sous-stellaires. En outre, la compréhension actuelle du FMI est résumée pour un échantillon de régions jeune star cluster formage et ouvert de la littérature.

Enfin, les questions ouvertes qui se posent encourager la recherche sur la fonction de masse initiale de faible masse des régions de formation stellaire et des amas ouverts en vue d'examiner le chevauchement entre les naines brunes et des objets de masse planétaire. Ceci est basé sur la faisabilité d'un nouveau terrain et télescopes spatiaux et détecteurs améliorés qui sont capables de plonger toujours plus profondément dans l'espace, et avec elle un approfondissement de notre compréhension du cosmos.



## Chapter 2

# Data Acquisition and Pipeline Development

### Contents

---

<b>2.1 Instrumentation &amp; Observations</b> . . . . .	<b>34</b>
2.1.1 Principal Observatory - Canada France Hawaii Telescope (CFHT) . . . . .	34
2.1.2 Observed Data . . . . .	38
<b>2.2 Infrared Surveys &amp; Astronomical Databases</b> . . . . .	<b>45</b>
2.2.1 2Micron All Sky Survey (2MASS) . . . . .	45
2.2.2 UKIRT Infrared Deep Sky Survey (UKIDSS) . . . . .	45
2.2.3 Spitzer Space Telescope . . . . .	46
2.2.4 Online Respositories . . . . .	47
<b>2.3 Pipeline Development</b> . . . . .	<b>48</b>
2.3.1 SExtractor First-Pass . . . . .	49
2.3.2 SExtractor Optimisation . . . . .	50
2.3.3 Point Source Function Extractor (PSFEx) . . . . .	53
2.3.4 PSFEx Optimisation . . . . .	55
2.3.5 SExtractor Second-Pass . . . . .	55
2.3.6 Catalogue Amalgamation . . . . .	56
2.3.7 Calibration . . . . .	56
<b>2.4 Summary</b> . . . . .	<b>62</b>
<b>2.5 Résumé</b> . . . . .	<b>63</b>

---



## 2.1 Instrumentation & Observations

### 2.1.1 Principal Observatory - Canada France Hawaii Telescope (CFHT)

The Canada France Hawaii Telescope<sup>1</sup> (CFHT) is 3.6m in diameter, located at an ideal location 4,200m up on the summit of the dormant volcano Mauna Kea in Hawaii. Islands classically make ideal locations for telescopes as the weather usually flows around the high-ground rather than over it, resulting in reduced atmospheric water vapour that is always problematic for any ground-based IR observations. There is still water absorption in the upper atmosphere which is especially problematic for IR observations resulting in the use of bands where the absorption in the atmosphere is at a minimum, discussed in Chapter 1. The optical/IR-capable telescope has historically had various instruments on the back end. There are currently three imaging instruments available for use, which are the wide-field imager MegaCam (Boulade et al., 2003) (on the MegaPrime focus), the Wide-Field Infrared Camera (WIRCam) (Puget et al., 2004), and the 1k x 1k Infrared detector (KIR), that last of which uses the Adaptive Optics Bonnette (AOB/PUEO). MegaCam and WIRCam were the main instruments used to image parts of the sky necessary to fulfil our motivation, whilst the KIR has not been used for any observations in this work. The fields of view and CCD layout of WIRCam and MegaCam are shown in Figure 2.1, and are discussed further in due course. Tabulated data of these two instruments on the CFHT can be found in Table 2.1, where the field of view (FOV), available filters and approximate quantum efficiency values of the filter regions are also neatly summarised. Figures 2.2 and 2.3 show the quantum efficiency of the detector and central *effective* wavelengths of each of the filters for the WIRCam and MegaCam detectors respectively, where the data originated from the CFHT website. The filters have all been convolved, excepting the *Y*-band filter, by the Spanish Virtual Observatory<sup>2</sup> (SVO - see 2.2.4) to produce useful extinction  $A_\lambda/A_V$  co-efficients. The WIRCam's *Y* extinction value was not available at the SVO and therefore will be discussed more thoroughly in section 3.3.

The CFHT offers various sets of dithering patterns where our observations usually used the greatest pattern of 7 dithered images per pointing in order to fill in the gaps between CCDs, to slightly increase the FOV and also to improve the reliability of the data at the borders of our fields of view.

#### 2.1.1.1 Wide-field Infrared Camera (WIRCam)

WIRCam<sup>3</sup> (Puget et al., 2004) is an upgraded IR version of the retired CFH12K CCD mosaic optical camera, and is located on the main CFHT prime focus upper end (PFUE) shown in the upper panels in Figure 2.1. The optics for WIRCam (Thibault et al., 2003) were made by the

---

<sup>1</sup>[www.cfht.hawaii.edu](http://www.cfht.hawaii.edu)

<sup>2</sup><http://svo.laeff.inta.es/theory/filters/index.php>

<sup>3</sup><http://www.cfht.hawaii.edu/Instruments/Imaging/WIRCam/>

Table 2.1: Instruments on the CFHT used listing the FOV, filters and FWHM's of the associated MegaCam ( $z'$ ) and WIRCam ( $J$ ,  $H$ ,  $K_s$ ,  $CH_4$ off and  $CH_4$ on) filters. Extinction values for each filter have also been convolved as a function of each filter by the SVO, with the exception of the WIRCam  $Y$  filter (see section 3.3). Values with an asterisk have uncertainties of more than 15%.

Telescope	FOV	Filter	AB to Vega offset	Detector Quantum Efficiency	$\lambda_c^{eff}$ $\mu\text{m}$	$\Delta\lambda^{eff}$ $\mu\text{m}$	$A_\lambda/A_V$
MegaCam	$0.96^\circ \times 0.94^\circ$	$z'$	-0.554	$\sim 0.30$ (20 webpage)	0.88	0.27	0.52
WIRCam	$20' \times 20'$	$Y$	-	0.50*	1.04	0.10	0.42
		$J$	-	0.75	1.25	0.16	0.30
		$CH_4$ off	-	$\sim 0.75^*$	1.58	0.10	0.21
		$H$	-	$0.75^*$	1.63	0.29	0.20
		$CH_4$ on	-	$\sim 0.75^*$	1.69	0.10	0.18
		$K_s$	-	0.80	2.15	0.33	0.13

Groupe D'Astrophysique at the University of Montreal<sup>4</sup> and the Institut National d'Optique in Quebec<sup>5</sup>. The IR camera has to be cooled to 80K using a cryostat developed at Laboratoire d'Astrophysique et Observatoire de Grenoble<sup>6</sup> (LAOG), where the mechanical structure of the camera system was also developed. The four CCDs which make up the WIRCam array each have dimensions of 2048x2048 pixels, of size 18  $\mu\text{m}$ , and gives a total of  $\sim 16$  Mpixels. The standard FOV is  $19.4' \times 19.4'$  and so yields a pixel scale of  $0.306'' \text{ pixel}^{-1}$  with dithering. Another addition to the camera, and the CFHT dithering option, is the Image Stabilizer Unit (ISU), which allows micro-dithering of up to 0.5 pixels to increase the pixel scale from  $0.306''$  to  $0.15'' \text{ pixel}^{-1}$  (used for both of the IC 348 and IC 4665  $J$ ,  $H$  and  $K_s$  images). The large gaps in between the CCDs, of size  $45''$ , are dealt with using a combination of the 7-pattern dithering of the CFHT, the 4 to 8 micro-dithering exposure per dither on the ISU, and also the associated weight (coverage) maps, which are discussed later in Section 2.1.2.2.

The imaging capabilities available on WIRCam include a range of broadband IR filters, primarily the IR  $Y$ ,  $J$ ,  $H$  and  $K_s$  filters. In addition to these broadband filters there are a number of narrowband ( $\delta\lambda \sim 0.1 \mu\text{m}$ ) filters including, and most notably for this work, the  $CH_4$ off filter at 1.58  $\mu\text{m}$  and the  $CH_4$ on filter at 1.69  $\mu\text{m}$ . Data on these filters can be found in Table 2.1, whilst filter curves and the approximate quantum efficiency of the detector for all the WIRCam broad and narrowbands can be found previously in Figure 2.2. Other narrowband filters not used in this work can be found on the CFHT WIRCam webpages<sup>7</sup>.

<sup>4</sup><http://www.astro.umontreal.ca/groupe/>

<sup>5</sup><http://www.ino.ca/fr/accueil.aspx/>

<sup>6</sup><http://www-laog.obs.ujf-grenoble.fr/>

<sup>7</sup><http://www.cfht.hawaii.edu/Instruments/Imaging/WIRCam/>

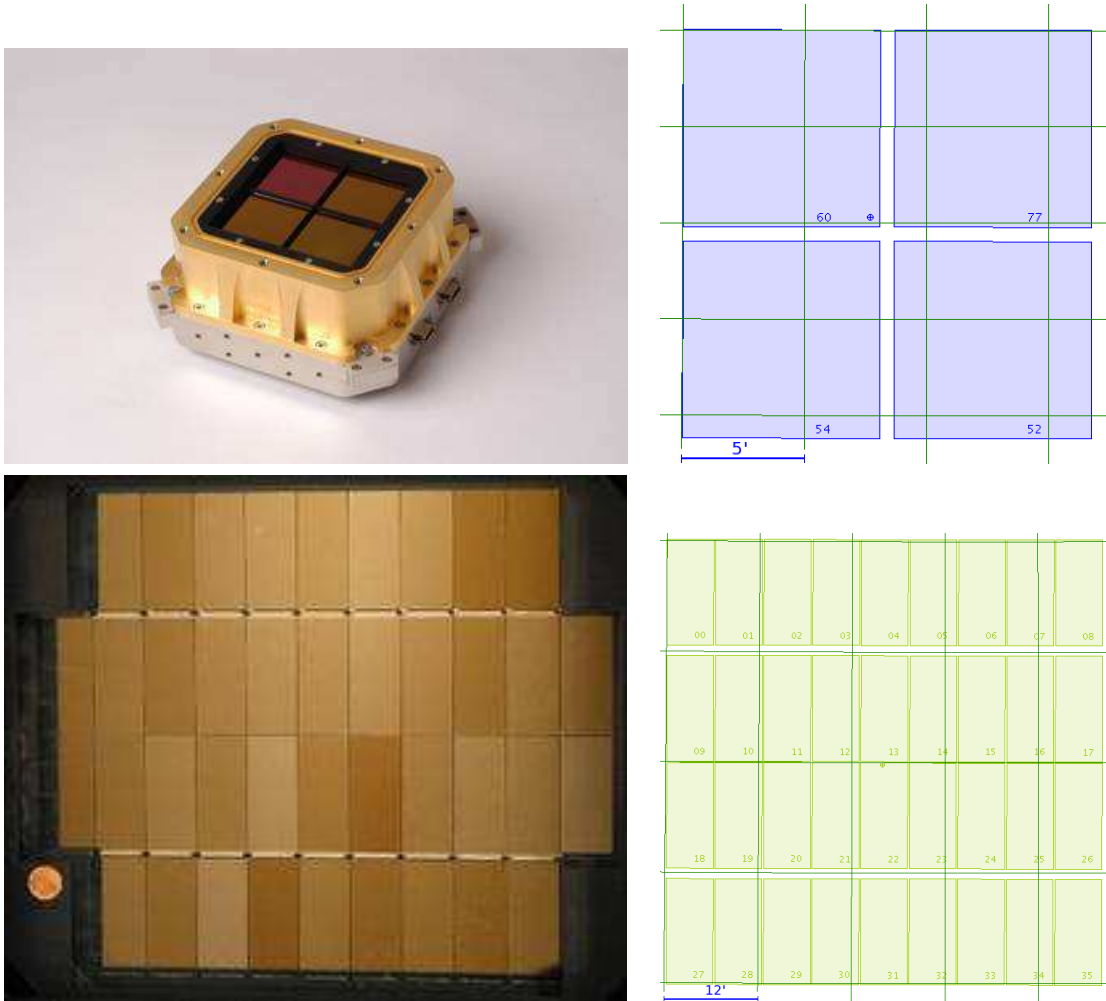


Figure 2.1: *top*: The four CCDs making up the WIRCam array with gaps of order  $45''$ . *bottom*: CCD arrangement of the MegaCam array with gaps ranging from  $\sim 13$  to  $\sim 80''$ . Gaps between the CCDs are dealt with primarily through dithering and micro-dithering and associated weight maps.

### 2.1.1.2 Mega-Pixel Camera (MegaCam) on MegaPrime

MegaCam (Boulade et al., 2003) is an optical camera which was built at the Commissariat l’Energie Atomique (CEA) in France, and is housed on the back end of MegaPrime<sup>8</sup>, the wide-field prime focus environment on the CFHT. It requires a cryostat to keep its 36 CCDs cooled to 153K. The CCD matrix is made from 4 rows of 9 rectangular CCDs, arranged into a square, as seen in the lower panels in Figure 2.1. Each CCD lattice has  $2048 \times 4612$  pixels equating to 360 Mpixels, and giving a pixel size of  $13.5 \mu\text{m}$ . The FOV of MegaPrime is  $0.96^\circ \times 0.94^\circ$  and relates to a pixel scale of  $0.185'' \text{pixel}^{-1}$ . There are small gaps ( $\sim 13''$ ) between each part of the CCD matrix and two large gaps between the first and third row of  $\sim 80''$ , and are treated in a similar manner to those gaps on the WIRCam CCD array (see Section 2.1.2). The two largest gaps, however,

<sup>8</sup><http://www.cfht.hawaii.edu/Instruments/Imaging/MegaPrime/>

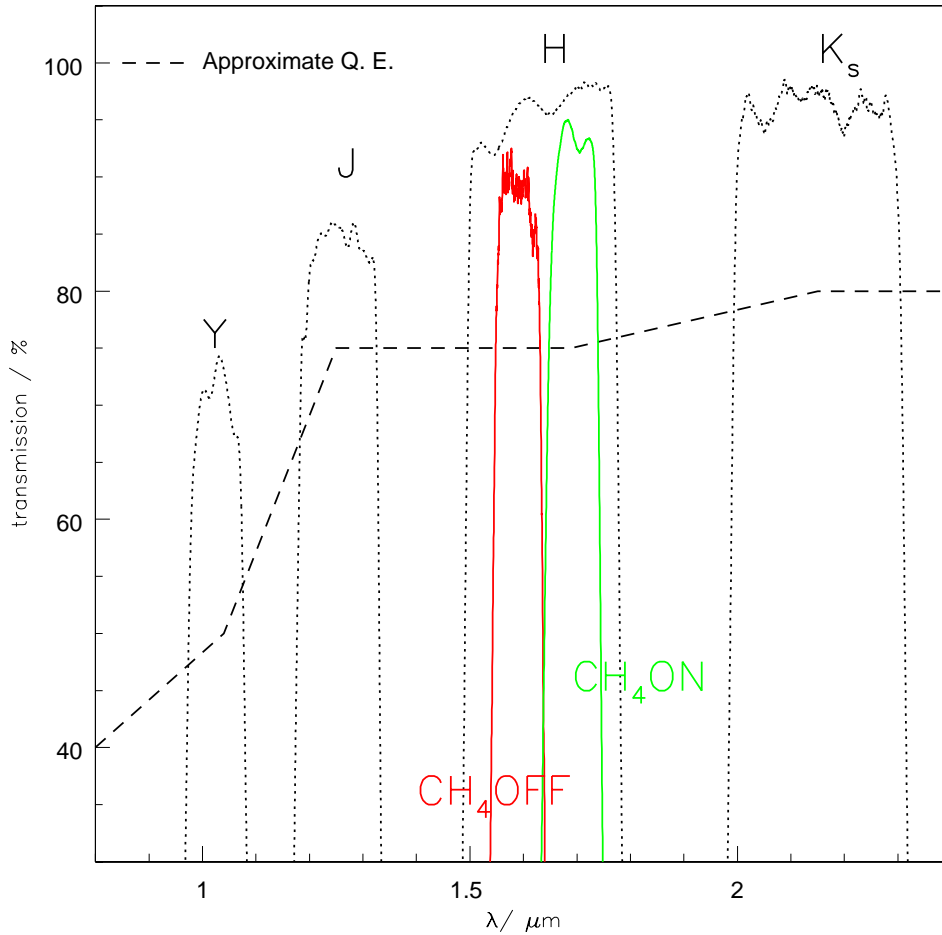


Figure 2.2: Black dotted curves are raw detector responses for the broadband filters (labelled  $Y$ ,  $J$ ,  $H$  and  $K_s$  left to right) whilst the red solid curve is the response for the  $CH_4$ off and green solid curve the  $CH_4$ on narrowband filters. The dashed line through the curves is the quantum efficiency of the detectors, where all points apart from  $J$  and  $K_s$  have uncertainties of more than 15%.

are not able to be addressed in this manner resulting in the MegaCam output images having two blank lines across its raw and then processed images, shown in Figure 2.6. MegaCam has been calibrated to output data in the modern CFHT AB system using the CFHT Elixir pipeline<sup>9</sup>.

The MegaCam filters are similar to the filters of the Sloan Digital Sky Survey (SDSS),  $u'$ ,  $g'$ ,  $r'$ ,  $i'$  and  $z'$ , (Fukugita et al., 1996; Bessell, 2005), and though all of these filters were available, observations from just the  $z'$  filter was proposed and then used in this work. Consequently only this MegaCam filter is discussed in any detail, found previously in Table 2.1. The  $z'$  central effective wavelength is  $0.88 \mu\text{m}$ , with an associated detector quantum efficiency of 30 %, where all filters

<sup>9</sup><http://www.cfht.hawaii.edu/Instruments/Elixir/>

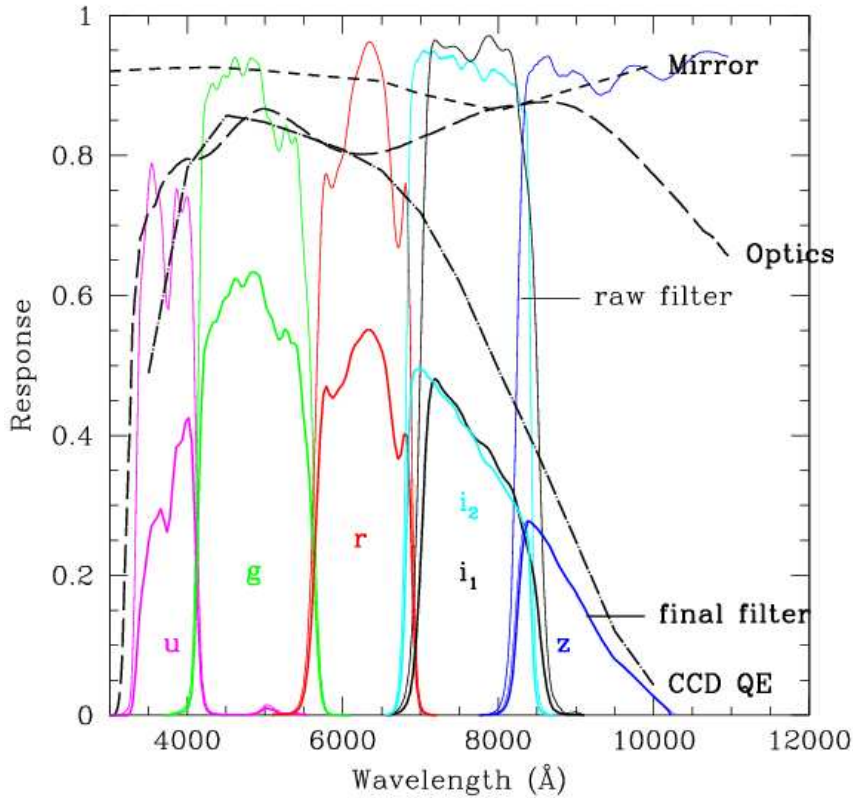


Figure 2.3: MegaCam  $u'$ ,  $g'$ ,  $r'$ ,  $i'$  and  $z'$  filters and associated CFHT quantum efficiency of the detector. The central effective wavelength of the  $z'$  is  $\lambda_c^{eff} 0.88 \mu\text{m}$  of width  $0.27 \mu\text{m}$ . Additional information regarding the effectiveness of the CFHT mirror and optics are also given, with the final throughput shown as bold coloured lines. The bold blue line is the  $z'$  filter convolved with the quantum efficiency of the detector, where the base response of this filter is shown as the thin blue line. Other filters are labelled as per the figure. Figure taken from the Canadian Astronomy Data Centre (see text for reference).

can be found in Figure 2.3 along with the other  $u'$ ,  $g'$ ,  $r'$  and  $i'$  filters for completeness (figure taken from the Canadian Astronomy Data Centre (CADC)<sup>10</sup>, data from the CFHT MegaCam pages). The effectiveness of the CFHT mirror and the optics are also taken into account to obtain the final, *effective*, filter values.

## 2.1.2 Observed Data

### 2.1.2.1 CFHT Pre-Processing Pipeline

MegaCam's raw output is pre-processed by the Elixir<sup>11</sup> (Magnier and Cuillandre, 2004) pipeline in-house at the CFHT. WIRCam data is also pre-processed at the CFHT using the 'I'wi

<sup>10</sup><http://www4.cadc-ccda.hia-ihc.nrc-cnrc.gc.ca/megapipeline/docs/filters.html>

<sup>11</sup><http://www.cfht.hawaii.edu/Instruments/Elixir/>

preprocessing pipeline<sup>1213</sup> (Albert et al., in prep.). Both pre-processing pipelines are meant to remove any detector-specific details from the outputted images and includes detrending the raw data and flagging the saturated pixels where saturated flags are assigned if the flux values exceed 36000 ADUs. Flat-fielding, sky subtraction and establishing an astrometric solution are also handled in this pipeline, before the photometric calibration is addressed. The photometric calibration is achieved using standard stars, except for the  $J$ ,  $H$  and  $K_s$  bands which are calibrated using the available 2MASS bands. Consequently, MegaCam data is outputted in the CFHT AB system whilst the WIRCam calibration uses a mixture of standard stars and 2MASS and is therefore outputted in the CFHT Vega system, as 2MASS is in the Vega system. Both sets of data are also zero-point calibrated to 30 mag by the 'I'iwi pipeline. This zeropoint is handled in two ways, depending on the filter. For 2MASS-similar filters ( $J$ ,  $H$ ,  $K_s$ ) the zeropoint is given in the 'I'iwi documentation by:

$$ZP_{measured} = mag_{2MASS} + 2.5 \log_{10}(flux_{total}) - 2.5 \log_{10}(\tau_{exp}), \quad (2.1)$$

whilst for the other filters,  $Y$  and the narrowbands for example, the zeropoint is calibrated using:

$$ZP_{measured} = mag_{modeled} + 2.5 \log_{10}(flux_{total}) - 2.5 \log_{10}(\tau_{exp}), \quad (2.2)$$

where  $mag_{2MASS}$  is the associated 2MASS magnitude,  $flux_{total}$  is the integrated flux from the star in the image,  $\tau_{exp}$  is the exposure time of the measured star, and  $mag_{modeled}$  is calculated by convolving the filter response curves with model spectra of the standard stars.

### 2.1.2.2 Elementary Treatment, Reduction and Analysis of PIXels (TERAPIX)

Both MegaCam post-Elixir pipeline data and WIRCam post-'I'iwi pipeline data is sent to Traitement Élémentaire, Réduction et Analyse des PIXels (TERAPIX)<sup>14</sup> before being calibrated using their pipeline. This pipeline, (Bertin et al., 2002), includes using various custom made programs<sup>15</sup>, for example SCAMP, SWarp and SkyMaker (Bertin, 2008), and custom IDL routines to calibrate the astrometry and photometry, and image stacking. Finally a catalogue of objects in the FOV is constructed using Source Extractor (SExtractor), discussed in Section 2.3, and outputted along with the qualityFITS analysis which is associated with each image, and a weight map and a flag map.

<sup>12</sup><http://www.cfht.hawaii.edu/Instruments/Imaging/WIRCam/WIRCamPreprocQueue.html>

<sup>13</sup><http://www.cfht.hawaii.edu/Instruments/Imaging/WIRCam/IiwiVersion1Doc.html>

<sup>14</sup>[terapix.iap.fr](http://terapix.iap.fr)

<sup>15</sup><http://astromatic.net/>

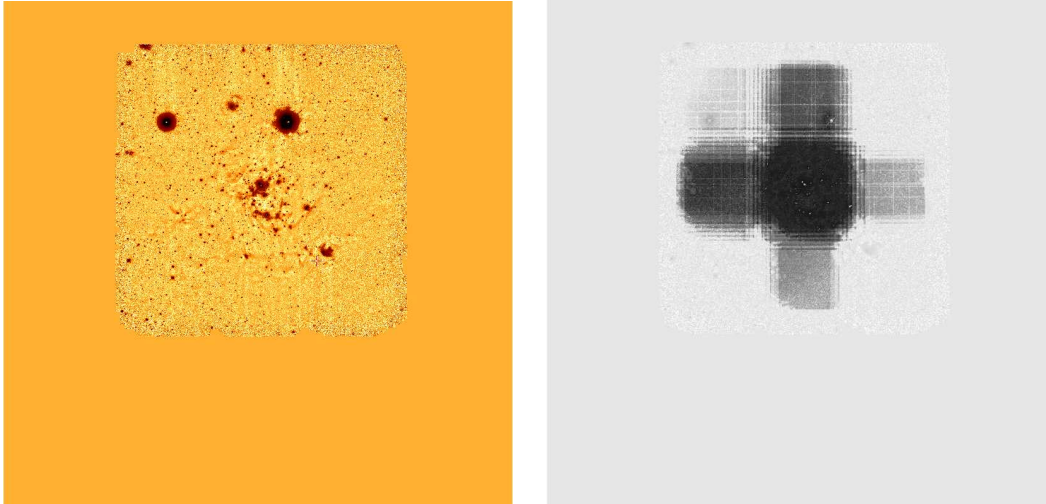


Figure 2.4: (*left*): *J*-band image from IC 348, shown with the FOV that has been extended using blank pixels to that of the  $z'$  MegaCam FOV. (*right*): Identical *J*-band image (faintened), as (*left*) but has the *J*-band associated weight map superimposed onto the *J*-band image, showing how the dithering patterns altered how much of the sky each part of the image was exposed to during the observation periods.

**Science-ready TERAPIX Data** The TERAPIX pipeline outputs two further data files on top of the pre-processed data from the CFHT. Weight maps, which have an associated weighting to each stacked image, and flag maps for each image that specify which pixels are bad and/or saturated or next to these types of pixels. Flag values are discrete values of 0, 4, 8 and 12, where 0 indicates an absence of saturated or bad pixels and 4, 8 or 12 the number of pixels that have or adjoin a saturated or bad pixel value. The left hand image in Figure 2.4 shows the science-ready WIRCam *J*-band image of IC 348 which is made up of a number of stacked images (see Section 2.1.2.4 for further information about this image). The dithering effect is seen in its associated weight map, on the right in Figure 2.4, where regions of different weight indicate how often that region has been observed prior to stacking and what factor that part of the image is weighted with. Note the less-observed regions form a cross due to the  $45''$  gaps between the WIRCam CCDs. These files can be used for the object extraction and are directly supported by SExtractor, which is discussed in more detail in Section 2.3.1. A single SExtractor-parsed catalogue is outputted for each stacked observation using a set of standard configuration values:  $1.5 \sigma$  detection and analysis thresholds, standard 30pixel aperture value and a 64/3 background map/block size for background subtraction. The full details of the TERAPIX SExtractor configuration file can be found in the Appendix 5.5, whilst specifics and optimisation of this file is discussed in Section 2.3.2.

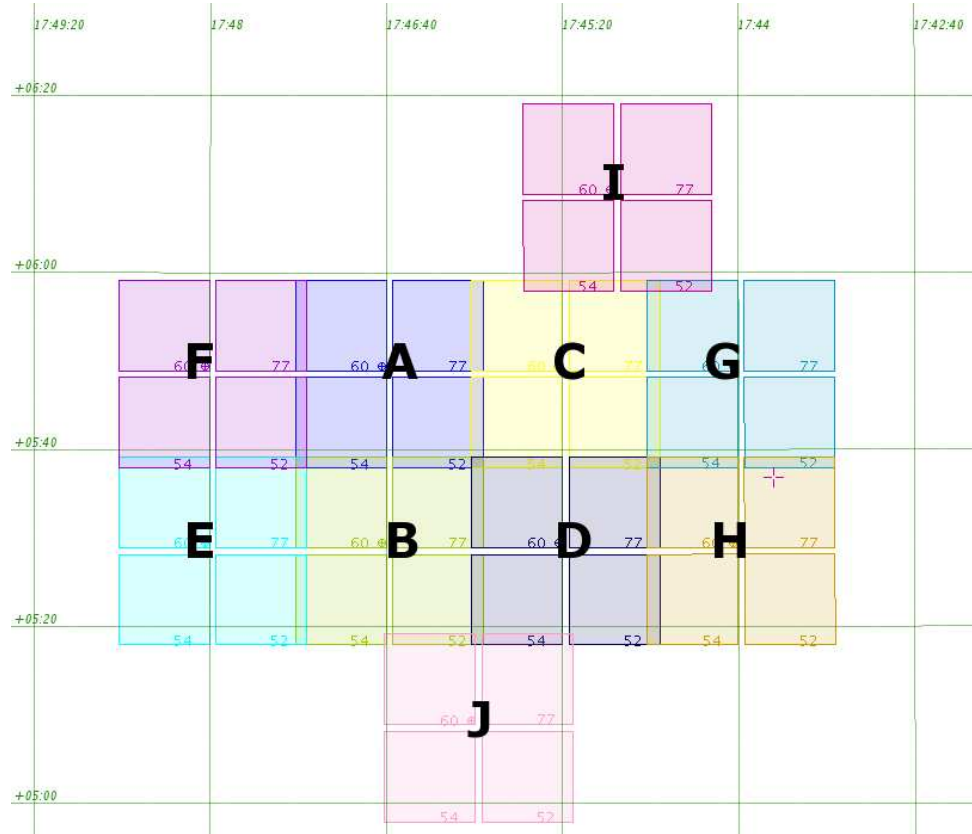


Figure 2.5: The FOV of observed fields A through to J of IC 4665. The two control fields are located outside the frame of this image.

### 2.1.2.3 IC 4665 Observations

IC 4665 is an open cluster whose centre is taken to be at  $17^{\text{h}}46^{\text{m}}18^{\text{s}}00 +05^{\circ}43'00''0$  (J2000), which is towards the constellation of Ophiuchus. The pointings in the direction of IC 4665 are spread across 12 overlapping fields, (see Table 2.2), which includes the cluster's centre and the two control fields all observed by the CFHT in service mode between September 2008 and December 2008.

The grid of 10 images of the cluster are shown graphically in Figure 2.5 where the existence of  $30''$  overlaps between each individual field can be clearly seen. The two control fields are located at least  $1^{\circ}$  outside the known cluster boundary to help assess the contamination from the presence of field stars within the cluster images, and so are not shown within the frame of this figure. The short and long observations were taken at the same time for each observing field and acquired using a 7-position dithering pattern to fill in the  $45''$ -wide gaps in between the IR arrays. The short and long exposure images were taken in  $Y$ ,  $J$  and  $H$  filters. Microdithering was used for the long images with 8 exposures per dithering pattern for the  $H$  and 4 for the  $Y$  and  $J$ , and were not used



Table 2.2: Field of view of the WIRCam images and the central coordinates of the pointings towards IC 4665. The  $Y$ ,  $J$ ,  $H$  and  $K_s$  long and short exposure images all have an overlap of  $30''$  and the centre of the cluster is taken from the SIMBAD database to be  $17^{\text{h}}46^{\text{m}}18^{\text{s}}.00 +05^{\circ}43'00''.0$  (J2000).

Instrument	Field of View (FOV)	Field	Coordinates (J2000)
WIRCam	$20' \times 20'$	A	$17^{\text{h}}46^{\text{m}}42^{\text{s}}.00 +05^{\circ}49'23''.0$
		B	$17^{\text{h}}46^{\text{m}}42^{\text{s}}.00 +05^{\circ}29'23''.0$
		C	$17^{\text{h}}45^{\text{m}}22^{\text{s}}.00 +05^{\circ}49'23''.0$
		D	$17^{\text{h}}45^{\text{m}}22^{\text{s}}.00 +05^{\circ}29'23''.0$
		E	$17^{\text{h}}48^{\text{m}}02^{\text{s}}.40 +05^{\circ}29'23''.0$
		F	$17^{\text{h}}48^{\text{m}}02^{\text{s}}.40 +05^{\circ}49'23''.0$
		G	$17^{\text{h}}44^{\text{m}}02^{\text{s}}.40 +05^{\circ}49'23''.0$
		H	$17^{\text{h}}44^{\text{m}}02^{\text{s}}.40 +05^{\circ}29'23''.0$
		I	$17^{\text{h}}44^{\text{m}}58^{\text{s}}.54 +06^{\circ}09'23''.0$
		J	$17^{\text{h}}46^{\text{m}}01^{\text{s}}.60 +05^{\circ}09'23''.0$
		Control1	$17^{\text{h}}51^{\text{m}}03^{\text{s}}.00 +08^{\circ}05'54''.0$
		Control2	$17^{\text{h}}40^{\text{m}}53^{\text{s}}.00 +02^{\circ}50'14''.0$

for the short observations. The  $K_s$  images were observed with the remaining allocated time and so have ‘medium’-length exposure times of between 532 and 700s. The differences in the lengths of these exposures are dealt with at TERAPIX whilst assessing the zeropoints to ensure that the  $K_s$  band observations are scaled to be equal over all 12 fields.

Total long exposure integration times of 1.07h, 0.54h, and 0.72h for the  $Y$ ,  $J$  and  $H$  and were obtained from multiple individual exposures of 128s, 60s and 13s respectively. The same observing strategy was used for the short  $Y$ ,  $J$  and  $H$  images, all with individual integration times of 5s. See Table 2.3 for more detail regarding the short and long exposure times and observing periods. The ‘medium’ exposure  $K_s$  observations are treated in this work as being associated with both the long and the short exposures, discussed further in Section 2.3.5. The TERAPIX pipeline outputs qualityFITS which give the details and plots on the results of the processing, and also outputs a SExtracted catalogue of objects for each field and each filter where the configuration file can be found in the Appendix 5.5.

#### 2.1.2.4 IC 348 Observations

IC 348 is a clustered star forming region towards Perseus and is located at  $03^{\text{h}}44^{\text{m}}34^{\text{s}}00 +32^{\circ}09'48''.0$  (J2000). WIRCam was used to take narrowband  $CH_4\text{off}$  and  $CH_4\text{on}$  along with  $J$ ,  $H$ , and  $K_s$  images of IC 348, whilst MegaCam was used to take a  $z'$  image of IC 348, where the properties have been shown previously in Table 2.1. The WIRCam observations were obtained

Table 2.3: IC 4665: List of the observing programs and respective exposure and integration times for the  $Y$ ,  $J$ ,  $H$  and  $K_s$  long and short exposure observations.

Filter	Programme(s)	Fields	Exposure length / s	Integration time / s
Short				
$Y$	07AF22 & 07AF99	ABC,C1C2,D + EFGHIJ	5	315
$J$	07AF22 & 07AF99	ABC,C1C2,D + EFGHIJ	5	315
$H$	07AF22 & 07AF99	ABC,C1C2,D + EFGHIJ	5	315
'Medium'				
$K_s$	07AF99	ABCD	15	700
$K_s$	08AF98	C1C2,EFGHIJ	15	532
Long				
$Y$	07AF22 & 07AF99	ABCD + C1C2EFGHIJ	128	3864
$J$	07AF22 & 07AF99	ABCD + C1C2EFGHIJ	60	1960
$H$	07AF22 & 07AF99	ABCD + C1C2EFGHIJ	13	2576

under programme 06BF23 in service mode between September 2006 and January 2007, whilst the MegaCam  $z'$  observations were obtained under programme 06BF28 in queue service mode on September 21-23, 2006. It was used to take 6, 7-pattern dithered  $z'$  images of 1500s each, yielding a total integration time of 9000 s, shown in Table 2.4. The  $CH_4$ on and  $CH_4$ off pointings are both centred at the same location, which includes the cluster's center, while four overlapping WIRCam fields were taken in  $J$ ,  $H$  and  $K_s$  to provide a larger areal coverage, shown in Table 2.4.

Table 2.4: IC 348: Instruments used with FOV, filters, and the central coordinates of the pointings of the cluster. The  $J$ ,  $H$  and  $K_s$  final WIRCam images are made up of four overlapping fields (A, B, C and D), where the total integration times are also included for each filter.

Telescope	FOV	Filter	Integration time (h)	Pointing coordinates (J2000)
MegaCam	$0.96^\circ \times 0.94^\circ$	$z'$	2.5	$03^h 44^m 36^s .00 + 32^\circ 01' 50'' 0$
WIRCam	$20' \times 20'$	$CH_4$ off, on	3.7, 1.4	$03^h 44^m 14^s .80 + 32^\circ 05' 06'' 0$
WIRCam	$20' \times 20'$	$J, H, K_s$	0.35, 0.16, 0.12	
	A			$03^h 44^m 14^s .80 + 32^\circ 05' 06'' 0$
	B			$03^h 44^m 14^s .80 + 32^\circ 15' 06'' 0$
	C			$03^h 45^m 02^s .00 + 32^\circ 05' 06'' 0$
	D			$03^h 45^m 02^s .00 + 32^\circ 15' 06'' 0$

Total integration times of 3.7h in  $CH_4$ off and 1.4h in  $CH_4$ on were obtained from multiple individual exposures of 30s using a 7-position dithering pattern to fill in the  $45''$ -wide gaps in between IR arrays. The same observing strategy with additional micro-dithering was used for the  $J$ ,  $H$  and  $K_s$  images with individual integration times of 45, 10, and 15s, respectively, yielding total integration times of 1260s ( $J$ ), 560s ( $H$ ) and 420s ( $K_s$ ) for each pointing.

The seeing (PSF FWHM) measured on the final WIRCam images was between  $0.55''$  and  $0.65''$ . The co-added  $J$ ,  $H$  and  $K_s$  images were photometrically calibrated using the 2MASS

catalogue over the same area and renormalised to the photometric zero-point of 30 mag. The methane images have no external photometric calibration and the  $CH_4$  magnitudes are given here on an arbitrary albeit internally consistent scale, so that  $CH_{4on}-CH_{4off}\simeq 0$  for unreddened field dwarfs. The MegaCam images were photometrically calibrated using standard stars routinely observed by the Queue Service Observing team at CFHT to the photometric zero-point of 30 mag. The seeing during these observations ranged from  $0.65''$  to  $0.80''$ . The WIRCam images were extended using blank pixels so that the dimensions of these science-ready images were the same dimensions as the  $z'$  MegaCam image, where the dithered  $CH_{4off}$  image is shown along with the WIRCam and MegaCam detector arrays, shown in Figure 2.6. The TERAPIX pipeline additionally produced a catalogue of objects with aperture photometry for each filter.

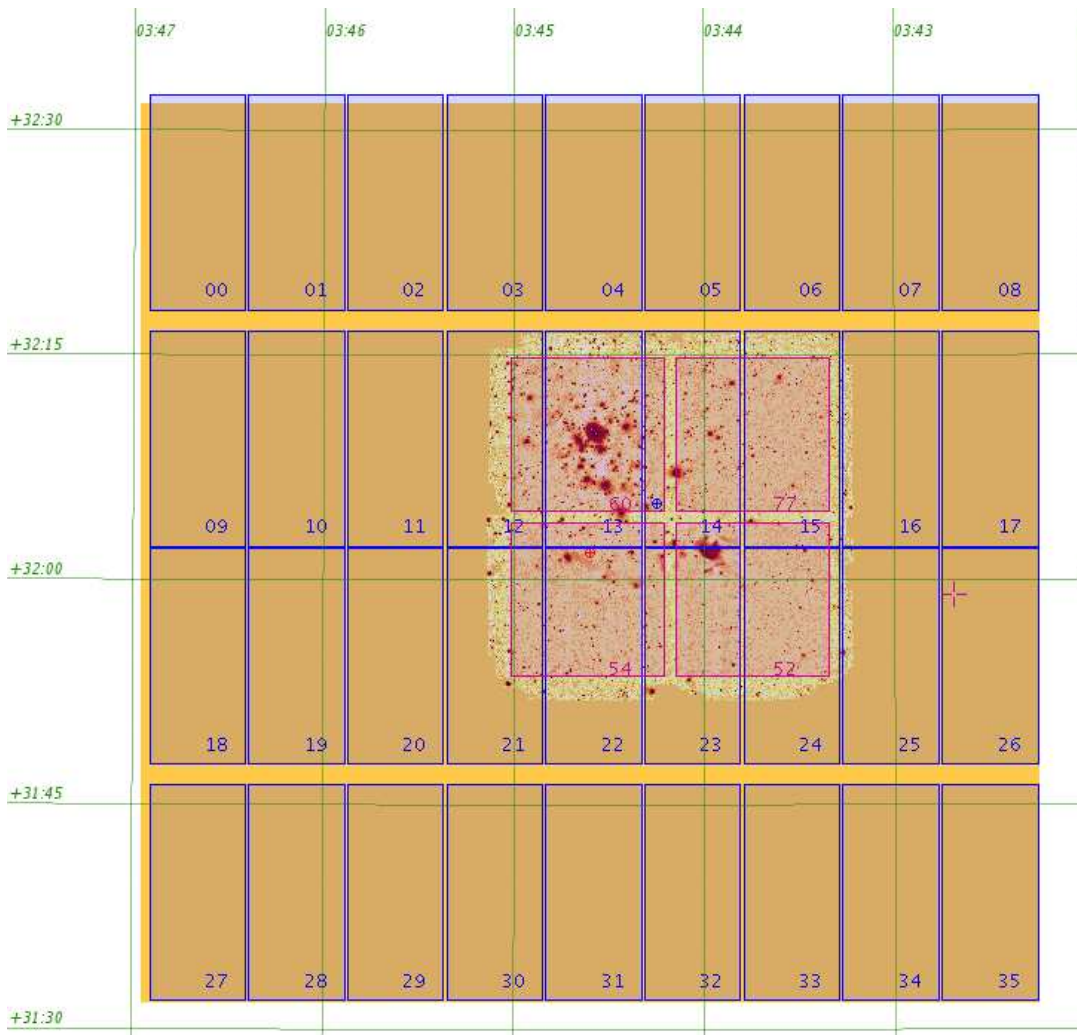


Figure 2.6: The  $CH_{4off}$  image with the extended blank pixels to the FOV of MegaCam is shown. The footprint of the WIRCAM detector is overlaid on the stellar field, whilst the footprint of MegaCam is overlaid over the whole image. The dithering effect can also be seen as the image boundaries are larger than the FOV of the WIRCAM detector footprint.

## 2.2 Infrared Surveys & Astronomical Databases

Various additional survey databases were queried in this work to add to our robust CFHT data, primarily the 2Micron All Sky Survey (2MASS) and the UKIRT Infrared Deep Sky Survey (UKIDSS). Further analysis was conducted using data from the *Spitzer Space Telescope*. Data from 2MASS and *Spitzer* can be found at NASA/IPAC Infrared Science Archives<sup>16</sup> (IRSA) whilst UKIDSS data can be accessed from the Royal Observatory of Edinburgh at the Wide-Field Camera (WFCAM) Science Archive<sup>17</sup>. All of the catalogues are fully searchable using both a selectable form or a SQL querier.

### 2.2.1 2Micron All Sky Survey (2MASS)

2MASS (Skrutskie et al., 2006) at IRSA<sup>18</sup> was an IR survey finished in 2001 which scanned the full sky using two telescopes in different hemispheres; in the north the Mt. Hopkins in Arizona, USA and in the south at Cerro Tololo Inter-American Observatory<sup>19</sup> (CTIO) in Chile. Its primary mission was to survey the whole sky at three, standard, IR wavelengths,  $J$  (1.25  $\mu\text{m}$ ),  $H$  (1.65  $\mu\text{m}$ ) and  $K_s$  (2.17  $\mu\text{m}$ ). Because of the whole sky survey, 2MASS has been used as a basis survey for IR data calibration for other missions and observations.

The 2MASS All-Sky Point Source Catalog (PSC) was accessed using the Gator catalogue querying engine at IRSA, accompanied by an input list of pointings. It is useful to parse the input catalogue using the input file tester<sup>20</sup> before trying to use Gator due to some peculiar formatting requirements<sup>21</sup>.

### 2.2.2 UKIRT Infrared Deep Sky Survey (UKIDSS)

The United Kingdom Infrared Telescope (UKIRT) Infrared Deep Sky Survey (UKIDSS) (Lawrence et al., 2007) comprises various deep sky surveys, for example the Galactic Plane Survey and the Galactic Clusters Survey, where UKIRT has a detector FOV of 0.21 deg<sup>2</sup>. The UKIDSS photometric system spans the  $z$ ,  $Y$ ,  $J$ ,  $H$  and  $K_s$  range covering a wavelength range of 0.83-2.37  $\mu\text{m}$  and is discussed by Hewett et al. (2006). The authors also discuss the colour differences between UKIDSS, and the SDSS and 2MASS for various objects, including brown dwarfs, and give associated colour terms.

---

<sup>16</sup><http://irsa.ipac.caltech.edu/>

<sup>17</sup><http://surveys.roe.ac.uk/wsa/>

<sup>18</sup><http://www.ipac.caltech.edu/2mass/>

<sup>19</sup><http://www.ctio.noao.edu/>

<sup>20</sup><http://irsa.ipac.caltech.edu/applications/TblCheck/>

<sup>21</sup>[http://irsa.ipac.caltech.edu/docs/table\\_upload\\_help.html](http://irsa.ipac.caltech.edu/docs/table_upload_help.html)

A login is required for the proprietary UKIDSS data and can be requested via an email the authorised community contact at one's home institution, a list<sup>22</sup> is available to find out who this is. This work uses the current DR6 data as the current UKIDSS data is currently at the DR7 release whilst the public data is at the DR4 release.

The WIRCam Y extinction value shown in Table 2.1, in Section 2.1.1, was taken from the UKIRT Infrared Deep Sky Survey (UKIDSS) section from the SVO and then adjusted by 0.01 in line with the small 0.01 differences in the  $J$ ,  $H$ , and  $K_s$  bands between the UKIDSS and CFHT extinction values. The basis for allowing this is because the IC 4665 long and short exposure data have been directly zero-point calibrated to the UKIDSS system and both CFHT and UKIDSS photometric systems are based on 2MASS as discussed in depth by Hodgkin et al. (2009), excepting the two control fields. The  $Y$ -band can be seen to have a calibration offset of approximately 0.1 mag from their Figure 16, shown in Figure 2.7, where this offset has been recalibrated in later data releases than DR2. Calibration is discussed further in Section 3.3.

### 2.2.3 Spitzer Space Telescope

The *Spitzer Space Telescope*<sup>23</sup> was launched in 2003 with two IR and mid-IR detectors which were the InfraRed Array Camera (IRAC) at 3.6, 4.5, 5.8 and 8.0  $\mu\text{m}$ , and the Multiband Imaging Photometer (MIPS) at 24, 70 and 160  $\mu\text{m}$ . There was also the Infrared Spectrograph (IRS) which offered low- to mid-resolution spectroscopy between 5.2 to 38  $\mu\text{m}$  though this was not used or had data accessed in this work. *Spitzer* continues to give solid 3.6 and 5.4  $\mu\text{m}$  data, even after the detector's cryostat's coolant was exhausted, leaving the 5.8  $\mu\text{m}$  band and redder too hot, and so too noisy, for any useful science.

Data pertaining to IC 348 was found by searching the *Spitzer* public archive for IRAC data. There was no public MIPS data available for this region at the time of writing the article. IC 348 was the IRAC prime target of programmes 6 (c2d, P.I. Fazio) and 36 (P.I. Fazio) to obtain deeper exposures, where relevant to this work was provided by H. Bouy<sup>24</sup>. The c2d data are made up of shorter exposures, resulting in the use of deep (16 $\times$ 100s) longer-exposure images of programme 36. The data was retrieved and was processed using standard procedures<sup>25</sup> with the recommended MOPEX software.

---

<sup>22</sup><http://www.ukidss.org/archive/comm-list-v2.txt>

<sup>23</sup><http://www.spitzer.caltech.edu/mission/32-Mission-Overview>

<sup>24</sup><http://www.iac.es/galeria/bouy>

<sup>25</sup><http://ssc.spitzer.caltech.edu/archanaly/quick.phot>

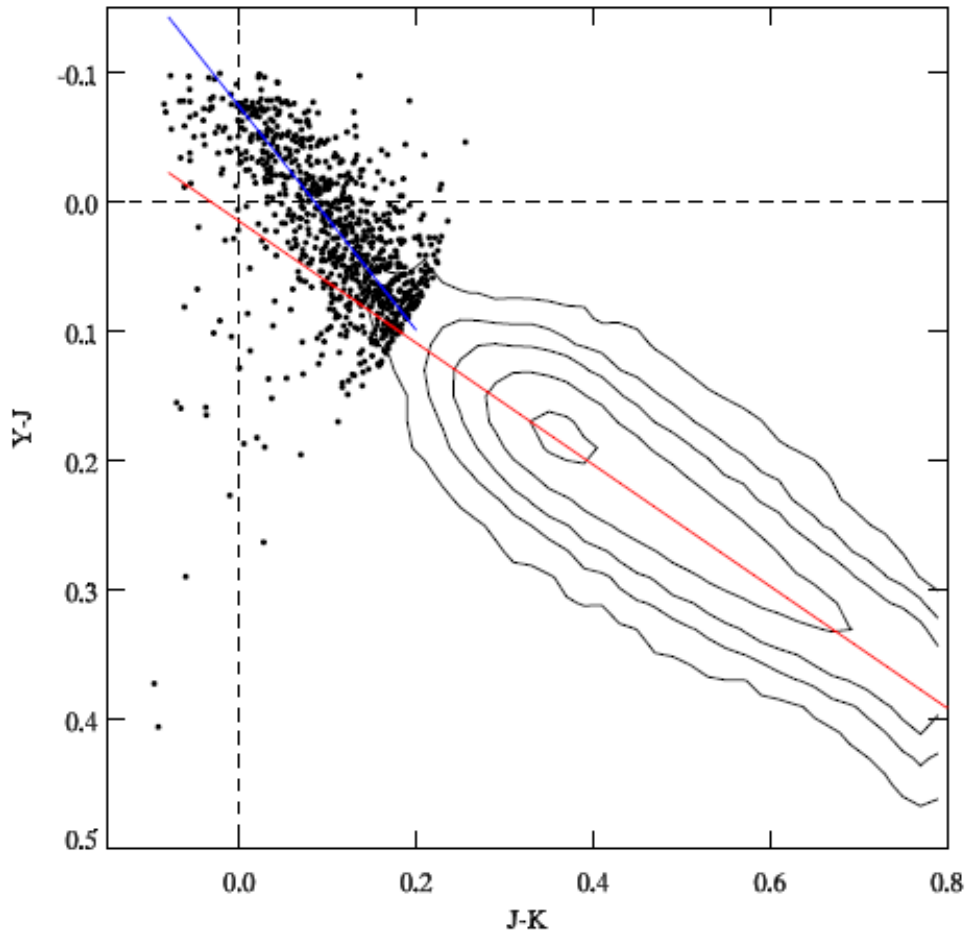


Figure 2.7: Data taken from the DR2 UKIDSS release showing the offset of the  $Y$ -band compared to the field stars. This is corrected for in later data releases and so is not treated in our data.

#### 2.2.4 Online Repositories

A number of online repositories, or stores of data, were used for this work. Great use was made of the ADS Abstract Service<sup>26</sup> in order to search for published and refereed journals, whilst *astro-ph*<sup>27</sup> was also used in order to be kept up to date for very recent developments in this field. Additional relevant repositories are the Star Cluster Young and Old Newsletter<sup>28</sup> (SCYON) which is updated by H. Baumgardt, E. Paunzen and P. Kroupa, and the Star Formation newsletter<sup>29</sup>, updated by B. Reipurth, and which both encourage authors to spread their newest article or conference proceedings via specific genre electronic newsletters.

The SIMBAD Astronomical Database<sup>30</sup> (SIMBAD) and associated VizieR database<sup>31</sup> are

<sup>26</sup>[http://adsabs.harvard.edu/abstract\\_service.html](http://adsabs.harvard.edu/abstract_service.html)

<sup>27</sup><http://arxiv.org/archive/astro-ph>

<sup>28</sup><http://astro.u-strasbg.fr/scyon>

<sup>29</sup><http://www.ifa.hawaii.edu/users/reipurth/newsletter.htm>

<sup>30</sup><http://simbad.u-strasbg.fr/simbad/>

<sup>31</sup><http://vizier.u-strasbg.fr/viz-bin/VizieR>

grand repositories of extrasolar data and bibliography with over 14 million identifiers, and is cross-correlates with the article service available at the ADS. The sites allow catalogue and online data retrieval based at the Centre de Données astronomiques de Strasbourg<sup>32</sup> (CDS).

Further databases which have been accessed in the course of this work include the Spanish Virtual Observatory<sup>33</sup> (SVO) which have a fairly comprehensive list of telescopes, their filters, effective bandpasses and wavelengths, widths and extinction co-efficients. The data originates from being convolved with the filters with each instrument and their empirical band passes. The Dwarf Archives<sup>34</sup> is an up-to-date collection of all known L and T-dwarfs, and M-dwarfs which have both photometry and spectroscopy.

The Star, Brown Dwarf and Planet Simulator<sup>35</sup>, mentioned in Chapter 1 for the AMES and BT theoretical models, also holds theoretical models based upon the Lyon groups work on the emission and absorption as a result of the presence of empirical and theoretical elemental and molecular lines in stellar and brown dwarf atmospheres.

## 2.3 Pipeline Development

After the observations were taken by WIRCam and MegaCam and pre-processed at the CFHT, and after being run through the TERAPIX pipeline they were then ready for the object extraction procedure and further analysis. The data taken of IC 348 and IC 4665 can be treated similarly *up to a point*. This section discusses a pipeline for image analysis, shown in Figure 2.8 where the data for IC 348 and for IC 4665 are shown to be treated similarly on an image-by-filter basis. Human intervention for this pipeline is limited to the creation of input variable tables, dependent on the particular fits headers and images, and for checking and constraining CMDs for survey comparison and calibration purposes. As the work has been done it is possible to run the script, using the predefined variables in order to output new catalogues. In essence it is possible to run the script, after updating the filenames, and with the exception of the calibration steps, which require SuperMongo, can be run from analysis-ready images to final calibrated catalogues and selected objects. It should be possible, with perhaps a little time, to analyse multiple data sets for multiple observing runs and regions. Of course this depends on the observations themselves, and what is required to be plotted. The main criteria is populating the parameter input files correctly and changing the path names of the files.

A combination of custom-made programs<sup>36</sup> called Source Extractor (SExtractor) (Bertin and Arnouts, 1996) and Point Source Function Extractor (PSFEx) (Bertin et al., in prep.) were used

---

<sup>32</sup><http://cdsweb.u-strasbg.fr/>

<sup>33</sup><http://svo.laeff.inta.es/theory/filters/index.php>

<sup>34</sup><http://spider.ipac.caltech.edu/staff/davy/ARCHIVE/index.shtml>

<sup>35</sup><http://phoenix.ens-lyon.fr/simulator/>

<sup>36</sup><http://astromatic.net/>

on each field for each band to extract sources and build photometric catalogues. On a first step, SExtractor extracts well defined stellar-like objects, which are used by PSFEx to compute a PSF model that is allowed to vary with position on the image. Then, the detection was done using one filter which was used to measure the photometry from all of the available filter images. SExtractor uses this PSF model to measure the photometry more accurately of all the sources detected on the image, producing a catalogue with a list of identically positioned objects for each filter. It is important to make sure that the available data is reliable, which requires optimisation and calibration checks. Parameter optimisation is conducted separately from this pipeline, discussed in 2.3.2. Finally, these catalogues are combined to construct a list of unique objects with associated filters and PSF information. The IC 348 data is ready for analysis at this point, whilst IC 4665 requires calibration. This calibration is necessary as the IC 4665 data has separate and multiple fields (images) for each filter so the fields need to be externally calibrated onto UKIDSS, before being internally calibrated to be consistent from field to field to account for the different seeing conditions. This pipeline relies heavily upon bash scripts and awk, and also uses SuperMongo<sup>37</sup> scripts for numerical analysis and plotting.

### 2.3.1 SExtractor First-Pass

Source Extractor (SExtractor) is used as the main method of allocating various parameters and magnitudes to objects obtained from the observations. The SExtractor manual<sup>38</sup> v.2.5 describes in detail of how the program works, whilst the SExtractor For Dummies manual<sup>39</sup> is a useful how-to guide. The versions used were 2.3.5 for IC 348 and version 3.1.0 for the extraction for IC 4665. SExtractor requires two configuration files to control the input and output data; the first is the data extraction parameter file with a `.sex` suffix; the second is the data presentation parameter file with a `.param` suffix. The parameters used are listed in the Appendix in Table 1, which are identical for both the first- and second-passes for IC 4665 and IC 348. Other files are also needed as inputs, for example a neural network file to differentiate between stars and galaxies, `.nnw`, and a filter file `.conv`, an example of which can be found in Figure 2.10 (*upper left*). The other required file is the data from the `.fits` file, though other file types are also supported. Additionally, it is possible to add the weight and the flag maps as further input files, which correspond to each observation image as discussed previously in Section 2.1.2.2.

Other useful functionalities of SExtractor are the check image outputs, `'CHECKIMAGE_TYPE'`, which can be one of various types of analysed data; `'BACKGROUND'`, `'OBJECTS'` and `'PROTOS'`, among others. The check image `'BACKGROUND'` is an image with the estimated background fluxes that have been subtracted from the apertures, whilst the `'OBJECTS'` are the

<sup>37</sup><http://www.astro.princeton.edu/~rhl/sm/> & <http://www.supermongo.net/>

<sup>38</sup><https://www.astromatic.net/pubsvn/software/sextractor/trunk/doc/sextractor.pdf>

<sup>39</sup><http://mensa.ast.uct.ac.za/~holwerda/SE/Manual.html>



extracted objects which now have a catalogue reference and data, and the ‘PROTOS’ is the residuals from the extraction from the original image. Each of these can have a name specified using the ‘CHECKIMAGE\_NAME’ parameter.

Data is also required which is unique to each fits image and can be taken from the fits header, which is a file information table associated with each .fits file. The ‘SATUR\_LEVEL’ is the saturation level is used by SExtractor to apply its own saturation flags, active for objects exceeding this threshold. Other fits-header given values are the ‘MAG\_ZEROPOINT’, here 30 mag, ‘GAIN’, and ‘PIXEL\_SCALE’ which are all related to the detector and pre-processing pipeline, extracted automatically using the ‘dfits’ and ‘fitsort’ commands. Other data can be taken from the image which is also needed for the photometric analysis; the ‘SEEING\_FWHM’ is the stellar FWHM in arcseconds is used to help differentiate an object between a galactic and a stellar PSF and is calculated using the pixel scale and the FWHM in pixels. The FWHM in pixels is found using the *iraf imexam* function taken on a randomly selected sample of faint and bright stars in the image and can be checked using the command line output when PSFEx runs.

**Usage** The basic command line syntax used for SExtractor is as follows:

```
sex <input_image_filename(image.fits)> -c <configuration file(firstpass.sex)> -FLAG_IMAGE <(flag.fits)> -WEIGHT_IMAGE <(weight.fits)>
```

and whilst it is possible to create multiple configuration.sex files to correspond to each input file, it is also possible to include command line arguments to change the parameters that are in the configuration.sex file by using the above ‘-KEYWORD <variable>’ syntax. It is also possible to automate this process by running a bash script with all of the variations that need to be tested. This is useful for optimisation of the input options that the configuration.sex file includes, see Section 2.3.2.

### 2.3.2 SExtractor Optimisation

All of these configuration options need to be assessed and optimised for the data sets that are being used. The methodology for obtaining these optimal parameters is discussed and the particular values for IC 4665 and IC 348 are summarised here, but cluster-specific optimisation is discussed further in Chapters 3 and 4 respectively. A list of configuration options discussed here that have been tweaked in relation to our extraction can be found in Table 2.5 for both the first pass and second pass of SExtractor. Optimisation is mainly necessary for the analysis and detection thresholds, object detection filters, and for the background estimation; all needed to obtain accurate photometry from the data.

**Detection** The detection optimisation requires a few parameters to be tested under the ‘Extraction’ heading in the parameters file. Many parameters can be changed permanently in

Table 2.5: The configuration options in the SExtractor configuration that were changed from the default. An example file for each SExtractor pass for each cluster can be found in the Appendix 5.5. Here the example given is for extraction data from the *H*-band image where the gain and saturation values are used for the photometry and not for the detection. It can be noted that the detection images are different to the analysis images for the second-passes of SExtractor, and the detection and analysis for the long IC 4665 exposures was run ‘hot/cold’, at two different thresholds.

config option	IC 4665 first-pass	IC 4665 second-pass	IC 348 first-pass	IC 348 second-pass
detection image	IC4665A_H.fits	IC4665A_J.fits	IC348_H.fits	IC348_CH4Off.fits
analysis image	IC4665A_H.fits	IC4665A_H.fits	IC348_H.fits	IC348_H.fits
PARAMETERS_NAME	sex1.param	sex2.param	sex1.param	sex2.param
CATALOG_NAME	LDAC_IC4665A_H.fits	IC4665A_H.cat	LDAC_IC348_H.fits	IC348_H.fits
MIN_AREA	3	3 & 3	5	3
DETECT_THRESH	15.0	(short) 1.5 (long) 1.0 & 5.0	8.0	3.5
ANALYSIS_THRESH	15.0	(short) 1.5 (long) 1.0 & 5.0	8.0	1.0
PHOT_APERTURES	31	31	51	50
GAIN	1.777276524E+01	1.777276524E+01	18.0508	18.0508
SATUR_LEVEL	5.795242200E+05	5.795242200E+05	500000	500000
FILTER_NAME	gauss_2.5_5x5.conv	gauss_2.5_5x5.conv	gauss_3.0_5x5.conv	gauss_3.0_5x5.conv
SEEING_FWHM	1.22	1.22	1.10	1.10
BACK_SIZE	64	64	128	128
BACK_FILTERSIZE	3	3	3	3

the configuration file without needing to be specified in the command line, for example the ‘DETECT.TYPE’ is from a ‘CCD’ and not from a photograph, ‘PHOTO’, and so does not need to be mentioned in the command line as long as it has been correctly changed in the configuration file. The ‘DETECT.THRESH’ and ‘ANALYSIS.THRESH’ control the confidence level that an object on the image must have to be eligible for extraction. The ultimate value is whichever one is the highest; if the detection threshold is higher than the analysis threshold then all objects detected will be analysed; if the analysis threshold is highest only those objects above this level will be analysed. An additional problem with the detection is the missing of objects around bright and saturated stars, shown in Figure 2.9. This is a dual-fold problem; a  $1.0\sigma$  detection level detects all the objects in the field but not around bright stars (*green squares*), whilst a  $5.0\sigma$  detection threshold would detect the objects around bright stars (*squares*) but then, obviously, miss all of the lower threshold objects in the field. This is a direct consequence of the isophotal algorithm SExtractor employs, where a higher threshold reduces the isophotal footprint and so alters the distance at which an object from the central pixel of this bright star could be treated as a different object. This is usually used in conjunction with the ‘DEBLEND\_NTHRESH’ algorithm. This details how the program distinguishes between objects that are in each others’ PSF footprint, where the value is the number of branches that are allowed within any one PSF, though in our case seems to fail

around bright stars. The solution, then, is to detect objects at both of these thresholds and then amalgamate the catalogues later, simplified when using a singular detection image for analysis. An additional problem is that the centres of the saturated stars have been removed, so whilst these objects have been flagged, SExtractor still detects objects around the locus.

A filter can be chosen, replacing the default filter, which defines as to what shape the PSF of an object should have to be classed as a detectable object. There are various filters and each has a different shape, pixel footprint and seeing values; thusly 'gauss\_2.5\_5x5.conv', for example, is a gaussian PSF with a 5x5 convolved mask (grid) and a seeing FWHM value of 2.5 pixels  $''^{-1}$ . This convolved mask is the number of data points to a side that define the filter. Other filters were tested which were either of a different shape or had different FWHMs and footprint sizes, where Figure 2.10 shows two types of filter, the gaussian and the mexhat on the *upper* and *lower* panels respectively. The gaussian shape was the best overall detection filter in both datasets, Figure 2.10 (*left lower panel*), based not only on the number of detections, but also on the quality of detections, indeed, there is no point detecting every pixel in the image as an object, which the mexhat almost seems to do as shown in Figure 2.10 (*left lower panel*). That the gaussian is the best filter form is no coincidence as the response of the CCD is gaussian for a point source.

**Analysis** The analysis optimisation needs to be carefully adjusted in order to extract the correct photometry from the objects. The 'PHOT\_APERTURES' is the size of the aperture in pixels and needs to be adjusted in order to take into account all of the flux with the circle. Here it was tested with values as low as 5 and as high as 45 against the default 'MAG\_AUTO' value. A plot showing the convergence of the colour magnitude diagram of the aperture magnitude - mag\_auto vs mag\_auto (used as a constant here) is shown in Figure 2.11. In this example for IC 4665 it can be seen that the colour converges to a difference of -0.03 with a 'PHOT\_APERTURES' value of 31 and whilst higher aperture values also give the same difference the dispersion increases dramatically. Physically, this means that as the aperture is enlarged it finds more stars within its enclosure and so cannot as accurately assign a magnitude value correctly to all of the objects, either because of the deblending but mainly because of the background estimation.

Further analysis optimisation parameters are the 'BACK\_SIZE' and 'BACK\_FILTERSIZE', which define the background estimated value that is subtracted from within the aperture around a detected object. 'BACK\_SIZE' is of dimension 64, 128, 256 or 512, indicative of the size of the side of a square in pixels in which to coallate flux in order to calculate the average background. 'BACK\_FILTERSIZE' is the size of a side of square, in units of 'BACK\_SIZE' over which the background level is smoothed, taking odd-numbered values of 3, 5, 7 etc. Underestimation means that too little background flux is removed locally, Figure 2.12 (*upper centre* for a 64x64 grid). If SExtractor overestimates the background level then there will be more flux overall subtracted eventually underestimating the flux for objects in that region, Figure 2.12 *lower right*, where a

larger 'BACK\_SIZE' could do this (for a 256x256 grid). The image on the *lower right* is the 128x128 grid which is between the two. If there are high levels of background flux, for example in nebulous or very crowded regions then it is hard to accurately estimate the background flux over the whole image. This concludes that the best aperture value to use for the IC 4665 data is 31, whilst a similar analysis gives a value of 51 for the mosaicked image for IC 348. Further, the background parameter values for IC 4665 were 64 and 3 though there was not a great difference with the 256 and 5 values were used as the fields are comparatively uncrowded. The values for IC 348 were 128 and 3 and although they helped smooth the variable and nebulous background, the smoothing should not be too aggressive as the nebulosities vary on scales of less than a few tens of pixels. The 'PSF\_PROTOS' residuals check image is very useful for both the aperture and background optimisation as it can be seen how SExtractor has extracted the flux from the aperture.

Further optimisation is the propagation of these aperture values through the next two steps in the catalogue extraction process, PSFEx and the SExtractor second-pass. Image attributes are unchangeable leaving most parameters used for the SExtractor first-pass unchanged, apart from the detection and analysis thresholds. For the IC 4665 first-pass a detection and analysis value of  $15 \sigma$  was used in order to obtain good quality PSFs, for the input into PSFEx, whilst for the second-pass a value of 1.5 was used for the short exposures, whilst the long exposures used the hot/cold method at both 1.0 and  $5.0 \sigma$ . This double catalogue can then be amalgamated for unique objects, where the details are discussed in Section 3.3.1. For IC 348 the first-pass value was  $8 \sigma$  and the second-pass detection value was at  $3.5 \sigma$ , enough to avoid detecting large amounts of nebulous material, discussed further in Chapter 4.

Lastly, the output catalogue should be in the LDAC format where this option is specified in the SExtractor first-pass configuration file and is required as an input for PSFEx. This configuration option for the 'CATALOG\_TYPE' is 'FITS\_LDAC', ready for the modeling of the PSF across the image, handled by PSFEx.

### 2.3.3 Point Source Function Extractor (PSFEx)

Point Source Function Extractor<sup>40</sup> is a program whose primary purpose is to model the small variations of the PSF across an image using a set of good-quality PSFs taken from that image as an input. This input is the LDAC.fits output from the first-pass of SExtractor where the detection threshold has been set high in order to find good quality PSFs. The PSF can vary across the image due to atmosphere or instrument distortion, but it can also be an artifact of image mosaicking where overlapping images are stitched together to make a larger, seamless image. In this case

---

<sup>40</sup><http://www.astromatic.net/wsvn/public/>

it is usual to have a dithering pattern which tries to increase the reliability of the data near the edges of the individual detector chips, for example the edges of the external border of the array or the edges adjacent to gaps between the CCDs. The problem associated with this method is that the PSF can vary across the image, depending on the number of dithers used to make up the final image and the accuracy of the flat fielding process. The output PSF model is then used as one of the inputs for the second-pass SExtractor which then offers first-order corrections to the final object magnitudes. The PSF input is optimised, as discussed in Section 2.3.2 for stars rather than galaxies. There is currently no manual for this software as it is still in development

Table 2.6: Configuraton options that were changed for this PSFEx analysis. The unchanged parameters for the PSEFex configuration files can be found in the Appendix 5.5. Options marked with an asterisk appear in the newer version only.

Parameter Name	IC 4665 value	IC 348 value
PSF_SIZE	35,35	51,51
SAMPLEVAR_TYPE*	-	SEEING
SAMPLE_FWHMRANGE	1.5,4.5	1.5,4.5
SAMPLE_MINSN	100	100
PSFVAR_KEYS	X_IMAGE,Y_IMAGE	X_IMAGE,Y_IMAGE
PSFVAR_DEGREES	2	6

although the location of where the manual should be is discussed in the program<sup>41</sup>, for future reference. The configuration file is located in the Appendix 5.5 though the more salient points are discussed here. Analysis for IC 348 was conducted with version 2.3.5 of PSFEx whilst the work for IC 4665 was done using version 3.1.0. There main additions present in version 3.1.0 are the check plot capability of outputting PSF ellipticity and FWHM maps, shown in Figure 2.13 for the *J*-band of IC 4665 field A; and changes of instead specifying an output PSF filepath and filename to specifying just the suffix; ‘PSF\_NSUPER’ has been removed whilst ‘BASIS\_TYPE’ and ‘BASIS\_NUMBER’ have been added, shown in Table 2.6. ‘PSF\_NSUPER’ is the number of super-resolved pixels and has a value of ‘0’; whilst the ‘BASIS\_TYPE’ defines the system the input .fits file uses (here ‘PIXEL\_AUTO’) and ‘BASIS\_NUMBER’ is the PSF basis vector coefficients for non-pixel bases, default of 16 in this version and is used for the output PSF file. The ‘snap’ check image is the PSFs that PSFEx eventually uses to model the PSF across the frame of the image.

‘PSFVAR\_DEGREES’, or ‘GROUP\_DEGREES’ depending on the version, is the order of freedom parameter that applies to the PSF over stacked or mosaicked images. This is a 6-degree polynomial

<sup>41</sup><http://terapix.iap.fr/soft/psfex>

over the final image for IC 348, whilst IC 4665 has no such mosaicking. For IC 348, this was used in conjunction with independent *iraf* aperture photometry on the selected candidates, where a final magnitude was taken as an average of these two values.

There needs to be a range of FWHMs for PSFEx to work with, defined with the ‘SAMPLE\_FWHMRANGE’ parameter, here between 1.5 and 4.5 pixels FWHM. This output file is a ‘.psf’ file which holds the model information and is selected as an input in the SExtractor second-pass configuration file with the option ‘PSF\_NAME’.

The command line usage is of the same format as SExtractor, and was again created through shell scripts and awk. For IC4665:

```
psfex <input PSFs(LDAC.fits)> -c <configuration file (psfex.psfex)> -SAMPLE_MINSN 100 -CHECKIMAGE_TYPE
SNAPSHOTS -CHECKIMAGE_NAME <snap.chk.fits>
```

### 2.3.4 PSFEx Optimisation

The total number of pixels in the mask of the PSF is an input to PSFEx and as this result is unchanged the value gained from the first-pass SExtractor optimisation can be used here, 31 for IC 4665 and 51 for IC348. The PSFex configuration option ‘PSF\_SIZE’ needs a similar aperture size as the ‘PHOT\_APERTURES’ in the SExtractor first-pass configuration file, and the value should always be an odd number as then number of pixels for the ‘Vignet(xx,xx)’ parameter in the .param file. These can be found previously in Table 2.5.

### 2.3.5 SExtractor Second-Pass

This section deals with the production of the output catalogues, per filter, from the second-pass of SExtractor. The major difference between the first- and second-passes of SExtractor are the input files, the detection/analysis thresholds, and the .param control file. All other parameters are the same as for the first-pass set as shown previously in Table 2.5, whilst the second-pass set can be seen and compared.

A further detection optimisation option involves using one image for the detection algorithm and another image for the analysis using the objects detected in the first instance. The particular images used for detection are the IC 4665 *J*-band image for the long and the short exposures due to the better photometric quality against depth of the image compared to the other images, and for IC 348 the CH<sub>4</sub>off image was used in order to certainly obtain a corresponding CH<sub>4</sub>on magnitude for each CH<sub>4</sub>off object. The reasons for using these particular images for detection are discussed in depth in the accompanying Sections 3.2.2 and 4.2, for IC 4665 and IC 348 respectively. Here, the IC 348 second-pass is run at  $3.5 \sigma$ , whilst the IC 4665 short exposure images are run at  $2.5 \sigma$ , with the long exposure hot/cold analysed at 1.0 and  $5.0 \sigma$ . The ‘medium’  $K_s$  band images for IC 4665 are used for both the long and short extraction, in essence, being extracted twice. This

was to ensure that each detected object had a  $K_s$  counterpart, but is also a useful check for the robustness of our tests as the magnitude differences between the short and the long  $K_s$  exposures should be  $\sim 0$ .

The second-pass configuration file is similar to the first-pass file (Table 5.5 in the Appendix) whilst the .param file is fuller and outputs more data such as the object location in (x,y) image coordinates, sexigesimal coordinates, and the associated aperture and PSF fluxes, magnitudes and errors, shown in Table 5.5 in the Appendix. Furthermore the output catalogue can now simply be an ascii file, selected using the option 'CATALOG\_TYPE' is 'ASCII\_HEAD' which includes the headers taken from the parameters in the .param file. It is possible to have just an ascii file with no header, 'ASCII', or a fits file, 'FITS\_1.0' that can be read by any fits text file-compatible program.

### 2.3.6 Catalogue Amalgamation

Catalogue matching between different SExtractor output files made heavy use of the TOPCAT<sup>42</sup> program and the associated STILTS<sup>43</sup> scripting environment. The amalgamation of single-band catalogues into one multi-band catalogue based on coordinates was used for both sets of data. This task was simplified due to the choice of a single image for the detection of objects. Essentially, each catalogue, for example the  $z'$  for IC 348 and the  $Y$  catalogue for both the short and long IC 4665 data were used as starting points. Then, each catalogue was matched with one of the other bands in the respective data set, and so on and so forth until there is a single catalogue which comprises all the filters observed for each object. For IC 348 the final, analysis-ready catalogue has a total of 22 columns per band so 132 columns for the  $z'$ ,  $J$ ,  $H$ ,  $K_s$ , CH<sub>4</sub>off and CH<sub>4</sub>on filters, whilst for IC 4665 the filter-amalgamated catalogue had just 92 columns, when an extra column per field was introduced, discussed in Section 3.2.3, to assist with the identification of saturated objects from the colour/magnitude diagrams, taking the form of a '0' or '1'.

At this stage, the IC 348 data can now be analysed and is discussed further in Chapter 4, whilst the IC 4665 data requires more treatment to increase its accuracy and reliability.

### 2.3.7 Calibration

**IC 348** did not require any calibration as it was internally consistent. This data was, however, compared with 2MASS in order to define the offsets between the CFHT and 2MASS, although no offsets were applied as the data stayed in the CFHT photometric system. Offsets were of order 0.05 magnitudes which is within errors for our purposes of finding methane colours greater than 0.4 magnitudes. This 2MASS check is discussed further in Section 4.2.2.

---

<sup>42</sup><http://www.star.bris.ac.uk/~mbt/topcat/>

<sup>43</sup><http://www.star.bris.ac.uk/~mbt/stilts/>

**IC 4665** also needed to be checked against 2MASS for the same reasons and whilst this is discussed in great detail in Section 3.3 it eventually had two sets of offsets applied. The first was to zero-point calibrate to UKIDSS, not 2MASS, as the 2MASS calibration technique needed a statistically significant number of stars which overlap with 2MASS and the long exposures had poor quality, mostly saturated, objects. An extra error was introduced, therefore, to this process as the long exposures would have to have been calibrated onto the short exposures which had been calibrated onto 2MASS. Additionally there is also a lack of  $Y$ -band data with which to calibrate the  $Y$  exposures onto 2MASS. UKIDSS was checked to be a useful calibrator by examining the number of A0 stars from our FOV over all the  $J$ ,  $H$  and  $K_s$  fields, and so then seeing whether these stars still had  $Y - J$ ,  $Y - H$  and  $Y - K_s$  colours  $\sim 0$ . A second calibration was conducted to compare and neutralise the differences between the 12 different fields, as each were taken under different photometric conditions. This was done using the overlaps between the fields, which constitute a band at least  $\sim 30''$  wide and  $\sim 20'$  long for each field, shown previously in Figure 2.5. Eventually only field J had to be re-calibrated, likely due to its position outside the rectangular region, and also the poor quality of the CCD in the bottom right hand corners meant that field D was not an appropriate calibration zero point, leaving a small overlap  $10'$  long in order to check the  $J$  field. Furthermore, the control fields lacked matching UKIDSS data, so it was best to calibrate these using 2MASS, but to also apply the calculated 2MASS-UKIDSS offset, indirectly calibrating them onto UKIDSS. The  $Y$ -band was calibrated using the median value from the 10 cluster fields and applying this offset to the  $Y$ -band data of control fields.



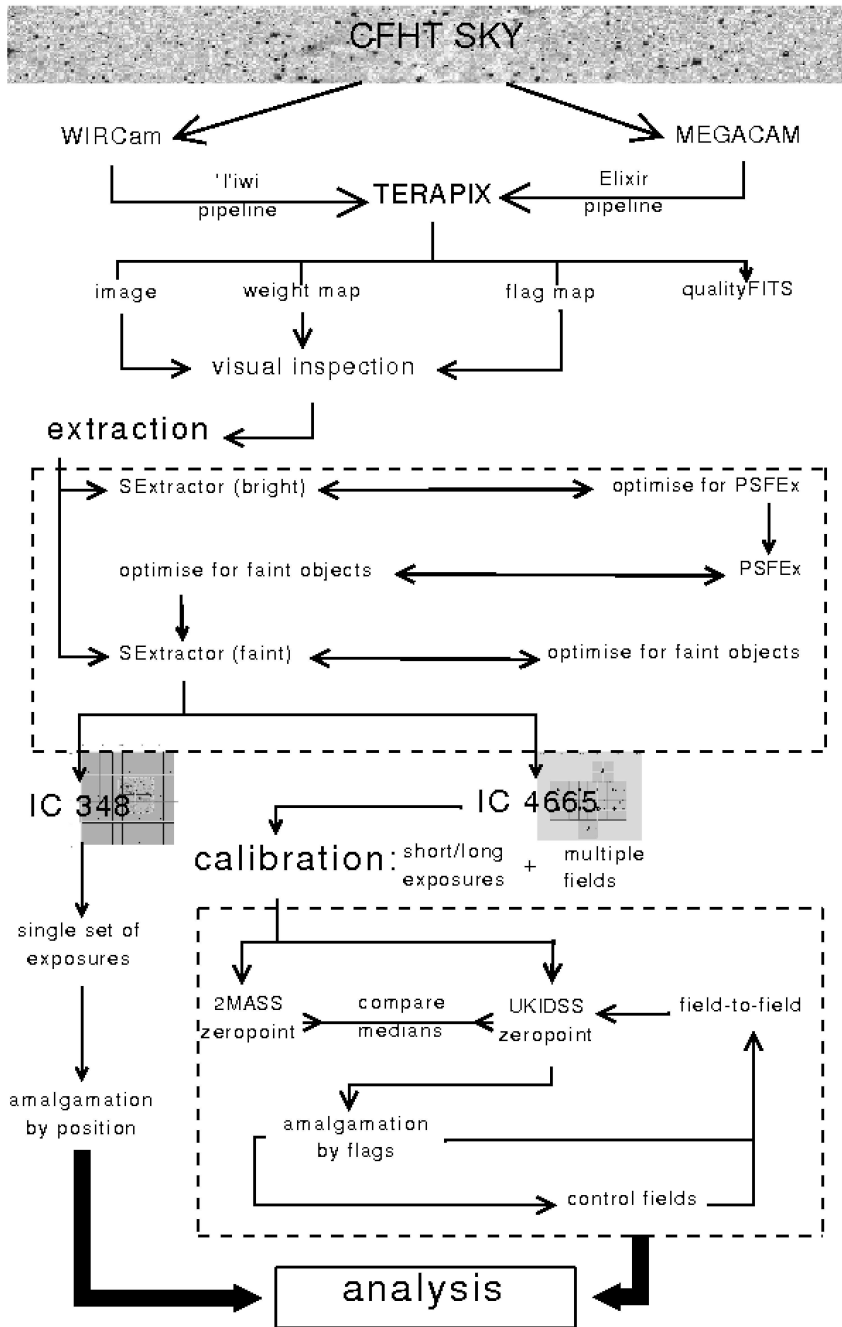


**Figure 2.8:** A Flowchart of the pipeline used to process the images taken of the observed regions into data that can then be analysed. The main procedure which was applied to all the data, including IC 348 and IC 4665 include SExtractor to extract well-defined objects (at 8 or 15  $\sigma$ ) in order to create a good sample for PSFEx to model the variations of the PSF across each image. These variations are then taken into account for the final SExtractor parse before outputting a catalogue for each band. IC 4665 has an extra process in the pipeline to calibrate the long and the short exposures directly onto UKIDSS, to calibrate for different seeing conditions across the different fields, and finally to calibrate the control fields as they have no associated UKIDSS data.

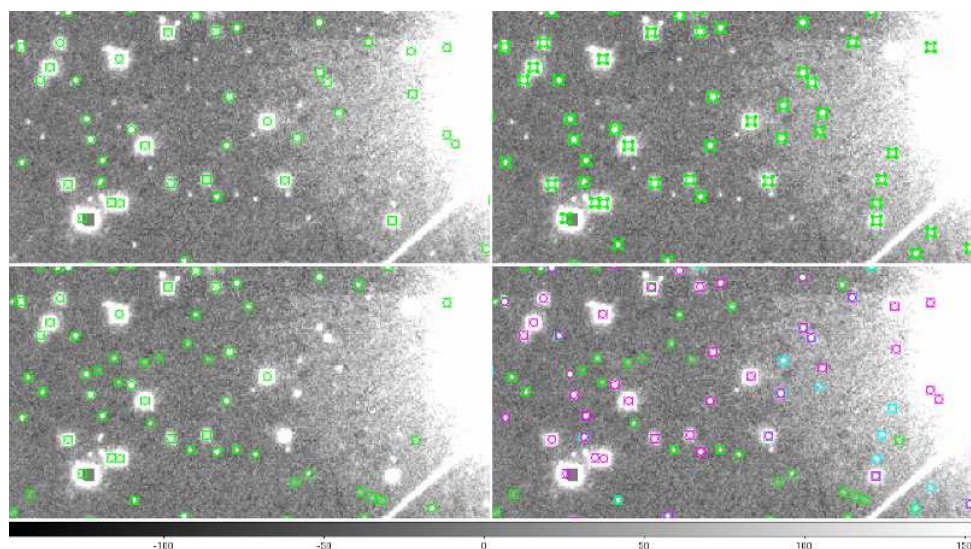


Figure 2.9: Cut-outs of the  $Y$ -band long image of IC 4665 of side  $42 \times 32''$ , where the *left* panels are detection at  $1.0 \sigma$  because they are within the PSF of the bright star, and where the *squares* are fainter objects that are not detected at the  $5.0 \sigma$ .

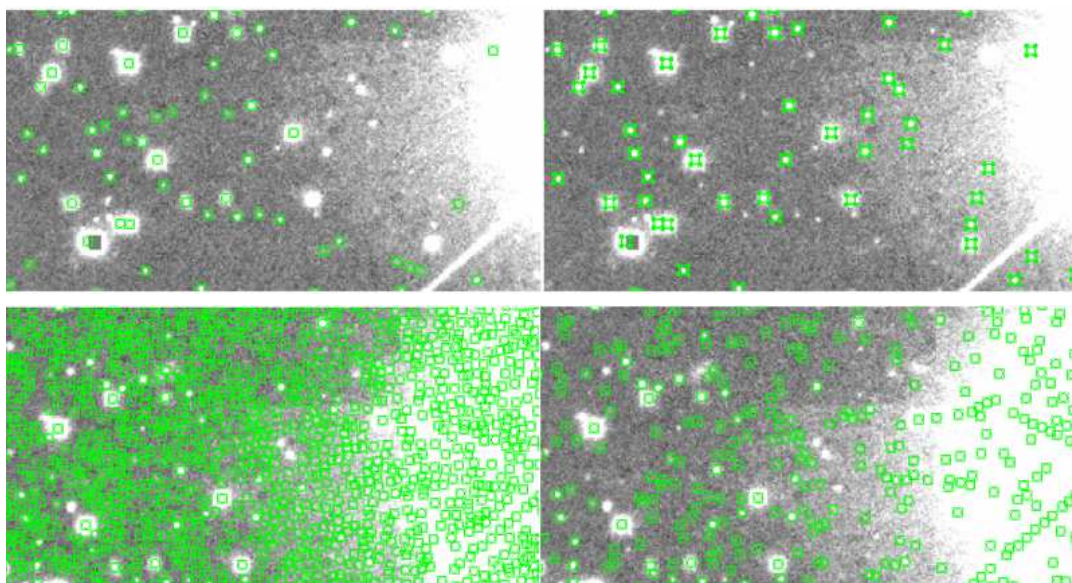


Figure 2.10: Gaussian and mexhat filters and their respective detections at  $1.0 \sigma$  overplotted onto the observed IC 4665A  $Y$ -band image. *upper left*: Gaussian `gauss_2.5_5x5.conv` filter detection at  $1.0 \sigma$  *upper right*: Gaussian `gauss_2.5_5x5.conv` filter detection at  $1.0 \sigma$ , note the absence of detections around the bright star on the left, but also the missing fainter objects with the higher threshold. *lower left*: mexhat `mexhat_2.5_7x7.conv` filter applied at  $6.0 \sigma$  where  $\sim 40,000$  objects are detected over the image and *lower right*: mexhat `mexhat_2.5_7x7.conv` filter applied with a detection of  $1.0 \sigma$  to an image and  $400,000$  detected objects. Note the missed detections of many bona fide objects in both of the lower panels irrespective of the detection threshold.

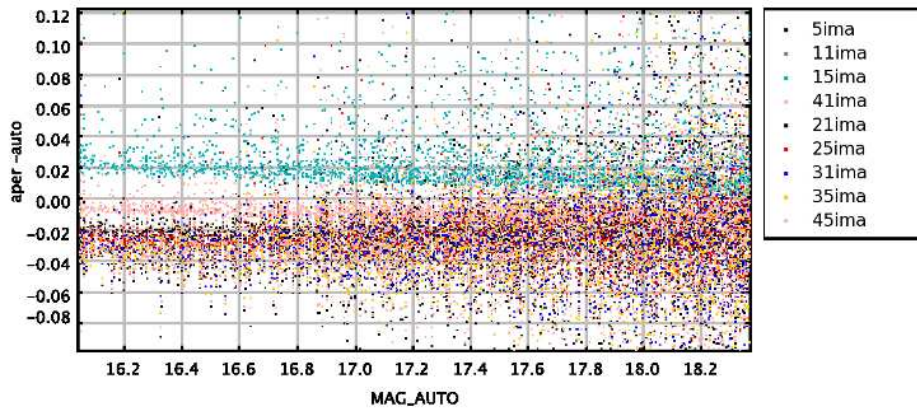


Figure 2.11: CMD of mag-auto vs mag-aperture–mag-auto for IC 4665 field A. The aperture footprint was tested at varying sizes using the constant mag-auto and the respective aperture magnitude. The smaller apertures have high divergence values whilst the larger apertures have much more dispersion due to the random locations of additional flux from objects within the aperture. Convergence occurs at mag-aperture–mag-auto = 0.03 for an aperture size of 31.

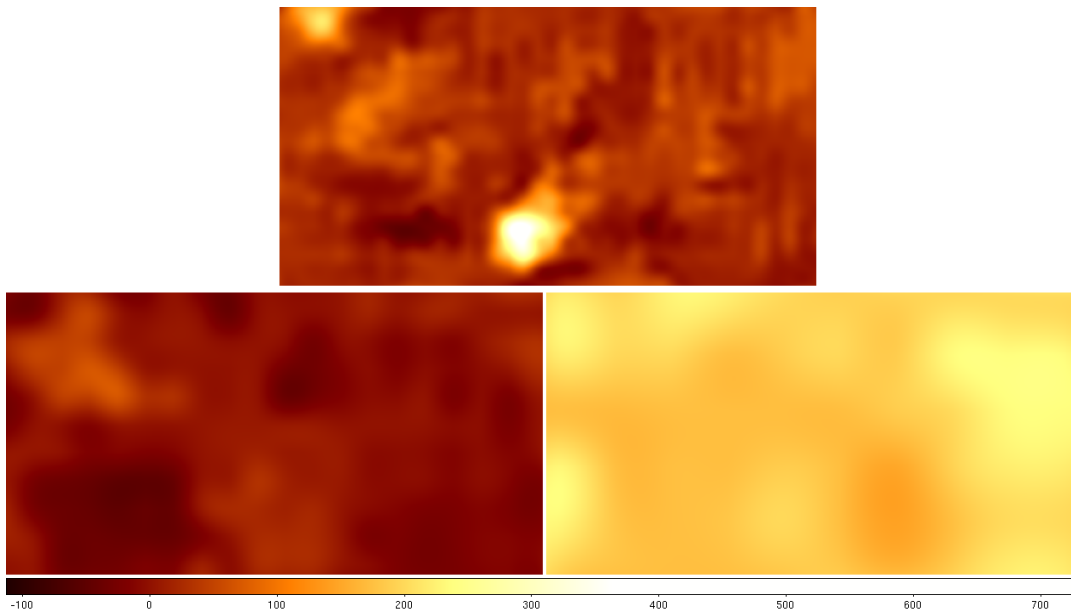


Figure 2.12: IC4665 field A, *J*-band: Comparison images of the SExtractor estimate of the background using different background sizes when over or underestimating the background that SExtractor uses as a zero point for the detection and photometry of objects. *Upper centre*: 64x64 grid which can locally underestimate the background, meaning SExtractor takes too little flux when removing the flux for the object but it will detect objects in the field well; *right*: 256x256 grid which can overestimate the background flux on a larger scale meaning the fainter objects risk being undetected, or objects will appear fainter than they otherwise are. *Left*: 128x128 grid is somewhere between the two and can be more useful for nebulous regions.

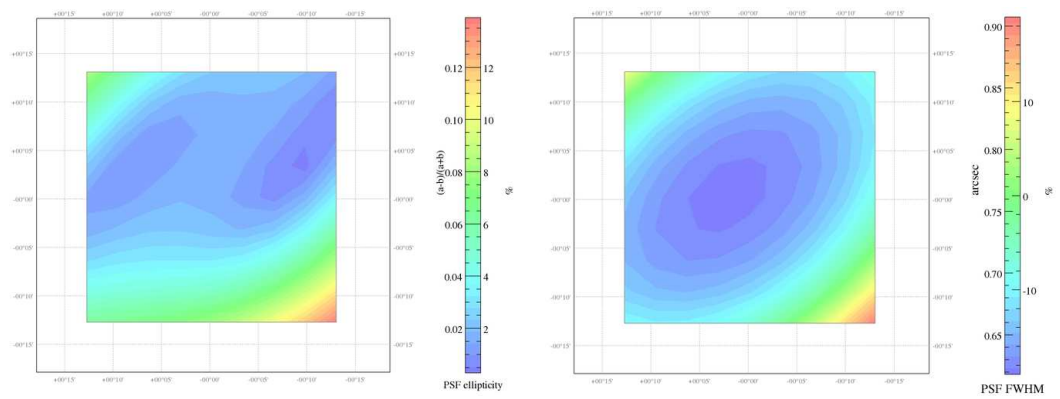


Figure 2.13: *J*-band diagnostic maps outputted by PSFEx for IC 4665 field A, *left*: FWHM map describes the how the size of the PSF varies across the image, and *right*: Ellipticity map describes the how the shape of the PSF varies across the image.

## 2.4 Summary

The observing capacities of both ground and space-based telescopes used in this work have been discussed. The primary telescope is the CFHT located in Hawaii where the two wide field detectors, WIRCam and MegaCam, were used to obtain deep exposures in the  $z'$ ,  $J$ ,  $H$  and  $K_s$  broadbands and CH<sub>4</sub>on and off narrowbands of the 3 Myr star-forming region IC 348; and shallow and deep exposures in the  $Y$ ,  $J$ ,  $H$  and  $K_s$  broadband for the  $\sim 40$  Myr open cluster IC 4665. The CH<sub>4</sub>on and off narrowbands were observed in order to filter and classify the lowest-mass objects in IC 348, here methane T-dwarfs which have  $T_{\text{Eff}} < 1300$  K and associated masses  $\sim 10 M_J$  for such young objects. Various other telescopes surveys are used, namely 2MASS and *Spitzer* for IC 348, and UKIDSS especially for IC 4665.

A major contribution is the development of an analysis pipeline for the MegaCam and WIRCam dataset using many tools from TERAPIX, and bash and awk scripts. Fits header data is extracted from the observed and TERAPIX-processed images, before running a combination of SExtractor and PSFEx in order to output raw catalogue files ready for processing. The major step here is the optimisation of the parameters for these two programs, from optimising the detection images and parameters to get the most from the data, from converging to the correct aperture size from CMDs using data from different apertures, and estimating background subtraction using different grids and blocks of the image as a whole. These results are then fed back into the extraction algorithm and an optimised set of catalogues are produced, before being amalgamated into one catalogue for each set of exposures. This data can then be checked with 2MASS and/or UKIDSS, where the associated regions will need to be downloaded from IRSA and calibration offsets can be calculated and applied if necessary. In this instance the IC 348 data required no calibration as the offsets with respect to 2MASS only where of the order 0.02 mag for the  $J$ -band. Calibration offsets for the IC 4665 data shared with value with the 2MASS data, but required the use of UKIDSS in order to calibrate the  $Y$ -band, detecting large offsets in some cases as large as 0.23 mag (for field E of the  $Y$ -band). Comparison is then available, in essence a 're-calibration' in order to check that the calibration values are correct. Additional amalgamation can be carried out in order to have a uniquely populated catalogue for each object, ostensibly for each field. Colour/magnitude and colour/colour diagrams can then be plotted in order to begin the analysis, before candidate selection. Narrowband data selection is simpler as the selection can be plotted and then checked. Specific cluster treatment holds for multiple-field observations where each field must be cross-checked and calibrated against the other fields.

At the end of this pipeline there are catalogues for each unique object where the physical analysis can be done, which is discussed in the following two chapters for the open cluster IC 4665 and heavily extincted star-forming region IC 348 respectively.

## 2.5 Résumé

Les capacités d'observation des télescopes du sol et spatiaux ont utilisés dans ce travail ont été discutées. Le télescope principal est le CFHT qu'est situé à Hawa, où les deux détecteurs de champ large, WIRCam et MegaCam, ont été utilisées pour obtenir des expositions de profondeur dans le broadband  $z'$ ,  $J$ ,  $H$  et  $K_s$  et  $CH_4$  sur et en dehors narrowbands de la région des 3 millions d'années de formation d'étoiles IC 348; expositions et superficielles et profondes dans le broadband de  $Y$ ,  $J$ ,  $H$  et  $K_s$  pour le  $\sim 40$  millions d'années amas ouvert IC 4665. Le  $CH_4$  sur et en dehors narrowbands ont été observées afin de filtrer et de classer les objets les plus bas de masse dans les IC 348, T méthane ici-nains qui ont  $T_{Eff} < 1300$  K et les masses associées  $\sim 10 M_J$  pour ces objets jeunes. Plusieurs autres enquêtes télescopes sont utilisés, à savoir 2MASS et *Spitzer* pour IC 348, et en particulier UKIDSS pour IC 4665.

Une contribution importante est le développement d'un pipeline d'analyse pour l'ensemble de données et de MegaCam WIRCam utilisant de nombreux outils de TERAPIX, et les scripts bash et awk. Données de l'entête FITS est extraite à partir des images observées et TERAPIX-traitées, avant d'exécuter une combinaison de SExtractor et PSFEx pour les fichiers de sortie catalogue premières prêtes à être traitées. L'étape majeure est ici l'optimisation des paramètres pour ces deux programmes, de l'optimisation des images de détection et de paramètres pour obtenir le maximum de données, de converger à la taille de l'ouverture correcte du CMD utilisant les données de différentes ouvertures, et l'estimation de la soustraction de fond en utilisant différents les grilles et les blocs de l'image dans son ensemble. Ces résultats sont ensuite réinjectées dans l'algorithme d'extraction et un ensemble optimisé de catalogues sont produits, avant d'être fusionnés en un seul catalogue pour chaque ensemble de l'exposition. Ces données peuvent ensuite être vérifiée avec 2MASS et / ou UKIDSS, où les régions associées devront être téléchargés à partir IRSA et les compensations d'étalonnage peuvent être calculées et appliquées si nécessaire. Dans ce cas, les données pour IC 348 requises aucun calibrage que les décalages par rapport à 2MASS que lorsque de l'ordre 0,02 mag pour le bande- $J$ . Les compensations d'étalonnage pour IC 4665 ont partagées avec la valeur avec les données 2MASS, mais nécessitait l'utilisation de UKIDSS afin de calibrer l' $Y$ , la détection de décalages importants dans certains cas, aussi grande que 0,23 mag (pour champ E de la  $Y$  bande). La comparaison est alors disponible, essentiellement en une re-calibrage afin de vérifier que les valeurs d'étalonnage sont corrects. fusion supplémentaires peuvent être effectués afin d'avoir un catalogue unique de population pour chaque objet, soi-disant pour chaque champ. Couleur / magnitude et la couleur / diagrammes couleur peut ensuite être tracée afin de commencer l'analyse, avant la sélection des candidats. Bande étroite de sélection des données est plus simple que la sélection peut être tracée et ensuite vérifiée. Traitement d'amas spécifique est valable pour de multiples observations-terrain où chaque champ doit être contre-vérifié et calibré contre les autres domaines.

la fin de ce pipeline Il existe des catalogues pour chaque objet unique où l'analyse physique qui peut être fait, qui est discuté dans les deux chapitres suivants de l'amas ouvert IC 4665 et fortement éteints région de formation d'étoiles IC 348 respectivement.

# Chapter 3

## Sub-Stellar Census of the Open Cluster IC 4665

### Contents

---

<b>3.1</b>	<b>Introduction</b> . . . . .	<b>66</b>
3.1.1	The Open Cluster IC 4665 . . . . .	67
<b>3.2</b>	<b>Object Catalogue Extraction</b> . . . . .	<b>71</b>
3.2.1	Data Testing . . . . .	71
3.2.2	Specifics of Object Detection . . . . .	72
3.2.3	Flags . . . . .	74
<b>3.3</b>	<b>Calibration</b> . . . . .	<b>75</b>
3.3.1	Short & Long Amalgamation . . . . .	81
3.3.2	Completeness . . . . .	82
<b>3.4</b>	<b>Candidate Selection</b> . . . . .	<b>87</b>
3.4.1	Colour/Magnitude Diagram Selection . . . . .	87
3.4.2	Colour/Colour Diagram Selection . . . . .	88
3.4.3	Candidate Cleaning . . . . .	88
<b>3.5</b>	<b>Discussion</b> . . . . .	<b>92</b>
3.5.1	Recovered Known Members . . . . .	92
3.5.2	Selection Considerations . . . . .	92
3.5.3	Contamination . . . . .	94
<b>3.6</b>	<b>Summary</b> . . . . .	<b>96</b>
<b>3.7</b>	<b>Résumé</b> . . . . .	<b>97</b>

---

A thorough grounding of IC 4665 is covered in this chapter, detailing cluster properties such as the age, distance, radial velocities and extinction, and difficulties in assigning these



properties. Subsequently, the CFHT data taken of IC 4665 is discussed and the final stages of the pipeline that was briefly discussed in Section 2.3 are laid out. Fruitfully, the analysis of this data leads to candidate members obtained via theoretical models superimposed upon the CMDs and colour/colour diagrams constructed with our data, before being cleaned from flags, spurious sources, by flux radius after being visually inspected and before being compared to known members. The contamination is then calculated using the control fields. It is then possible to assign temperatures, masses and spectral types in order to produce an IMF for IC 4665. This can then be compared to the IMF of other young clusters in the literature.

### 3.1 Introduction



Figure 3.1: A composite image of IC 4665 using  $J$ ,  $H$ , and  $K_s$  band data. (See text for image origin).

IC 4665 is a fairly young, open cluster whose centre taken to be at  $17^{\text{h}}46^{\text{m}}18^{\text{s}}.00 +05^{\circ}43'00''.0$  from Kharchenko et al. (2005) and SIMBAD, located towards the constellation of Ophiuchus,

shown in Figure 3.1<sup>1</sup>. It is located about 100 pc outwards from the Galactic plane has low radial velocity of  $-10.3 \text{ km s}^{-1}$  or proper motion  $-7.4 \text{ mas yr}^{-1}$ . Its age is between  $\sim 30$  and  $50 \text{ Myr}$ , where different methods give different ages, and is discussed below. The cluster also seems to have a near solar metallicity of  $\frac{[Fe]}{[H]} = 0.077$ , derived statistically by Pöhl and Paunzen (2010). This cluster also has very low extinction where a value of  $A_v = 0.59 \pm 0.16 \text{ mag}$ , from Jeffries et al. (2009) is used in this work. This extinction value was found using the intrinsic colours for a pre-main-sequence star as defined by Bessell et al. (1998), where the JHKLM colours are based upon the Johnson-Cousins-Glass system (Bessell and Brett, 1988) and UBVRI colours defined by Bessell (1990). The extinction co-efficients towards this cluster can be found previously in Table 2.1. Additionally, the low levels of extinction mean that it is possible to have a more complete picture of the IMF, here possibly probing brown dwarfs to a spectral type of  $\sim L3$ , where no objects should be hiding in extremely extinguished regions as is the case for younger, more occluded star-forming regions. An additional problem, however, is the contamination due to relatively unextinguished foreground and background dwarfs which are harder to separate from the sample. In essence this is a good place to study the IMF in terms of both distance and extinction and consequently IC 4665 is a comparatively well-observed cluster where there have been many surveys, both optical and infrared.

### 3.1.1 The Open Cluster IC 4665

**of Pioneering Surveys** Prosser (1993) made the first CCD survey of this cluster using the 1m Nickel telescope at the Lick Observatory. The  $500 \times 500$  pixels CCD was used to take 80  $V$  and  $I$ -band images with a total field of view of  $41' \times 32'$ , covering the centre of the cluster. They obtain a list of 170 astrometric, 13 known bright and 213 new photometric, and 39  $H\alpha$  candidate members of IC 4665. Through the use of  $V/B-V$  and  $V/V-I$  CMDs and comparison to the upper and pre-main-sequence empirical isochrones from Mermilliod (1981), they conclude with 35 bright candidates, 57 proper motion/photometric and 23  $H\alpha$  emission stars as good candidate members warranting follow-up astrometric, photometric and spectroscopic surveys for confirmation. A further  $H\alpha$  emission survey, which also included Li abundances of low-mass stars was undertaken by Martin and Montes (1997). Their  $H\alpha$  activity results agree with a young age for this cluster, however the results show a depletion for their Li I abundances, which usually indicates an older age. This low  $H\alpha$ -Li I depletion correlation seems to occur for young, 20-100 Myr, low-mass stars, as shown in the Pleiades (120Myr) and  $\alpha$  Persei (90 Myr). This has recently been confirmed using spectroscopic data observed by Jeffries et al. (2009), who discuss the pre-main-sequence Li depletion. Their isochronal ages are consistent with the Li depletion boundary (LDB) at  $28 \pm 5 \text{ Myr}$ , but find that the late-type K/early M sequence gives a cluster age  $> 100 \text{ Myr}$ . A possible

---

<sup>1</sup>Credit: Stefan Binnewies and Josef Pöpsel

explanation could be the difference in radiative opacities which had not been included with the theoretical isochrones (Baraffe 2002) used for comparison, and also difference in metallicities between different clusters or even within different stellar groups within a particular cluster.

**of Age & Distance** The most recent survey was by Cargile and James (2010), who conducted a photometric survey of IC 4665 using  $B$ ,  $V$ , and  $I_c$  photometry to try to pin down the age of the cluster, however, there are variations depending on the method used. Comparing the standard photometric turn off of the pre-main-sequence to theoretical isochrones they established an age of  $36 \pm 9$  Myr and a distance of  $360 \pm 12$  pc, in general agreement with the upper-main-sequence of  $42 \pm 12$  Myr and  $357 \pm 12$  pc. Conversely, the age taken from the lithium depletion boundary method is much less for this cluster,  $28 \pm 5$  Myr which is opposite to the trend for an older cluster age usually seen when comparing the difference between the main-sequence isochronal ages and the lithium ages (Manzi et al., 2008). This age disparity is addressed with respect to our selection criteria within the candidate extraction section, Section 3.4, in order to achieve a conservative list of candidate cluster members. The envisaged distances, however, coincide very well with previous estimates taken by Kharchenko et al. (2005) of  $350 \pm 15$  pc.

### **of Membership**

Manzi et al. (2008) focused on the lithium depletion boundary but also assigned levels of membership to candidates taken from the surveys by Prosser (1993); Giampapa et al. (1998); de Wit et al. (2006) and a SIMBAD literature search whose locations are shown in an I, I-Z CMD in Figure 3.2 (from Manzi et al. (2008), their Figure 1), using data taken from FLAMES on the VLT (Pasquini et al., 2002). They based this membership on radial velocity measurements from the average shift of the spectral lines in their spectroscopic data; and assigned ‘Y’, ‘Y?’ and ‘N’ flags to each of their 137 objects in order to clarify the cluster membership status. The average radial velocity for this cluster was found to be  $15.95 \pm 1.13$  km  $^{-1}$  using this data, taken from a peak clearly seen in their data, shown in Figure 3.3. A previous radial velocity survey by Prosser and Giampapa (1994) found 20 of 42 candidates (of spectral type F5-K0) which are likely members with an average radial velocity of  $13.1$  km  $^{-1}$  for this cluster.

**of Rotation & Variability** Rotation and variability studies were conducted by Scholz et al. (2009), adding to the other surveys and helping to build up a comprehensive picture of this open cluster. After observing  $\sim 100$  cluster members they found periodic changes in observed flux from sub-stellar objects which seem to indicate the presence of solar spots on the surface of  $\sim 20$  %

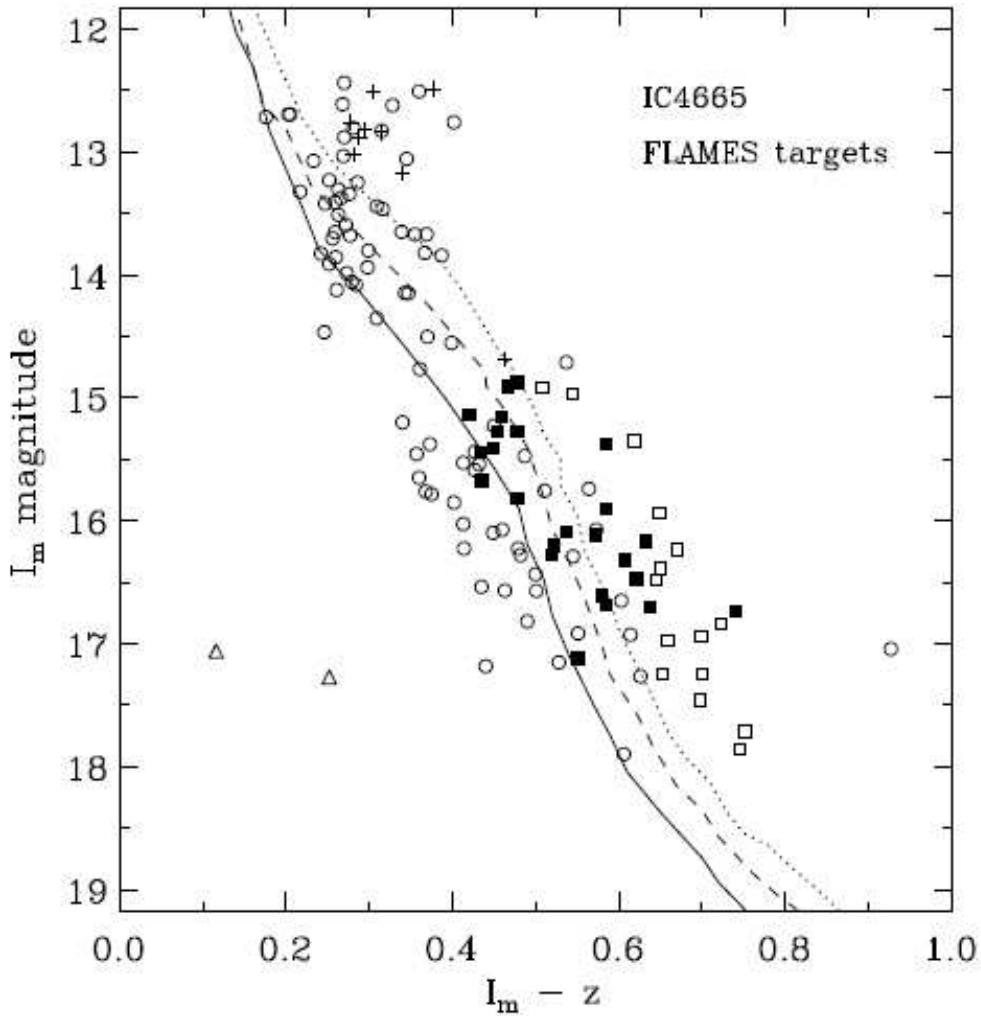


Figure 3.2: 137 Manzi et al. (2008) candidate objects taken from the literature and observed using FLAMES are plotted on an I/I-Z CMD. *circles* 89 stars from Prosser and Giampapa (1994); *open squares and crosses* 15 and 8 from de Wit et al. (2006) respectively; *triangles* 2 stars from Luyten (1961). 30, 50 and 100 Myr NextGen isochrones adjusted to the distance of IC 4665 (here 370 pc).

of their sample, lower than for similarly-aged, solar-mass objects. Possible explanations for this could either be the occurrence of few solar spots or evidence of symmetric geometries, multiply around the photosphere or just a large and single polar spot. The rotation rates range from between 3 and 30 hours which are relatively fast especially when compared to more massive objects. The observed lack of slow rotators in this young cluster is thought to be genuine and affects all low-mass objects, where older, more massive objects can lose angular momentum from wind braking.

**of X-Rays** ROSAT X-ray data was taken of IC 4665 by Giampapa et al. (1998) using the High Resolution Imager which detected 28 stellar sources towards the cluster. Further spectra was obtained for the 22 of these that were thought to be cluster members. Interestingly, they suggest that the high Galactic latitude of IC 4665 could be explained by a unique formation

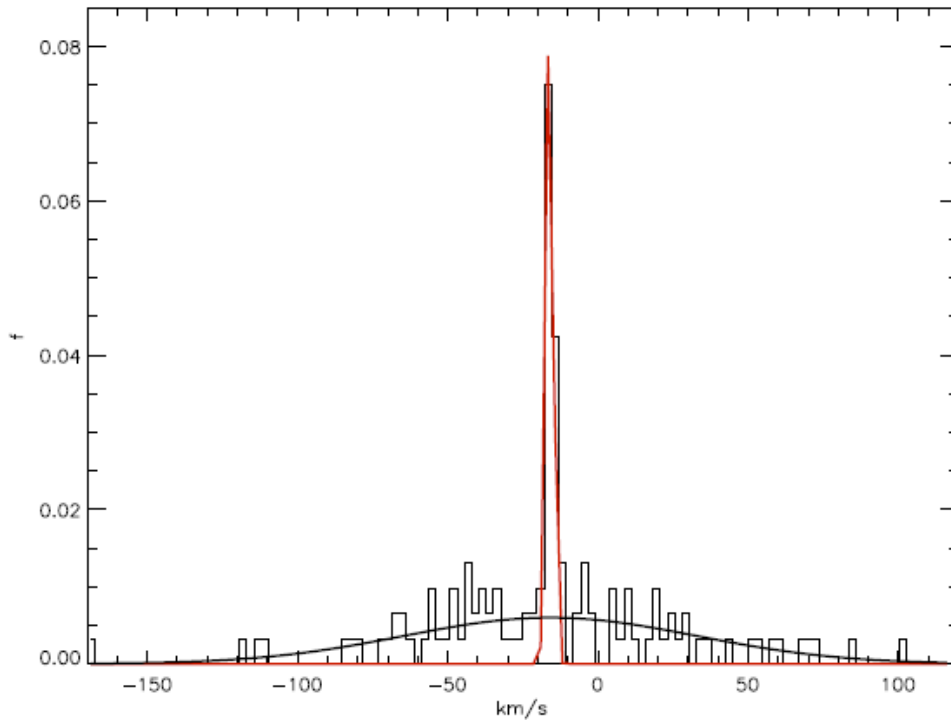


Figure 3.3: Manzi et al. (2008) radial velocity data with an obvious peak at  $\sim 16 \text{ km s}^{-1}$ .

history different to those clusters at lower Galactic latitudes. Comparison with other clusters, the Pleiades,  $\alpha$  Persei, IC 2391 and IC 2602, suggest large similarities based on their absolute B-V colours. These colours, and normalised luminosities for low-mass stars, also suggest a similar age to the Pleiades ( $\sim 30$ -100 Myr). Analysis of the higher-mass stars, in particular 5 B stars and their broad equivalent width  $H\alpha$  emission, indicate that the formation history of open clusters with solar metallicities cannot be deduced from coronal observations. Their absolute B-V  $\sim 0.6$  colour-rotational distribution seem to be similar for younger clusters such as IC 4665 and the Pleiades.

**of the IMF** IC 4665 has been well studied where the most complete IMF work to date was undertaken by de Wit et al. (2006) down to mass limit of  $40M_J$  with a mean mass of  $0.32 M_\odot$ . From a photometrically-selected sample of low-mass and brown dwarf candidates they found that a power law fit between 1 and  $0.04 M_\odot$  had a fit of  $\alpha=-0.6$ , in keeping with other clusters. Caballero et al. (2007), for example, found a power law of  $\alpha=-0.6$  for  $\sigma$  Orionis and Lodieu et al. (2007)  $-0.6$  for Upper Scorpius, both for the lower mass end between  $0.3$  and  $0.01 M_\odot$ . This work aims to constrain the lower end of the IMF down to the survey completeness limit of  $\sim 0.015 M_\odot$  using both short and long exposures of IC 4665.

## 3.2 Object Catalogue Extraction

Following on from the basic details outlined in Section 2.1.2.3, there are, in total, 216 images for the entire IC 4665 data sample, of which there are 12 fields each having  $Y$ ,  $H$ ,  $J$  and  $K_s$ -band images with 2 sets of exposures each, and where the rest of the images are complimentary weight and flag maps for each image. Clearly this cannot be maintained manually and to this end, this work relies heavily on *bash shell* and *awk* scripts in order to make sure the right variable and datacube is in the right place, examples can be found in Appendix section 5.5. The pipeline, mentioned in Section 2.3, covers the details up to the calibration section, except for cluster-specific testing.

### 3.2.1 Data Testing

The IC 4665 data from TERAPIX needed to be tested to ensure it was of good quality. Using the QualityFITS data from TERAPIX it was possible to see various properties of the data, for example the star/galaxy separation, astrometric accuracy, and photometric errors. Additionally, visually inspecting each image was also a good test to make sure that there was data in the file and that the images were not of an obviously poor quality. The main tests are in relation to the SExtractor and PSFEx extraction routines and involve finding various parameters from the images to facilitate and optimise this extraction. Two different filters were tested with the IC 4665 data; the Gaussian-shaped filter and the mexican hat (!) shaped filter. These were tested at different convolved masks in order to find the best filter for object detection within SExtractor. The filters tested for the detection objects on the image were the `gauss_2.5_5x5.conv`, `gauss_2.5_7x7.conv`, `mexhat_2.5_7x7.conv`, and `mexhat_3.0_9x9.conv`. The mexican hat filter was tested because of problems with many undetections in the PSFs of bright stars with the Gaussian-like filter. Whilst this helped in detecting many of these objects, the filter missed many faint field objects and sometimes very good quality objects. Another drawback with this filter was the detection of >400,000 objects on each image making a rather large catalogue file for each band and image. See Figure 2.10 to see the differences between the Gaussian and mexican hat filters, and their associated detections at  $1.0 \sigma$ .

The background subtraction handled by SExtractor affects the final magnitude and is directly related to the amount of flux within a configurable grid of size much greater than the footprint of the PSF. This map is smoothed depending on the number of blocks of grids, for example a 3x3 or 5x5 block of 128 pixel grids.

The analysis to be done on the detected objects takes into account the background subtracted level, and also the amount of flux with its catchment area. This catchment area is the aperture and is a grid of pixels, a footprint, around the central detected pixel of the PSF. It is necessary

to optimise this parameter depending on the depth and crowdedness of the image, for example if the image is towards the Galactic centre it will, usually, be very crowded and so using an aperture that is too large would mean counting flux from stars or objects which are not part of the detected object, or using an aperture that is too small would mean rejecting flux and so making the object fainter than it actually is. Whilst SExtractor does take into account some of the flux present in overlapping apertures, this is not an ideal method and is poorer the worse-fitting the aperture. Consequently the aperture footprint was tested at varying sizes, where a figure of this method has been shown in Section 2.11. A table summarising the convergence of the footprint size of the aperture, based upon the difference between the ‘mag-auto’ property and the varying aperture magnitude, is shown in Table 3.1. It can be seen that the magnitude varies for apertures that are too small, whilst for apertures that are too large the dispersion increases as it begins to include flux from other objects within the perimeter, where these objects are randomly situated giving rise to the increased dispersion. An aperture size of 31 was found to be the best for the work on IC 4665.

Table 3.1: Aperture selection offsets for aperture optimisation using the mag\_auto value. Increasing scatter appeared with a higher incidence of contamination from additional objects within the aperture footprint. Here, an aperture of 31 was found to be the best to use for this analysis.

Aperture size (pixel)	offset mag	dispersion level
5	+0.220	nominal
11	+0.250	nominal
15	-0.005	nominal
21	-0.015	nominal
25	-0.020	nominal
31	-0.030	preferential
35	-0.030	increasing scatter
41	-0.030	more scatter
45	-0.030	most scatter

### 3.2.2 Specifics of Object Detection

Initially, detection could have been attempted using a merging of two images, for example the  $J$  and  $K_s$  band images, for each field, but the nature of the gain and total exposure time would be unknown as the process for this within the pipeline from TERAPIX is not fully known. The  $J$ -band image could be more useful as it could detect many near-infrared objects whilst the  $K_s$  image would be useful for those object detected which favour the presence of dust. A better solution, for both for detection and for the amalgamation of catalogues after extraction, would be to use just

one image of the four for the detection. This is also superior because to have a cluster member, as discussed in Section 1.5, an object would need to be detected in the  $Y$ ,  $J$  and  $H$  band. The  $K_s$  band is useful to have as well, but it is not the primary method of detection and analysis that were the main motivation of this work. Indeed, whilst the short exposures have to have a detection in the  $K_s$  band, in fact the long exposures may not necessarily have a detection. In Figure 3.4 it

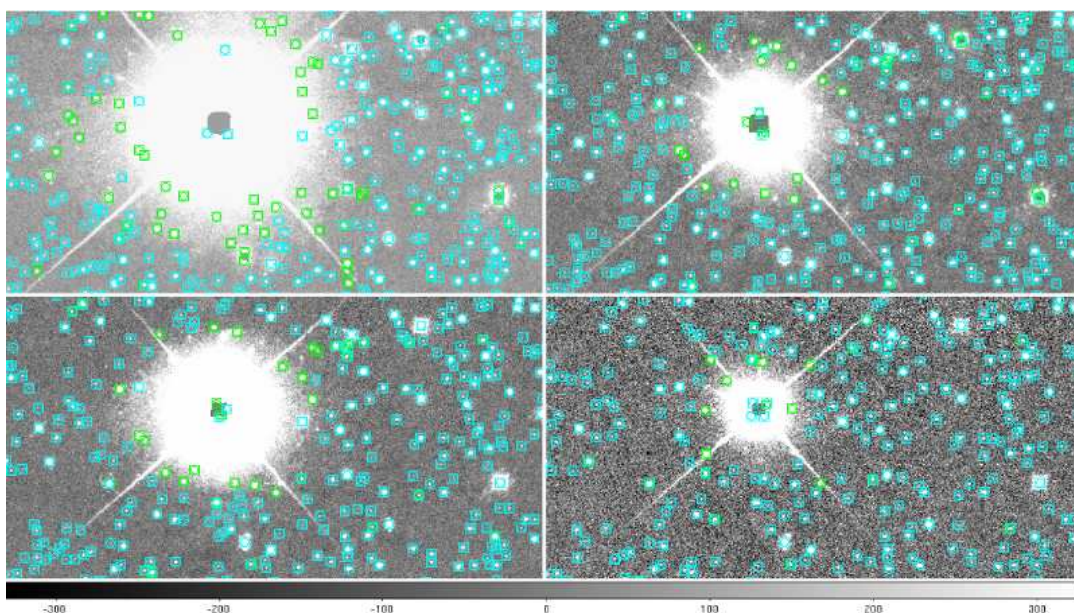


Figure 3.4: These cut-outs are from the IC 4665 field A long image for the four different filters, where it can be seen that each band has a different exposure length. Superimposed on all images are the object detections for each band. Where the PSF wings are the largest (around the brightest stars) there are the fewest detections, in the  $Y$ ,  $H$ ,  $J$  and  $K_s$  images respectively. This resulted in the  $J$  being used as it was the clearest, and also to be considered as a cluster member an object must be well detected in at least the  $Y$ ,  $J$  and  $H$  bands. *upper left: Y-band image, upper right: J-band image. lower left: H-band image. lower right:  $K_s$ -band image.*

can be seen that the  $Y$ -band image has many brighter and saturated stars due to the comparatively longer exposure lengths, which are known to be problematic for the detection of objects at low detection threshold; the  $K_s$  band image is not as deep as the other three images due to its shorter (500-732s) exposure times; and this leaves the  $J$  and  $H$ -band images which are both similar in quality but the  $J$ -band image is slightly deeper. Additionally, the  $J$ -band is the peak bandpass for M and L-dwarfs, resulting in the  $J$ -band image being used for the detection for both the long and the short exposures.

SExtractor and PSEFEx extraction example scripts can be found in the Appendix 5.5. First-pass SExtractor thresholds were at  $15\sigma$  for both the long and short exposure set. Note the comma-separated .fits files for the input observation images and for the weight map and flag maps in the second-pass; the first file is the detection image and the second file is the analysis image. Note



the detection and analysis threshold of  $1.5 \sigma$  for the short exposures. Long exposures were treated similarly, except that the detection and analysis thresholds were different, at both  $1.0$  and  $5.0 \sigma$ , because the  $1.0 \sigma$  seemed not to detect any objects around the brightest stars, as discussed.

### 3.2.3 Flags

Here, the flag file that exists for each image is used to mark each object with an appropriate ‘IMA’ flag. Additionally, SExtractor labels each object with a flag depending on the saturation level defined in the configuration option. These SExtractor flags are purely dependent on this value. In some cases the data concerning this level was uncertain or found to be incorrect when compared to the 2MASS or UKIDSS catalogues due to the non-linearity of the detector, so another flag value ‘SAT’ was defined. This non-linearity occurs as the NIR detectors act, partially, like a capacitor, where typically 5% of the signal will be non-linear before the detector saturates, compared to just 1% non-linearity at saturation. This custom flag was defined visually from CMDs for each of the four bands to mark exactly the saturation point. The saturation levels vary between fields and exposures but each detected object was assigned a flag, ‘0’ for unsaturated and ‘1’ for saturated. CMDs of the limits where these values were chosen are shown in Figure 3.5 for the *J*-band, whilst the additional plots are shown in the Appendix 2 for readability.

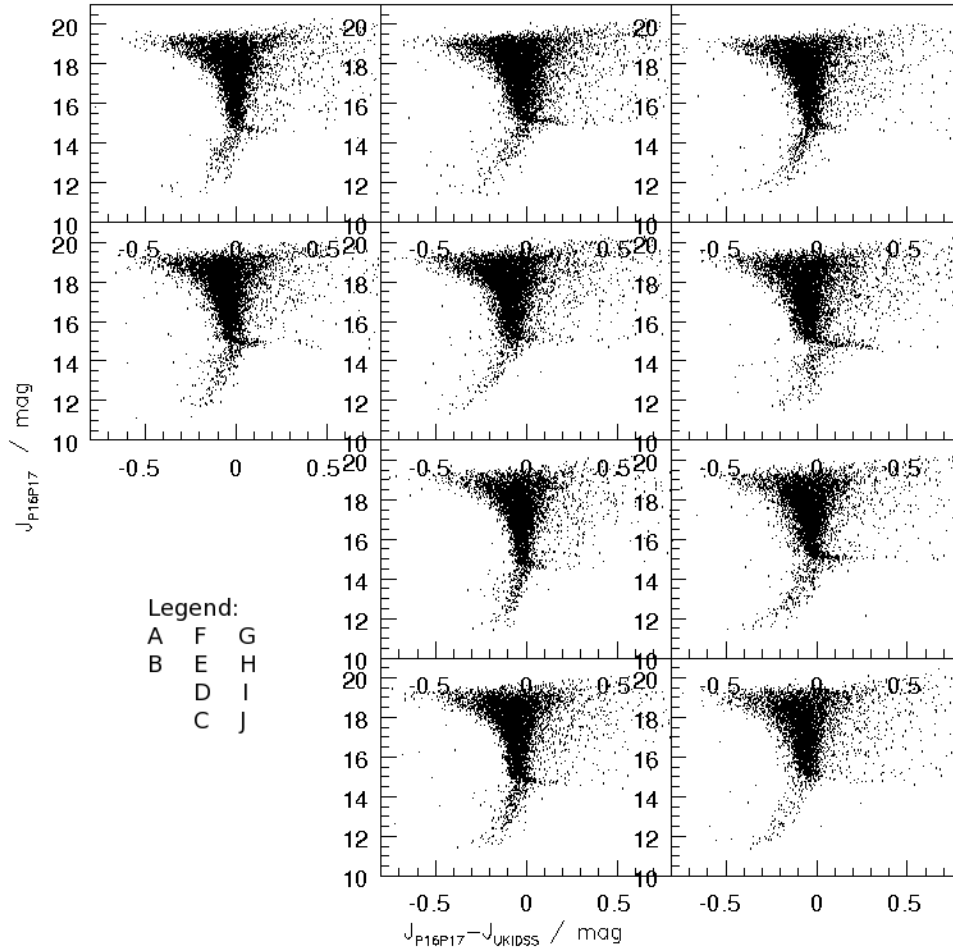


Figure 3.5: Short exposure  $J$  saturation plots showing the offsets arising due to saturation between the CFHT IC 4665 data and UKIDSS data over the same FOV. Note the offset at the brightest magnitudes, and the two-way saturation curves - one apparent because those objects are in the non-linear region of the detector, whilst the other objects are incomplete due to their saturated cores being removed during pipelining. Fields labelled A through to J.

### 3.3 Calibration

A major part of the treatment of the IC 4665 data concerns the calibration between the observed fields. In this section the method of calibrating the short and long WIRCam  $Y$ ,  $J$ ,  $H$  and  $K_s$  images is discussed, using both 2MASS and UKIDSS as photometric zero-points. 2MASS was chosen initially because of its relations to the calibration within the TERAPIX pipeline for the  $J$ ,  $H$  and  $K_s$ -bands, however, the  $Y$ -band eventually proved problematic therefore a different calibration zero-point needed to be found for this band, UKIDSS. To test this, a good set of stars were taken for each field for these calibration methods, and of having flux radius less than 4.0 which is a conservative estimate of PSF stellar quality and had bad pixel IMA flags of zero.

Additionally, the sample of stars was selected for low photometric errors  $<0.05$  mag and our SAT flags of zero as well. Using these stars, they were matched with data from the respective survey catalogue, then the median of the colours were taken, along with the dispersion of the median in bins across each sample for each field/image. Differences between the two calibration systems are discussed, as well as possible differences arising between the calibrated data and the models that had been convolved with the CFHT system.

Whilst tests were performed using 2MASS data for the short  $J$ ,  $H$  and  $K_s$  bands (150 overlapping) then the long onto the short (double calibration) the final option was to use all UKIDSS data as the  $Y$  band can be calibrated to the same data as the JHK where possible. For the control fields there was no data available under UKIDSS, so the  $Y$  band was calibrated using the median offset over all 10 fields, whilst the  $J$ ,  $H$  and  $K_s$  bands were calibrated using the 2MASS  $J$ ,  $H$  and  $K_s$  short and long-short values.

**Calibration onto 2MASS** Initially, comparing the data to 2MASS was taken as the first logical step to check the data had been treated properly within the pipeline, as the WIRCam images are also calibrated to the 2MASS excepting the  $Y$ -band, but also as a double check for any offsets seen between the fields. Each field was treated separately as the seeing on each field was slightly different and so the saturation line occurred at different magnitudes. The use of the short and long exposures complicates this as there needs to be a statistically significant sample of stars in order to compare the zero-points of the long and short to the 2MASS zero-point. The short exposures had on average  $\sim 1000$  stars per field which had a position-matched 2MASS counterpart, whilst the long exposures had  $\sim 3250$  of stars matched where the long catalogues are at least four times as populous.

The saturation level taken from the TERAPIX flags for the long exposures is between 12.5 and 13.5mag for  $J$  and  $H$ , with  $K_s$  saturating at 14.5 mag, whilst the depth of the 2MASS  $J$ ,  $H$ , and  $K_s$  filters are 15.8, 15.1, 14.3 mag respectively. The short exposures were saturated at  $\sim 12$  mag.

In conclusion the best way to calibrate the short and long exposures was to calibrate the short exposures directly onto 2MASS, then calculate the difference between the short and the long exposures and calibrate by using this difference *and* the difference between the short exposure catalogues and 2MASS. A good set of stars was selected on the conditions of having no flags present and having magnitudes of  $12.5 < J > 15.8$ ,  $12.5 < H > 15.1$  and  $12.5 < K_s > 14.3$ , used to avoid large errors present at fainter magnitudes. The differences between the short  $J$ ,  $H$  and  $K_s$  values and 2MASS differed by up to  $\sim 0.04$  mag. The differences between the short and long exposures varied by up to  $\sim 0.04$  mag on a field-by-field basis, and by up to  $\sim 0.5$  mag for the  $Y$  exposures. The full 2MASS calibration and dispersion values for each field, along with the number of stars used for the calculation, are shown in Table 3.2. An example SuperMONGO program used for this dispersion calculation and for further dispersion calculations is shown in

the Appendix 5.5. The  $K_s$  had negligible differences of less than 0.001 mag as these objects were extracted from the same analysis image but different detection images for the long and short exposure sets, as discussed in Section 2.3.5. In Table 3.2 it can be seen that we have a  $Y$  value between the short and long but not between the short and 2MASS, where this large variation is explained by the lack of a  $Y$  2MASS band in the TERAPIX pipeline and consequently is dealt with separately. An exceptional variation of 0.090 is associated with the long  $H$ -band in field F where there were problems with the reduction, but this has now been calibrated properly using the zero-point method.  $\sim 400$  stars were used for the calibration of the short images onto 2MASS, whilst there were  $\sim 1200$  stars for the calibration of the long onto the short exposures.

Table 3.2: Calibration values for the 2MASS calibration attempt. Median values, dispersion values and the average number of stars used are shown for the 2MASS calibration analysis:  $\sim 400$  for the short-onto-2MASS comparison and  $\sim 1200$  for the long-onto-short comparison. Note the lack of  $Y$ -band data in order to calibrate the short exposures onto 2MASS.

Field	$Y_{med}$	$Y_{\sigma}$	$J_{med}$	$J_{\sigma}$	$H_{med}$	$H_{\sigma}$	$K_{smed}$	$K_{s\sigma}$	no. stars
SHORT	onto	2MASS:							
A	-	-	-0.058	0.016	-0.075	0.036	-0.046	0.042	324
B	-	-	-0.057	0.016	-0.064	0.015	-0.053	0.007	363
C1	-	-	-0.057	0.014	-0.059	0.017	-0.044	0.013	331
C2	-	-	-0.059	0.008	-0.065	0.014	-0.040	0.014	340
C	-	-	-0.051	0.004	-0.052	0.013	-0.047	0.007	292
D	-	-	-0.053	0.018	-0.070	0.005	-0.047	0.005	370
E	-	-	-0.056	0.022	-0.087	0.023	-0.049	0.019	267
F	-	-	-0.055	0.029	-0.085	0.023	-0.047	0.014	342
G	-	-	-0.051	0.006	-0.066	0.016	-0.026	0.007	276
H	-	-	-0.053	0.027	-0.068	0.018	-0.057	0.027	324
I	-	-	-0.061	0.015	-0.065	0.024	-0.042	0.008	367
J	-	-	-0.050	0.010	-0.073	0.003	-0.054	0.008	281
LONG	onto	SHORT :							
A	0.028	0.007	0.014	0.007	0.025	0.009	<0.001	<0.001	1108
B	0.005	0.009	0.003	0.006	0.013	0.006	<0.001	<0.001	1155
C1	0.220	0.009	0.005	0.016	0.007	0.008	<0.001	<0.001	1101
C2	0.158	0.009	0.001	0.013	0.007	0.007	<0.001	<0.001	1212
C	0.129	0.006	<0.001	0.015	-0.001	0.016	<0.001	<0.001	982
D	0.056	0.015	0.025	0.005	0.039	0.008	<0.001	<0.001	1041
E	-0.234	0.007	-0.014	0.013	0.014	0.008	<0.001	<0.001	606
F	0.267	0.016	0.024	0.009	0.090	0.022	<0.001	<0.001	1019
G	-0.201	0.009	0.012	0.014	0.012	0.006	<0.001	<0.001	851
H	<0.001	0.017	0.015	0.013	0.025	0.004	<0.001	<0.001	1134
I	-0.059	0.011	0.032	0.014	0.012	0.015	<0.001	<0.001	914
J	-0.181	0.014	-0.012	0.012	-0.017	0.014	<0.001	<0.001	622

A second test was required in order to find whether our set of CFHT  $Y$  exposures were properly calibrated, which was done using the definition of the Vega system. A0 stars are routinely used as standard reference stars (Gerbaldi et al., 1999) from this very definition. It was not possible to do this test with 2MASS data as there is no comparable  $Y$  data set. For the A0 calibration check we used the DR6 UKIDSS data release, over our FOV. The control fields had no UKIDSS data,

and data for the FOV of fields E and I were only 19% and 80% complete for the short  $Y$ -band, and 14% and 72% for the long exposures respectively, which can be seen in Figure 2. Poor or missing  $Y$ -band values were given a nominal 9999, meaning the deficit of  $Y$ -band data for these fields could significantly skew the median value used for calibration, therefore only the stars with good  $Y$ ,  $J$ ,  $H$  and  $K_s$  data were used for these dispersion calculations (see Appendix 5.5 for an example script). Fields E and I were treated separately with their fewer number of associated stars in order to increase the confidence of the results in all of the other fields.

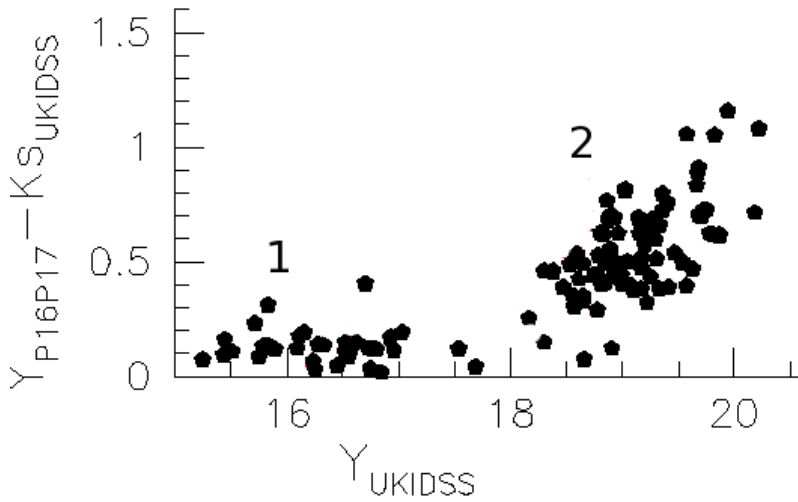


Figure 3.6:  $Y$  vs.  $Y - K_s$  CMD showing objects detected from our fields, matched with data that was taken from the DR5 UKIDSS catalogue, and which have  $J - H$  and  $J - K_s$  and  $H - K_s$  colours within the range of  $\pm 0.1$  mag. Objects in group ‘2’ all have photometric errors  $< 0.1$  mag, whilst objects in group ‘1’ have photometric errors  $< 0.05$  mag. The objects from group ‘1’ can be said to be A0 stars, as they have a median offset of 0.1 mag over all three CMD permutations. The  $Y$  vs.  $Y - J$  median colour offset over all ten fields is 0.068 mag, the  $Y$  vs.  $Y - H$  median colour offset is 0.114 and here (this plot) shows the  $Y$  vs.  $Y - K_s$  CMD with median colour offset of 0.120.

Twenty-five A0 stars had a  $J$ ,  $H$  and  $K_s$  colour range of no more than  $\pm 0.1$  mag and errors less than 0.05 mag which were found from the DR5 UKIDSS catalogue. These stars were used to see whether the UKIDSS  $Y$ -band is an acceptable calibrator for the CFHT WIRCam  $Y$ -band. When the  $Y - J$ ,  $Y - H$  and  $Y - K_s$  were analysed these objects still had colours with a mean median of 0.101 mag but had a dispersion of  $\sim 0.011$  mag, validating their identity as A0 stars. It can be seen from Figure 3.6 that these objects are not particularly well groups, even those with photometric errors  $< 0.05$  mag, meaning that they cannot be used to acceptably calibrate our  $Y$ -band short exposures. Clearly an additional calibration method was required in order to calibrate the  $Y$ -band, and it was envisaged to calibrate our entire long on short sample onto UKIDSS, in

place of 2MASS.

**Calibration onto UKIDSS** This used the DR6 and not the DR7 data as this data was not available at the time of the data analysis. A further check was made but no new data in our FOV of IC 4665 was available. The  $Y$ -band was tested where the mean difference was -0.008 and -0.011 mag for the short and long catalogues respectively. There was, however, a spread of 0.15 to 0.3mag between individual field comparisons for the short and long data. Hodgkin et al. (2009) found that the UKIDSS  $Y$  data was significantly bluer offset by up to 0.08mag, but also discusses that this offset is an artefact of their extrapolation based on the red-ward selection of  $J - K_s$  stars. An offset was applied to all further UKIDSS releases from DR3 of  $-0.078 \pm 0.010$  in order to fit the  $Y$ -band to the Vega photometric system. Additionally, the similarities between the CFHT and UKIDSS systems allow the use of the  $\frac{A_\lambda}{A_V} = 0.42$  extinction co-efficient. The difficulty, however, is making sure that the  $Y$ -band data could be compared to the 2MASS calibrated data, so it was then prudent to calibrate not just the WIRCam  $Y$  data onto UKIDSS, but also to calibrate the  $J$ ,  $H$  and  $K_s$  data as well. Applied, calibrated values are shown in Table 3.3. Hence, the data in this work is zero-point calibrated to UKIDSS DR6 release.

Table 3.3: The average number of stars used for the short-onto-UKIDSS calibration was 676, whilst 1621 stars, on average, were used for the long-onto-UKIDSS comparison over all four bands. The number of stars for fields E and I in the  $Y$ -band (not explicitly shown) are 19% and 80% complete for the short  $Y$ -band exposures, and 14% and 72% for the long  $Y$ -band exposures because of the lack of coverage of the UKIDSS  $Y$ -band over the survey area.

Field	$Y_{med}$	$Y_\sigma$	$J_{med}$	$J_\sigma$	$H_{med}$	$H_\sigma$	$K_{smed}$	$K_{s\sigma}$	no. stars
SHORT	onto	UKIDSS:							
A	-0.100	0.010	-0.012	0.009	-0.074	0.010	-0.067	0.022	646
B	-0.150	0.011	-0.041	0.006	-0.090	0.011	-0.087	0.007	750
C	-0.215	0.019	-0.049	0.025	-0.088	0.031	-0.083	0.012	645
D	-0.135	0.012	-0.045	0.005	-0.103	0.022	-0.081	0.010	692
E	0.014	0.013	-0.053	0.022	-0.106	0.024	-0.085	0.023	377
F	-0.231	0.010	-0.038	0.020	-0.100	0.028	-0.077	0.019	891
G	0.102	0.002	-0.049	0.011	-0.094	0.024	-0.056	0.021	676
H	-0.109	0.022	-0.044	0.029	-0.080	0.014	-0.065	0.019	758
I	-0.011	0.008	-0.054	0.018	-0.088	0.015	-0.052	0.009	658
J	0.007	0.006	-0.029	0.029	-0.087	0.020	-0.051	0.032	672
LONG	onto	UKIDSS :							
A	-0.076	0.013	-0.002	0.014	-0.052	0.015	-0.075	0.019	1499
B	-0.151	0.012	-0.041	0.008	-0.080	0.014	-0.092	0.009	1734
C	-0.087	0.017	-0.049	0.014	-0.091	0.021	-0.091	0.010	1725
D	-0.080	0.011	-0.029	0.011	-0.071	0.014	-0.086	0.012	1673
E	-0.229	0.010	-0.075	0.012	-0.095	0.018	-0.091	0.021	1428
F	0.027	0.006	-0.024	0.020	-0.017	0.023	-0.087	0.018	1947
G	-0.105	0.015	-0.039	0.012	-0.083	0.017	-0.060	0.019	1722
H	-0.116	0.021	-0.035	0.015	-0.062	0.021	-0.069	0.022	1650
I	-0.077	0.013	-0.032	0.011	-0.077	0.004	-0.057	0.011	1530
J	-0.179	0.010	-0.057	0.015	-0.109	0.021	-0.058	0.031	1304

**Comparison** To this end, as the UKIDSS system has already shown to be photometric, and as its  $J$ ,  $H$  and  $K_s$  bands have essentially already been calibrated using 2MASS (Hewett et al., 2006), we then finally calibrated the long and short exposures directly onto UKIDSS. As a check, the difference between the two calibration methods was calculated. Residual differences between the two calibration methods can be found in Table 3.4, excepting the  $Y$ -band for 2MASS.

Table 3.4: Comparison between the two calibration methods. Values are compared to the calibrated UKIDSS data, explaining the low UKIDSS differences, and the slightly larger 2MASS differences. Note the increasing difference with wavelength with the 2MASS data.

Field	$Y_{med}$	$Y_{\sigma}$	$J_{med}$	$J_{\sigma}$	$H_{med}$	$H_{\sigma}$	$K_{smed}$	$K_{s\sigma}$	
2MASS-	UKIDSS								
A	-	-	-	-0.018	0.033	0.034	0.042	0.031	0.034
B	-	-	-	0.004	0.023	0.023	0.026	0.030	0.012
C	-	-	-	0.013	0.016	0.043	0.016	0.043	0.011
D	-	-	-	-0.005	0.005	0.038	0.010	0.036	0.007
E	-	-	-	-0.007	0.028	0.001	0.019	0.038	0.016
F	-	-	-	0.017	0.046	0.003	0.030	0.029	0.025
G	-	-	-	0.018	0.023	0.023	0.031	0.050	0.020
H	-	-	-	0.076	0.026	0.025	0.017	0.002	0.031
I	-	-	-	0.034	0.013	0.020	0.008	0.023	0.009
J	-	-	-	-0.072	0.027	-0.049	0.005	0.015	0.006
Residual	UKIDSS								
A	Y	-0.001	0.014	<0.001	0.016	0.006	0.016	<0.001	0.022
B	Y	-0.009	0.012	<0.001	0.011	<0.001	0.013	-0.003	0.010
C	Y	<0.001	0.021	<0.001	0.017	<0.001	0.022	-0.001	0.009
D	Y	-0.009	0.014	-0.001	0.012	-0.001	0.015	-0.005	0.013
E	Y	-0.005	0.024	-0.001	0.012	<0.001	0.017	-0.006	0.022
F	Y	-0.005	0.013	0.004	0.021	<0.001	0.024	-0.007	0.021
G	Y	-0.007	0.014	-0.002	0.014	-0.002	0.018	-0.001	0.018
H	Y	-0.021	0.032	<0.001	0.016	<0.001	0.020	-0.011	0.022
I	Y	-0.003	0.015	-0.002	0.012	<0.001	0.010	-0.001	0.011
J	Y	-0.050	0.015	-0.061	0.017	-0.060	0.021	<0.001	0.030

An additional comparison was made between the BT models which had been convolved with the CFHT WIRCam system and those models convolved with the UKIDSS system, and is shown in Figure 3.7. It can be seen that the offsets are below 0.005 mag for the  $J - K_s$  colour range -1 to 1. This was necessary in order to see if any offsets needed to be applied to the models to bring them into line with the photometric catalogues, required for the candidate selection. The offsets were  $Y \leq +0.005$  mag,  $J \lesssim -0.0005$  and for  $H$  and  $K_s \lesssim 0.0005$ , resulting in no necessary calibration offsets to be added to the models.

**Interfield Calibration** The final step in the calibration pipeline is to check each cluster field against its adjoining fields and see which ones have large discrepancies. The control field had no such overlapping regions. There were naturally some small discrepancies between each field caused by the different observing conditions. The calibrated data was plotted in the standard set

of CMDs and it could be seen that for the CMDs that include the  $Y$ -band there is an offset with field J, shown in Figure 3.8. Thus, an interfield calibration must be performed taking each field and iteratively calculate the median difference. The central fields ABCD were found to have the smallest interfield offset, as expected. All of the short and long exposures of field J, for the  $Y$ ,  $J$  and  $H$ -bands were observed within the same observing program. The  $K_s$  was observed at a different time. Field J overlaps just two corners, one on field B and one on field D, as shown in Figure 2.5. The lower left corner of field D is of poor quality with large flagged regions from the poor response of the detector and missing pixels, and could be the cause of this offset compared to the other fields. Offsets that were needed to be applied to the  $Y$ ,  $J$  and  $H$ -bands were 0.038, 0.053 and 0.064 mag respectively.

**Control Fields** The control fields which lacked matching UKIDSS data which means they could not be calibrated directly onto UKIDSS as was the method with the other fields. Once the data has been found to be correctly calibrated, the  $J$ ,  $H$  and  $K_s$ -band fields could be calibrated onto 2MASS and then have the 2MASS-UKIDSS offset applied, listed in Table 3.4, to indirectly calibrate them onto UKIDSS. The  $Y$ -band was then calibrated by calculating the median offset value from the other 10  $Y$ -band cluster fields, and then applying the average of these medians to the  $Y$ -band data of control fields. Final control field calibration values are listed in Table 3.5.

Table 3.5: Median  $Y$ -band calibration values of C1 and C2 compared to median of other 10 fields; JHK from C1C2 onto 2MASS median difference, PLUS residual 2MASS-UKIDSS offsets.

Field	$Y_{med}$	$J_{med}$	$H_{med}$	$K_{smed}$
Short				
C1	-0.088	-0.054	-0.057	-0.035
C2	-0.088	-0.061	-0.059	-0.034
Long				
C1	-0.075	-0.037	-0.051	-0.035
C2	-0.075	-0.041	-0.044	-0.034

### 3.3.1 Short & Long Amalgamation

Two methods were used to amalgamate the  $Y$ ,  $J$ ,  $H$  and  $K_s$  data into a single, uniquely-populated catalogue. In the first instance the short and long catalogues were matched together to obtain a catalogue with the total number of duplicate objects, those objects appearing in both the short and long catalogues, and the total number of unique objects from both exposure sets. A flag was introduced here to describe the origin of each line in the new catalogue, from short or long, and unique or duplicate. The unique object amalgamation is trivial, whilst the duplicate can



be problematic. Initially, a string of either/or statements described each band to build a list of duplicate objects. These statements included the IMA flags, and the errors; if an object is saturated in the long then the corresponding object from the short catalogue was chosen; if the flags were identical then the entry with the lowest errors was selected. An unforeseen problem with this method is that if the data for an object was taken from both the long and short catalogues there then occurred a discontinuity in colour-space. Bright objects existed that had not been flagged as saturated in the IMA flag file because they fell within the non-linearity response region, mostly occurring for objects in the long exposures. Consequently a new set of flags were created as discussed, taken from the calibration CMDs to take these objects into account. These SAT flags and IMA flags were then used in conjunction to obtain the uniquely populated catalogues.

Duplicates still exist, however, in the overlaps between the fields but these will be either accepted or rejected as candidate members depending on the quality of the photometry. Further, those duplicates which both pass through to the final selection stage can then be accepted or rejected on a duplicate-by-duplicate basis, discussed in Section 3.4.3.

### 3.3.2 Completeness

Figure 3.9 shows the completeness and other diagnostic plots as a function of magnitude for field A for all four bands. The top panel is the completeness histogram where the limit can be seen when the number of objects begins to drop off, shown by the solid line. The middle panel shows the flux radius, and the bottom panel the photometric errors. Dotted lines show the saturation and completeness limits. Errors at this limit are  $<0.1$  mag. Final completeness limits are calculated in order to ascertain the depth of the survey and to see what mass objects the survey was sensitive to. Using the BT-Cond models the lowest detected mass could be as low as  $0.015 M_{\odot}$ , listed in Table 3.6.

Table 3.6: Average completeness magnitudes are shown over all cluster fields, as well as associated masses for both 30 and 40 Myr BT-Cond models. The depth of the  $K_s$ -band is less than the other three bands, where the  $Y$  is the deepest. The mass values hold for the  $Y$ ,  $J$  and  $H$  magnitudes.

Depth	$Y$	$J$	$H$	$K_s$	Mass	Model	$Y$	$J$	$H$	$K_s$
	/ mag	/ mag	/ mag	/ mag	Limit	Age / Myr	/ $M_{\odot}$	/ $M_{\odot}$	/ $M_{\odot}$	/ $M_{\odot}$
Short	19.00	18.25	17.50	18.50		30	0.0020	0.0200	0.0300	0.0150
Short	19.00	18.25	17.50	18.50		40	0.0030	0.0300	0.0400	0.0150
Long	21.00	20.50	19.75	18.50		30	0.0120	0.0120	0.0120	0.0150
Long	21.00	20.50	19.75	18.50		40	0.0120	0.0120	0.0120	0.0150

### 3.3.2.1 Previously Known Members

Four surveys were initially compared to the catalogues which have been discussed fully in the introduction to this chapter. Prosser (1993) had a catalogue with photometrically selected objects, which spawned a follow up paper, Prosser and Giampapa (1994), that focused on obtaining radial velocity data for 42 candidates of spectral types F5 to K0, which had both BVI and proper motion data from the previous paper. Of these 42 candidates, 20 were found to have velocities consistent with membership of  $\sim 13 \text{ km s}^{-1}$ . A more recent survey by de Wit et al. (2006) explored the lower mass function with again a photometrically selected sample of objects, 691 low mass stellar and 94 brown dwarf member candidates. Of these candidates, 265 were uniquely recovered from these 785 objects where the discrepancy is shown because of the fields of view of the comparative surveys was different. Of these recovered candidates, 224 had no IMA or SAT flags. Jeffries et al. (2009) selected sample objects from Cargile and James (2010) and present 40 candidate objects of which 30 should be within the central square degree of the cluster and have magnitudes less than  $V = 18 \text{ mag}$ . Of these objects, all objects are recovered in our sample, however 25 of the 48 matched objects are saturated, 8 are undetected in at least one of our photometric bands and none are otherwise fainter than  $J = 13.9 \text{ mag}$ .

Manzi et al. (2008) collated a sample of 147 objects where all 147 objects are recovered over our FOV. Of these 147, 124 are without flags. Additionally, they also confirm the membership of 39 objects from both radial velocity and or  $H\alpha$  data, down to a magnitude of  $I \sim 17.2 \text{ mag}$ , and of these objects, 32 have no IMA or SAT flags. Hence, the most useful set of sample objects for this work originate from Manzi et al. (2008), and so are plotted in the CMDs and COLDs for comparison to our CFHT selected objects. Objects were considered cluster members if they had a radial velocity of  $\sim -15 \text{ km s}^{-1}$ , or within  $3 \sigma$  of the cluster average  $\pm 8.7 \text{ km s}^{-1}$ .

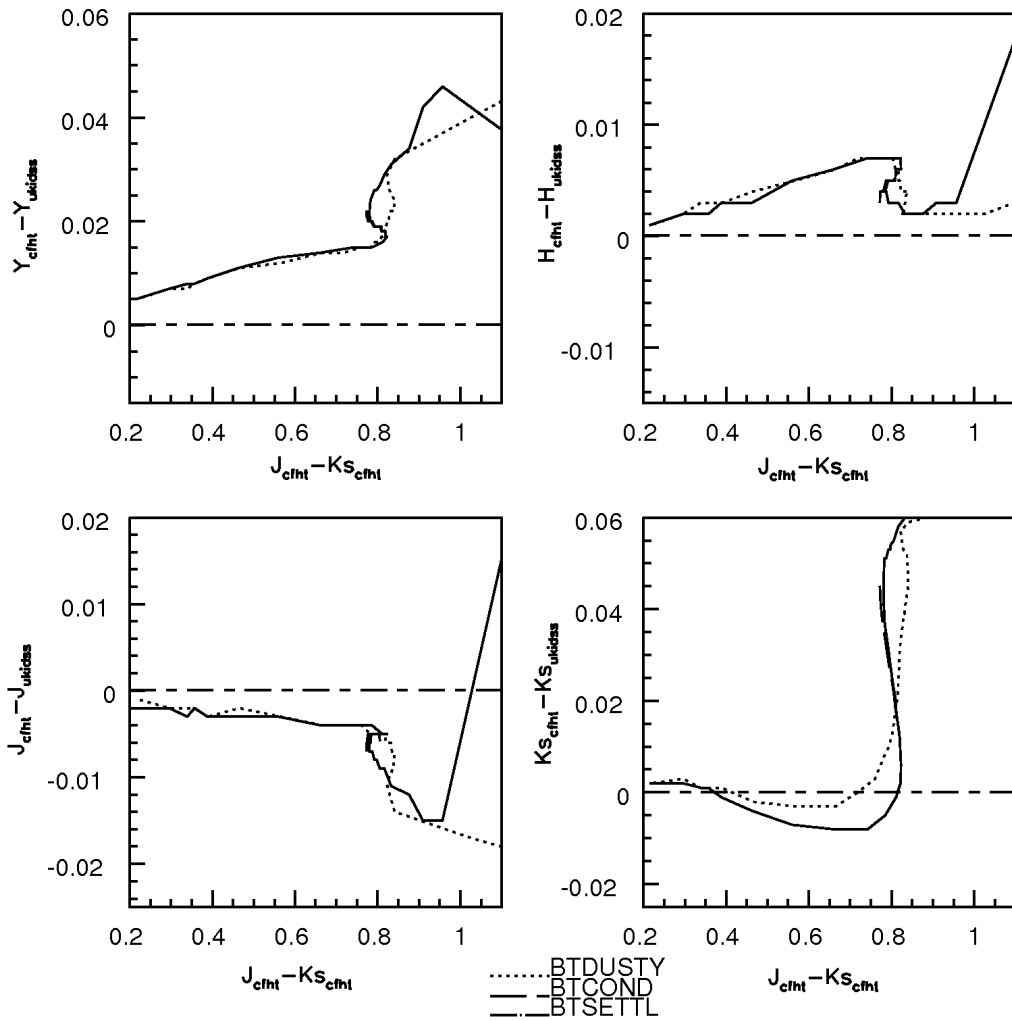


Figure 3.7: The models used in this work, which have been convolved with the WIRCcam detectors and the UKIDSS detectors at the Phoenix site, are compared. The offsets are negligible, and whilst the colour term takes over at  $J - K_s$  colours greater than 1 which does not affect the calibration values.

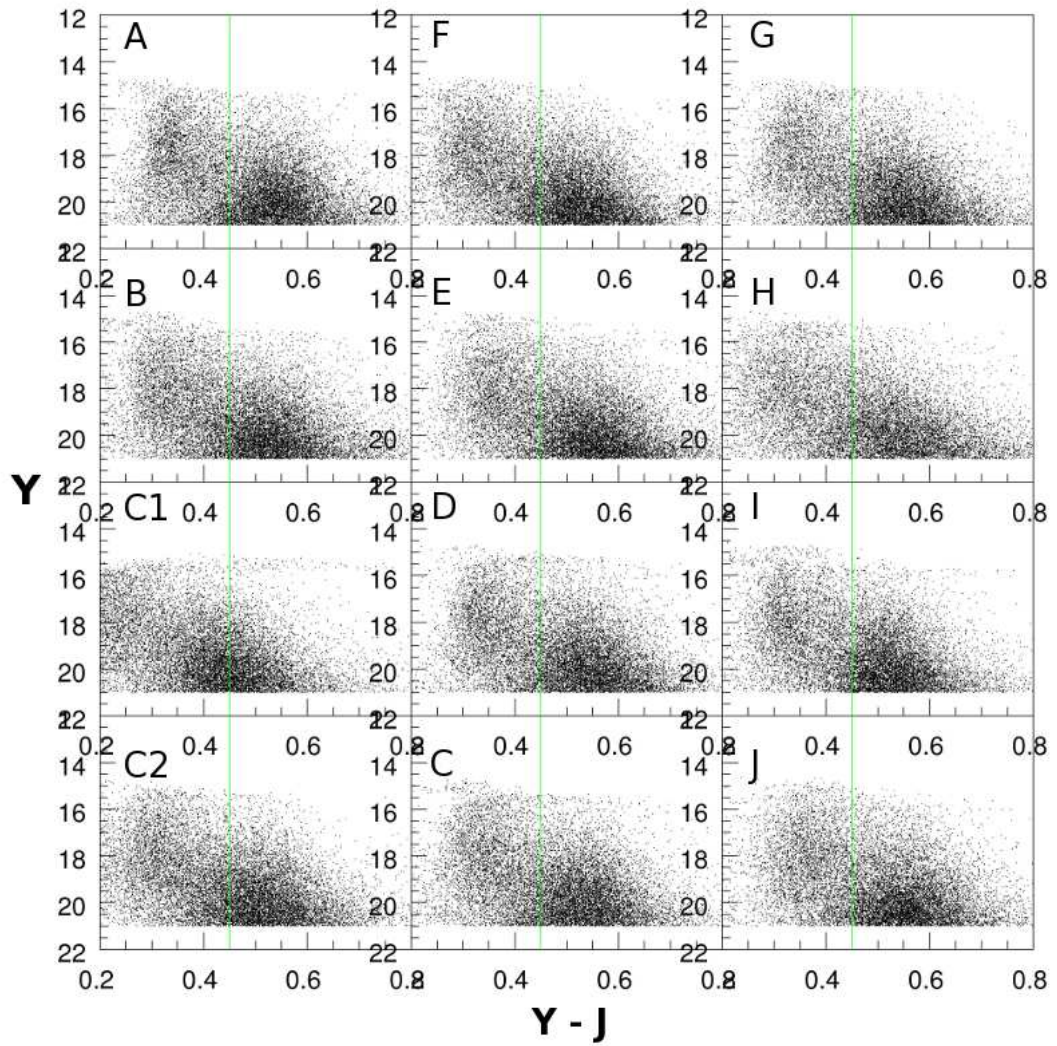


Figure 3.8: Real offset for the data in field J for the amalgamated Y-band. The offset is of the order 0.1 mag. Note that in these plots the control fields C1 and C2 are not calibrated.

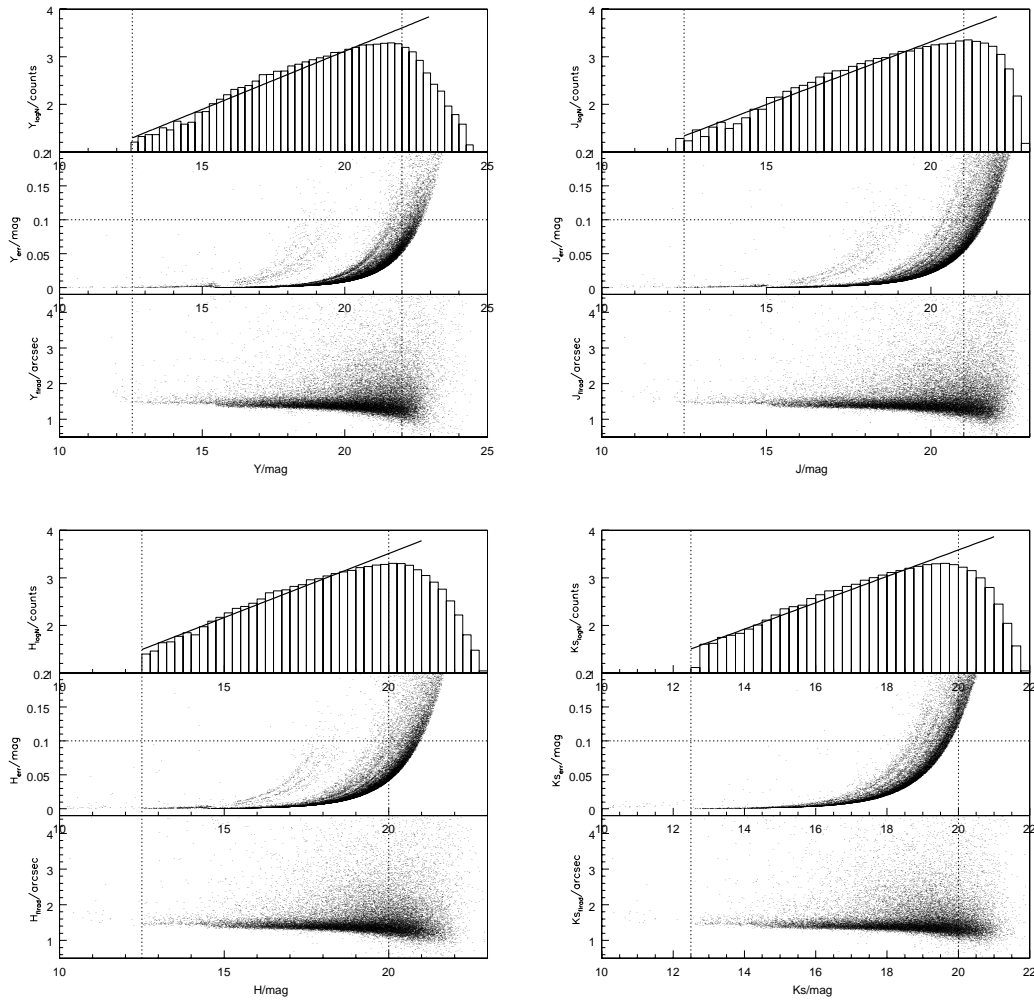


Figure 3.9: Diagnostic sample showing the completeness limit, rms error, and the flux radius, as a function of magnitude for the amalgamated short and long exposures. The solid line on the completeness plots is the least-squares fit to the data, where the dotted lines are the saturation and completeness limits. Here the data for field A and for all four bands is shown as an example.

### 3.4 Candidate Selection

CMDs and COLDs are used to select the candidates over the field of view. To this end a selection algorithm was adapted (C. Alves de Oliveira, priv. comm) in the form of an IDL routine, where the main selection criteria are located in the Appendix 5.5.

To be conservative because of the uncertainty in the age, all objects over the unfiltered catalogues were selected if they were redder than either the 30 and 50Myr BT-models. This selection was cumulative over the CMDs, such that only objects selected in all six permutations were then classed as preliminary candidates. Residual offsets for the  $YJHK$  calibration are on the order of a few 100dths of a magnitude on average so errors for the calibration are taken to be a conservative 0.05 mag. An additional error stems from the uncertainty in the distance, here  $\pm 15$  pc which corresponds to  $\sim 0.09$  mag. Both of these errors, on top of the photometric error associated with the uncalibrated data point, are taken into account when interpolating the model values for candidate selection. This is shown in Figure 3.10, where the central point, 0, takes the extracted value of from the calibrated data. Points 1-8 in the rectangle take into account the residual offset (in colour and magnitude space) or distance error (in magnitude space). If any part of this object's square 'footprint' falls within the ascribed range of the models then it is selected as a candidate.

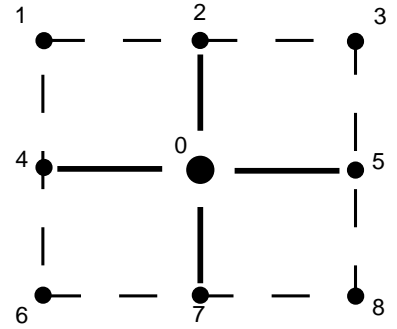


Figure 3.10: IDL selection criteria including the x and y axis error bars for each object in the input catalogue. An object is classed as a candidate if any part of this schematic is greater than the model in the CMD selection, or greater or less then for the COLD selection.

#### 3.4.1 Colour/Magnitude Diagram Selection

The first part of the candidate selection method require objects to be chosen using the theoretical models in the six permutations of the CMDs available. Initially each permutation had a candidate selection list, where the values for the  $Y$  vs  $Y - J$ ,  $Y - H$  and  $Y - K_s$ ;  $J$  vs  $J - H$ ,  $J - K_s$  and  $H$  vs  $H - K_s$  CMDs were 4,483, 10,842, 17,222, 140,538, 72,089 and 61,790 objects respectively. The fewest number of objects, 4483, are selected in the  $Y/Y - J_s$  permutation, clearly showing that this colour is the most powerful constraint in this candidate selection method. The  $J/J - H$  CMD was the least useful with more than 140,000 candidates selected over the ten fields. This was done on a field-by-field basis before being collated into a single catalogue with 2278 objects chosen

from all ten fields comprising 380,944 objects. These totals include duplicates from the overlaps between the fields. Figure 3.11 shows the objects taken from each step of the CMD selection for just two permutations,  $Y/Y - J$  and  $J/J - H$ , where they can be clearly seen to follow the path of the bluest-appearing model, which can be either the 30 or 50 Myr isochrone. 39 confirmed cluster members from Manzi et al. (2008) are plotted as well, where all 39 are present before the start of the candidate selection, but only 32 are included in the CMD-selected catalogue. 40 M- and 5 L-dwarfs from the Pleiades (Bihain et al., 2010) are plotted using UKIDSS data and adjusted for extinction and distance, along with the 120 Myr BT-Settl isochrone for comparison. It can be seen that the Pleiades sequence is generally fainter/brighter than the associated 120 Myr model for the  $Y$ -band, suggesting a possible problem with the models, especially with the  $Y$ -band. This could be attributed to the difference in the treatment of the interior compared to the exterior with respect to the new abundances in the new models.

### 3.4.2 Colour/Colour Diagram Selection

CMD candidate objects were re-accepted as COLD candidate members if they followed both the 30 and 50 Myr BT-Settl theoretical isochrones, in a similar manner to the CMD selection phase. In this analysis, however, the selection script required objects to be present, depending on errors, in a band around both of the 30 or 50 Myr isochrones. There are 15 permutations of colour/colour diagram for these four bands and to be a good candidate using this method they must adhere to the models over all permutations. 1173 unfiltered candidates were selected from this method. Figure 3.12 shows two examples of these COLDs with the final filtered selection of 608 objects overplotted. This filtering is discussed in Section 3.4.3. Black constraining boxes are the expected regions for M and L-dwarfs (marked) taken from the  $Y - J/J - H$  and  $J - H/H - K_s$  plots from Hewett et al. (2006). The full CMD-selected sample is also plotted for completeness.

### 3.4.3 Candidate Cleaning

Further candidate member catalogue treatment involved visually inspecting these candidate members, and removing those objects that were obviously giants, or have flags, poor PSFs, appear in defect detector regions, or which are simply spurious objects. This candidate member catalogue may still contain duplicates and these are accepted or rejected depending on similar criteria, flags, flux radius and if necessary comparing nearby regions on the image to ascertain the field that has a better local quality of data. For example, duplicate objects between field J and D would be chosen from field J, because the bottom left hand corner of the WIRCam detector had many holes and blank pixels in this region, as discussed before. Candidate objects must also have good photometry in all four bands. Finally, there are  $\sim 608$  preliminary candidate members, down from

2278 selected using the CMD selection criteria over all fields, and down from 1173 after the COLD exclusion phase. These 608 objects have no IMA or SAT flags and have flux radii  $< 5.0$  pixels. It can also be seen from Figures 3.11 & 3.12 that there are many objects with  $Y - J$  colours  $> 1.3$ , which also have associated magnitudes greater than  $Y \sim 21$  mag. This magnitude is below the completeness limit for even the  $Y$ -band, and the distribution of these objects in the  $J - H$  vs.  $Y - J$  plot also indicate their uncertainty in being good candidates. The same can be said for objects that have an  $H - K_s$  value  $> 0.85$  as these objects too fall outside of our completeness limit. 590 of these are not duplicated in other fields. Visual scrutiny of the images for candidate objects is not part of the pipeline but is handled by an *iraf* routine that allows each group of four images for IC 4665 to be viewed at the same time for full comparison using *imexamin*. 178 of these 590 unique candidates are well detected with a good PSF, surface contours and FWHM and in each of the four bands and were given the label ‘OK’ or ‘OK:diam\*’. To be more conservative 510 objects, listed in Table 3.7, passed the visual inspection where imperfections in one or more bands were kept, whilst objects which had imperfections in all bands were discarded, for example flat topped PSFs, non-Gaussian PSFs or extended emission in one or more bands.

Table 3.7: Sample final candidate list of the 510 objects that have passed the CMD, COLD, filtering and visual inspection analysis. The last four digits of the identifier in column two indicate the origin of the data for that object, either from the short and/or long exposure set. The full list can be found in the Appendix.

Field	Identifier	RA	DEC	Y / mag	Yerr / mag	J / mag	Jerr / mag	H / mag	Herr / mag	K / mag	Kerr / mag	Observation Note
D	168841111	266.46933	5.47968	20.131	0.141	18.974	0.141	18.327	0.141	17.818	0.142	OK:diam:faint
B	6280000	266.82553	5.31048	17.305	0.141	16.309	0.140	15.811	0.140	15.207	0.140	OK:diam:faintY
A	8280000	266.75516	5.65025	19.200	0.148	18.138	0.144	17.493	0.144	17.059	0.140	OK
...	...	...	...	...	...	...	...	...	...	...	...	...



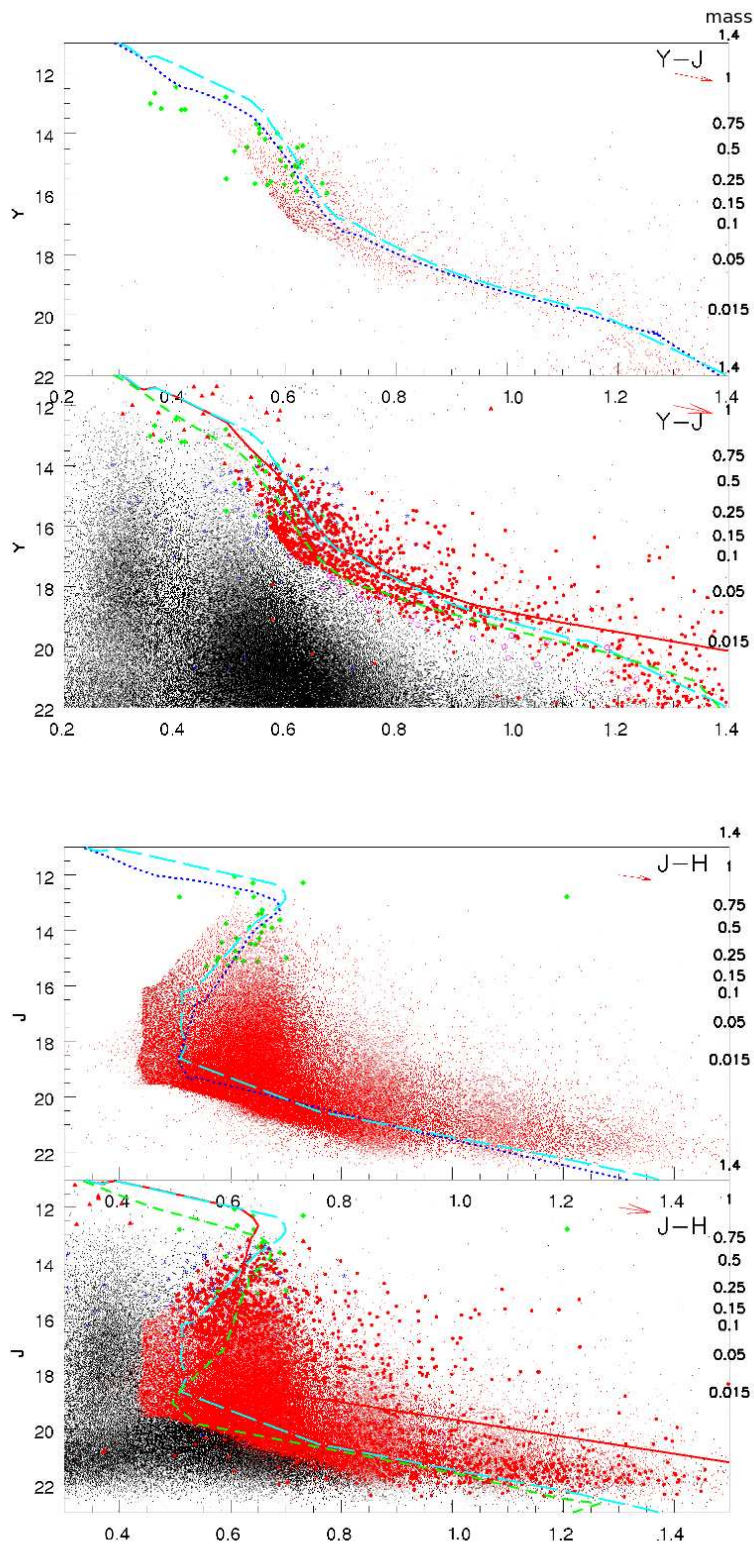


Figure 3.11: CMD candidate selection using the 30 and 50 Myr BT-Settl isochrones, plotted as dashed cyan and dotted blue lines respectively. The  $Y/Y - J$  top and  $J/J - H$  bottom CMDs are shown. *top level*: Objects selected from that particular CMD (red points) are plotted, along with the 39 confirmed cluster members from the Manzi et al. (2008) can be seen as green diamonds. *bottom level*: Similar to *top level* but where the full catalogue for one field (here, field G) is plotted (black dots) and the *final* candidate selection (red squares) which fulfil the selection conditions over all six variations of the CMDs for the four bands and all ten fields. The 100 Myr Pleiades sequence from Bihain et al. (2010) is also plotted (purple circles) and the associated 100 Myr BT-Settl isochrone for comparison. 2278 objects were selected from 380,944 amalgamated objects over all fields. Note that duplicates in the overlaps between the fields are included in these totals at this stage.

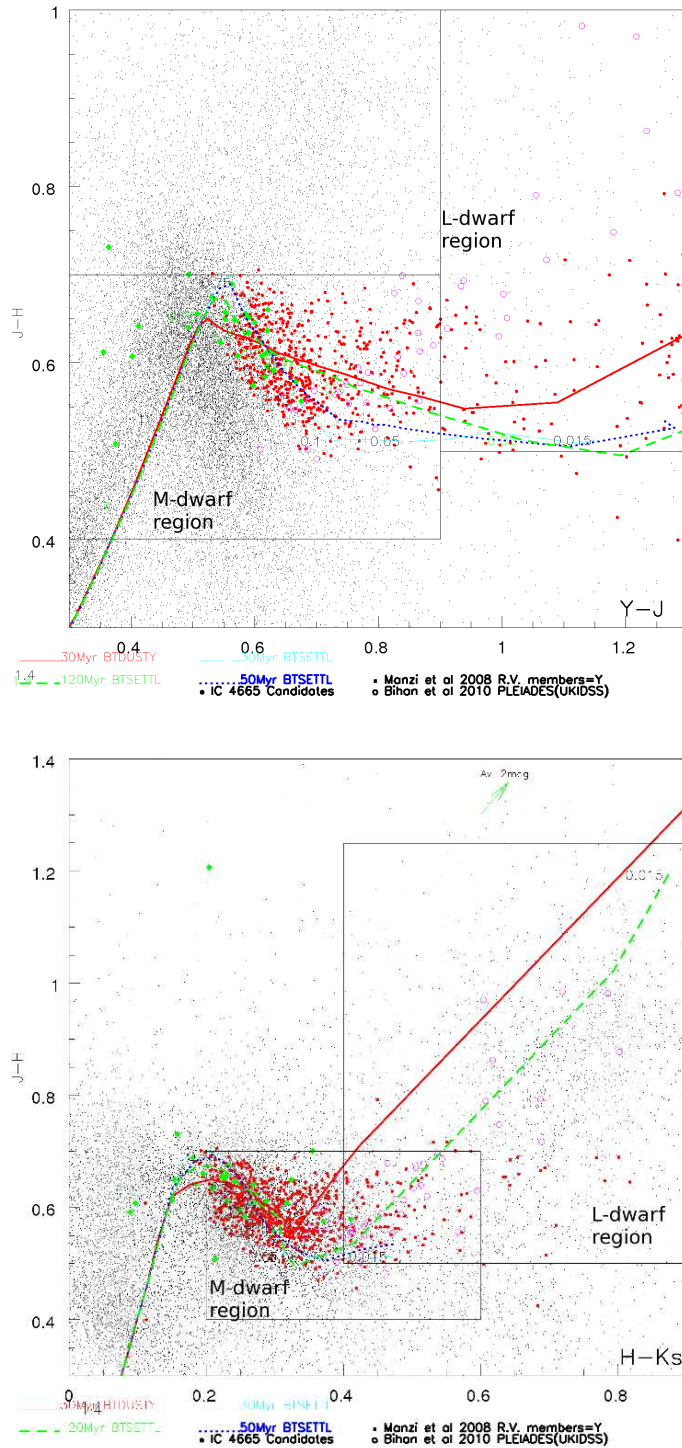


Figure 3.12: Similar to Figure 3.11, COLD candidate selection using the 30 and 50 Myr BT-Settl isochrones, plotted as dashed cyan and dotted blue lines respectively. The 39 confirmed cluster members from the Manzi et al. (2008) can be seen as green diamonds. The full catalogue for one field (here, field G) is plotted (black dots) for comparison, and the *final* 608 selected candidates *red squares* which fulfil the selection conditions over all 15 variations of the COLDs for the four bands and over all ten fields. The small green squares are the unselected COLD candidate members for comparison.

## 3.5 Discussion

In this section there is an outline of the confidence in the quality of these isochrone-selected candidate objects, what can be done with these 510 preliminary candidates, and associated possibilities for further and complimentary analysis.

### 3.5.1 Recovered Known Members

All 39 confirmed candidates from Manzi et al. (2008) were recovered in the unfiltered objects over all ten fields. Of these 32 objects had not IMA or SAT flags and were recovered in our pre-selected sample, whilst only 15 remain recovered at the end of the selection using theoretical models over all CMD and COLDs which selected 590 objects. Of these, just 13 remain in the sample of 510 visually inspected acceptable objects and are then plotted in the IR CMDs with the 30 and 50 Myr BT-Settl models for comparison as shown Figure 3.13. In the 178 heavily cleaned candidate list just 6 of the 32 were recovered. Further analysis could be conducted on other members from Jeffries et al. (2009) as an additional check and comparison.

If the candidate selection was done perfectly then is no reason why all 32 of 39 candidates could not be recovered in the sample of 590 objects, but as it is more than half of these are rejected from this methodology. There could also be another problem, which is that the selection itself is non-optimal, not least because the models are simply (yet thorough) approximations to reality.

### 3.5.2 Selection Considerations

The selection method appears to have some shortcomings related to how much the models can be trusted for this candidate selection. Specifically, the  $Y$ -band appears to be problematic for *at least* the 120 Myr BT-Settl model which fails to follow the Pleiades sequence, as seen in the  $Y/Y - J$  plot in Figure 3.11. The empirical sequence can be clearly seen as 1-2 mag fainter than the corresponding model in the  $Y/Y - J$ . The Pleiades data is in the UKIDSS photometric system, whilst our data is in the CFHT system, but zero-point calibrated to UKIDSS. The offsets for these two systems have been discussed as negligible and plotted in Section 3.3 and Figure 3.7, though colour differences greater than  $\sim 0.02$  mag do begin to appear for  $J - K_s$  colours  $> 0.8$  mag on average, and certainly for the  $Y$ -band. This small difference in the colour term, therefore, seems not to be the cause of this discrepancy. Further disparity occurs in the  $Y - J/J - H$  COLD where the models are approximately static between  $Y - J = 0.7$  and 1.2 mag. To this end, it seems to be also acceptable to select candidate members from empirical isochrones and not from the models. Indeed, it could be suggested that objects should be selected empirically and then tested against the models, instead of using the models and then comparing them against empirical sequences,

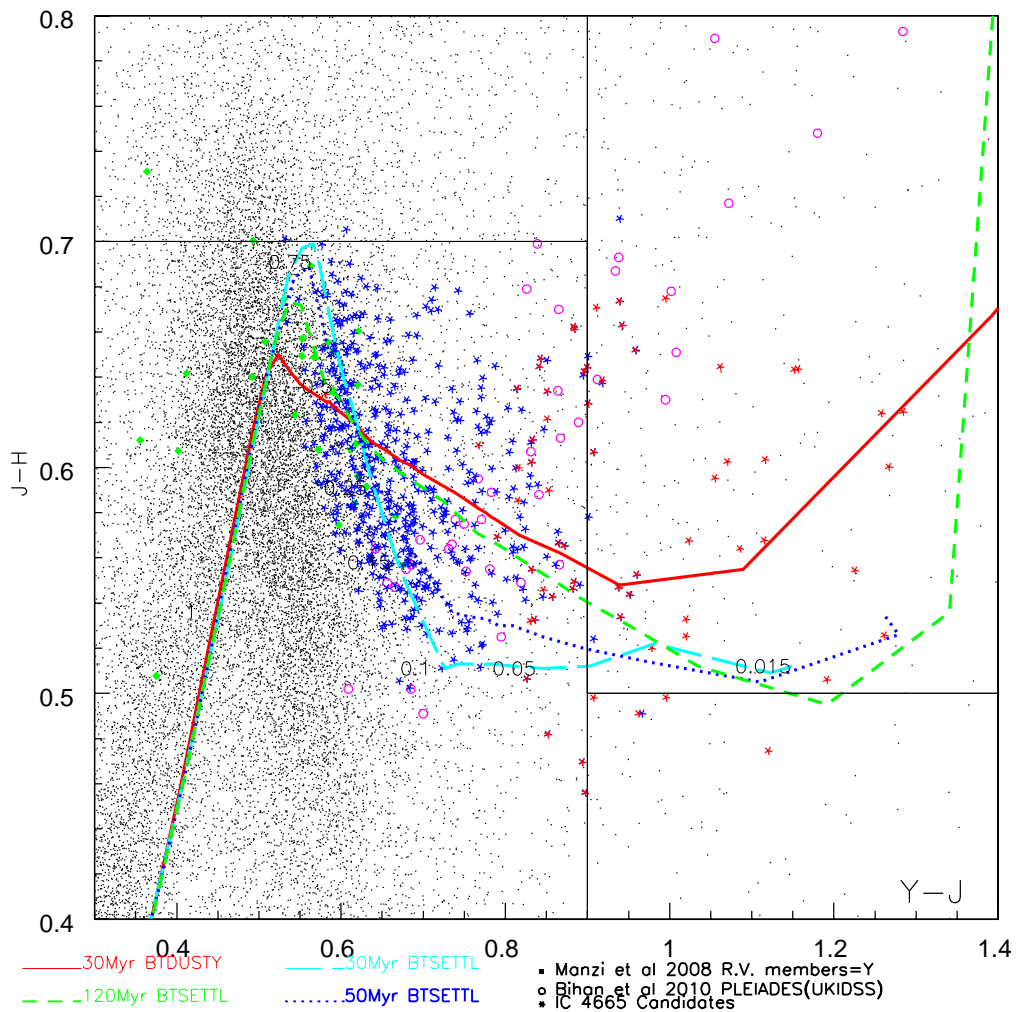


Figure 3.13:  $Y - J/J - H$  showing the location of the final selected candidates (as blue and red stars) split into L- and M-dwarfs selected empirically from Hewett et al. (2006), compared to the 30 and 50 Myr BT-Settl isochrones (as labelled). Other features as in Figure 3.12.

which is what this stage of work has achieved. A good test, then, would be to define a box around the empirical sequence from the Pleiades and to use this to extract objects from the CMDs. For the COLDs the same approach can be taken where an empirical region of the diagram can be marked, including errors, in order to select objects.

An additional possibility is to use empirical locations of the brown dwarfs, from the literature, in order to attempt to broadly classify members of this selection. It is possible to use the colours computed from the spectra of 15 M and 30 L-dwarfs selected by Hewett et al. (2006), their Figure 2. These boxes are superimposed onto the two COLD in Figure 3.12. This resulted in 63 L-dwarfs and 485 M-dwarf candidates for the 510 reasonable candidate objects. When compared to just the 178 ‘very good’ candidate list there appear just 3 L-dwarfs and 164 M-dwarf candidates

with 12 candidates being either a M- or a L-dwarf. This duplication is due to borderline objects that were selected by the criteria defined by both of the two empirical boxes. The observations were sensitive down to  $\sim 15 M_J$  which concurs with around the L3 spectral type for a 40 Myr brown dwarf.

### 3.5.2.1 Y-band Considerations

It can be seen that most important selector in this work is the  $Y$  band which greatly reduced the number of objects, however, this also was the band that had the largest spread of median values across the ten fields of  $\pm 0.33$  mag, though the dispersion was similar to the other  $J$ ,  $H$  and  $K_s$ -bands.

Whilst the final candidate list presented here made great use of this band there are also other problems involved with the selection criteria. It can be seen from Figure 3.11 that the Pleiades empirical sequence does not follow the 120 Myr BT-Settl isochrone in the  $Y - J$  colour space whilst it does in the  $H - K_s$  colour space. This suggests that the models are incomplete, at least in the  $Y$ -band part of the theoretical spectra used to compute the isochrones. This could be tested further by conducting the CMD and COLD selection analysis using the 120 Myr isochrones, and using just the  $J$ ,  $H$  and  $K_s$ -bands, before seeing how many of these objects fall in line with the empirical sequence. It would be hard to compare the current selection because a lot of objects have been removed when using the  $Y$ -band.

In fact, the  $Y$ -band is greatly affected by telluric lines, as discussed by the recent paper regarding the BT-models by Allard et al. (2010) (their Figure 2), meaning that the BT-model which was used for the selection *had not yet* had an additional calibration adjustment included to take this extra absorption into account, to close the gap between the model and the observations. The presence of strong atmospheric absorption could explain some of the large calibration differences found over the 12 fields if they were certainly dependent on the proportion and turbulence of water vapour in the atmosphere at the time of the observations. It should also explain why the  $Y$ -band is the strongest filter used in the selection process.

### 3.5.3 Contamination

The low extinction of this cluster means that it is relatively hard to ascertain membership based on having a high extinction levels, as is possible for younger or more compact and dusty star-forming regions. It is possible to estimate the population of field objects lying in the foreground of the cluster, but the clearest is a purely statistical stance where control fields are used to estimate the distribution and population of stars on regions of the sky away from IC 4665. The number of

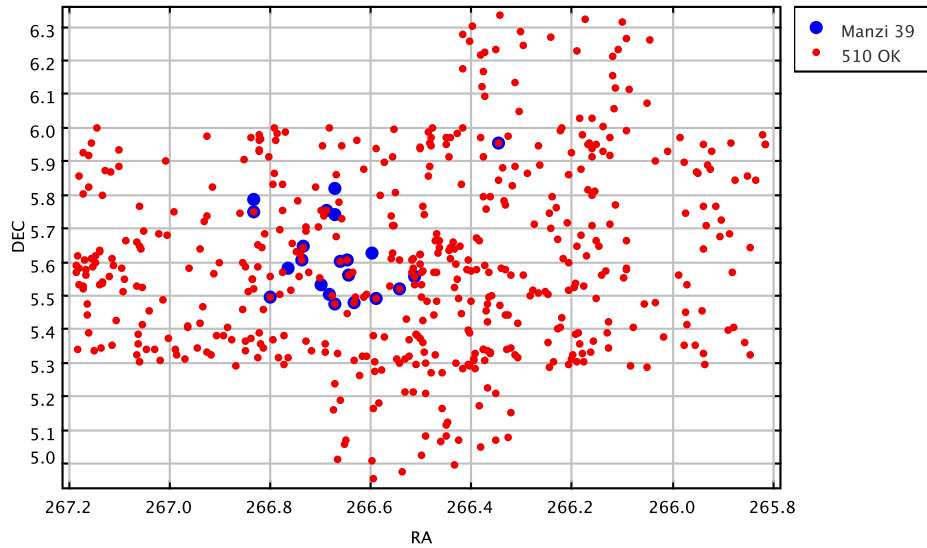


Figure 3.14: Distribution of 510 unique and good selected candidates over the FOV of the IC 4665 observation (filled red circles), and the 39 Manzi et al. (2008) candidates as large filled blue circles. 15/39 candidates were reselected from the 590 selection, down from 32/39 after the CMD selection, and 13/39 members recovered after visual inspection.

objects that were detected in control fields C1 and C2, after the CMD selection were 122 and 97 respectively, whilst there were 61 and 60 objects detected after both the CMD and COLD selection methods, and 28 and 33 respectively after filtering and cleaning. 23 and 29 objects were present in these fields after visual inspection. The location of the candidates over all ten fields is shown in 3.14 in sexagesimal J2000 coordinates, and with the full 39 Manzi et al. (2008) members. 13 of these 39 members were recovered after visual inspection and filtering out of bad candidates. An additional complication is that IC 4665 is very much centred on fields A, B, C and D so it is expected that these fields have proportionally more cluster members than fields E, F, G, H, I and J, when compared to the confirmed Manzi et al. (2008) cluster members. It is worth treating these two sets of fields separately with respect to the control field contamination estimates as the contamination here will be lower compared to the surrounding fields. A good method to estimate the contamination of non-cluster objects within our fields would be to add together and multiply by 5 the number of objects detected in the control fields to have a broad idea of the contamination within this cluster. From the aforementioned values this value is 110, so broadly speaking  $\sim 110$  of our 510 objects will have a high probability of being either foreground or background objects and not cluster members. The trick is to work out which objects within the candidate list these objects could be. A method of doing this is by assuming that the majority of contaminants when observing towards an open cluster lie behind the cluster, this means that they should be fainter on

average than the cluster members. It is then possible to plot the number of these control objects against magnitude and compare them to the selected candidates (Muench et al., 2002).

### 3.6 Summary

The young open cluster IC 4665 was the target of an observing program that took short and long exposures over 10 fields around the cluster centre and of 2 control fields held off-centre. These two sets of exposures consisted of  $Y$ ,  $J$ ,  $H$  and  $K_s$  broadband photometry which was taken by the WIRCam on the CFHT. Detection and analysis parameters of SExtractor and PSFEx were then tested and optimised to extract this data, where various filters, background estimation, aperture sizes, and PSF models were created in order to accurately detect and refine the data. The  $J$ -band image was used as a detection image to be sure that each object had a chance of having data in each of these four bands which was a requirement for cluster membership.

A pipeline was developed which took the input images and a few tables of input parameters to analyse and extract the images. This output was then tested against 2MASS and UKIDSS data in order to check the quality of the data. Calibration was then performed by zero-point calibrating to the UKIDSS photometric system before amalgamating the long and short exposures together. Interfield calibration was then performed so that each field can be treated identically.

A candidate was kept if it fulfilled the selection criteria with respect to the BT-Settl 30 and 50 Myr isochrones in both the CMD and COLD selection phase, and if its magnitude is at or above the completeness limit in all four photometric bands. These objects were visually inspected to determine the status of the object on each image, where the more definite candidates were further selected using empirical colour selection criteria in the  $Y - J$ ,  $J - H$  and  $H - K_s$  colour space. Vigorous cleaning using completeness limits, flux radii and assigned flags reduced the total number of objects from 1173 to 608 after the COLD selection phase. Of these 608, 18 objects were duplicated (with in  $1''$ ) in the overlaps between the images, and 80 of the remaining objects were rejected from visual inspection, which accounted for 13.5% of the total number of objects. This data was then tabulated in Table 3.7, where the final candidate list held a possible 485 M-dwarfs and 63 L-dwarfs from empirical colour constraints. Vigorous rejection of all but the perfect objects in the field of view reduces this figure to just 178 objects ('OK' and 'OK:diam') but with only 6 confirmed members from Manzi et al. (2008) being present.

### 3.7 Résumé

Le amas ouvert jeune IC 4665 a été la cible d'un programme d'observation qui a eu une exposition court et longue de plus de 10 champs dans le centre de l'amas et de 2 champs de contrle lieu décentré. Ces deux séries d'expositions se composait de  $Y$ ,  $J$ ,  $H$  et  $K_s$  photométrie à large bande qui a été prise par le WIRCam sur le CFHT. paramètres de détection et d'analyse des SExtractor et PSFEx ont ensuite été testées et ont optimisées pour extraire ces données, où les différents filtres, estimation du fond, des tailles d'ouverture, et les modèles de PSF ont été créés afin de détecter avec précision et d'affiner les données. La bande- $J$  de l'image a été utilisée comme une image de détection pour être sr que chaque objet avait une chance de disposer de données dans chacun de ces quatre bandes qui était une condition pour être membre du cluster.

Un pipeline a été élaboré qui a pris des images d'entrée et quelques tables de paramètres d'entrée pour analyser et extraire les images. Cette sortie a ensuite été testé contre 2MASS et les données UKIDSS afin de vérifier la qualité des données. L'étalonnage a été ensuite réalisée par étalonnage du point zéro de la UKIDSS système photométrique avant la fusion des expositions à long et à court ensemble. Calibration inter-champs a ensuite été effectuée de telle sorte que chaque champ peut être traités de façon identique.

Un candidat a été conservée si elle satisfait aux critères de sélection à l'égard des isochrones BT-Settl 30 et 50 Myr dans les CMD et la phase de sélection COLD, et si sa magnitude est égale ou supérieure à la limite de l'exhaustivité dans les quatre bandes photométriques. Ces objets ont été inspectés visuellement pour déterminer le statut de l'objet sur chaque image, où les candidats ont été encore plus précis sélectionnés à l'aide des critères de sélection empirique de couleur dans le  $Y - J$ ,  $J - H$  et  $H - K_s$  espace de couleur. Nettoyage vigoureux utilisant des limites de l'exhaustivité, les rayons de flux et les indicateurs attribués réduit le nombre total d'objets de 1173 à 608 après la phase de sélection FROID. Parmi ces 608, 18 objets ont été dupliqués (en 1 arcsec) dans les chevauchements entre les images, et 80 des objets restants ont été rejetés de l'inspection visuelle, qui représentaient 13,5 % du nombre totale d'objets. Ces données ont été ensuite présentés dans le tableau 3.7, où la liste finale des candidats a tenu une possible 485 M-nains et 63 L-nains de couleur contraintes empiriques. rejet vigoureux de tous les objets, mais parfait dans le champ de vision réduit ce chiffre à un peu 178 objets (OK et OK:diam\*) mais avec seulement 6 membres ont confirmé à partir de Manzi et al. (2008) être présent.





# Chapter 4

## Young T-dwarf Candidates in IC 348

### Contents

---

<b>4.1</b>	<b>Introduction &amp; Context</b> . . . . .	<b>99</b>
4.1.1	Searching for T-dwarfs . . . . .	100
4.1.2	The Young Star-Forming Region IC 348 . . . . .	101
<b>4.2</b>	<b>Specific Data Treatment</b> . . . . .	<b>103</b>
4.2.1	Photometric Catalogue . . . . .	104
4.2.2	Photometric Comparison . . . . .	104
4.2.3	Methane Photometry . . . . .	106
<b>4.3</b>	<b>Results</b> . . . . .	<b>109</b>
4.3.1	T-dwarf Candidate Selection . . . . .	109
4.3.2	Reddening & Spectral Type Estimates . . . . .	111
<b>4.4</b>	<b>Discussion</b> . . . . .	<b>112</b>
4.4.1	Membership . . . . .	112
4.4.2	Contaminants . . . . .	114
4.4.3	Comparison of IC348_CH4_2 with S Ori 70 . . . . .	115
4.4.4	The Lower End of the IMF . . . . .	119
<b>4.5</b>	<b>Conclusions</b> . . . . .	<b>120</b>
<b>4.6</b>	<b>Résumé</b> . . . . .	<b>121</b>

---

### 4.1 Introduction & Context

The vast majority of detected brown dwarfs are old (3-6 Gyr) field dwarfs (Faherty et al., 2009), having cooled over time. The importance of discovering and cataloguing the lowest mass objects

is necessary in determining the full IMF, and is critical in furthering our understanding of the low-mass end of stellar evolution. Star-forming regions are well suited to search for the lowest mass brown dwarfs. Young objects are hottest and brightest immediately after formation as they are simply not massive enough to begin or sustain fusion via hydrogen or deuterium synthesis so their temperature decreases from their peak as they radiate their original thermal energy away over time. This proves difficult when searching for the lowest mass objects in the field, as detected T-dwarfs in the field have masses much greater than in star forming regions and they have had billions of years to cool below  $\sim 1300$  K. This extra mass also complicates their cooling rate, and the age estimate as they are heavier than the deuterium fusion limit so it is uncertain how much extra heat energy has been made available through this mechanism to slow the decrease in temperature from formation.

T-dwarfs are also referred to as methane dwarfs, stemming from the change in the atmospheric properties, specifically the increased formation of methane and the cloud clearing of dust occurring at an effective temperature of around 1300 K which allows the methane to be observed more readily in the H and  $K_s$  bands. This is usually termed as the L – T transition - the transition between L-dwarfs and T-dwarfs as a spectral type. Consequently methane can both form more readily in the atmosphere, and can be detected from its absorption effect in the spectrum. Spectroscopic or narrowband photometry have both been used to not only classify, but also detect T-dwarfs in star-forming regions and in the field, based on atmospheric absorption of methane.

This chapter chronicles the search for the lowest mass objects in the star-forming region IC 348 using the WIRCam narrowband filters  $\text{CH}_4$  ‘off’ and ‘on’ at 1.58 and 1.69  $\mu\text{m}$  respectively. These methane-selected detections are supported by MegaCam  $z'$  and WIRCam  $J$ ,  $H$  and  $K_s$  broadband data. The data extraction method has been discussed in Section 2.3 though specific results, for example aperture sizes and filter are discussed here. *Spitzer* data, membership, contamination and the log-normal and power-law IMFs are then discussed. The article on this chapter was accepted on the 21st August 2009 before being published in the *Astronomy and Astrophysics Highlights*, Volume 508, Issue 2, pp.823-831 in December 2009.

#### 4.1.1 Searching for T-dwarfs

To date, there have been a good set of surveys with respect to searching for field T-dwarfs using methane data, either from large scale surveys with follow-up spectroscopy or observations of specific regions, namely star-forming regions. Burgasser et al. (1999), for example, searched the 2MASS data for field brown dwarfs using two data releases and filtering for known ranges of brown dwarf colours, and a good signal-to-noise ratio. The obtained NIR, 1.4–2.4  $\mu\text{m}$  spectra using the Keck telescope and compared their objects with the spectrum of Gliese 299B. They confirm five objects as T-dwarfs from their 1.6 and 2.2  $\mu\text{m}$   $\text{CH}_4$  absorption bands, which become

apparent at  $\sim 1300$  K. They also confirm that their temperatures are greater than 950 K and that they are consistent with the space density for T-dwarfs from Kirkpatrick et al. (1999), with an upper limit of 0.01 T-dwarfs  $\text{pc}^{-3}$ . Other lowest-mass-focussed surveys, aimed at usually young star forming regions, have turned up just one young T-dwarf with confirmed spectroscopy, S Ori 70 by Zapatero Osorio et al. (2002) in  $\sigma$  Orionis (1-8 Myr). Since its discovery there has been some contention as to the authenticity of the objects, where in fact it could have been an old foreground field dwarf in the line of sight (Burgasser et al., 2004) rather than a young cluster object (Martín, 2004). Further proper motion and follow-up membership work has confirmed its authenticity as one of the lowest mass objects found in a star forming region at 2-7  $M_J$ . The most recent data using IR and *Spitzer* data to confirm its existence and membership of  $\sigma$  Orionis (Zapatero Osorio et al., 2008).

#### 4.1.2 The Young Star-Forming Region IC 348

IC 348 is a region of continuing star formation (Tafalla et al., 2006), resulting in the opportunity to see the youngest members, however these may not necessarily be the lowest-mass members. There is evidence of clumps (Bachiller et al., 1987) and disks (Luhman et al., 2005a), where around  $50\% \pm 6\%$  of detected objects from a *Spitzer* survey by Lada et al. (2006), of spectral types later than K6, peaking at  $47\% \pm 12\%$  for K6-M2 stars. A composite image of IC 348 is shown in Figure 4.1 where its spectacular reflection nebula, illuminated by the brightest objects in the cluster can be seen.

**of Pioneering Surveys** Recent broadband surveys of IC 348 have been conducted by various groups ranging from *Chandra* X-ray observations (Stelzer et al., 2009), through the optical using the *Hubble Space Telescope* (Najita et al., 2000; Luhman et al., 2005c), other optical surveys (Cernis, 1993; Herbig, 1998; Luhman et al., 2003), then further into the near-IR (Lada and Lada, 1995; Luhman, 1999; Preibisch et al., 2003), *Spitzer* mid-IR (Lada et al., 2006; Cieza and Baliber, 2006; Muench et al., 2007; Muzerolle et al., 2010) and the sub-mm continuum (Tafalla et al., 2006). Spectroscopic follow-up surveys have been conducted by Liu et al. (2003); Muench et al. (2003); Luhman et al. (2005b) of candidate young brown dwarfs and other low-mass cluster members.

A narrowband survey of IC 348 was conducted by Mainzer and McLean (2003) who used the Lick observatory and the 1-5  $\mu\text{m}$  First Light Camera for SOFIA (FLITECAM) to observe two custom narrowband  $\text{H}_2\text{O}$  and  $\text{CH}_4$  filters at 1.495  $\mu\text{m}$  and 1.66  $\mu\text{m}$  respectively. They used further  $J$ ,  $H$  and  $K_s$ , achieving a depth of  $H \sim 19.5$  mag, to filter out the lower mass T-dwarfs from the L-dwarfs, by their  $H - \text{CH}_4$  and  $\text{H}_2\text{O} - \text{CH}_4$  colour differences. They found 12-15 candidates



Figure 4.1: A composite image of IC 348 using  $J$ ,  $H$ , and  $K_s$  band data. Image produced by Adam Block and Tim Puckett.

which could be late M, L or T-dwarfs, with masses  $\geq 5 M_{Jup}$ , although none have been confirmed spectroscopically because of their faint nature.

**of Age & Distance** IC 348 is a young star-forming region towards the direction of Perseus, centred at (J2000)  $03^{\text{h}}44^{\text{m}}34^{\text{s}}$ ,  $+32^{\circ}09'8''$ , and embedded in the foreground part of the Per OB2 association. The age of IC 348 has been determined to be  $\sim 1\text{--}3$  Myr (Muench et al., 2003). Star-forming regions generally have high levels compared to open clusters because of the presence of the necessary dust and gas. IC 348 is relatively nearby, has a low cluster proper motion, and is held to be an ideal system in which to observe young brown dwarfs and constrain the lowest mass end of the IMF. Controversy surrounds its distance, though IC 348 is generally held to be located between  $261^{+27}_{-23}$  pc (Scholz et al., 1999) and 316 pc (Herbig, 1998) from the Solar System, whilst the OB Per association, of which IC 348 is a member, is taken to be between 315 pc (Luhman

et al., 2003) and 340 pc (Cernis, 1993). An average value of 300 ( $\pm 15$  pc) has been used for this work in line with the review by Herbst (2008).

**of Membership** IC 348 is a dense star-forming region and is young enough where the dynamical interactions means that not a great many objects should have been ejected. This region is very dense and it is thought that there are more than  $\sim 420$  cluster objects (Muench et al., 2007) constrained within a halo radius of about  $10'$ , but no more than  $15'$  (Herbig, 1998). The core radius is taken to be  $\sim 4'$ . Extinction maps for IC 348, ranging from  $\sim 2 < A_V < 20$  mag depending on the cluster region, were derived by Cernis (1993), Muench et al. (2003), and Cambr esy et al. (2006). Its low proper motion also indicates a cohesive structure.

**of IMF** Muench et al. (2003) derived the IMF of IC 348 complete down to  $35 M_{Jup}$  (for  $A_v < 4$  mag) and found it to be similar to the IMF of the Trapezium cluster, having a mode between  $0.1-0.2 M_{\odot}$ . Approximately 15-25% of the population of the cluster appear to be brown dwarfs and their spatial density is independent of the distance from the cluster centre. The lowest mass objects were not detected in their work because of the detection limits.

## 4.2 Specific Data Treatment

The data was treated as laid out in the pipeline in Chapter 2, where the data images were visually checked for obvious defects, then the aperture size were optimised to a grid of 51 pixels, before being handled by SExtractor and PSFEx. As with IC 4665, one image was used for detection whilst the analysis was done on each image in turn. As late-type T-dwarfs may remain undetected in the  $CH_4$ on image, and due to strong  $CH_4$  absorption, object detection was performed at  $3.5\sigma$  on the  $CH_4$ off image, where PSF photometry was then performed at the location of these objects on both the  $CH_4$ off and  $CH_4$ on images. This ensured that all objects that could possibly be T-dwarfs are searched for in both filters, rather than obtaining undetections in the  $CH_4$ on that could be due to  $CH_4$  absorption. IC 348 is a nebulous region which is a consequence of its youth, and as such there were many false detections. In most cases this would have been most problematic if galaxies were important, as by their nature most of the nebulosities would not have nice PSFs but rather flatter or more elongated PSFs which could then be rejected through their flux radius or  $\chi^2$  values. The background level estimation was tested in the same manner to IC 4665 and were found to use 128 and 5 for the 'BACK\_SIZE' and 'BACK\_FILTERSIZE' respectively, whilst the detection threshold seemed to strike the best balance between too many nebulous detections and too few stellar detections at  $3.5 \sigma$ , using the gauss\_3.0\_5x5 filter. An example commandline entry is: `sex IC348.H.long.fits -c prepsfex.H.sex -CATALOG_NAME prepsfex.H.fits`

```
psfex prepsfex_H.fits -c psfex1_Hlong.psfex -PSF_NAME H_psf_6.psf -GROUP_DEGREES 6 sex IC348_CH4Off.fits
IC348_H_long.fits -c postpsfex_H.sex -CATALOG_NAME postpsfex_H_6_1.0.cat -PSF_NAME H_psf_6.psf
```

### 4.2.1 Photometric Catalogue

Each waveband had a catalogue created which was then collated and cleaned of saturated objects, obvious artefacts, and a fraction of extended sources identified from their large PSF FWHM. An approximation of the completeness of the photometric catalogues was estimated from  $\log(N_{obj})$  vs. magnitude histograms, where  $N_{obj}$  is the number of stellar-like objects detected on the images. We thus derived completeness limits from Figure 4.2 (*top*) of  $\sim 23.5$  ( $z'$ ), 21.5 ( $J$ ), 20.0 ( $H$ ), 18.9 ( $K_s$ ), 20.3 ( $CH_4on$ ), and 20.7 ( $CH_4off$ ). SExtractor photometric errors for each of the six bands are plotted in Figure 4.2 (*bottom*), highlighting the increasing photometric error for the faintening of the objects' brightness. Uniquely, the  $CH_4off$  error terminates at 0.06 magnitudes as the  $CH_4off$  image was used for the detection of objects over all bands, discussed in Section 4.2.

### 4.2.2 Photometric Comparison

Further analysis was conducted using publicly-available 2MASS data for those detected objects that were bright enough to have a 2MASS counterpart. This was useful for two reasons: firstly that the photometric accuracy and pipeline reduction of the WIRCam images could be compared with those from 2MASS; and secondly that the difference in the photometric systems could be estimated from the photometric differences between the CFHT and 2MASS. The extracted  $J$ ,  $H$  and  $K_s$  catalogues were matched with the  $J$ ,  $H$  and  $K_s$  2MASS catalogues resulting in 206 stars that had overlapping magnitudes. Based on these, the dispersion between the extracted  $J$ ,  $H$  and  $K_s$  catalogues and the 2MASS  $J$ ,  $H$  and  $K_s$  catalogues was calculated. Good agreement was shown by mean magnitude differences of  $0.08 \pm 0.02$ ,  $0.03 \pm 0.05$ , and  $0.04 \pm 0.02$  for  $J$ ,  $H$  and  $K_s$  respectively. These values hold for the brightest stars in our images, since fainter ones are undetected in the 2MASS survey. In turn, this means that colour effects arising from CFHT filters are not taken into account in this calibration. Indeed, while the photometric zero-point used here is obtained from 2MASS, colour effects are not corrected for and our WIRCam  $J$ ,  $H$ ,  $K_s$ ,  $CH_4on$  and  $CH_4off$  photometry is given in the CFHT Vega system and MegaCam  $z'$  in the AB system. These colour effects should be negligible ( $< 0.05\text{mag}$ ) for colours up to  $J - K_s \sim 1$  mag, but increase above this level, thought colours should be systematically different for old (field) and young (star-forming) objects.

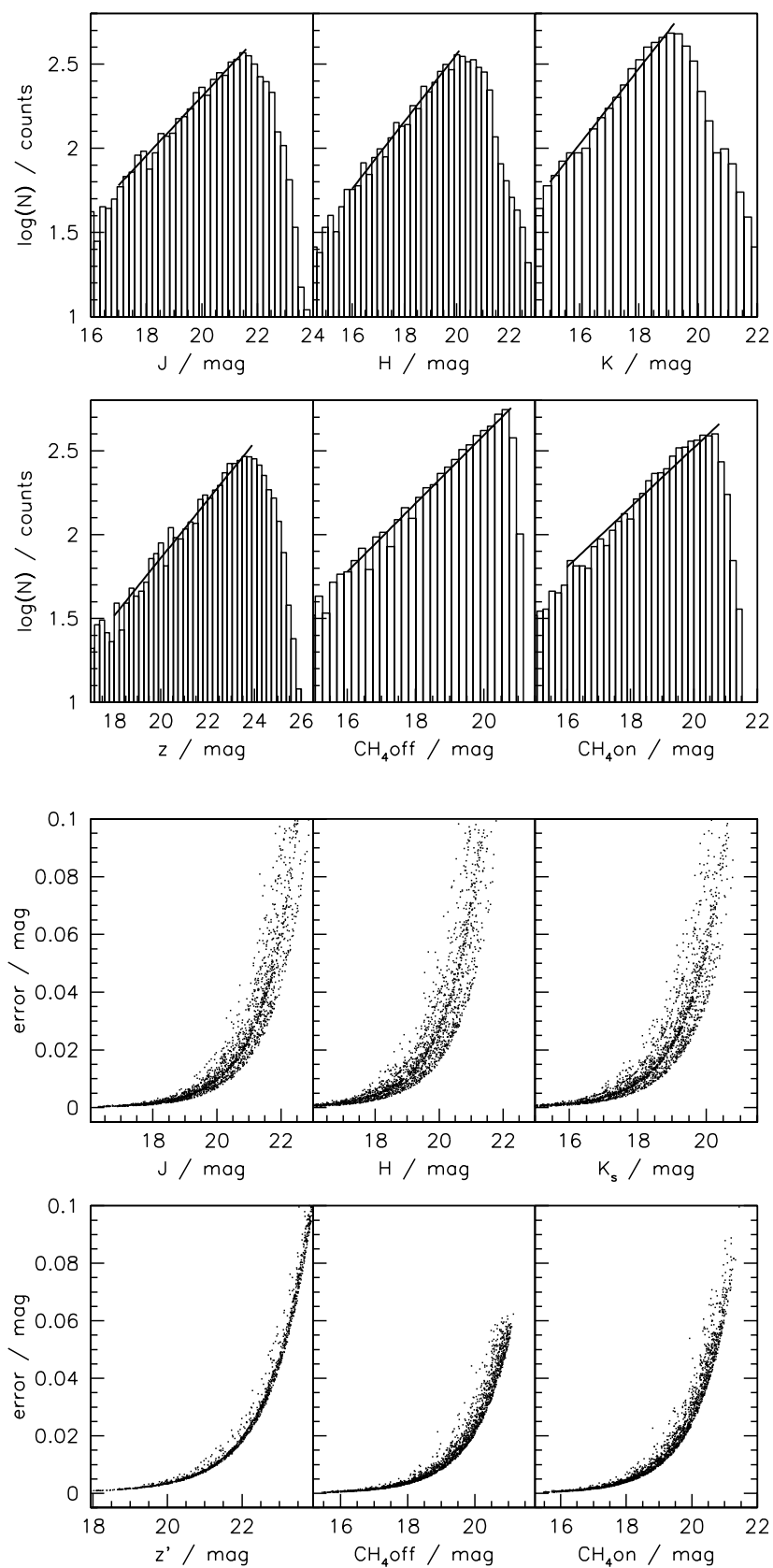


Figure 4.2: *top*:  $\log(N_{Obj})$  vs. magnitude (where  $N_{Obj}$  is the number of detected objects in each band): The completeness limits are found from these plots for the six imaged bands,  $z$ ,  $J$ ,  $H$ ,  $K$ ,  $CH_4on$  and  $CH_4off$ . The line has been fitted to the histogram to find where the turning point occurs, thereby indicating our completeness limit. *bottom*: Photometric error, as measured by SExtractor, against magnitude. Note that the  $J$ ,  $H$ ,  $K_s$  images have multiple tracks as they are composed from 4 fields which were not acquired at the same time.



### 4.2.3 Methane Photometry

The presence of methane absorption bands in the near-IR spectrum of T-dwarfs can be used to identify T-dwarf candidates photometrically (e.g. Tinney et al. 2005). Narrowband  $CH_4\text{off}$  and  $CH_4\text{on}$  data was taken in order to classify these objects.  $CH_4\text{off}$  measures the pseudo-continuum at  $1.58 \mu\text{m}$  while  $CH_4\text{on}$  samples the methane absorption band at  $1.69 \mu\text{m}$ . The passband of the two filters is overlain onto the spectra of a T0.5 and a T8 dwarfs in Figure 4.3. Note the greater methane absorption in the T8 dwarf spectrum compared to the T0.5 spectrum in the region around  $1.69 \mu\text{m}$ . The methane images have no external photometric calibration and the  $CH_4$  magnitudes are given here on an arbitrary albeit internally consistent scale, so that  $CH_4\text{on}-CH_4\text{off}\simeq 0$  for unreddened field dwarfs, shown in Figure 4.3.

Spectra<sup>1</sup> of field dwarfs from L1 to T8 were convolved with the WIRCam  $CH_4\text{on}$  and  $CH_4\text{off}$  filters and the resulting methane colours plotted against spectral type in Figure 4.3. The methane colours are seen to smoothly increase towards later spectral types. Whilst L-dwarfs have  $CH_4\text{on}-CH_4\text{off}$  colours equal to zero, T-dwarfs have colours above 0.1 mag which rapidly increase towards later T-types. To date, no other types of objects in current knowledge has this sequence of methane colours. Thus, the  $CH_4\text{on}-CH_4\text{off}$  colour provides a useful means to separate L and T-dwarfs. Additionally, as late-type T-dwarfs may remain undetected in the  $CH_4\text{on}$  image, and due to strong  $CH_4$  absorption, we first performed object detection at  $3.5\sigma$  on the  $CH_4\text{off}$  image, then performed PSF photometry at the location of these objects on both the  $CH_4\text{off}$  and  $CH_4\text{on}$  images. This ensures that all objects that could possibly be T-dwarfs are searched for in both filters.

Figure 4.3 provides an empirical calibration of the methane colours against spectral type for field dwarfs. For comparison, Figure 4.4 shows the  $CH_4\text{on}-CH_4\text{off}$  colour as a function of effective temperature ( $T_{\text{eff}}$ ) as predicted by COND and DUSTY 3 Myr and 5 Gyr models (Chabrier et al., 2000; Allard et al., 2001; Baraffe et al., 2003). While the DUSTY models are roughly similar at both ages, with  $CH_4\text{on}-CH_4\text{off} \sim 0$  at  $T_{\text{eff}} \geq 1500$  K, the COND models predict bluer colours for younger objects at  $T_{\text{eff}} < 1500$  K. According to the models, IC 348 T-dwarfs would then have a smaller  $T_{\text{eff}}$  and thus a later spectral type than field T-dwarfs for the same  $CH_4\text{on}-CH_4\text{off}$  colour.

---

<sup>1</sup>[www.jach.hawaii.edu/~skl/LTdata.html](http://www.jach.hawaii.edu/~skl/LTdata.html)

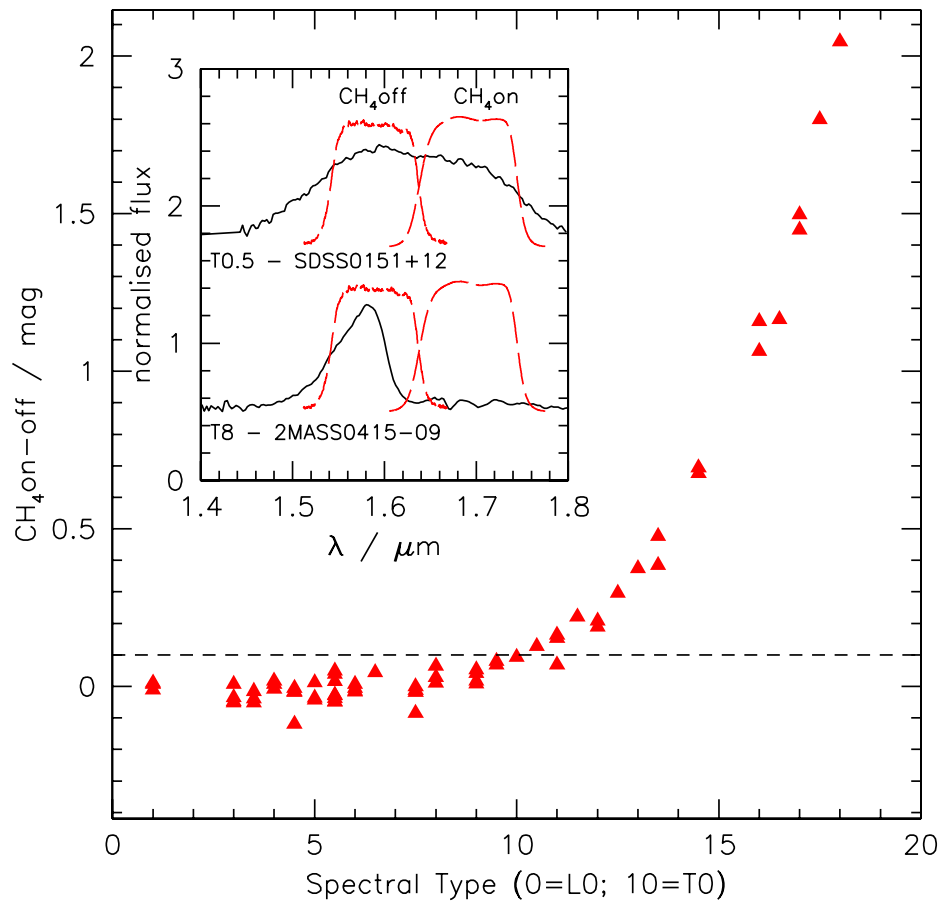


Figure 4.3:  $CH_4on-CH_4off$  colour vs. spectral type. The triangles are computed methane colours for a spectral sequence of field L and T dwarfs (see text). The dotted line at  $CH_4on-CH_4off=0.1$  mag highlights the limit where methane absorption becomes conspicuous in the photometric index, which occurs at a spectral type T0. Note how rapidly the methane index increases towards later spectral types. *Inset:* Dwarf T0.5 and T8 spectra are shown in the region of the  $1.6 \mu m$  methane absorption band. The passband of the WIRCam  $CH_4off$  and  $CH_4on$  filters is superimposed (dashed).

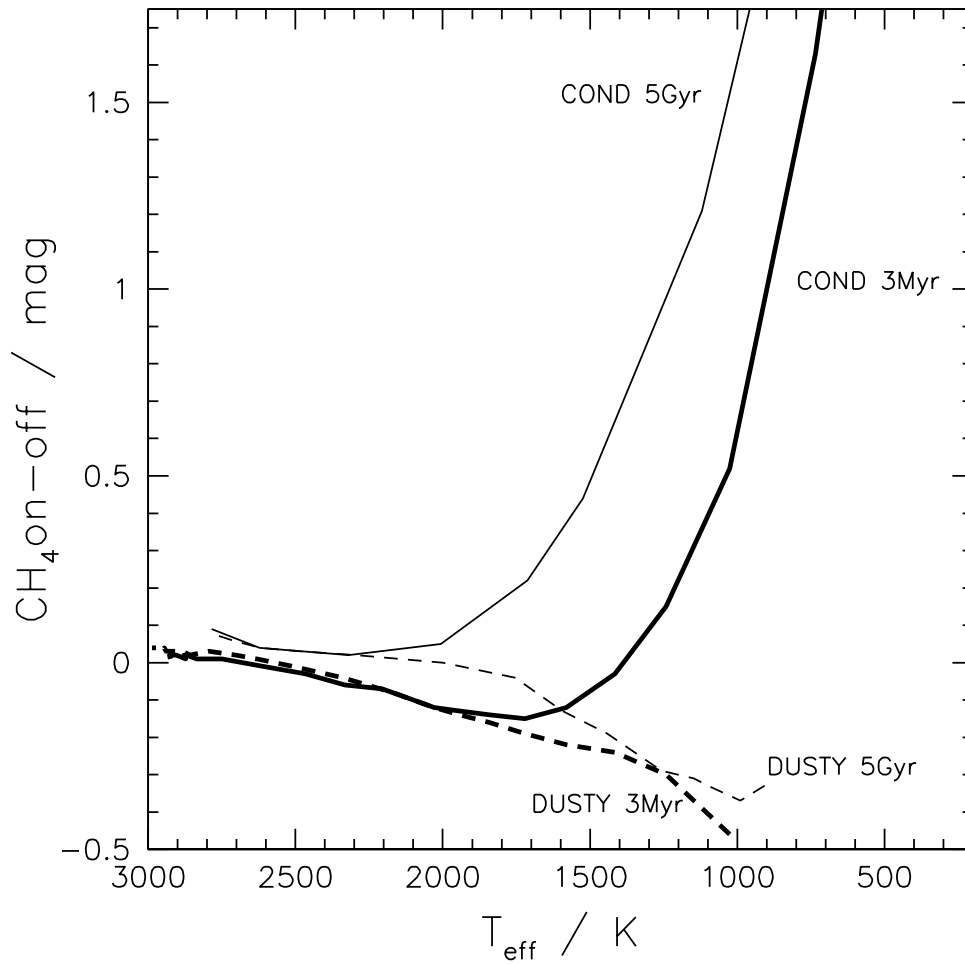


Figure 4.4:  $CH_{4on}-CH_{4off}$  colour vs.  $T_{eff}$ . 3 Myr COND (*thick solid*), 5 Gyr COND (*thin solid*) 3 Myr DUSTY (*thick dashed*) and 5 Gyr DUSTY (*thin dashed*) models are shown. The COND models predict later spectral types for 3 Myr IC 348 objects than for field dwarfs for given methane colours.

## 4.3 Results

Catalogues were obtained as described above for each of the MegaCam/WIRCam images. The COND and DUSTY 3 Myr and 5 Gyr models<sup>2</sup> are also in the CFHT Vega system where the  $z'$  band has been converted into AB magnitudes for our purposes. Similarly, the empirical field L-T dwarf sequence photometry has been adjusted to be consistent with the models and our data. In the colour/magnitude diagram presented the field dwarf sequence has been shifted to the distance of IC 348, taken to be at 300 pc.

### 4.3.1 T-dwarf Candidate Selection

Figure 4.5 shows  $CH_{4on}-CH_{4off}$  against  $CH_{4off}$  for stellar-like objects detected on WIRCam methane images. An object was considered as a T-dwarf candidate if  $CH_{4on}-CH_{4off} \geq 0.4$  mag, which corresponds to  $\geq 3.5 \sigma$  above the L/T transition ( $CH_{4on}-CH_{4off} = 0$ ) for the faintest detected objects. Assuming that young T-dwarfs follow the field dwarf methane relation, the spectral type of those objects with  $CH_{4on}-CH_{4off} = 0.4$  mag is close to T3 from Figure 4.3.

Objects with  $CH_{4on}-CH_{4off} \geq 0.4$  mag were initially all classified as T-dwarf candidates. The objects just below this limit could still be T-dwarfs from their  $CH_{4on}-CH_{4off}$  colours as shown in Figure 4.3, but would be more difficult to extract because of photometric errors. With this criterion 136 sources were selected. This sample was then visually scrutinised on both the  $CH_{4off}$  and  $CH_{4on}$  images before being reduced to a short-list of 12 possible candidates. Upon visual inspection, we found that the rejected 124 ‘objects’ were saturated stars, nebulous detections or ghosts. Of these 12 possible candidates, the shape of the PSF and the contours were further examined using *iraf*, where 9 were identified as ghosts or detector cross-talk, so reducing this figure to 3 likely candidates. Thumbsized  $CH_{4off}$  images of the three candidates are shown in Figure 4.6.

The PSF photometry of the 3 candidates in  $z'$ ,  $J$ ,  $H$ ,  $K_s$  and  $CH_{4on}/CH_{4off}$  filters is listed in Table 4.1. Candidate IC348\_CH4\_2 was not detected in the  $z'$ -band. The  $z'$ -band detection limit was estimated by simulating a set of 1948 stars with magnitudes between 20 and 26 using Skymaker (Bertin, 2008). These synthetic stars were then stacked onto the  $CH_{4off}$  footprint of the original  $z'$  image using Swarp (Bertin et al., 2002). At the  $3\sigma$  level, 1688 objects were detected where the faintest had an input magnitude of 25.7, which we take as being the detection limit in the  $z'$  filter.

Most of the objects detected on the WIRCam images lie along the line  $CH_{4on}-CH_{4off} = 0$  in Figure 4.5 as expected for field dwarfs (Tinney et al., 2005), the photometric error increasing

---

<sup>2</sup><http://phoenix.ens-lyon.fr/simulator/>

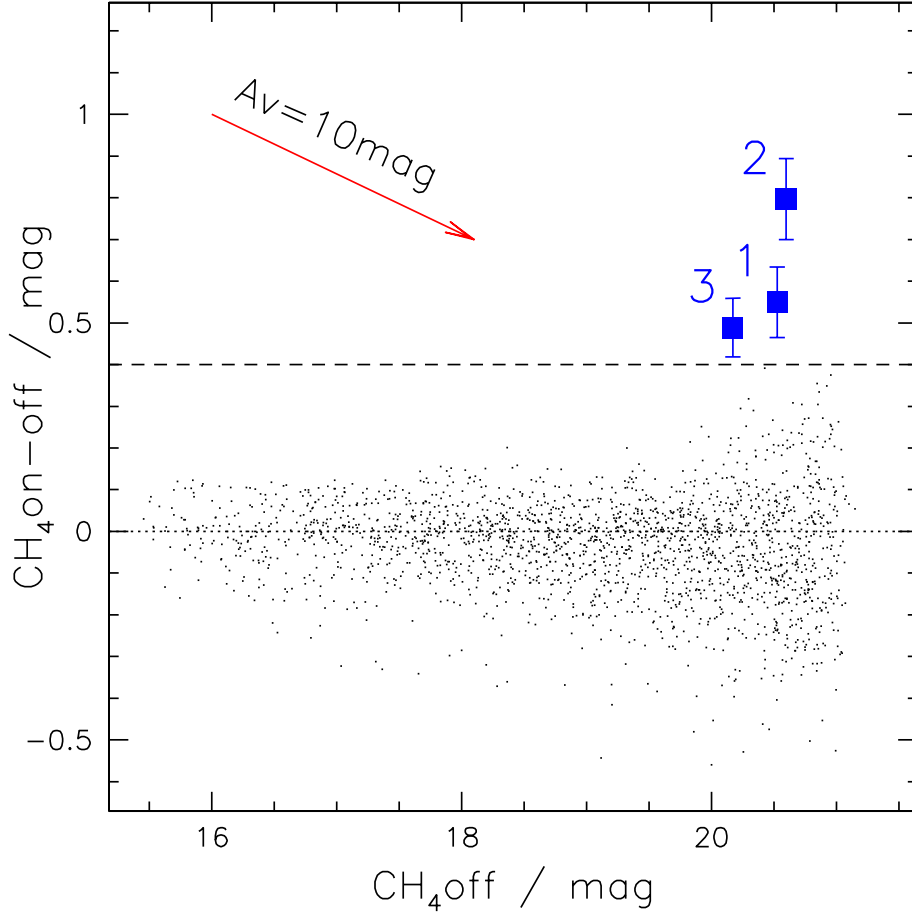


Figure 4.5:  $CH_{4on}-CH_{4off}$  colour vs  $CH_{4off}$ . The large (blue) squares show the three T-dwarf candidates with  $CH_{4on}-CH_{4off} \geq 0.4$ . The extinction vector is shown for  $A_V = 10$  mag. The sources with strongly negative colours are deeply embedded objects (see text).

with magnitude. The 3 candidates are located in the faintest region of the plot, whilst also having increasing methane colours. The  $CH_{4on}-CH_{4off}$  rms photometric error at the magnitude of the candidates is  $\sigma \sim 0.12$  mag. The 3 candidates have  $CH_{4on}-CH_{4off}$  colours of 0.54, 0.78, and 0.49 mag, respectively, corresponding to a detection level of  $> 4\sigma$  (see Table 4.2).

Note that a number of objects in Figure 4.5 have strongly *negative*  $CH_{4on}-CH_{4off}$  colours, well beyond the rms photometric error. Upon inspection of the images, all these objects turn out to be young IC 348 members deeply embedded in bright compact nebulosities. The large extinction they suffer results in strong reddening, thus yielding blue (i.e. negative)  $CH_{4on}-CH_{4off}$  colours in spite of the small wavelength difference between the 2 narrow-band methane filters. Reddening also accounts for the asymmetric colour distribution of the faint background objects in this plot.

Finally, a cross-comparison was made with the study of Mainzer and McLean (2003). They classified 5 candidates as being possibly M, L or T-dwarfs, all of which are detected in our images but with  $CH_{4on}-CH_{4off}$  colours between -0.14 and 0.04 mag, placing them out of our T-dwarf

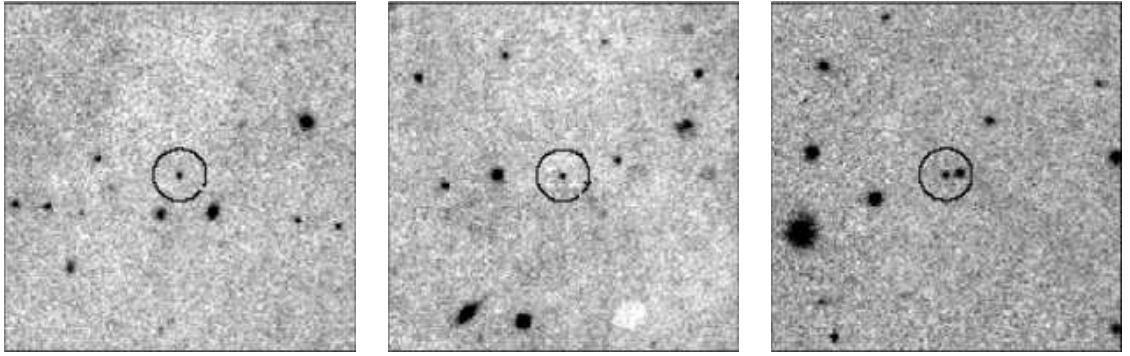


Figure 4.6: Thumbsized  $CH_4$ off images of the three T-dwarf candidates, left to right, IC348.CH4.1, IC348.CH4.2 and IC348.CH4.3, respectively. Black circles highlight the location of the T-dwarf candidates. The images are  $48''$  to a side, where North is up and East is to the left.

Table 4.1: PSF photometry and photometric errors of the three T-dwarf candidates, in magnitudes.

Object	$z'$	$\sigma_{z'}$	$J$	$\sigma_J$	$H$	$\sigma_H$	$K_s$	$\sigma_{K_s}$	$CH_4$ off	$\sigma_{CH_4off}$	$CH_4$ on	$\sigma_{CH_4on}$
IC348.CH4.1	23.32	0.07	21.62	0.04	20.95	0.07	20.22	0.06	20.52	0.04	21.06	0.08
IC348.CH4.2	$\geq 25.7$	-	22.51	0.07	21.65	0.08	20.10	0.04	20.59	0.04	21.37	0.10
IC348.CH4.3	23.85	0.10	22.02	0.07	21.02	0.07	19.94	0.05	20.17	0.03	20.66	0.06

candidate criteria.

### 4.3.2 Reddening & Spectral Type Estimates

Estimation of the candidates' extinction is required in order to be able to calculate their absolute magnitude and estimate their spectral type. Extinction has been estimated using colour/colour diagrams of  $CH_4$ on– $CH_4$ off versus  $J - H$ ,  $J - K_s$  and  $H - K_s$ , as plotted in Figure 4.7. The extinction was computed for each candidate using the extinction vector and regressing the objects back towards the 3 Myr COND model. The final extinction value is the average of the 3 results obtained from each colour/colour diagram and is summarised in Table 4.2, along with  $CH_4$ on– $CH_4$ off colour, detection level and spectral type for the three candidates. The estimated extinction is an upper limit if the candidates belong to the cluster as their true dereddened colours are probably intermediate between the 3 Myr COND and DUSTY models. If they are field dwarfs however, the given value is a lower limit as the objects should be dereddened towards the 5 Gyr field dwarf sequence that is bluer than the 3 Myr COND model.

We then used these results to compute the dereddened  $CH_4$ on– $CH_4$ off colour for each candidate. We found these values to be  $0.69 \pm 0.16$ ,  $1.15 \pm 0.24$  and  $0.76 \pm 0.15$  mag for IC348.CH4.1, IC348.CH4.2 and IC348.CH4.3, respectively. From Figure 4.3, these dereddened colours correspond to a spectral type of  $T5_{-1}^{+0.5}$ ,  $T6_{-0.5}^{+1}$ , and  $T5_{-0.5}^{+0.5}$  for IC348.CH4.1, IC348.CH4.2 and IC348.CH4.3, respectively. As noted above, this may be a lower estimate as the models suggest that young T-dwarfs have a lower effective temperature than field T-dwarfs for the same  $CH_4$ on– $CH_4$ off colour (see Fig.4.4). Moreover, if the candidates were 5 Gyr field objects,

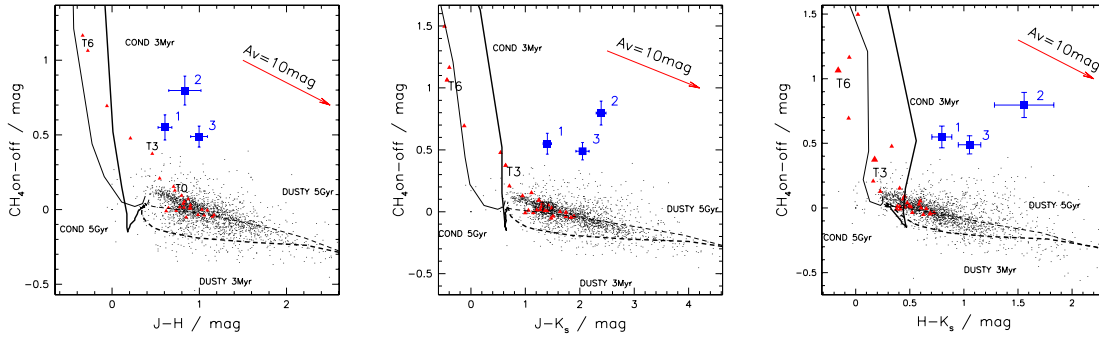


Figure 4.7:  $CH_{4on}-CH_{4off}$  vs.  $J-H$ ,  $J-K_S$  and  $H-K_S$ . T-dwarf candidates are plotted as (blue) squares. Photometric error bars are from SExtractor. Field T-dwarfs (red triangles) are shown for comparison. Lines show the 5 Gyr COND and DUSTY, and 3 Myr COND and DUSTY models as in Fig. 4.4. Candidates were dereddened towards the 3 Myr COND model using the extinction vector.

Table 4.2: Summary of values for the three candidates, where the cluster centre is taken to be at  $03^h44^m34^s + 32^\circ09'48''0$  (J2000).

IAU name	$CH_4$ (on-off) (mag)	Det. level	$A_V$ /mag	Est. sp. type	Distance from cluster centre	Object coordinates
CFHT_J0344+3202_(IC348_CH4_1)	0.54	$4.3 \sigma$	$5.0 \pm 1.2$	$T5^{+0.5}$	$7'35''$	$03^h44^m49^s.24 + 32^\circ02'48''4$
CFHT_J0344+3206_(IC348_CH4_2)	0.78	$6.2 \sigma$	$12.4 \pm 3.9$	$T6^{+1}_{-0.5}$	$4'20''$	$03^h44^m49^s.52 + 32^\circ06'35''4$
CFHT_J0344+3156_(IC348_CH4_3)	0.49	$4.3 \sigma$	$9.0 \pm 1.3$	$T5 \pm 0.5$	$13'56''$	$03^h44^m57^s.95 + 31^\circ56'43''3$

they would have a larger extinction and therefore an even larger intrinsic  $CH_{4on}-CH_{4off}$  colour, which would also yield a later spectral type.

## 4.4 Discussion

We discuss here the likelihood that the methane candidates reported above are *bona fide* young, very low-mass members of the IC 348 star-forming region instead of being more evolved field T-dwarfs located on the line of sight to the young cluster. We also compare the number of T-dwarf candidates we identify in our survey to the number of expected planetary mass objects in IC 348, by extrapolating recent estimates of the substellar IMF to the planetary mass domain.

### 4.4.1 Membership

Further colour/colour and colour/magnitude diagrams (CMD) were plotted to constrain the candidates' status. Figure 4.8 shows the  $J/J-K_S$  CMD. Also plotted are the synthetic magnitudes and colours of the field T-dwarfs when shifted to the cluster distance. The 5 Gyr DUSTY and COND models are drawn to highlight the agreement between the models and the field dwarf sequence. The field T-dwarf sequence begins in between the 5 Gyr DUSTY and COND models, before sweeping towards the 5 Gyr COND model at  $\sim 1500$  K that sharply increases in faintness

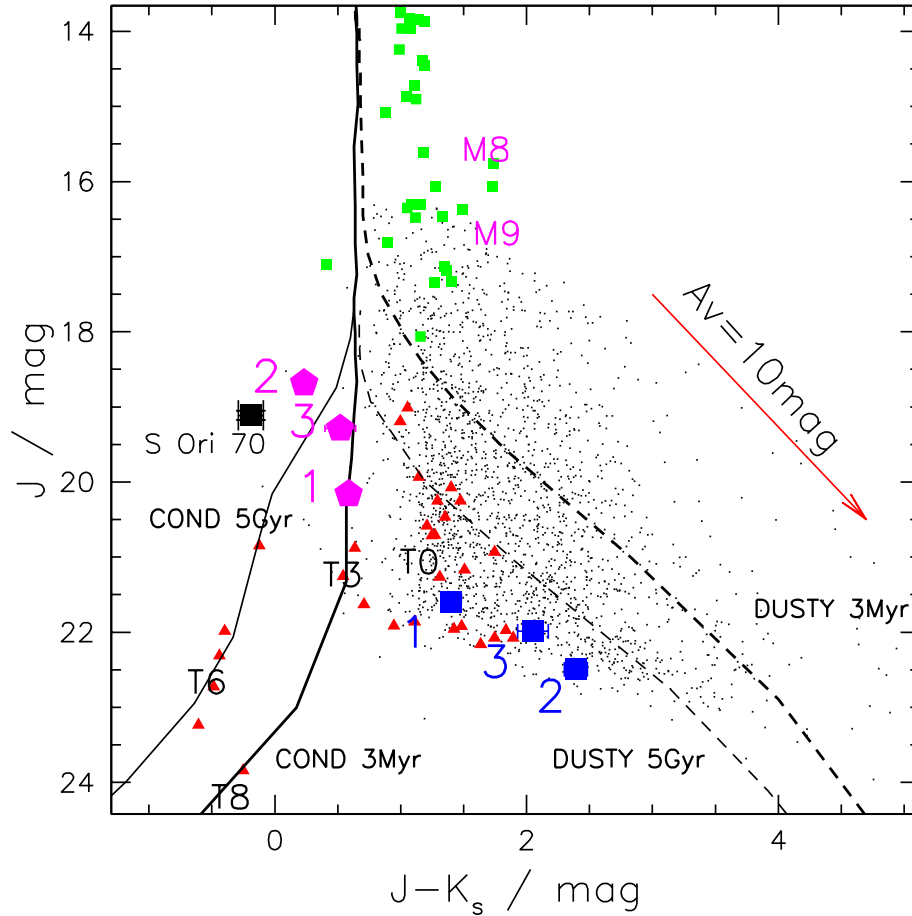


Figure 4.8:  $J$  vs  $J - K_s$  CMD. The (blue) squares are the three T-dwarf candidates as observed, whilst the (magenta) pentagons represent their dereddened location in the CMD. Field T-dwarfs (red triangles) as well as S Ori 70 (black square, labelled) shifted to the distance of IC 348 are shown for comparison. Dereddened M6-M9 IC 348 dwarfs from Luhman et al. (2003) are plotted for comparison (small green squares). DUSTY and COND models are shown as in Fig. 4.4.

with the late-T set.

In this diagram the three candidates appear to be confused with the late-L, early-T field dwarfs. However, once they are dereddened using the extinction values given in Table 4.2, they become bluer and brighter. All three candidates appear to follow the 3 Myr COND model quite closely. The fact that the dereddened candidates appear brighter than field T-dwarfs shifted to the cluster distance suggest that they are younger indeed. A young T-dwarf has a larger radius than a field T-dwarf for a given spectral type as it is still contracting. According to the COND models, the difference amounts to about a factor of 2 in radius between 3 Myr and 5 Gyr (for  $T_{eff}=1000-1500$  K), which results in a 1.5 magnitude increase, consistent with the observed location of the candidates in Figure 4.8.

There is a possibility that the candidates are in fact field T-dwarfs located at a closer distance



(between  $\sim 100$  and  $200$  pc) along the line of sight to IC 348. The probability of one of the candidates being a field T-dwarf instead of an IC 348 cluster member can be estimated independently from extinction. According to Figure 4.3, the spectral type range T3-T5.5 corresponds to the measured  $CH_{4on}-CH_{4off}$  colours of our candidates at an age of 5 Gyr. Thusly, using the number density of T3-T5.5 field dwarfs in the solar neighbourhood, i.e.  $\sim 1$  per  $714 \text{ pc}^3$  according to Metchev et al. (2008) and the footprint of the  $CH_4$  image of  $0.11 \text{ sq.deg.}$  gives an estimate of  $0.11 \pm 0.06$  T3-T5.5 foreground field dwarfs in the direction of IC 348. As we are concerned here with the probability of one of our candidates being a foreground field dwarf, this is a fairly robust method for determining the population density for field dwarfs in the direction of IC 348. However, this estimate is put into context when taking into account the large extinction values of the three candidates estimated from Figure 4.7. Even the least extinguished candidate, IC348\_CH4\_1, has four magnitudes more extinction than expected for a foreground field dwarf ( $< 1 \text{ mag}$ ), so all three objects must be near to or behind IC 348. However, the candidates cannot be background field T-dwarfs, seen through the IC 348 cloud, as their luminosity would then be much too high for their estimated spectral type. Finally, as indicated in Table 4.2, all three candidates are located within the cluster's boundary ( $4'$  core radius,  $10-15'$  halo; Herbig 1998, Herbst 2008) and are thus spatially consistent with being IC 348 members.

#### 4.4.2 Contaminants

A further, useful diagram in defining these candidate objects is the  $z' - J/J - H$  colour/colour diagram shown in Figure 4.9, (note that the  $z'$  is in the AB system). Here it can be seen that the two detected dereddened candidates are much bluer in  $z' - J$  than both the field dwarf sequence and the COND 3Myr and 5Gyr models. There is mounting empirical evidence for young T-dwarfs to have bluer  $z' - J$  colours than field T-dwarfs because of the effects reduced gravity has on the opacities (P. Delorme, priv. comm.). This effect stems from the strong potassium KI ( $7687\&7701 \mu\text{m}$ ) doublets, whose wings fall within the  $z'$  band. The lower the gravity the lesser the line broadening of these elements so less flux is lost by absorption in the  $z'$  band, resulting in the observed bluer  $z' - J$  colours (F. Allard, priv. comm). However, these effects are unlikely to explain the extreme blueness of two of the three objects and suggests that candidates IC348\_CH4\_1 and IC348\_CH4\_3 are unlikely to be T-dwarfs. The final remaining candidate, IC348\_CH4\_2, remains a good T-dwarf candidate because of its non-detection in  $z'$ .

If candidates IC348\_CH4\_1 and IC348\_CH4\_3 are not young T-dwarfs then what are they? We checked whether extragalactic objects could contaminate this region of the diagrams. To this end, galaxies<sup>3</sup> from SWIRE, 2MASS and SDSS were found to have very different colours ( $z' - J \sim 6-8 \text{ mag}$ ) to our candidates. Similarly, quasars (Labita et al., 2008) also have J-band magnitudes

---

<sup>3</sup>iras.ipac.caltech.edu

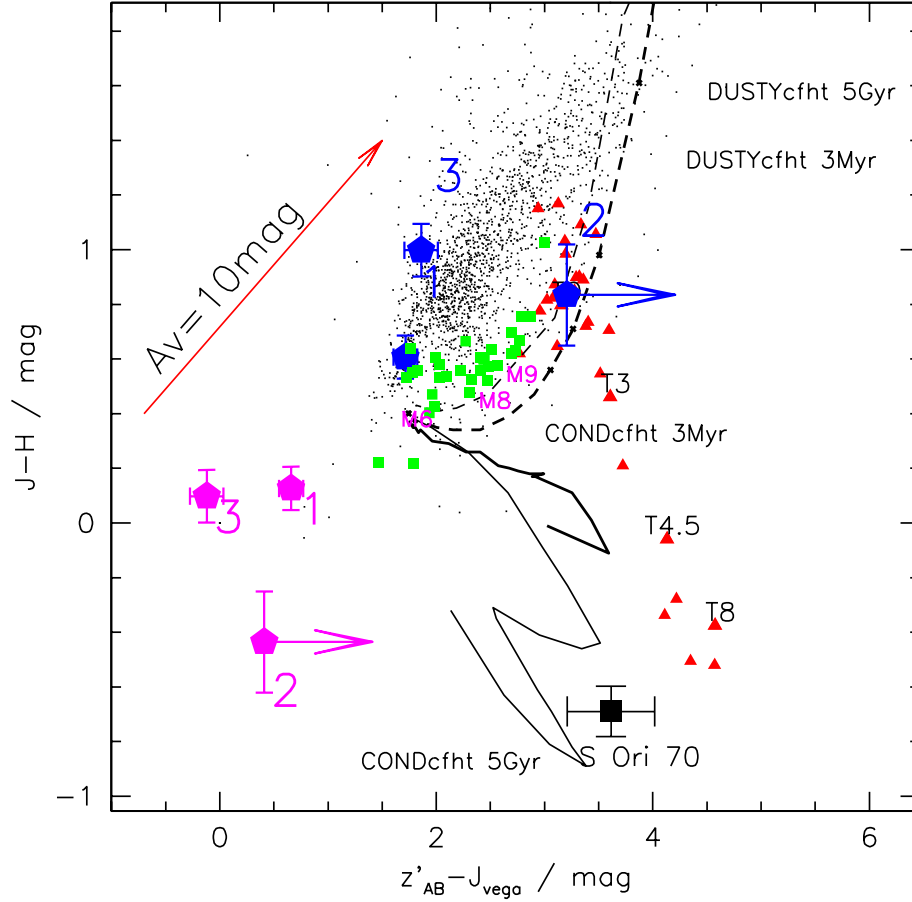


Figure 4.9:  $z' - J$  vs  $J - H$  CMD. DUSTY and COND models are shown as in Fig. 4.4. Symbols shown as per Figure 4.8.

of  $\sim 24$ - $25$  mag, making them much fainter than our objects. Late-type (emission line) galaxies appear tightly in the region  $J - K \sim 0.95$  mag and  $J - H \sim 0.88$  mag and so again cannot be confused with our candidates (Chang et al., 2006). Cool subdwarfs have been put forward as an explanation for the identity of these two objects, but further analysis is required. At this point, the status of the two rejected candidates continues to be unclear.

#### 4.4.3 Comparison of IC348\_CH4\_2 with S Ori 70

Zapatero Osorio et al. (2002) found S Ori 70 to be a faint mid-T type object towards the direction of the young  $\sigma$  Orionis cluster, with an estimated mass in the interval  $2$ - $7 M_{Jup}$ . However, there has been some contention with regard to the membership of S Ori 70 to the  $\sigma$  Orionis cluster. Further work by Scholz and Jayawardhana (2008) indicated that this was a true cluster member by looking at the IRAC data, and suggested that there is a possibility of a disk structure which gives rise to the MIR excess.

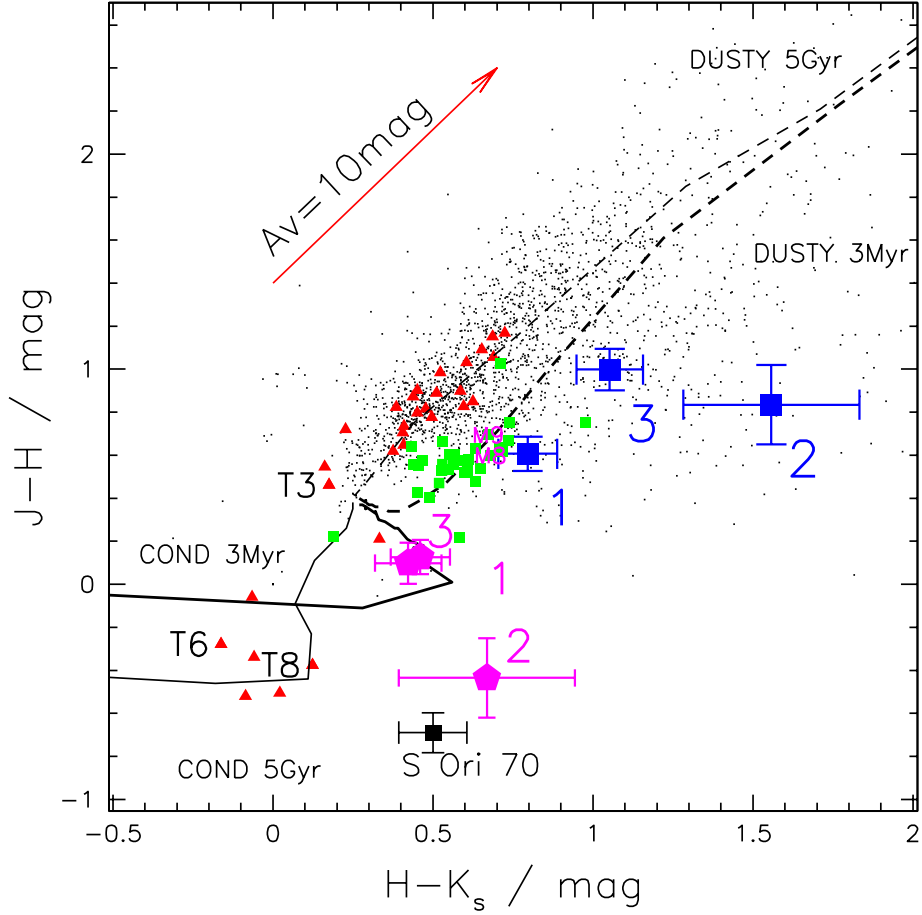


Figure 4.10:  $J - H$  vs  $H - K_s$ . Symbols as per Figure 4.8.

The  $J/J - K_s$  CMD in Figure 4.8 has the IC 348 dereddened candidates plotted alongside S Ori 70 for comparison. The  $J$ ,  $H$  and  $K_s$  data for S Ori 70 was taken from Zapatero Osorio et al. (2008) and adjusted to the CFHT photometric system using the 3 Myr COND CFHT and 2MASS models. The differences for  $\lambda_{2MASS} - \lambda_{CFHT}$  due to colour effects are 0.6 mag, -0.1 mag, and -0.05 mag, for  $J$ ,  $H$  and  $K_s$  respectively. In this diagram, candidate IC348.CH4.2, for which we estimated a spectral type of  $T6_{-0.5}^{+1}$ , falls at approximately the same location as S Ori 70, shifted to IC 348's distance.

Figure 4.10 shows the  $J - H/H - K_s$  colour/colour diagram. The dereddened  $J - H$  colours of remaining IC348.CH4.2 T-dwarf candidate is -0.44 which corresponds to a spectral type of around T6-T8 (Luhman et al., 2007b) and so is consistent with our previous estimate. Again in this plot, the location of IC348.CH4.2 is similar to that of S Ori 70. A remarkable property of these two objects is that they have  $H - K_s$  colours too red for their estimated spectral types, yet also have blue  $J - H$  colours consistent with them being T6 dwarfs. According to Zapatero Osorio et al. (2008), this may be a signature of youth.

Table 4.3: Spitzer PSF photometry and photometric errors of the three T-dwarf candidates. IC348\_CH4\_1 appeared outside the FOV in the [4.5] $\mu$ m image.

Object	F[3.6]/mJy	F[3.6]_error	F[4.5]/mJy	F[4.5]_error	[3.6]/mag	[3.6]_error	[4.5]/mag	[4.5]_error
IC348_CH4_1	0.0035	0.0001	-	-	19.75	0.03	-	-
IC348_CH4_2	0.0093	0.0003	0.0136	0.0004	18.70	0.03	17.80	0.03
IC348_CH4_3	0.0245	0.0003	0.0365	0.0007	17.65	0.02	16.73	0.02

#### 4.4.3.1 Spitzer Data

We searched the *Spitzer* public archive for IRAC data. IC 348 was the prime target of programmes 6 (c2d, P.I. Fazio) and 36 (P.I. Fazio). The c2d data are made up by shorter exposures, resulting in our use of the deeper ( $16 \times 100$ s) images of programme 36. We retrieved the data and processed them using standard procedures with the recommended MOPEX software. All three candidates are detected in the [3.6] and [4.5] bands, except IC348\_CH4\_1 which falls out of the [4.5] band field of view. PSF photometry was performed using Starfinder (Diolaiti et al., 2000) and the fluxes were translated into magnitudes using the zeropoint fluxes provided by the Spitzer Science Center<sup>4</sup>. Measurement uncertainties were tentatively estimated from the Poisson noise weighted by the coverage maps of the mosaics. The final photometry is given in Table 4.3, and the final errors include both measurement and zeropoint flux uncertainties.

In Figure 4.11, the  $K_s - [3.6]$  vs  $[3.6] - [4.5]$  colour/colour diagram is plotted with the two candidates, S Ori 70 and the IC 348 M6-M9 dwarf sequence from Luhman et al. (2005a). The M, L and T IRAC field dwarf sequence from Patten et al. (2006) have also been plotted for comparison. The  $[3.6] - [4.5]$  colour could be a good indicator of effective temperature, or spectral type, giving IC348\_CH4\_2 a spectral type of  $\sim T5$ , in line with our other estimates of T6. The  $K_s - [3.6]$  colour, however, relates to a spectral type of L1, which is far too early for such a low-mass and cool object.

The  $K_s - [3.6]$  colour of IC348\_CH4\_2 appears significantly bluer compared to the field sequence, which may be because of reduced gravity (Leggett et al., 2007). For mid-type and later T-dwarfs the reduced pressure broadening of  $H_2$ , as a gravity effect, makes the  $K_s$  band brighter, whilst the [3.6] band faintens because of additional  $CH_4$  absorption at  $\sim 3 \mu$ m, resulting in a bluer  $K_s - [3.6]$  colour. Another consequence of lower gravity is the faintening effect the CO abundances have on the [4.5] band for early T-types, thus balancing the  $[3.6] - [4.5]$  colour. These colour effects of low gravity are in agreement with this object being a young IC 348 T-dwarf.

Other effects such as strong sedimentation and little or no vertical mixing in the atmosphere could also contribute to the observed bluer  $K_s - [3.6]$  colours (Leggett et al., 2007). The possible existence of a hot inner dusty disc around S Ori 70, in keeping with other young members of S Orionis, can give rise to its redder  $[3.6] - [4.5]$  colour.

<sup>4</sup><http://ssc.spitzer.caltech.edu/>

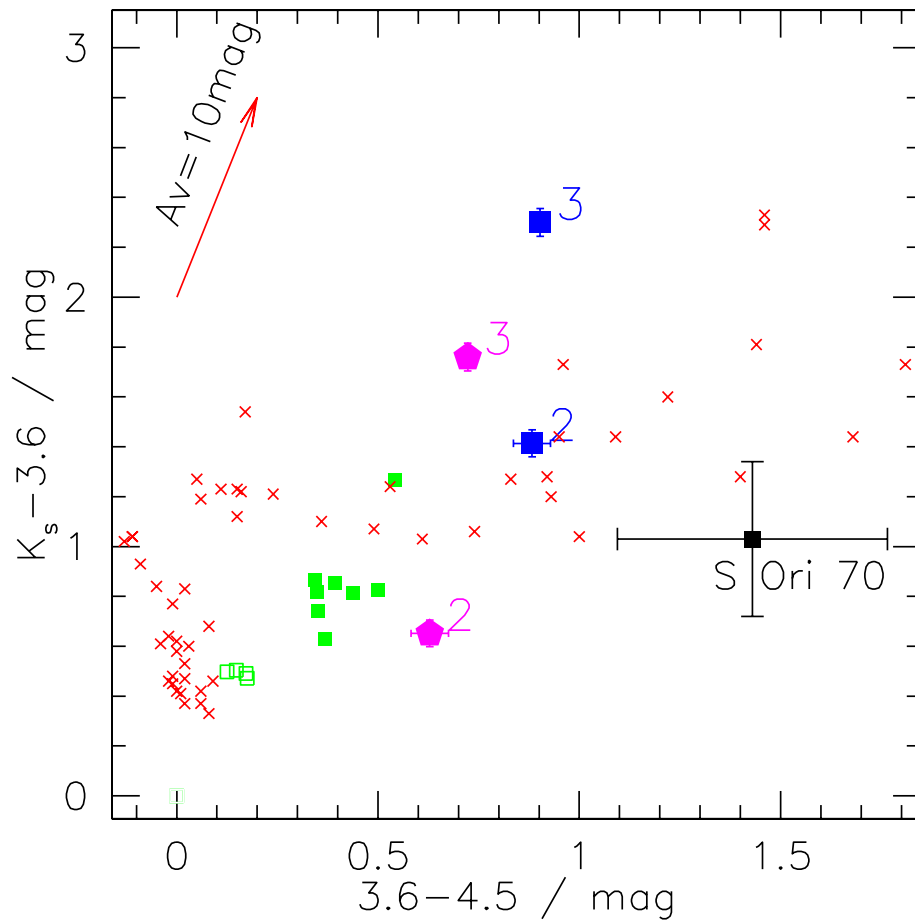


Figure 4.11:  $K_s - [3.6]$  vs  $[3.6] - [4.5]$  COLD. The field dwarf sequence from Patten et al. (2006) has been plotted (red crosses) for comparison. IC 348 M6-M9 dwarfs with disks (filled green squares) and those without (hollow green squares) are plotted (Luhman et al., 2005a). IC348\_CH4\_2 and S Ori 70 appear significantly bluer in the  $K_s - [3.6]$  colour than for field dwarfs. The extinction vector has also been plotted using values from the Spanish Virtual Observatory<sup>3</sup>.

#### 4.4.4 The Lower End of the IMF

Luhman et al. (2003) derived a nearly complete IMF for IC 348 down to  $0.03 M_{\odot}$  for  $A_V \leq 4$  mag. They find a ratio of brown dwarfs (BDs,  $0.02$ - $0.08 M_{\odot}$ ) to stars of about 12%. Muench et al. (2003) similarly derived an IMF for IC 348 down to  $0.04 M_{\odot}$ , with a mode between  $0.08$  and  $0.2 M_{\odot}$ , finding a ratio of BDs to stars of about 14%. From a deep J-band survey of the cluster, Preibisch et al. (2003) derived a BD to star ratio of 10%.

According to the COND and DUSTY models, the mass range of 3 Myr old T-dwarfs is between  $0.001 M_{\odot}$  and  $0.005 M_{\odot}$ , corresponding to masses from  $\sim 1 M_{Jup}$  to  $\sim 5 M_{Jup}$ . However, the models are somewhat uncertain at very low masses and young ages. Currently the models can have up to a 50% discrepancy in the masses for objects younger than 5 Myr (Chabrier, priv. comm). Still, the T-dwarf candidate IC348\_CH4\_2 is likely to be less massive than  $10 M_{Jup}$  if belonging to IC 348. In order to obtain an estimate of the number of objects within this mass range that are expected to be in IC 348, we extrapolated current estimates of the IMF to the planetary mass regime. A log-normal estimate of the field IMF for unresolved systems was provided by Chabrier (2003), where the mode of the distribution,  $m_0$ , is  $0.22 M_{\odot}$  and its width,  $\sigma$ , is 0.57. This log-normal IMF would predict  $\sim 1\%$  objects in the mass range below  $10 M_{Jup}$ . Similarly, Moraux et al. (2007) suggested a universal log-normal IMF for systems in young open clusters, with  $m_0 = 0.30 \pm 0.05 M_{\odot}$  and  $\sigma = 0.55 \pm 0.03$ , which would predict  $\sim 0.4\%$  of objects in the  $1$ - $10 M_{Jup}$  mass range. Muench et al. (2007) conducted a Spitzer census of IC 348 and stated that the population of IC 348 is in excess of 400 members when taking into account unseen disk-less members. Based on the above IMF and population estimates, we would thus expect about  $1.6$ - $4$  objects in the mass range  $1$ - $10 M_{Jup}$  in the cluster. The discovery of one T-dwarf candidate close to the completeness limit is thus consistent with the extrapolation of current log-normal IMF estimates down to the planetary mass domain.

Another estimate can be found using the power law derived by Caballero et al. (2007) and Lodieu et al. (2009b) for  $\sigma$  Orionis and Lodieu et al. (2007) for Upper Sco,  $\frac{dN}{dM} \propto M^{-\alpha}$ , where  $\alpha = 0.6$  for the mass range  $0.3 - 0.01 M_{\odot}$ . Using the IMF from the  $A_V \leq 4$  mag selected census of IC 348 by Luhman et al. (2003) and extrapolating the power law for the last two data points above their completeness limit towards the lowest mass domain gives a different estimate. This corresponds to a much larger number of predicted objects than for the log-normal estimate,  $25 \pm 16$  objects in the  $1$ - $10 M_{Jup}$  mass range and  $15 \pm 9$  objects in the  $1$ - $5 M_{Jup}$  mass range. Even though our survey is complete down to  $A_V \sim 12$  mag for T3 - T5.5 dwarfs, we did not detect any such object with an  $A_V \leq 4$  mag. This suggests that the current power law approximation over-estimates the number of low-mass objects in IC 348.

## 4.5 Conclusions

From a deep methane imaging survey of the star-forming region IC 348 we identified 3 T-dwarf candidates over the area of the cluster. After colour/colour and colour/magnitude diagram analysis two candidates have been rejected for being too bright at optical wavelengths. The remaining candidate, has an estimated spectral type of T6 and theoretical models suggest a mass of a few  $M_{Jup}$  for this object at 3 Myr. From its luminosity, colour, extinction and spatial location, IC348\_CH4\_2 is a probable IC 348 T-dwarf member, and so is among the lowest mass objects observed so far in a star-forming region. The frequency of isolated planetary mass objects reported here for IC 348 is consistent with the extrapolation of current log-normal IMF estimates to the planetary mass domain.

## Acknowledgements

We thank F. Allard for many discussions during the writing of this subject, and also to the paper referee, Eduardo Martín, for providing insightful comments with regard to the paper on this work. Many thanks goes to P. Delorme for his empirical sequence of field dwarfs which was used in many figures here, and other useful comments. We thank also Manuel Perger and David Barrado y Navascués for discussions and Subaru data. We thank the QSO team at CFHT for their efficient work at the telescope and the data pre-reduction as well as the Terapix group at IAP for the image reduction. This work is based in part on data products produced and image reduction processes conducted at TERAPIX. This research has made use of the NASA/ IPAC Infrared Science Archive, which is operated by the Jet Propulsion Laboratory, California Institute of Technology, under contract with the National Aeronautics and Space Administration. This research has also made use of the SIMBAD database, operated at CDS, Strasbourg, France.

## 4.6 Résumé

D'après une enquête d'imagerie méthane profonde de la région de formation d'étoiles IC 348 nous avons identifié 3 candidats du nains-T sur la zone de la grappe. Après la couleur / couleur et / analyse des diagrammes de magnitude deux candidats ont été rejetés pour être trop lumineux aux longueurs d'onde optiques. Les candidats restants, a estimé un type spectral de T6 et des modèles théoriques suggèrent une masse de quelques-uns  $M_{Jup}$  pour cet objet à 3 Myr. De sa luminosité, la couleur, l'extinction et la localisation spatiale, IC348\_CH4\_2 est probable IC 348 membres de nain-T, et il est donc parmi les objets les plus bas de masse observées jusqu'à présent dans une région de formation d'étoiles. La fréquence des objets de masse planétaire isolés signalés ici pour IC 348 est compatible avec l'extrapolation des estimations du FMI log-normale dans le domaine de masse planétaire.





# Chapter 5

## Discussion and Conclusions

### Contents

---

<b>5.1 IC 4665 &amp; IC 348 Revisited</b> . . . . .	<b>123</b>
<b>5.2 Future Work</b> . . . . .	<b>124</b>
<b>5.3 Context</b> . . . . .	<b>125</b>
<b>5.4 Conclusion</b> . . . . .	<b>127</b>
<b>5.5 Résumé</b> . . . . .	<b>129</b>

---

This chapter is devoted to sewing the working chapters together to make a final coherent garment with no extraneous holes. Initially, the evolution of the work that has been done is discussed with respect to how this can be built on for both of the observed clusters, before detailing the observations and further work required in order to build on these foundations for the betterment of this subject. Subsequently the questions that were posed in Chapter 1 are expanded and discussed with respect to the preliminary results of the census of IC 4665 and the candidate mid-type T-dwarf in IC 348. Additional questions are then posed in light of the aspects of star formation, brown dwarfs and the initial mass function that have been described in this work.

### 5.1 IC 4665 & IC 348 Revisited

The data of IC 4665 has been calibrated and analysed as discussed in Chapter 3 and a set of candidate objects has been selected from all permutations of colour/magnitude and colour/colour diagrams. The stage reached with the work on IC 4665 indicate that more work needs to be done in order to comprehensively confirm the existence of L-dwarfs, but there is potential, with the current list of candidates to have at least 3. The selection criteria are too conservative because the *Y*-band is too faint compared to the isochrone in the lower mass domain meaning many good candidate objects could have been rejected.

Moving to the lower mass regimes, IC 348 was targeted using methane narrowband observations in order to distinguish likely T-dwarf candidates as discussed in Chapter 4. IC 348 is young enough to enjoy the company of lowest mass objects before dynamical interactions could have removed them all from the cluster centre. The additional interest with this cluster is that its footprint on the sky is very small directly because of its low proper motion and young age; there has not been enough time for all of the objects to have evaporated from the cloud. The problem is still the high extinction in this region which is almost certainly occluding from view additional low mass objects, and possibly the lowest possible mass objects than could be formed within this cluster. One such detection has a very good chance of being a T-dwarf, given a preliminary spectral type of T5.5, whilst two other detections have not been identified. The possibility of contamination by a foreground T-dwarf or by a methane-rich cloud in the line of sight has been entertained but rejected from number-density arguments and the likelihood of having a cloud of sufficient density to impact on the  $1.69 \mu\text{m}$  methane band to cause a 0.3 mag reduction in emission. Added to the fact that there are *two* objects which are unidentified and the relatively large separation within the cluster indicates that these are either new objects, or objects which have yet to fully pass the cloud-clearing stage of their evolution and so are beset by atmospheric convection. When these objects are dereddened they appear fainter than IC348\_CH4\_2 so could be even younger, less massive and diskless objects within the same cluster. The *Spitzer* colours of one of the objects suggests that it is diskless, compared to other objects with known disks.

## 5.2 Future Work

Further work is required in order to compare these data with *Spitzer* observations, and then a spectroscopic follow-up survey to confirm or reject not only the membership status of the cluster members, but also spectral type. It is with only this data that a confident assessment of the IMF can be established for IC 4665. It is possible to plot the number of objects as a function of mass and to overplot the previously found IMF for this cluster, and to calculate the new IMF of this cluster taking into account these new objects. The two can then be compared to see whether the log-normal or the power law IMF fits the data more closely. Hypothetically there can be three outcomes to this work; that the census finds a plethora of low-mass members at odds with the prediction of the previously found IMF; that a dearth is found of low-mass objects which would also be at odds with previously found members; or that the distribution of objects are various masses are in reasonable agreement with previous work on this cluster.

IC348\_CH4\_2 requires spectroscopy to confirm its authenticity as a T5.5 dwarf and IC 348 cluster member, currently hard to achieve with current ground and space based telescopes which would have to probe to  $J \sim 21$  mag. Burgasser (priv. comm.) suggested that the 10 m

Keck telescope<sup>1</sup> using NIRC-2 might be able to obtain a low resolution  $K_s$ -band spectrum. Collaboration would be required to achieve this as the Keck is not in part of the ESO operating program. It is strongly recommended to apply for time on the 6.5m James Webb Space Telescope (JWST) when it is operational some time in 2014, in order to obtain high a resolution spectrum of this object, and also to measure its proper motion and any possible association with another cluster member. Additionally, it would also be extremely informative to obtain spectra for the two unidentified objects which appeared to have quite blue  $z' - J$  colours. Comparison of the candidate T-dwarf, and the two rejected candidate objects to the new BT-Settl model might also be useful and worth doing as a comparison to how much the newer models agree with the analysis conducted previously. Cool subdwarfs have been put forward as an explanation for the identity of these two objects, but further analysis is required, comparing them to existing subdwarfs, at the derived extinction.

IC 348 also requires a full census to be taken using the data used for the methane analysis, though using a different detection image to avoid filtering on the methane narrowbands alone. The most recent census saw objects of masses as low as  $35 M_J$  detected to a completeness of  $A_v = 4$  mag, indicating the gap between the lowest-mass candidate T-dwarf so far detected in this cluster and the next least massive confirmed member. Alves Oliveria et al. (in Prep.) are currently working a census of this cluster using the broadband data that was used for the IC 348 work here.

Additionally, the datasets from both of these sets of work are able to be used in conjunction with future observations of each respective cluster to achieve proper motion estimates of the candidates discussed in this work.

### 5.3 Context

The main aim of Constellation Work Package 3 is to try to answer relevant questions aimed at explaining the origin of the lower mass objects that exist in the universe. To this end it is necessary to ask what their properties are, how they form, how the low-mass sequence in one particular cluster can be extrapolated to and tested on other more unknown clusters, and how this data can be used to the fullest extent.

- How do the lowest mass objects form?

Additional implications from this work is with respect to the models and how the discovery of this young and low-mass object in IC 348, and candidate discoveries of M and L-dwarfs in IC 4665, impact upon known star-formation and atmospheric models. Are they ejected embryos or can they form individually as mini-versions of a stellar disk? The work on IC 348 should help to

---

<sup>1</sup><http://www2.keck.hawaii.edu/inst/index.php>

further constrain the parameters and conditions required for modeling the formation of the lowest-mass isolated objects and how they can form within a time-scale of a few million years. The slight evidence for the existence of a disk around IC348\_CH4\_2 from *Spitzer* data could constrain the possibility of individual formation, however, it is entirely possible for objects to form in the disk around a more massive object which can then be perturbed from nearby objects in the, usually, densely populated cluster, increasing its eccentricity and allowing the object to take material from this disk to make a disk on its own. These objects could be classed not as an ejected embryo, but as a perturbed embryo as they are still bound to their parent disk. This would be less likely to happen in older clusters as they are usually more dynamically evolved and objects are spaced further apart.

- How do the lowest-mass objects affect the IMF?

The mass of the initial cloud which goes on to collapse and form a plethora of objects of differing masses is the main parameter for the distribution of masses of objects in the cluster, at a particular age. If the cloud is turbulent then the dynamical time-scale for ejection and expansion of the cloud is lower than for a more stable cloud, which could artificially skew the calculations of the IMF into having fewer lower mass members compared to higher mass members. The effect of turbulence could be offset by the possibility that a more turbulent cloud *also* produces more lower mass members than higher mass members for a more stable cloud.

- How do the lowest-mass objects overlap with the largest planets?

This question requires high resolution spectroscopy of the lowest-mass objects detected in this work to be taken. IC 4665 should have detected some early L-dwarfs but even these would be of the order of at least  $15 M_J$ . Jupiter is a 4.5 Gyr object that could have started as a late T-dwarf after its formation within the solar system's primordial disk, though its surface has now cooled to a mere  $\sim 550$  K and core  $T_{Eff}$  to just 125 K. The largest observed objects defined as planets reach upwards of  $30 M_J$  and are known as hot Jupiters, which also orbit within a few tens of AUs of the host star. Eccentricity could also be a defining factor as to how an object formed, and how long an object that is perturbed could re-synchronise its orbit with its host star.

IC348\_CH4\_2 has an estimated mass from the 3 Myr theoretical AMES-COND isochrone of between  $\sim 1 M_J$  to  $\sim 5 M_J$ , but with uncertainties registering possibly more than 50% this object could have a mass in the region of  $10 M_J$ . Objects of this mass and just a few lighter have been found circling other stars, or indeed, other brown dwarfs. More analysis and observations need to be undertaken in order to probe for any possible planetary companions around many known free floating brown dwarfs in these clusters.

- How does this work add to the current scientific understanding?

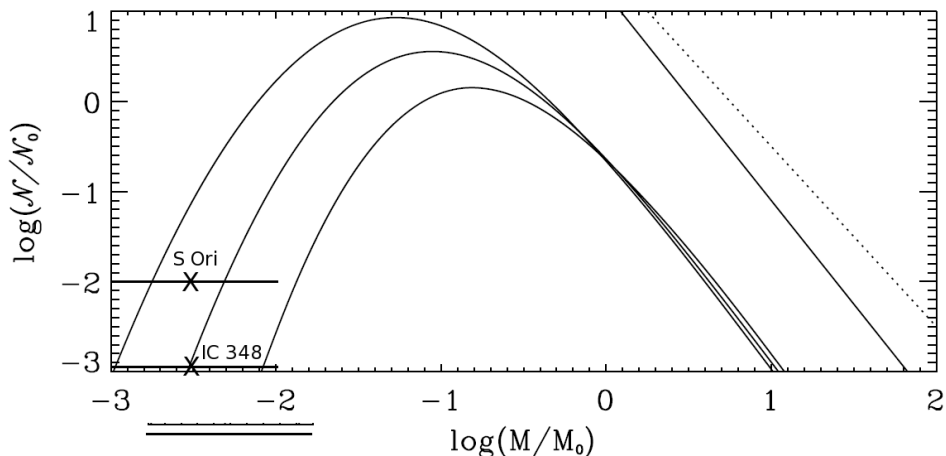


Figure 5.1: Detected objects between 1 and 10  $M_J$  for  $\sigma$  Orionis (8 objects in total) and IC 348 (1 object). The curves are the normalised mass function v.s. mass for predicted MF for different numerical simulations (and so different initial conditions) from Hennebelle and Chabrier (2009), and the diagonal lines are the power laws for the Salpeter value and unity.

The deeper census of IC 4665 should add to the IMF for this 30–50 Myr open cluster, which can be compared to existing data for other clusters, namely the Pleiades, the Trapezium cluster, Orion, to name but a few. In this way, differences between the age and masses of different clusters can be statistically examined in order to refine the initial conditions and to compare the frequency of low-mass and lowest mass objects. An additional use of these observations of IC 348 is to use it to extend the depth of the IMF into the brown dwarf regime, where the completeness limits given earlier for this cluster’s observations should allow objects of at least mid-L spectral type to be detected (Alves Oliveria et al. in Prep.).

## 5.4 Conclusion

The salient point of the work on IC 348 is the agreement, bar spectroscopic disagreement as to the nature of the candidate T-dwarf, with current estimates and the extrapolation of the lognormal IMF to the planetary-mass domain. This helps to confirm that the star-formation theories are broadly correct and that there is not a plethora of low mass objects hidden away at the low mass end of the IMF. In Figure 5.1 these results from IC 348 are compared with the number objects found in  $\sigma$  Orionis for a similar mass range (Zapatero Osorio et al., 2002; Caballero et al., 2007), overplotted onto the predictions of the IMF by Hennebelle and Chabrier (2009), based upon cloud collapsing models using different initial conditions from Hennebelle and Chabrier (2008). Whilst there are approximately ten times fewer objects in IC 348 than in  $\sigma$  Orionis it can be seen, interestingly, that in each case, the log-normal IMF can describe *both* paths, depending only on the initial conditions of the collapse of the cloud. The results for IC 348 support the notion that

the lower-mass end of the IMF is wholly dependent on the initial conditions and therefore will certainly vary from cluster to cluster unless the properties of the initial cloud, e.g. turbulence, mass and internal velocity, are similar. Further support for this notion will certainly require the detailed examination of additional clusters, and comparing this data with the predictions of the IMF.

Whilst it is slightly more difficult to conclude with the work stage reached with the IC 4665 data, it can be possible to conclude that the 510 possible candidates should span at least the M-dwarf range and probe into the L-dwarf spectral type range. If the comparison with the L- and M-dwarf domains are broadly correct then it also seems that this cluster should follow the IMF predictions to the lower mass domain, because there were not a multitude of possible low-mass objects detected in the L-dwarf region of colour/colour space. This, however, is entirely dependent on the selection criteria and it is still possible that many more L-dwarfs are detected in the observations but were not selected as discussed. T-dwarfs can still exist in this cluster but they will be very faint.

To conclude, further questions relating to this work can be raised and the original questions still proposed until a full and complete understanding of the theory of star formation is achieved:

- How do the lowest mass objects form?
- How do the lowest-mass objects affect the IMF?
- How do the lowest-mass objects overlap with the largest planets?
- What direct effects do gravity and age have on objects the IMF?
- How do the atmospheres of the lowest mass brown dwarfs evolve?
- How does a young cluster form the lowest mass objects?

## 5.5 Résumé

Le point saillant de l'ouvrage sur IC 348 est l'accord, bar désaccord spectroscopiques quant à la nature du candidat nain-T, avec des estimations actuelles et l'extrapolation des log-normale du FMI dans le domaine de masse planétaire. Cela permet de confirmer que les théories de formation d'étoiles sont globalement correcte et qu'il n'y a pas une multitude d'objets de faible masse cachée à la fin de faible masse du FMI. Dans la figure 5.1 ces résultats IC 348 sont comparés avec les objets trouvés dans le numéro de  $\sigma$  Orionis pour une gamme de masse similaire (Zapatero Osorio et al., 2002; Caballero et al., 2007), sous-plotté sur les prévisions du FMI par Hennebelle and Chabrier (2009), fondée sur les modèles nuage s'effondre en utilisant différentes conditions initiales de Hennebelle and Chabrier (2008). Alors, il ya environ dix fois moins objects en IC 348 que  $\sigma$  Orionis il peut être vu, il est intéressant que, dans chaque cas, le log-normale FMI peut décrire deux chemins, ne dépendant que de la conditions initiales de l'effondrement du nuage. Les résultats pour IC 348 appuient la notion que l'extrémité inférieure de masse du FMI est entièrement dépendant des conditions initiales et donc certainement varier d'un cluster à cluster, sauf si les propriétés du nuage initial, par exemple turbulence, la masse et la vitesse interne, sont similaires. Un appui supplémentaire pour cette notion qui nécessitera certainement l'examen détaillé des grappes supplémentaires, et en comparant ces données avec les prévisions du FMI.

Bien qu'il soit un peu plus difficile de conclure avec l'étape de travail conclu avec les données de IC 4665, il peut être possible de conclure que les 510 candidats possibles devrait s'étendre sur au moins les nain-M plage et de la sonde dans le nain-L de type spectral largeur. Si la comparaison avec les domaines L nains-M et sont globalement correcte, alors il semble également que ce groupe devrait suivre les prévisions du FMI dans le domaine de masse plus basse, parce qu'il n'y avait pas une multitude d'objets de faible masse détectés possible dans la région nain-L de couleur / espace de couleur. C'est dépend entièrement sur des critères de sélection et il est toujours possible que de nombreux autres nains-L sont détectées dans les observations mais n'ont pas été sélectionnés comme nous le verrons. nains-T peuvent encore exister dans ce groupe, mais ils seront très faibles.

Pour conclure, d'autres questions relatives à ces travaux peuvent être soulevées et les questions d'origine sont toujours proposées jusqu'à une compréhension pleine et entière de la théorie de la formation des étoiles est atteint:

- Comment masse la plus faible sous forme d'objets?
- Comment les objets les plus bas de masse affectent le FMI?
- Comment les objets les plus bas de masse chevauchement avec la plus grande des planètes?
- Quels sont les effets directs ne gravité et l'âge ont sur les objets du FMI?
- Comment les atmosphères de la plus faible masse des naines brunes évoluer?
- Comment un jeune amas forment les objets les plus bas de masse?





# Bibliography

- Allard, F., Allard, N. F., Homeier, D., Kielkopf, J., McCaughrean, M. J., and Spiegelman, F.:2007, *A&A* **474**, L21
- Allard, F., Guillot, T., Ludwig, H., Hauschildt, P. H., Schweitzer, A., Alexander, D. R., and Ferguson, J. W.:2003, in E. Martín (ed.), *Brown Dwarfs*, Vol. 211 of *IAU Symposium*, pp 325–+
- Allard, F., Hauschildt, P. H., Alexander, D. R., and Starrfield, S.:1997, *ARA&A* **35**, 137
- Allard, F., Hauschildt, P. H., Alexander, D. R., Tamanai, A., and Schweitzer, A.:2001, *ApJ* **556**, 357
- Allard, F., Homeier, D., and Freytag, B.:2010, *ArXiv e-prints*
- Alves de Oliveira, C., Moraux, E., Bouvier, J., Bouy, H., Marmo, C., and Albert, L.:2010, *A&A* **515**, A75+
- Asplund, M., Grevesse, N., Sauval, A. J., and Scott, P.:2009, *ARA&A* **47**, 481
- Bachiller, R., Guilloteau, S., and Kahane, C.:1987, *A&A* **173**, 324
- Baraffe, I. and Chabrier, G.:1996, *ApJ* **461**, L51+
- Baraffe, I., Chabrier, G., Allard, F., and Hauschildt, P. H.:1998, *A&A* **337**, 403
- Baraffe, I., Chabrier, G., Barman, T. S., Allard, F., and Hauschildt, P. H.:2003, *A&A* **402**, 701
- Barrado y Navascués, D., Bouvier, J., Stauffer, J. R., Lodieu, N., and McCaughrean, M. J.:2002, *A&A* **395**, 813
- Barrado y Navascués, D., Stauffer, J. R., Bouvier, J., Jayawardhana, R., and Cuillandre, J.-C.:2004, *ApJ* **610**, 1064

- Bate, M. R.:2009a, MNRAS **392**, 590
- Bate, M. R.:2009b, MNRAS **397**, 232
- Bate, M. R.:2009c, MNRAS **392**, 1363
- Bate, M. R. and Bonnell, I. A.:2005, MNRAS **356**, 1201
- Bate, M. R., Bonnell, I. A., and Bromm, V.:2002a, MNRAS **332**, L65
- Bate, M. R., Bonnell, I. A., and Bromm, V.:2002b, MNRAS **336**, 705
- Bate, M. R., Bonnell, I. A., and Bromm, V.:2003, MNRAS **339**, 577
- Bertin, E.:2008, *SAIt* **75**, 282
- Bertin, E. and Arnouts, S.:1996, A&AS **117**, 393
- Bertin, E., Mellier, Y., Radovich, M., Missonnier, G., Didelon, P., and Morin, B.:2002, in D. A. Bohlender, D. Durand, and T. H. Handley (eds.), *Astronomical Data Analysis Software and Systems XI*, Vol. 281 of *Astronomical Society of the Pacific Conference Series*, pp 228–+
- Bessell, M. S.:1990, PASP **102**, 1181
- Bessell, M. S.:2005, ARA&A **43**, 293
- Bessell, M. S. and Brett, J. M.:1988, PASP **100**, 1134
- Bessell, M. S., Castelli, F., and Plez, B.:1998, A&A **333**, 231
- Bihain, G., Rebolo, R., Zapatero Osorio, M. R., Béjar, V. J. S., and Caballero, J. A.:2010, *ArXiv e-prints*
- Boulade, O., Charlot, X., Abbon, P., Aune, S., Borgeaud, P., Carton, P.-H., Carty, M., Da Costa, J., Deschamps, H., Desforge, D., Eppellé, D., Gallais, P., Gosset, L., Granelli, R., Gros, M., de Kat, J., Loiseau, D., Ritou, J.-., Roussé, J. Y., Starzynski, P., Vignal, N., and Vigroux, L. G.:2003, in M. Iye and A. F. M. Moorwood (eds.), *Society of Photo-Optical Instrumentation Engineers (SPIE) Conference Series*, Vol. 4841 of *Presented at the Society of Photo-Optical Instrumentation Engineers (SPIE) Conference*, pp 72–81
- Bouvier, J., Kendall, T., Meeus, G., Testi, L., Moraux, E., Stauffer, J. R., James, D., Cuillandre, J., Irwin, J., McCaughrean, M. J., Baraffe, I., and Bertin, E.:2008, A&A **481**, 661
- Boyd, D. F. A. and Whitworth, A. P.:2005, A&A **430**, 1059

- Burgasser, A. J., Kirkpatrick, J. D., Brown, M. E., Reid, I. N., Gizis, J. E., Dahn, C. C., Monet, D. G., Beichman, C. A., Liebert, J., Cutri, R. M., and Skrutskie, M. F.:1999, *ApJ* **522**, L65
- Burgasser, A. J., Kirkpatrick, J. D., McGovern, M. R., McLean, I. S., Prato, L., and Reid, I. N.:2004, *ApJ* **604**, 827
- Burrows, A.:2009, in T. Henning, E. Grün, & J. Steinacker (ed.), *Astronomical Society of the Pacific Conference Series*, Vol. 414 of *Astronomical Society of the Pacific Conference Series*, pp 115–+
- Burrows, A., Hubbard, W. B., Lunine, J. I., and Liebert, J.:2001, *Reviews of Modern Physics* **73**, 719
- Burrows, A., Marley, M., Hubbard, W. B., Lunine, J. I., Guillot, T., Saumon, D., Freedman, R., Sudarsky, D., and Sharp, C.:1997, *ApJ* **491**, 856
- Burrows, A., Sudarsky, D., and Hubeny, I.:2006, *ApJ* **640**, 1063
- Caballero, J. A., Béjar, V. J. S., Rebolo, R., Eisloffel, J., Zapatero Osorio, M. R., Mundt, R., Barrado Y Navascués, D., Bihain, G., Bailer-Jones, C. A. L., Forveille, T., and Martín, E. L.:2007, *A&A* **470**, 903
- Cambrésy, L., Petropoulou, V., Kontizas, M., and Kontizas, E.:2006, *A&A* **445**, 999
- Cargile, P. A. and James, D. J.:2010, *AJ* **140**, 677
- Cernis, K.:1993, *Baltic Astronomy* **2**, 214
- Chabrier, G.:2003, *PASP* **115**, 763
- Chabrier, G., Baraffe, I., Allard, F., and Hauschildt, P.:2000, *ApJ* **542**, 464
- Chang, R., Shen, S., Hou, J., Shu, C., and Shao, Z.:2006, *MNRAS* **372**, 199
- Chapman, N. L., Mundy, L. G., Lai, S.-P., and Evans, II, N. J.:2008, *ArXiv e-prints* 809
- Cieza, L. and Baliber, N.:2006, *ApJ* **649**, 862
- de Wit, W. J., Bouvier, J., Palla, F., Cuillandre, J.-C., James, D. J., Kendall, T. R., Lodieu, N., McCaughrean, M. J., Moraux, E., Randich, S., and Testi, L.:2006, *A&A* **448**, 189
- Diolaiti, E., Bendinelli, O., Bonaccini, D., Close, L., Currie, D., and Parmeggiani, G.:2000, *A&AS* **147**, 335

Drimmel, R. and Spergel, D. N.:2001, ApJ **556**, 181

Faherty, J. K., Burgasser, A. J., Cruz, K. L., Shara, M. M., Walter, F. M., and Gelino, C. R.:2009, AJ **137**, 1

Fitzpatrick, E. L. and Massa, D.:2007, ApJ **663**, 320

Fortney, J. J., Marley, M. S., Saumon, D., and Lodders, K.:2008, ApJ **683**, 1104

Freudenreich, H. T.:1998, ApJ **492**, 495

Freytag, B., Allard, F., Ludwig, H., Homeier, D., and Steffen, M.:2010, A&A **513**, A19+

Fukugita, M., Ichikawa, T., Gunn, J. E., Doi, M., Shimasaku, K., and Schneider, D. P.:1996, AJ **111**, 1748

Gerbaldi, M., Faraggiana, R., Burnage, R., Delmas, F., Gómez, A. E., and Grenier, S.:1999, A&AS **137**, 273

Giampapa, M. S., Prosser, C. F., and Fleming, T. A.:1998, ApJ **501**, 624

Guieu, S., Dougados, C., Monin, J.-L., Magnier, E., and Martín, E. L.:2006, A&A **446**, 485

Guieu, S., Pinte, C., Monin, J.-L., Ménard, F., Fukagawa, M., Padgett, D. L., Noriega-Crespo, A., Carey, S. J., Rebull, L. M., Huard, T., and Guedel, M.:2007, A&A **465**, 855

Habets, G. M. H. J. and Heintze, J. R. W.:1981, A&AS **46**, 193

Halder, G., Callaerts, P., and Gehring, W. J.:1995, Nature **5**, 602

Hauschildt, P. H., Allard, F., and Baron, E.:1999, ApJ **512**, 377

Helling, C., Ackerman, A., Allard, F., Dehn, M., Hauschildt, P., Homeier, D., Lodders, K., Marley, M., Rietmeijer, F., Tsuji, T., and Woitke, P.:2008a, MNRAS **391**, 1854

Helling, C., Woitke, P., and Thi, W.:2008b, A&A **485**, 547

Hennebelle, P. and Chabrier, G.:2008, ApJ **684**, 395

Hennebelle, P. and Chabrier, G.:2009, ApJ **702**, 1428

Herbig, G. H.:1998, ApJ **497**, 736

Herbst, W.:2008, *Star Formation in IC 348*, pp 372–+

Hewett, P. C., Warren, S. J., Leggett, S. K., and Hodgkin, S. T.:2006, MNRAS **367**, 454

Hodgkin, S. T., Irwin, M. J., Hewett, P. C., and Warren, S. J.:2009, MNRAS **394**, 675

- Jeffries, R. D., Jackson, R. J., James, D. J., and Cargile, P. A.:2009, *MNRAS* **400**, 317
- Jones, H. R. A. and Tsuji, T.:1997, *ApJ* **480**, L39+
- Kendall, T. R., Bouvier, J., Moraux, E., James, D. J., and Ménard, F.:2005, *A&A* **434**, 939
- Kharchenko, N. V., Piskunov, A. E., Röser, S., Schilbach, E., and Scholz, R.:2005, *A&A* **438**, 1163
- Kirkpatrick, J. D., Reid, I. N., Liebert, J., Cutri, R. M., Nelson, B., Beichman, C. A., Dahn, C. C., Monet, D. G., Gizis, J. E., and Skrutskie, M. F.:1999, *ApJ* **519**, 802
- Kroupa, P.:2001, *MNRAS* **322**, 231
- Labita, M., Treves, A., and Falomo, R.:2008, *MNRAS* **383**, 1513
- Lada, C. J., Muench, A. A., Luhman, K. L., Allen, L., Hartmann, L., Megeath, T., Myers, P., Fazio, G., Wood, K., Muzerolle, J., Rieke, G., Siegler, N., and Young, E.:2006, *AJ* **131**, 1574
- Lada, E. A. and Lada, C. J.:1995, *AJ* **109**, 1682
- Langhoff, S. R. and Bauschlicher, Jr., C. W.:1994, in U. G. Jorgensen (ed.), *IAU Colloq. 146: Molecules in the Stellar Environment*, Vol. 428 of *Lecture Notes in Physics*, Berlin Springer Verlag, pp 310–+
- Lawrence, A., Warren, S. J., Almaini, O., Edge, A. C., Hambly, N. C., Jameson, R. F., Lucas, P., Casali, M., Adamson, A., Dye, S., Emerson, J. P., Foucaud, S., Hewett, P., Hirst, P., Hodgkin, S. T., Irwin, M. J., Lodieu, N., McMahon, R. G., Simpson, C., Smail, I., Mortlock, D., and Folger, M.:2007, *MNRAS* **379**, 1599
- Leggett, S. K., Saumon, D., Marley, M. S., Geballe, T. R., Golimowski, D. A., Stephens, D., and Fan, X.:2007, *ApJ* **655**, 1079
- Liu, M. C., Najita, J., and Tokunaga, A.:2003, in A. Brown, G. M. Harper, and T. R. Ayres (eds.), *The Future of Cool-Star Astrophysics: 12th Cambridge Workshop on Cool Stars, Stellar Systems, and the Sun (2001 July 30 - August 3)*, eds. A. Brown, G.M. Harper, and T.R. Ayres, (University of Colorado), 2003, p. 141-147., Vol. 12, pp 141–147
- Lodieu, N., Burningham, B., Hambly, N. C., and Pinfield, D. J.:2009a, *MNRAS* pp 802–+
- Lodieu, N., Hambly, N. C., Jameson, R. F., Hodgkin, S. T., Carraro, G., and Kendall, T. R.:2007,

- Lodieu, N., Zapatero Osorio, M. R., Rebolo, R., Martin, E. L., and Hambly, N. C.:2009b, *ArXiv e-prints*
- Luhman, K. L.:1999, *ApJ* **525**, 466
- Luhman, K. L.:2004, *ApJ* **614**, 398
- Luhman, K. L., Adame, L., D'Alessio, P., Calvet, N., McLeod, K. K., Bohac, C. J., Forrest, W. J., Hartmann, L., Sargent, B., and Watson, D. M.:2007a, *ApJ* **666**, 1219
- Luhman, K. L., Lada, C. J., Hartmann, L., Muench, A. A., Megeath, S. T., Allen, L. E., Myers, P. C., Muzerolle, J., Young, E., and Fazio, G. G.:2005a, *ApJ* **631**, L69
- Luhman, K. L., Lada, E. A., Muench, A. A., and Elston, R. J.:2005b, *ApJ* **618**, 810
- Luhman, K. L., Mamajek, E. E., Allen, P. R., Muench, A. A., and Finkbeiner, D. P.:2009, *ApJ* **691**, 1265
- Luhman, K. L., McLeod, K. K., and Goldenson, N.:2005c, *ApJ* **623**, 1141
- Luhman, K. L., Patten, B. M., Marengo, M., Schuster, M. T., Hora, J. L., Ellis, R. G., Stauffer, J. R., Sonnett, S. M., Winston, E., Gutermuth, R. A., Megeath, S. T., Backman, D. E., Henry, T. J., Werner, M. W., and Fazio, G. G.:2007b, *ApJ* **654**, 570
- Luhman, K. L., Rieke, G. H., Young, E. T., Cotera, A. S., Chen, H., Rieke, M. J., Schneider, G., and Thompson, R. I.:2000, *ApJ* **540**, 1016
- Luhman, K. L., Stauffer, J. R., Muench, A. A., Rieke, G. H., Lada, E. A., Bouvier, J., and Lada, C. J.:2003, *ApJ* **593**, 1093
- Luyten, W. J.:1961, in *The Observatory, Univ. Minnesota, Minneapolis, 1953*, *23, 1 (1961)*, pp 1–+
- Magnier, E. A. and Cuillandre, J.:2004, *PASP* **116**, 449
- Mainzer, A. K. and McLean, I. S.:2003, *ApJ* **597**, 555
- Manzi, S., Randich, S., de Wit, W. J., and Palla, F.:2008, *A&A* **479**, 141
- Martín, E. L.:2004, *ArXiv Astrophysics e-prints*
- Martín, E. L., Basri, G., and Zapatero Osorio, M. R.:1999a, *AJ* **118**, 1005

- Martín, E. L., Delfosse, X., Basri, G., Goldman, B., Forveille, T., and Zapatero Osorio, M. R.:1999b, *AJ* **118**, 2466
- Martin, E. L. and Montes, D.:1997, *A&A* **318**, 805
- Martin, E. L., Rebolo, R., and Zapatero-Osorio, M. R.:1996, *ApJ* **469**, 706
- McLean, I. S., McGovern, M. R., Burgasser, A. J., Kirkpatrick, J. D., Prato, L., and Kim, S. S.:2003, *ApJ* **596**, 561
- Mermilliod, J. C.:1981, *A&A* **97**, 235
- Metchev, S. A., Kirkpatrick, J. D., Berriman, G. B., andLooper, D.:2008, *ApJ* **676**, 1281
- Momany, Y., Zaggia, S., Gilmore, G., Piotto, G., Carraro, G., Bedin, L. R., and de Angeli, F.:2006, *A&A* **451**, 515
- MorauX, E., Bouvier, J., and Clarke, C.:2005, *Astronomische Nachrichten* **326**, 985
- MorauX, E., Bouvier, J., Stauffer, J. R., Barrado y Navascués, D., and Cuillandre, J.-C.:2007, *A&A* **471**, 499
- MorauX, E., Bouvier, J., Stauffer, J. R., and Cuillandre, J.-C.:2003, *A&A* **400**, 891
- MorauX, E., Kroupa, P., and Bouvier, J.:2004, *A&A* **426**, 75
- Muench, A. A., Lada, C. J., Luhman, K. L., Muzerolle, J., and Young, E.:2007, *AJ* **134**, 411
- Muench, A. A., Lada, E. A., Lada, C. J., and Alves, J.:2002, *ApJ* **573**, 366
- Muench, A. A., Lada, E. A., Lada, C. J., Elston, R. J., Alves, J. F., Horrobin, M., Huard, T. H., Levine, J. L., Raines, S. N., and Román-Zúñiga, C.:2003, *AJ* **125**, 2029
- Muzerolle, J., Flaherty, K., Balog, Z., Furlan, E., Herbst, W., and Rieke, G.:2010, in *Bulletin of the American Astronomical Society*, Vol. 41 of *Bulletin of the American Astronomical Society*, pp 355–+
- Najita, J. R., Tiede, G. P., and Carr, J. S.:2000, *ApJ* **541**, 977
- Nakajima, T., Oppenheimer, B. R., Kulkarni, S. R., Golimowski, D. A., Matthews, K., and Durrance, S. T.:1995, *Nature* **378**, 463
- Oppenheimer, B. R., Kulkarni, S. R., Matthews, K., Nakajima, T., and Golimowski, D. A.:1996, in *Bulletin of the American Astronomical Society*, Vol. 28 of *Bulletin of the American Astronomical*



- Society*, pp 1300–+
- Oppenheimer, B. R., Kulkarni, S. R., Matthews, K., and van Kerkwijk, M. H.:1998, *ApJ* **502**, 932
- Padoan, P. and Nordlund, A.:1997, *ArXiv Astrophysics e-prints*
- Padoan, P. and Nordlund, Å.:2002, *ApJ* **576**, 870
- Padoan, P. and Nordlund, Å.:2004, *ApJ* **617**, 559
- Partridge, H. and Schwenke, D. W.:1997, *J. Chem. Phys.* **106**, 4618
- Pasquini, L., Avila, G., Blecha, A., Cacciari, C., Cayatte, V., Colless, M., Damiani, F., de Propriis, R., Dekker, H., di Marcantonio, P., Farrell, T., Gillingham, P., Guinouard, I., Hammer, F., Kaufer, A., Hill, V., Marteaud, M., Modigliani, A., Mulas, G., North, P., Popovic, D., Rossetti, E., Royer, F., Santin, P., Schmutzer, R., Simond, G., Vola, P., Waller, L., and Zoccali, M.:2002, *The Messenger* **110**, 1
- Patten, B. M., Stauffer, J. R., Burrows, A., Marengo, M., Hora, J. L., Luhman, K. L., Sonnett, S. M., Henry, T. J., Raghavan, D., Megeath, S. T., Liebert, J., and Fazio, G. G.:2006, *ApJ* **651**, 502
- Pöhl, H. and Paunzen, E.:2010, *A&A* **514**, A81+
- Preibisch, T., Stanke, T., and Zinnecker, H.:2003, *A&A* **409**, 147
- Prosser, C. F.:1993, *AJ* **105**, 1441
- Prosser, C. F. and Giampapa, M. S.:1994, *AJ* **108**, 964
- Puget, P., Stadler, E., Doyon, R., Gigan, P., Thibault, S., Luppino, G., Barrick, G., Benedict, T., Forveille, T., Rambold, W., Thomas, J., Vermeulen, T., Ward, J., Beuzit, J.-L., Feautrier, P., Magnard, Y., Mella, G., Preis, O., Vallee, P., Wang, S.-y., Lin, C.-J., Hall, D. N., and Hodapp, K. W.:2004, in A. F. M. Moorwood and M. Iye (eds.), *Society of Photo-Optical Instrumentation Engineers (SPIE) Conference Series*, Vol. 5492 of *Presented at the Society of Photo-Optical Instrumentation Engineers (SPIE) Conference*, pp 978–987
- Rebolo, R., Zapatero Osorio, M. R., and Martín, E. L.:1995, *Nature* **377**, 129
- Reipurth, B. and Clarke, C.:2001, *AJ* **122**, 432
- Rieke, G. H. and Lebofsky, M. J.:1985, *ApJ* **288**, 618

- Salpeter, E. E.:1955, ApJ **121**, 161
- Saumon, D., Hubbard, W. B., Burrows, A., Guillot, T., Lunine, J. I., and Chabrier, G.:1996, ApJ **460**, 993
- Savage, B. D. and Mathis, J. S.:1979, ARA&A **17**, 73
- Scholz, A., Eislöffel, J., and Mundt, R.:2009, MNRAS **400**, 1548
- Scholz, A. and Jayawardhana, R.:2008, ApJ **672**, L49
- Scholz, R.-D., Brunzendorf, J., Ivanov, G., Kharchenko, N., Lasker, B., Meusinger, H., Preibisch, T., Schilbach, E., and Zinnecker, H.:1999, A&AS **137**, 305
- Skrutskie, M. F., Cutri, R. M., Stiening, R., Weinberg, M. D., Schneider, S., Carpenter, J. M., Beichman, C., Capps, R., Chester, T., Elias, J., Huchra, J., Liebert, J., Lonsdale, C., Monet, D. G., Price, S., Seitzer, P., Jarrett, T., Kirkpatrick, J. D., Gizis, J. E., Howard, E., Evans, T., Fowler, J., Fullmer, L., Hurt, R., Light, R., Kopan, E. L., Marsh, K. A., McCallon, H. L., Tam, R., Van Dyk, S., and Wheelock, S.:2006, AJ **131**, 1163
- Stelzer, B., Micela, G., Flaccomio, E., and Sciortino, S.:2009, in E. Stempels (ed.), *American Institute of Physics Conference Series*, Vol. 1094 of *American Institute of Physics Conference Series*, pp 628–631
- Tafalla, M., Kumar, M. S. N., and Bachiller, R.:2006, A&A **456**, 179
- Thibault, S., Cui, Q., Poirier, M., Vallee, P., Doyon, R., Rabou, P., and Salmon, D. A.:2003, in M. Iye and A. F. M. Moorwood (eds.), *Society of Photo-Optical Instrumentation Engineers (SPIE) Conference Series*, Vol. 4841 of *Presented at the Society of Photo-Optical Instrumentation Engineers (SPIE) Conference*, pp 932–943
- Tinney, C. G., Burgasser, A. J., Kirkpatrick, J. D., and McElwain, M. W.:2005, AJ **130**, 2326
- Vallée, J. P.:2005, AJ **130**, 569
- Wegner, W.:2003, *Astronomische Nachrichten* **324**, 219
- Whitworth, A. P. and Stamatellos, D.:2006, A&A **458**, 817
- Whitworth, A. P. and Zinnecker, H.:2004, A&A **427**, 299
- Wuchterl, G. and Tscharnuter, W. M.:2003, A&A **398**, 1081

Zapatero Osorio, M. R., Béjar, V. J. S., Bihain, G., Martín, E. L., Rebolo, R., Villó-Pérez, I., Díaz-Sánchez, A., Pérez Garrido, A., Caballero, J. A., Henning, T., Mundt, R., Barrado Y Navascués, D., and Bailer-Jones, C. A. L.:2008, *A&A* **477**, 895

Zapatero Osorio, M. R., Béjar, V. J. S., Martín, E. L., Rebolo, R., Barrado y Navascués, D., Mundt, R., Eislöffel, J., and Caballero, J. A.:2002, *ApJ* **578**, 536

# Appendix

## TERAPIX Configuration

### TERAPIX command

Command line used at TERAPIX during the processing.

```
sex *_newxt.fits *_newxt.fits -c qualityFITS.sex -CATALOG_NAME *_newxt.ldac
-CHECKIMAGE_TYPE -OBJECTS -CHECKIMAGE_NAME *_newxt_mob.fits
-PARAMETERS_NAME qualityFITS.param -STARANNW_NAME qualityFITS.nnw
-WEIGHT_IMAGE *_newxt.weight.fits,*_newxt.weight.fits
-FLAG_IMAGE *_newxt_flag.fits -DETECT_MINAREA 3 -DETECT_THRESH 1.5
-ANALYSIS_THRESH 1.5 -FILTER_NAME gauss_2.5_5x5.conv -MAG_ZEROPOINT 30.
-SATUR_LEVEL 100000 -WRITE_XML Y -XML_NAME sex.xml -PHOT_APERTURES 10
-MAG_ZEROPOINT 30.0
```

### TERAPIX input files

Input files used for the TERAPIX processing.

```
qualityFITS.sex
qualityFITS.param
qualityFITS.nnw
gauss_2.5_5x5.conv
```

### TERAPIX filter: gauss.2.5.5x5.conv

Example of the gauss.2.5.5x5.conv detection filter.

```
CONV NORM
```

```

# 5x5 convolution mask of a gaussian PSF with FWHM = 2.5 pixels.
0.034673 0.119131 0.179633 0.119131 0.034673
0.119131 0.409323 0.617200 0.409323 0.119131
0.179633 0.617200 0.930649 0.617200 0.179633
0.119131 0.409323 0.617200 0.409323 0.119131
0.034673 0.119131 0.179633 0.119131 0.034673

```

## TERAPIX neural network file: qualityFITS.nnw

Galaxy neural network file.

NNW

# Neural Network Weights for the SExtractor star/galaxy classifier (V1.3)

# inputs: 9 for profile parameters + 1 for seeing.

# outputs: ``Stellarity index`` (0.0 to 1.0)

# Seeing FWHM range: from 0.025 to 5.5'' (images must have 1.5 < FWHM < 5 pixels)

# Optimized for Moffat profiles with 2<= beta <= 4.

3 10 10 1

-1.56604 -2.48265 -1.44564 -1.24675 -0.94491 -0.52245 0.04613 0.83196 2.15505 0.26477  
3.03477 2.69561 3.16188 3.34497 3.51885 3.65570 3.74856 3.84541 4.22811 3.27734

-0.32248 -2.12804 0.65075 -1.11242 -1.40683 -1.55944 -1.84558 -0.11895 0.55240 -0.43656 -5.30052  
0.46259 -3.29127 1.10950 -0.60186 0.12949 1.42290 2.90741 2.44058 -0.91912 0.84285 -4.69824  
-2.57424 0.89647 0.83478 2.18845 2.46526 0.08609 -0.68808 -0.01336 0.09304 1.64942 -1.01231  
4.81041 1.53747 -1.12216 -3.16008 -1.67404 -1.75767 -1.29310 0.55955 0.80847 -0.01016 -7.54052  
10.19330 -20.94840 -1.07426 0.98791 0.60521 -0.06045 -0.58783 -0.79412 -0.48919 -0.08127 -20.70670  
-5.31793 7.94240 -4.64165 -4.37436 -1.55417 0.75437 1.09608 1.45967 1.62946 -1.01301 0.11351  
0.22034 1.70056 -0.52011 -0.42833 0.00157 -0.33650 -0.08186 -7.16163 8.23195 -0.01716 -11.37490  
3.75075 7.25399 -1.75325 -2.68814 -3.71128 -4.62933 -2.13747 -0.18919 1.29122 -0.74938 0.67171  
-0.84192 4.64997 0.56581 -0.30828 -1.01687 0.17313 -0.89213 1.89044 -0.27554 -0.77283 0.53675  
-3.65598 7.56997 -3.76373 -1.74542 -0.13754 -0.55540 -0.15920 0.12791 1.91906 1.42119 -4.35502

-1.70059 -3.65695 1.22367 -0.57437 -3.29571 2.46316 5.22353 2.42038 1.22919 -0.92225 -2.32028

0.00000

1.00000

## TERAPIX configuration qualityFITS.sex

### SExtractor Configuration file.

```
#-----
# Default configuration file for SExtractor 2.4.2
# EB 2005-09-22
#

# #cfhtls shows parameters different from the default value (sex -d)

#----- Catalog -----

CATALOG_NAME      test.ldac #cfhtls # name of the output catalog
CATALOG_TYPE      FITS_LDAC #cfhtls # "NONE", "ASCII_HEAD", "ASCII", "FITS_1.0"
                  # "FITS_LDAC" or "FITS_TPX"

PARAMETERS_NAME   default.param # name of the file containing catalog contents

#----- Extraction -----

DETECT_TYPE       CCD          # "CCD" or "PHOTO"
FLAG_IMAGE        flag.fits    # filename for an input FLAG-image
WEIGHT_TYPE       MAP_WEIGHT #cfhtls # e.g. map_weight
DETECT_MINAREA    3           #cfhtls # minimum number of pixels above threshold
DETECT_THRESH     1.5         # <sigmas> or <threshold>,<ZP> in mag.arcsec-2
ANALYSIS_THRESH  1.5         # <sigmas> or <threshold>,<ZP> in mag.arcsec-2

FILTER            Y           # apply filter for detection ("Y" or "N")?
FILTER_NAME       default.conv # name of the file containing the filter

DEBLEND_NTHRESH   32          # Number of deblending sub-thresholds
DEBLEND_MINCONT   0.002 #cfhtls # Minimum contrast parameter for deblending

CLEAN             Y           # Clean spurious detections? (Y or N)?
CLEAN_PARAM       1.0         # Cleaning efficiency

MASK_TYPE         CORRECT     # type of detection MASKing: can be one of
                              # "NONE", "BLANK" or "CORRECT"

#----- Photometry -----

PHOT_APERTURES    27          #cfhtls # MAG_APER aperture diameter(s) in pixels
PHOT_AUTOPARAMS   2.5, 3.5    # MAG_AUTO parameters: <Kron_fact>,<min_radius>
PHOT_PETROPARAMS 2.0, 3.5    # MAG_PETRO parameters: <Petrosian_fact>,<min_radius>

SATUR_LEVEL       30000.0 #cfhtls # level (in ADUs) at which arises saturation

MAG_ZEROPOINT     0.0         # magnitude zero-point
MAG_GAMMA         4.0         # gamma of emulsion (for photographic scans)
GAIN              0.0         # detector gain in e-/ADU
PIXEL_SCALE       0           #cfhtls # size of pixel in arcsec (0=use FITS WCS info)
```

```

#----- Star/Galaxy Separation -----

SEEING_FWHM      0.9      #cfhtls # stellar FWHM in arcsec
STARNNW_NAME     default.nnw # Neural-Network_Weight table filename

#----- Background -----

BACK_SIZE        64          # Background mesh: <size> or <width>,<height>
BACK_FILTERSIZE  3          # Background filter: <size> or <width>,<height>

BACKPHOTO_TYPE   GLOBAL      # can be "GLOBAL" or "LOCAL"

#----- Check Image -----

CHECKIMAGE_TYPE  NONE        # can be one of "NONE", "BACKGROUND",
                              # "MINIBACKGROUND", "-BACKGROUND", "OBJECTS",
                              # "-OBJECTS", "SEGMENTATION", "APERTURES",
                              # or "FILTERED"
CHECKIMAGE_NAME  check.fits  # Filename for the check-image

#----- Memory (change with caution!) -----

MEMORY_OBJSTACK  5000      #cfhtls # number of objects in stack
MEMORY_PIXSTACK  400000   #cfhtls # number of pixels in stack
MEMORY_BUFSIZE   1024      # number of lines in buffer

#----- Miscellaneous -----

VERBOSE_TYPE     NORMAL     # can be "QUIET", "NORMAL" or "FULL"

```

## Extraction

### Extraction Configuration files

The SExtractor first and second-pass configuration files are similar to the TERAPIX files.

```

#----- PSF model -----

BASIS_TYPE       PIXEL_AUTO  # NONE, PIXEL, GAUSS-LAGUERRE or FILE
BASIS_NUMBER     16          # Basis number or parameter

#PSF_NAME        IC348_CH4Off.psf # Output PSF filename
PSF_ACCURACY     0.01        # Accuracy to expect from PSF "pixel" values
#PSF_NSUPER      0           # Max number of super-resolved pixels
PSF_SAMPLING     0.0         # Sampling step in pixel units (0.0 = auto)
PSF_SIZE         51,51       # Image size of the PSF model
                              #, note: only takes these stars into account
PSF_RECENTER    Y           # Allow recentering of PSF-candidates Y/N ?

#----- Sample selection -----

```

```

SAMPLE_AUTOSELECT Y          # Automatically select the FWHM (Y/N) ?
SAMPLEVAR_TYPE     SEEING    # File-to-file PSF variability: NONE or SEEING
SAMPLE_FWHMRANGE  1.5,4.5    # Allowed FWHM range
SAMPLE_VARIABILITY 0.3       # Allowed PSF variability (1.0 = 100%)
SAMPLE_MINSN      100        # Minimum S/N for a source to be used
SAMPLE_MAXELLIP   0.3       # Maximum A/B for a source to be used
BADPIXEL_FILTER Y          # Filter bad-pixels in samples (Y/N) ?
BADPIXEL_NMAX     0          # Maximum number of bad pixels allowed

#----- PSF dependencies -----

PSFVAR_KEYS       X_IMAGE,Y_IMAGE # SExtractor or FITS (preceded by :) params
PSFVAR_GROUPS     1,1           # Group tag for each context key
PSFVAR_DEGREES    2            # Polynom degree for each group
#CONTEXT_NSAP     7            # Number of PSF snapshots per axis

#----- Check-plots -----

CHECKPLOT_DEV      PNG          # NULL, XWIN, TK, PS, PSC, XFIG,PNG,
                          # or JPEG
CHECKPLOT_TYPE     FWHM,ELLIPTICITY # NONE, FWHM or ELLIPTICITY
CHECKPLOT_NAME     fwhm, ellipticity

#----- Check-Images -----

CHECKIMAGE_TYPE    SNAPSHOTS # Check-image types PROTOTYPES
# ,SAMPLES,RESIDUALS,RAWDATA,SNAPSHOTS,MOFFFAT,-MOFFFAT,-SYMMETRICAL

CHECKIMAGE_NAME    snap.fits # Check-image filenames

#CHECKIMAGE_TYPE  CHI,PROTOTYPES,SAMPLES,RESIDUALS,SNAPSHOTS,MOFFFAT
# , -MOFFFAT, -SYMMETRICAL
#CHECKIMAGE_NAME  chi.fits,proto.fits,samp.fits,resi.fits,snap.fits
# ,mofffat.fits,submofffat.fits,subsym.fits

#----- Galaxy Principal Components -----

#PC_INCLUDE        N          # Process galaxy Principal Components (Y/N) ?
#PC_NAME           default.pc # File to store galaxy Principal Components
#PC_NPC            0          # Number of principal components

#----- Miscellaneous -----

PSF_SUFFIX         .psf       # Filename extension for output PSF filename
VERBOSE_TYPE       NORMAL     # can be QUIET,NORMAL,LOG or FULL
WRITE_XML          N          # Write XML file (Y/N)?
XML_NAME           psfex40.xml # Filename for XML output
XSL_URL            file:///usr/local/share/psfex/psfex.xsl # Filename for XSL style-sheet
NTHREADS          1          # 1 single thread

```



## Extraction Parameter files

The parameters used in this work are listed below. .

Table 1: The parameters that are included for IC 4665 and IC 348. Not the Vignet for the first-pass needs to be of similar dimensions as 'PHOT\_APERTURE' in the configuration.sex file, and also for the 'PSF\_SIZE' in the PSFEx file

Parameter		
first-pass	second-pass	Notes
-	NUMBER	
VIGNET(35,35)	-	
FLUX_APER(1)	FLUX_APER(1)	
-	FLUXERR_APER(1)	
-	MAG_APER(1)	
-	MAGERR_APER(1)	
-	FLUX_PSF	
-	FLUXERR_PSF	
-	MAG_PSF	
-	MAGERR_PSF	
-	MAG_AUTO	
-	MAGERR_AUTO	
-	KRON_RADIUS	
FLUX_MAX	FLUX_MAX	
FLUX_RADIUS	FLUX_RADIUS	
X_IMAGE	X_IMAGE	
Y_IMAGE	Y_IMAGE	
-	ALPHA_J2000	
-	DELTA_J2000	
FLAGS	FLAGS	
-	IMAFLAGS_ISO(1)	
-	#CHI2_PSF(2)	#fails to function new version at LAOG
ELONGATION	ELONGATION	
-	ELLIPTICITY	

## Example Scripts

The work for IC 4665 made heavy use of awk to manipulate the data variables, Smongo to interpret and analysis the data, and bash shell scripts to automate these processes. Of course these multiple shell scripts were then run using a single command from the terminal. The work conducted for IC 348 used no such automation, unfortunately, and time was spent manually making the extraction scripts for the SExtractor passes and PSFex into a text file to run in the command line.

Of course, time was further lost due to human (my) error with misplaced variables. The work for IC 4665 was conducted after IC 348.

Below is an example of the preliminary bright star extraction script for the short *H*-band for field A in IC 4665, where the parameter file and the configuration files can be found in the Appendix 5.5 & 5.5 respectively: `sex IC4665A_H_newxt.fits -c prepsfex.sex -PARAMETERS_NAME sex1.param -CATALOG_NAME LDAC_IC4665A_H.P16.fits -DETECT_THRESH 15.0 -ANALYSIS_THRESH 15.0 -PHOT_APERTURES 31 -FLAG_IMAGE IC4665A_H_newxt.flag.fits -GAIN 1.777276524E+01 -SATUR_LEVEL 5.795242200E+05 -FILTER_NAME gauss_2.5_5x5.conv -SEEING_FWHM 1.22 -BACK_SIZE 64 -BACK_FILTERSIZE 3 -WEIGHT_IMAGE IC4665A_H_newxt.weight.fits,`

for PSFEx: `psfex LDAC_IC4665A_H.P16.fits -c psfex.psfex -PSF_SIZE 35 -SAMPLE_MINSN 100 -PSFVAR_GROUPS 1,1 -PSFVAR_DEGREES 2 -CHECKIMAGE_TYPE SNAPSHOTS -CHECKIMAGE_NAME psfex1_snap_IC4665A_H.P16.chk.fits,`

and finally for the second-pass of SExtractor for the short images: `sex IC4665A_J_newxt.fits,IC4665A_H_newxt.fits -c postpsfex.sex -PARAMETERS_NAME sex2.param -CATALOG_NAME H/sex2_IC4665A_H.P16_psfexed.cat -DETECT_THRESH 1.5 -ANALYSIS_THRESH 1.5 -GAIN 1.777276524E+01 -SATUR_LEVEL 5.795242200E+05 -PHOT_APERTURES 15 -FLAG_IMAGE IC4665A_J_newxt.flag.fits,IC4665A_H_newxt.flag.fits -WEIGHT_IMAGE IC4665A_J_newxt.weight.fits,IC4665A_H_newxt.weight.fits -PSF_NAME H/LDAC_IC4665A_H.P16.psf -BACK_SIZE 64 -BACK_FILTERSIZE 3 -FILTER_NAME gauss_2.5_5x5.conv -CHECKIMAGE_TYPE -PSF_PROTOS -CHECKIMAGE_NAME H/res_IC4665A_H.chk.fits.`

Scripts were used for most purposes when dealing with this large dataset; 216 input files including weight maps and flag maps for the object extraction (SExtractor/PSFEx) meant automation was immediately necessary and obvious.

This section of example code is a double nested awk script in order to output the business-end of the plotting smongo scripts for the candidate selection. This was required to be double-nested as in initial input file 'CLUSTER\_fields.input.txt' there were the 12 fields and in the second file 'CLUSTER\_splots.txt' the various colour/magnitude and colour/colour plots. Note the use of `"\047"` for a nested `" ' "`, and the use of `" \\"` to escape characters so they are active in the next awk script.

## Candidate Selection IDL script

This script is tailored version originally compiled by C. Alves de Oliveira, where a candidate is selected if any part of it with errors falls close enough to the interpolated ('interpol' command) model isochrone, as described in Section 3.4. The business part of the IDL CMD selection script follows, whilst the COLD selection script is similar but includes both less than and greater than the model isochrone in order to collect objects in a band around the models that fulfil the selection criteria:

```
;CMD J vs J-H
int4y=interpol(jhcfht50,jcfht50,j(mark)-sqrt(jerr(mark)^2.+0.14^2.))
int4x=interpol(jhcfht50,jcfht50,j(mark))
int4m=interpol(jh2cfht50,j2cfht50,j(mark)+sqrt(jerr(mark)^2.+0.14^2.))
int4n=interpol(jh2cfht50,j2cfht50,j(mark))
int4a=interpol(jhcfht30,jcfht30,j(mark)-sqrt(jerr(mark)^2.+0.14^2.))
int4b=interpol(jhcfht30,jcfht30,j(mark))
int4c=interpol(jh2cfht30,j2cfht30,j(mark)+sqrt(jerr(mark)^2.+0.14^2.))
int4d=interpol(jh2cfht30,j2cfht30,j(mark))
mark_yjhk=WHERE (( j(mark)-h(mark)-jherr ge int4a or j(mark)-h(mark)-jherr ge int4b $
or j(mark)-h(mark)-jherr ge int4c or j(mark)-h(mark)+jherr ge int4a $
or j(mark)-h(mark)+jherr ge int4b or j(mark)-h(mark)+jherr ge int4c) $
OR ( j(mark)-h(mark) ge int4a or j(mark)-h(mark) ge int4b or j(mark)-h(mark) ge int4c) $
OR ( j(mark)-h(mark) ge int4a and j(mark)-h(mark)+jherr ge int4b) $
OR ( j(mark)-h(mark) ge int4a and j(mark)-h(mark)-jherr ge int4b) $
OR ( j(mark)-h(mark) ge int4c and j(mark)-h(mark)+jherr ge int4d) $
OR ( j(mark)-h(mark) ge int4c and j(mark)-h(mark)-jherr ge int4d) $
OR ( j(mark)-h(mark)-jherr ge int4y or j(mark)-h(mark)-jherr ge int4x $
or j(mark)-h(mark)-jherr ge int4m or j(mark)-h(mark)+jherr ge int4y $
or j(mark)-h(mark)+jherr ge int4x or j(mark)-h(mark)+jherr ge int4m) $
OR ( j(mark)-h(mark) ge int4y or j(mark)-h(mark) ge int4x or j(mark)-h(mark) ge int4m) $
OR ( j(mark)-h(mark) ge int4y and j(mark)-h(mark)+jherr ge int4x) $
OR ( j(mark)-h(mark) ge int4y and j(mark)-h(mark)-jherr ge int4x) $
OR ( j(mark)-h(mark) ge int4m and j(mark)-h(mark)+jherr ge int4n) $
OR ( j(mark)-h(mark) ge int4m and j(mark)-h(mark)-jherr ge int4n) ) )
```

## SuperMongo

Data was read into smongo using this terminology:

```
#input directory and filename
data "~/AMALG/thin/"CALIB_IC4665A_YJKs_SP.cat
```

```
#assigned columns and labels for object magnitudes
    read {A_CAL_Y 2 A_CAL_J 4 A_CAL_H 6A_CAL_Ks 8}
#sets colour, can be used for other calculations
    set A_YminusJ = A_CAL_Y - A_CAL_J
```

## Script Input

Bash shell script utilising awk to automatically output a set of files which can be run within the SuperMongo environment. Note that it is possible to run SuperMongo within the shell script for full automation.

```
awk '!/^#/ && $1~/[A-E]/ {print " awk
\047!/^#/ && $1~/SP/ && $2~/M/{print \"echo
\047 \\t window \"(-$23),(-$24),$25,$26\" \\n \\t expand 1.0 \\n \\t ctype 0 ptype 1 1
\\n \\t limits \"($8),($9),($10),($11)\" \\n \\t box 1 2 3 3 \\n \\t ylabel \"\$4\"
\\n \\t expand 0.8 \\n \\t points \"$16\"_\"$6\"minus\"$7\" \"$16\"_CAL_\"$4\"
\\n \\t ctype 4 ptype 4 3 angle 45 \\n \\t points man_\"$6\"minus\"$7\" man_CAL_\"$4\"
\\n \\t expand 0.5 ctype 3 ptype 1 1 \\n \\t points \"$6$7\"_\"$6\"minus\"$7\" \"$6$7\"_CAL_\"$4\"
\\n \\t ctype 3 ptype 20 3 \\n \\t points cand_\"$6\"minus\"$7\" cand_CAL_\"$4\"
\\n \\t expand 1\\n \\t
\047 >> \"$3\"_\"$16\".sm \" }
\047 $DIR6/CLUSTER_smplots.txt >> cluster_plot.sh "
}' $DIR6/CLUSTER_fields_input.txt >> cluster.sh
```

## Script Output

The candidates are taken from the IDL extraction script described in Section 3.4 and found here in the Appendix 5.5. File Y.vs..JH\_A.sm:

```
window -1 -2 1 2 #position in output plot
expand 1.0 #size adjustment
ctype 0 ptype 1 1 #colour and shape of IC 4665 catalogue objects
limits -1.5 3 24 9 #axes limits
box 1 2 3 3 #plot area
expand 0.8 #colour and shape of points
points A_JminusH A_CAL_Y #objects plotted from field A
ctype 4 ptype 4 3 angle 45 #colour and shape of manzi et al. 2008 points
points man_JminusH man_CAL_Y #confirmed IC 4665 members from the Manzi et al. 2008 work
```

```

ctype 3 ptype 20 3          #colour and shape of IC 4665 candidates objects
points cand_JminusH cand_CAL_Y #IC 4665 candidates objects from IDL extraction script

```

## Dispersion Script

This is the active part of the dispersion Smongo script, adapted from the script from Bouvier (priv. comm), which has been used in both Chapters 3 and 4 to calculate statistics on the dispersed datasets. The output gives either a mean or a median, depending on the dispersion and also an rms of the dispersion away from this mean/median value. Again this was scripted to work on all bands and fields. <magnitude> and <difference in magnitude> are taken directly from the extracted catalogues. <parameters> include details about the field, filter used, and particular dispersion run.

```

#dispersion script
set starmin = 50
set nbin = 4
set dim = dimen(<magnitude>) - 1
define _dim (dim+1)
if (dim >= starmin) {
define _nbin (nbin)
define _nstarperbin (int((dim+1.)/nbin))
do j=1,nbin {
set DIMEN(bin1$j) = $_nstarperbin
}
do j=1,nbin {
set DIMEN(binlmin$j) = $_nbin
set DIMEN(binlmax$j) = $_nbin
}
do j=1,nbin {
define binlmin$j (int(1.e3*<magnitude>[(j-1)*$_nstarperbin])/1.e3)
define binlmax$j (int(1.e3*<magnitude>[j*$_nstarperbin-1])/1.e3)
}
do j=1,nbin {
define _nmin ((j-1)*$_nstarperbin)
define _nmax ( j*$_nstarperbin)
define _compt (0)
do i=0,dim {
if ( $i >= $_nmin && $i < $_nmax) {
set bin1$j[_compt] = <difference in magnitude>[$i]
define _compt ($_compt+1)
}
}
}
do j=1,nbin {
stats_med bin1$j med1$j siqr1$j
define med1$j (int(1.e3*$med1$j)/1000.)
}
set DIMEN(meandiff1) = $_nbin
do j=1,nbin {
set meandiff1[j-1] = $med1$j
}
stats meandiff1 mean1 sig1 kurt1

```

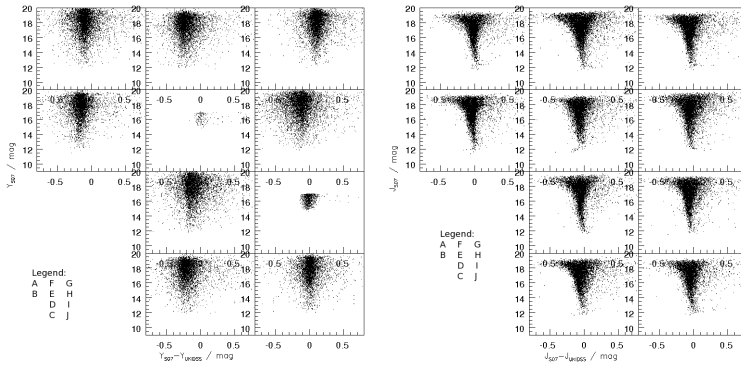
```

stats_med meandiff1 med1 sig1
echo <field> <filter> <mode> $mean1 +/- $sig1
define med1 (int(1.e3*$med1)/1.e3)
define mean1 (int(1.e3*$mean1)/1.e3)
define sig1 (int(1.e3*$sig1)/1.e3)
write +<filename_<parameters>.disp> <parameters> $mean1 pm $sig1 $_dim $med1
}

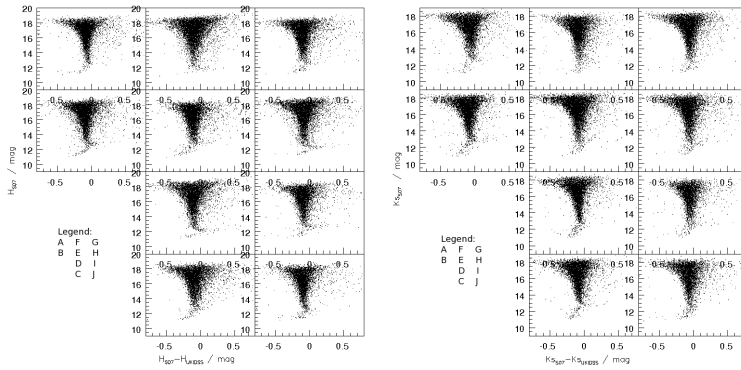
```

## Saturation Limit

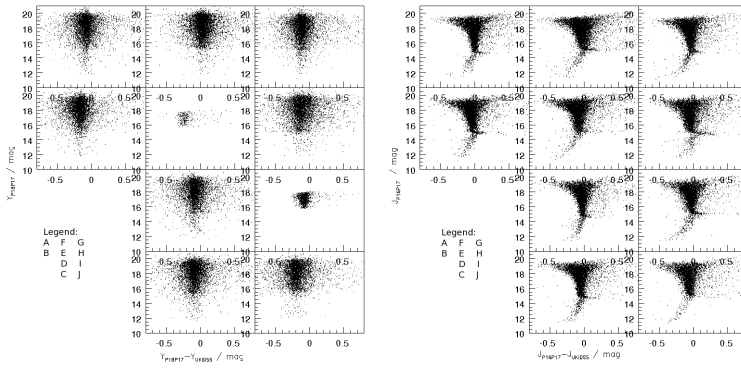
Figure 2 shows the IC 4665 magnitudes against the difference between the data and the UKIDSS data which had matching objects over the field of view. These plots were used to ascertain our own SAT flags in lieu of the TERAPIX or SExtractor flags. This was because there were many objects that were bright enough to appear in the non-linearity part of the detector, yet were not fully saturated as detailed by the TERAPIX pipeline. Additional objects that had their saturated centres removed can only be expunged from the catalogues on an object-by-object basis, for example in the Candidate extraction. This is because the magnitudes are given by our SExtractor/PSFEx/SExtractor extraction routines and so they appear far fainter than they should as they have no centre to their PSF, yet are a detected object.



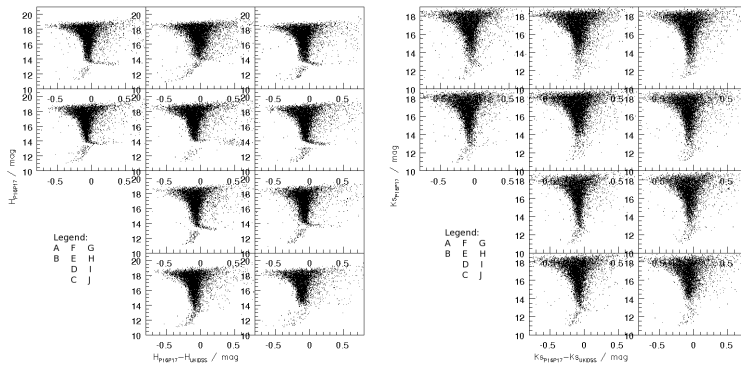
(a) *L-R*: Short *Y* and *J*-UKIDSS bands exposures.



(b) *L-R*: Short *H* and *K<sub>s</sub>*-UKIDSS bands exposures.



(c) *L-R*: Long *Y* and *J*-UKIDSS bands exposures.



(d) *L-R*: Long *H* and *K<sub>s</sub>*-UKIDSS bands exposures.

Figure 2: Saturation plots showing the offsets between the CFHT IC 4665 data and UKIDSS data over the same FOV. Fields labelled A through to J as per the legends. Note lack of data in fields E and I in the *Y*-band plots due to lack of matching *Y*-band UKIDSS data. Note also the much lower level of saturated objects compared to the UKIDSS bands in the short exposures than in the long exposures.





